

Physics beyond the Standard Model: Exploring Dark Matter and Leptoquarks at the Large Hadron Collider

Stefan Andreas Schulte

Vollständiger Abdruck der von der TUM School of Natural Sciences der Technischen Universität München zur Erlangung des akademischen Grades eines

Doktors der Naturwissenschaften (Dr. rer. nat.)

genehmigten Dissertation.

Vorsitz:

Prof. Dr. Bastian Märkisch

Prüfer*innen der Dissertation:

1. Prof. Dr. Andreas Weiler
2. Priv.-Doz. Dr. Mathias Garny

Die Dissertation wurde am 08.05.2023 bei der Technischen Universität München eingereicht und durch die TUM School of Natural Sciences am 29.05.2023 angenommen.



Physics beyond the Standard Model: Exploring Dark Matter and Leptoquarks at the Large Hadron Collider

Stefan Andreas Schulte

MAX-PLANCK-INSTITUT
FÜR PHYSIK



München 2023

Acknowledgments

I was only able to complete this dissertation thanks to the support of a great number of people. First, I would like to thank Ulrich Haisch for his supervision and the many discussions about physics. Moreover, I would like to express my gratitude toward Andreas Weiler for accepting me as a doctoral student in his group at TUM. I would also like to thank Giulia Zanderighi for her hospitality as the group leader at MPP and all the colleagues at the institute. My time there would not have been the same without the many chats with Giordano Cintia, Daniele Lombardi, Alessandro Ratti, Darren Scott, William Torres Bobadilla, Marius Wieseemann, and Silvia Zanoli. In particular, I would like to thank my former office mates Amando Hala and Gabriël Koole, who have been important references for both work-related and personal matters throughout my Ph.D. journey. In this regard, I would also like to especially thank Luc Schnell, who has, moreover, been an amazing collaborator on our joint projects, as presented in Chap. 4. I am thankful for the support of the SFB 1258 and all the people from the IMPRS EPP. The latter includes Frank Steffen, who I am especially indebted to for his role as a mentor and advisor. I am grateful for the collaboration with Giacomo Polesello, and I would also like to thank Robert Harlander for providing me access to beta versions of `FeynGame`. Furthermore, I would like to thank the authors of Ref. [319] for their valuable input regarding the work presented in Chap. 3.

My doctorate took place in very unusual times—both globally and personally—and I am beyond grateful for the many people who supported me in moments of distress. This applies to all my close friends, both from my time in Aachen and from my hometown Menden. Above and beyond, I want to thank my family for their never-ending love and support. My parents, Doris and Andreas, have provided me with care throughout my whole life and have supported me in every life decision. I am also thankful to my brothers and their partners, Johannes and Katharina, and Christoph and Miriam. I will never forget that Greta and Valentin were always able to make me smile and forget about whatever was worrying me. Lastly, my deepest gratitude belongs to my love, Giorgia. Without her everlasting patience soothing me in moments of doubt, I would have never made it to this point.

Abstract

Exploring the phenomenology of elementary particle interactions at the Large Hadron Collider (LHC) represents one of the most promising research directions to directly discover new particles beyond the Standard Model (BSM) at high energies. In this dissertation, we consider two popular BSM models to address some of the most profound questions of the Standard Model (SM). First, we examine the prospects of producing pseudo Nambu–Goldstone boson Dark Matter (pNGB DM) in association with top quarks. Models in which both a candidate for DM and the SM Higgs boson emerge as pNGBs from a strongly-coupled sector at the TeV scale provide solutions to the DM puzzle as well as the electroweak hierarchy problem. The couplings of pNGB DM to SM particles generically evade the stringent constraints from direct detection experiments but suggest considerable interactions with top quarks. Therefore, we expect BSM contributions to the $t\bar{t} + E_T^{\text{miss}}$, $tW + E_T^{\text{miss}}$, and mono-jet channels. In addition, pNGB DM contributes to the invisible decay width of the SM Higgs boson. In order to provide a comprehensive overview of the pNGB DM phenomenology, we further investigate DM annihilations relevant to explain the observed DM relic abundance and to derive constraints from indirect detection experiments. Moreover, we analyze how loop-induced interactions with the SM gauge bosons can improve the discovery potential of direct detection experiments. Next, we study the sensitivity of non-resonant dilepton searches at the LHC to the presence of TeV-scale leptoquarks (LQs). LQs are a generic consequence of Grand Unification and can alleviate the recently observed flavor anomalies and the anomalous magnetic moment of the muon. Among the three established search strategies for LQs at the LHC, non-resonant dilepton production via the t -channel exchange of an LQ is the most promising discovery opportunity for LQs with larger masses. We compute the $\mathcal{O}(\alpha_s)$ corrections to the tree-level process for both scalar S_1/\tilde{S}_1 LQs and vector U_1 LQs within the UV-complete 4321 model. We implement our calculations into the `POWHEG-BOX` hence providing a Monte Carlo event generator crucial for future precision studies of LQ phenomenology at the LHC. Furthermore, we particularly demonstrate how the requirement of b -jets accompanying the dilepton pair in the final state can significantly enhance the sensitivity of the LHC to the presence of LQs. Our results improve the existing experimental limits published by the ATLAS and CMS collaborations.

Zusammenfassung

Die Erforschung der Phänomenologie der Elementarteilchenwechselwirkungen am Large Hadron Collider (LHC) stellt eine der vielversprechendsten Forschungsrichtungen dar, um direkt neue Teilchen jenseits des Standardmodells (BSM) bei hohen Energien zu entdecken. In dieser Dissertation betrachten wir zwei verschiedene populäre BSM-Modelle, welche einige der tiefgreifendsten Fragen des Standardmodells (SM) lösen. Zunächst untersuchen wir die Aussichten auf die Erzeugung von Dunkler Materie (DM) als pseudo-Nambu-Goldstone-Bosonen (pNGBs) in Verbindung mit Top-Quarks. Modelle, in denen sowohl ein Kandidat für DM als auch das SM-Higgs-Boson als pNGBs aus einem stark gekoppelten Sektor an der TeV-Skala hervorgehen, bieten Lösungen für das DM-Problem sowie das elektroschwache Hierarchieproblem. Die Kopplungen von pNGB DM an SM-Teilchen entziehen sich im Allgemeinen den strengen Einschränkungen von Experimenten zum direkten Nachweis, gewähren allerdings relevante Wechselwirkungen mit Top-Quarks. Daher erwarten wir BSM-Beiträge zu den $t\bar{t} + E_T^{\text{miss}}$ -, $tW + E_T^{\text{miss}}$ - und Mono-Jet-Kanälen. pNGB DM trägt außerdem zur unsichtbaren Zerfallsbreite des SM-Higgs-Bosons bei. Um einen umfassenden Überblick über die Phänomenologie von pNGB DM zu geben, untersuchen wir ferner DM-Annihilationen, die für die Erklärung der beobachteten Menge von DM im Universum relevant sind, und leiten Beschränkungen aus indirekten Nachweisexperimenten ab. Darüber hinaus analysieren wir, wie schleifeninduzierte Wechselwirkungen mit den SM-Eichbosonen das Entdeckungspotenzial von Experimenten zum direkten Nachweis verbessern können. Als nächstes untersuchen wir die Sensitivität nicht-resonanter Dilepton-Suchen am LHC auf die Existenz von Leptoquarks (LQs) an der TeV-Skala. LQs sind eine generische Konsequenz der Großen Vereinheitlichung und können u.A. die kürzlich beobachteten Flavor-Anomalien und das anomale magnetische Moment des Myons erklären. Unter den drei etablierten Suchstrategien für LQs am LHC ist die nicht-resonante Dileptonproduktion über den t -Kanal-Austausch eines LQs der vielversprechendste Weg, LQs mit größeren Massen zu entdecken. Wir berechnen die $\mathcal{O}(\alpha_s)$ -Korrekturen für den Prozess führender Ordnung sowohl für skalare S_1/\tilde{S}_1 LQs als auch für vektorielle U_1 LQs innerhalb des Ultraviolett-vollständigen 4321-Modells. Wir implementieren unsere Berechnungen in die POWHEG-BOX und entwickeln damit einen Monte-Carlo-Event-Generator, der für zukünftige Präzisionsstudien der LQ-Phänomenologie am LHC entscheidend ist. Außerdem demonstrieren wir insbesondere, wie die Bedingung, dass das Dileptonenpaar im Endzustand von b -Jets begleitet wird, die Sensitivität des LHC auf die Existenz von

LQs deutlich erhöhen kann. Unsere Ergebnisse verbessern die bestehenden experimentellen Ausschlussgrenzen, die von den ATLAS- und CMS-Kollaborationen veröffentlicht wurden.

Preface

This dissertation is based on the publications:

- [1] U. Haisch, G. Polesello and S. Schulte, *Searching for pseudo Nambu-Goldstone boson dark matter production in association with top quarks*, *JHEP* **09** (2021) 206 [[2107.12389](#)],
- [2] U. Haisch, L. Schnell and S. Schulte, *On Drell-Yan production of scalar leptoquarks coupling to heavy-quark flavours*, *JHEP* **11** (2022) 106 [[2207.00356](#)],
- [3] U. Haisch, L. Schnell and S. Schulte, *Drell-Yan production in third-generation gauge vector leptoquark models at NLO+PS in QCD*, *JHEP* **02** (2023) 70 [[2209.12780](#)].

During the course of the doctorate, also the following paper was published:

- [4] F. Kahlhoefer, A. Mück, S. Schulte and P. Tunney, *Interference effects in dilepton resonance searches for Z' bosons and dark matter mediators*, *JHEP* **03** (2020) 104 [[1912.06374](#)].

Since the latter piece of work is based on a collaboration prior to the doctorate, we refrain from discussing it in further detail. The contents of this thesis presuppose a solid knowledge of Quantum Field Theory and General Relativity, as provided by Refs. [5–11]. We acknowledge the comprehensive *Review of Particle Physics* that is updated regularly by the PARTICLE DATA GROUP (see, e.g., Refs. [12, 13]) and served as a useful reference for any topic related to particle physics phenomenology.

The results presented in this thesis rely on a variety of different dedicated codes that shall be acknowledged. For our analytical calculations, we made use of the `Mathematica` packages `FeynArts` [14], `FormCalc` [15], `Package-X` [16, 17], and `FeynCalc` [18–20]. The numerical evaluation of loop integrals was assisted by `LoopTools` [15]. Model files both for `FeynArts` and in the UFO format [21] for Monte Carlo event generators were created using `FeynRules` [22, 23]. Events were generated using `MadGraph` [24] and `MadSpin` [25], as well as the POWHEG-BOX [26–30]. The generators made use of the LHAPDF library [31] for parton distribution functions, and generated events in the LHE format [32] were showered using `PYTHIA 8` [33–35]. The resulting event files in the HEPMC format [36] were analyzed using `MadAnalysis 5` [37–42] and `CheckMATE 2` [43–45]. Both these codes make use of `FastJet` [46, 47] for jet modeling and `DELPHES 3` [48] as a detector simulation

tool. For the numerical calculation of the relic abundance of Dark Matter in the present universe, we utilized `micrOMEGAs` [49], which employs the `CalcHEP` [50] format. Feynman diagrams in this dissertation were created with `FeynGame` [51].

Contents

Acknowledgments	iii
Abstract	v
Zusammenfassung	vii
Preface	ix
List of Figures	xiii
Acronyms	xv
1 Introduction	1
2 Review of the Standard Model of Particle Physics	9
2.1 The Standard Model of Particle Physics	9
2.2 The Standard Model and the Cosmological History of the Universe . . .	22
3 Probing Pseudo Nambu–Goldstone Boson Dark Matter Interactions with Top Quarks	27
3.1 An Introduction to pNGB Dark Matter	27
3.2 Theoretical Framework	31
3.3 MC Event Generation and Detector Simulation	33
3.4 Mono- X Analysis Strategies	35
3.4.1 $tX + E_T^{\text{miss}}$ Final States	35
3.4.2 $j + E_T^{\text{miss}}$ Final State	40
3.5 Constraints from $tX + E_T^{\text{miss}}$ and $j + E_T^{\text{miss}}$ Searches at the LHC	41
3.6 Constraints from Invisible Higgs Decays at the LHC	42
3.7 Constraints from DM (In)Direct Detection and the Relic Density	45
3.7.1 pNGB DM scattering off Atomic Nuclei	45
3.7.2 The Annihilation of pNGB DM in the Early and Present Universe	48
3.8 Discussion	51
4 Searching for Leptoquarks in the Dilepton Channel at the LHC	57
4.1 An Introduction to Leptoquarks	57

4.2	Scalar Leptoquarks in the Dilepton Channel	65
4.2.1	NLO Calculations of SLQ-mediated Dilepton Production	66
4.2.2	Phenomenological Analyses	71
4.2.2.1	Inclusive Light Dilepton Final States	71
4.2.2.2	Light Dilepton Final States with one b -Jet	74
4.2.2.3	Heavy Dilepton Final States with and without a b -Jet	76
4.2.3	Exclusion Limits	78
4.3	Vector Leptoquarks in the Dilepton Channel	81
4.3.1	The 4321 Model	83
4.3.2	Renormalization at $\mathcal{O}(\alpha_s)$	86
4.3.3	Numerical Applications	91
4.3.3.1	The Partial Decay Width $U \rightarrow b\tau$	91
4.3.3.2	NLO Dilepton Production	94
4.3.4	Phenomenological Analyses	98
4.3.5	Exclusion Limits	100
4.4	Conclusion on Leptoquarks	104
5	Concluding Remarks	109
A	Appendix	113
A.1	The Dark Matter Relic Abundance and the WIMP Miracle	113
A.2	The Direct Detection of Dark Matter	116
A.3	Systematic Errors for the Higgs Portal Operators of pNGB DM	119
A.4	Ditau Production from Z' Exchange	119
	Bibliography	123

List of Figures

3.1	Feynman diagrams for $t\bar{t} + E_T^{\text{miss}}$ and $tW + E_T^{\text{miss}}$ production from DM-Higgs interaction.	34
3.2	Feynman diagrams for $t\bar{t} + E_T^{\text{miss}}$ and $tW + E_T^{\text{miss}}$ production from DM-top interaction.	35
3.3	Example Feynman diagrams for DM-top interactions mixing into marginal Higgs portal operator.	44
3.4	Example Feynman diagrams for pNGB DM interacting with SM gauge bosons via one-loop DM-Higgs and DM-top interactions.	46
3.5	Example diagrams for loop-induced DM annihilation into photons.	50
3.6	Constraints in the $m_\chi - f$ plane for the derivative Higgs portal model.	52
3.7	Constraints in the $m_\chi - f$ plane for the derivative Higgs portal model with additional Yukawa-type DM-top interactions.	53
3.8	Constraints in the $m_\chi - f$ plane for the derivative Higgs portal model with additional current-current-type DM-top interactions.	53
3.9	Constraints in the $m_\chi - \lambda $ plane for the marginal Higgs portal model.	54
4.1	Generic leptoquark interactions.	58
4.2	Leptoquark contributions to Lepton Flavor Universality Violation observables.	60
4.3	Pair and single production of leptoquarks at hadron colliders.	61
4.4	Leptoquark tree-level diagram for $\ell^+\ell^-$ production at hadron colliders.	62
4.5	Generic QCD corrections to $\ell^+\ell^-$ production with leptoquarks.	63
4.6	Mixed electroweak and leptoquark contributions to $u\bar{u} \rightarrow \mu^+\mu^-$	69
4.7	Inclusive $pp \rightarrow \mu^+\mu^-$ production cross sections as functions of $m_{\mu\mu}$ for scalar leptoquarks.	72

4.8	Dependence of scalar leptoquark contributions to $\mu^+\mu^-$ production on leptoquark mass and couplings.	73
4.9	Inclusive $pp \rightarrow \mu^+\mu^-$ production cross sections with scalar leptoquarks as functions of $m_{\mu\mu}$ for two different b -jet categories.	75
4.10	Distributions of m_T^{tot} in the no b -tag and the b -tag categories in the $\tau_h^+\tau_h^-$ final state generated from scalar leptoquarks.	78
4.11	Exclusion limits from $\mu^+\mu^-$ and $\tau^+\tau^-$ production on scalar leptoquarks coupling to bottom quarks.	79
4.12	Exclusion limits from $\mu^+\mu^-$ and $\tau^+\tau^-$ production on scalar leptoquarks coupling to strange and charm quarks.	81
4.13	Feynman diagrams for the $\mathcal{O}(\alpha_s)$ renormalization of the 4321 model. . .	87
4.14	Numerical size of the $\mathcal{O}(\alpha_s)$ correction to the partial decay width $U \rightarrow b\tau$ as a function of the coloron mass $M_{G'}$	93
4.15	Inclusive $pp \rightarrow \tau^+\tau^-$ production cross sections with vector leptoquarks as functions of $m_{\tau\tau}$	96
4.16	Dependence of vector leptoquark contributions to $\tau^+\tau^-$ production on leptoquark mass and coupling.	97
4.17	Distributions of m_T^{tot} in the no b -tag and the b -tag category in the final state containing two hadronic tau leptons from vector leptoquarks. . .	99
4.18	Exclusion limits from $\tau^+\tau^-$ production on vector leptoquarks.	101
4.19	Further exclusion limits from $\tau^+\tau^-$ production on vector leptoquarks. .	103
A.1	Constraints in the m_χ - f plane for the derivative Higgs portal model and in the m_χ - $ \lambda $ plane for the marginal Higgs portal model for different systematic background uncertainties.	118
A.2	Distributions of m_T^{tot} in the no b -tag and the b -tag category in the final state containing two hadronic tau leptons from vector leptoquarks and Z' bosons.	120

Acronyms

ATLAS	A Toroidal LHC Apparatus
BNL	Brookhaven National Laboratory
BSM	Beyond the Standard Model
CDF	Collider Detector at Fermilab
CDM	Cold Dark Matter
CKM	Cabibbo–Kobayashi–Maskawa
CL	Confidence Level
CM	Center of Mass
CMB	Cosmic Microwave Background
CMS	Compact Muon Solenoid
DM	Dark Matter
DY	Drell–Yan
EFT	Effective Field Theory
EW	Electroweak
EWsb	Electroweak Symmetry Breaking
FCC	Future Circular Collider
FCNC	Flavor-Changing Neutral Current
FLRW	Friedman–Lemaître–Robertson–Walker
GIM	Glashow–Iliopoulos–Maiani
GR	General Relativity
GSW	Glashow–Salam–Weinberg
GUT	Grand Unified Theory
HE	High-Energy
HL	High-Luminosity
IR	Infrared

LAT	Large Area Telescope
LFU	Lepton Flavor Universality
LHC	Large Hadron Collider
LHCb	Large Hadron Collider beauty
LL	Leading Logarithmic
LO	Leading Order
LQ	Leptoquark
MC	Monte Carlo
MFV	Minimal Flavor Violation
MSSM	Minimal Supersymmetric Model
NLO	Next-to-Leading Order
NNLO	Next-to-Next-to-Leading Order
NR	Non-Relativistic
OS	Opposite-Sign
OSSF	Opposite-Sign Same-Flavor
PDF	Parton Distribution Function
pNGB	pseudo Nambu–Goldstone Boson
PQ	Peccei–Quinn
PS	Parton Shower
PV	Passarino–Veltman
QCD	Quantum Chromodynamics
QED	Quantum Electrodynamics
QFT	Quantum Field Theory
QM	Quantum Mechanics
RG	Renormalization Group
RGE	Renormalization Group Equation
SI	Spin Independent
SLAC	Stanford Linear Accelerator
SLQ	Scalar Leptoquark

SM	Standard Model of Particle Physics
SMEFT	Standard Model Effective Field Theory
SR	Signal Region
SSB	Spontaneous Symmetry Breaking
SUSY	Supersymmetry
ToE	Theory of Everything
UV	Ultraviolet
VBF	Vector-Boson Fusion
VEV	Vacuum Expectation Value
VLQ	Vector Leptoquark
WIMP	Weakly-Interacting Massive Particle

1 Introduction

Modern particle physics thrives as a result of decades of curiosity for the most fundamental truths about the universe. It is the story of a constant exchange of insights and the collaboration of the theoretical and experimental physics communities, culminating in the formulation of the Standard Model of Particle Physics (SM) in the 1960s and its experimental completion in the year 2012 with the discovery of the Higgs boson at the Large Hadron Collider (LHC) at CERN. It is the very interplay between theory and experiment that nurtures progress in the field and leads to a profound understanding of nature. Striving for a comprehensive description of the organization of the fundamental building blocks of the universe and the confrontation with experimental data fosters innovation in the field. The many examples of the past guide the continuing efforts toward a consistent picture of reality.

In the 1920s, quantum mechanics (QM) was established as a theory describing the physics of atoms at energy scales of the order of 1 eV accurately. However, being formulated in agreement with the energy conservation laws from classical mechanics, it was unclear how QM should be modified at high energies in order to be consistent with Einstein's Special Theory of Relativity [52] which describes the physics close to the speed of light. Early attempts to generalize QM led to the discovery of the Klein–Gordon equation, which still lacked an explanation of the spin of the electron. Relatedly, it led to incorrect energy spectra of the hydrogen atom, contradicting the results predicted by the non-relativistic Schrödinger equation. In 1928, Dirac succeeded in formulating an adequate equation describing the physics of electrons by introducing the spinor representation of the Lorentz group. Intriguingly, the resulting Dirac equation not only described electrons correctly as spin- $\frac{1}{2}$ fermions, but it also predicted its antiparticle, the positron [53–55]. Its existence as a fundamental particle was confirmed just four years later by Anderson [56], which was the first observation of antimatter. This represents a perfect example of how mathematical knowledge and theoretical insight drive scientific progress and pave the way to new experimental discoveries. Moreover, Dirac's theory correctly predicts the g factor of the electron at the leading order, relating the

particle's magnetic moment to its spin. While $g_e = 2$ has to be imposed ad hoc in non-relativistic QM, it is a direct consequence of its relativistic generalization. The findings of Dirac laid the foundation for the formulation of Quantum Electrodynamics (QED) as the first proper relativistic Quantum Field Theory (QFT), which remains among the most precisely tested scientific theories until this day. To give an astounding example: the anomalous magnetic moment of the electron, as predicted at the fourth loop order in QED, is known up to seven significant digits and is in perfect agreement with current measurements [57, 58].

Pauli's postulation of the neutrino in 1930 was rooted in advances in nuclear physics [59]. As opposed to α decays of radioactive nuclei, β decays lead to continuous energy spectra of emitted electrons, contradicting the assumption of a two-body decay process. After Pauli's proposal of a third decay product, Fermi was able to formulate an effective theory, including the novel neutrino, to describe the physics of β decays, explaining the observed electron spectra. The direct observation of the only weakly-interacting neutrino succeeded in 1956 [60–62].

The back-and-forth between theory and experiment continued in the era of particle colliders. After the early successes and the establishment of the quark model to explain the observed spectrum of hadrons, particle theory lacked an explanation for the absence of flavor-changing neutral currents (FCNCs) in experiments. However, in 1970, an explanation for this non-observation was found by means of the Glashow–Iliopoulos–Maiani (GIM) mechanism [63]. At the time of its proposal, only up, down, and strange quarks were known. For the GIM mechanism to work, the existence of a fourth quark was required. Just four years later, with the almost simultaneous observation of the J/ψ meson at the Stanford Linear Accelerator (SLAC) and the Brookhaven National Laboratory (BNL) [64, 65], the existence of the charm quark was established as a scientific fact.

Indirect CP violation was first observed in kaon decays in 1964 [66]. However, it took almost a decade to understand that this could not be explained by any theory with only two generations of quarks. In 1973, the formulation of the Cabibbo–Kobayashi–Maskawa (CKM) matrix [67, 68] provided a simple explanation of the riddle while it required the existence of at least a third quark generation, i.e., two more quarks left to discover. In the aftermath, the bottom quark was found already in 1977 at Fermilab [69], whereas the top quark was just discovered in 1995 by the CDF and $D\bar{O}$ experiments at the same facility [70, 71]. The latter discovery completed the search for quarks within the SM. In the context of Adler–Bell–Jackiw anomalies [72, 73], it became clear that for the SM to be consistent, the number of quark and lepton generations have

to match. Hence, the 1975 discovery of the τ lepton [74], which constitutes the third generation of leptons, already anticipated the existence of a third quark generation.

The most famous example of this intertwining of theory and experiment is the discovery of the Higgs boson. In the early 1960s, particle physics only had a weak theoretical footing. At the time, it was known that the existence of massive gauge bosons, namely the W and Z bosons, spoils the gauge symmetry used to describe the interactions of fundamental particles. Therefore, the renormalizability of the theory is compromised. A series of independent papers in 1964 proposed the spontaneous breaking of gauge symmetries as a solution to the conundrum [75–79], offering a dynamical explanation for the presence of gauge-boson masses. Intriguingly, it was further noted that this Brout–Englert–Higgs mechanism predicts the existence of a scalar particle, namely the Higgs boson, that couples to all other particles with a strength proportional to their respective masses. Drawing on these results as well as the theoretical advances of Glashow and Salam on the structure of weak interactions [80, 81], Weinberg was able to formulate a unified theory for electromagnetic and weak interactions in 1967 [82]. This electroweak (EW) theory, sometimes referred to as the GSW model after its most relevant contributors, predicted the existence of a massive neutral gauge boson, the Z boson. The first indirect observation of weak neutral currents succeeded already in 1973 by the Gargamelle collaboration at CERN [83–85]. The direct detection of the Z boson supervened in 1983 at the UA1 and UA2 detectors at the Super Proton-Antiproton Synchrotron at CERN [86–90]. EW theory combined with Quantum Chromodynamics (QCD) make up the SM as it is known today. With ’t Hooft’s proof of the renormalizability of spontaneously broken non-abelian gauge theories in 1971 [91–93], the SM was ready to be established as the leading paradigm of particle physics for the decades to come.

When the operation of the LHC started in 2008, it was guaranteed that it would either find the Higgs boson or discover some new physics beyond the SM (BSM) that would change our view on nature entirely. This peculiarity led to the idiom *no-lose theorem* (see, for instance, Ref. [94]). From the theory side, driven by unitarity arguments, it was understood that an SM-like Higgs boson must have a rest mass below $\mathcal{O}(1\text{ TeV})$. This can be derived from a partial wave analysis of massive gauge-boson scattering, implying either the existence of the Higgs boson or the breakdown of perturbation theory [95, 96]. Furthermore, the experimental 95 % confidence level (CL) upper bound on the Higgs mass derived from LEP data was $m_h \lesssim 166\text{ GeV}$ at the time [97].

These energy regimes are accessible with the LHC. Hence, finding the SM Higgs boson or something completely new was the dedicated goal of the research program of the LHC. Finally, in 2012, the ATLAS and CMS collaborations reported the observation of a scalar boson with a rest mass of around 125 GeV [98, 99]. Further studies confirmed its evenness under CP transformations [100–102] and that its Yukawa couplings are in perfect agreement with the assumption of the SM Higgs boson (see, for instance, Ref. [103]). Until today, there is no direct evidence that the newly found particle is any other than the SM Higgs boson—as J. Ellis put it: ”It walks and quacks like a Higgs boson.” [104]

This accumulation of developments, from the anticipation of the positron to the prediction of the Higgs boson, begs the question about the current state of the field and its future directions. The SM appears to be bulletproof since it correctly answers *almost all* measurements at particle colliders, and, with accumulating data, observed deviations tend to fade away.¹ Moreover, there is no urgent need for BSM physics at the TeV scale due to theory consistency, as was the case for the Higgs boson. The SM certainly is one of the greatest success stories of 20th-century physics and one of the pillars of fundamental physics. However, several puzzles motivated by both theoretical considerations and experimental observations demand explanations.

As an obvious example, the SM in its current form has nothing to say about the most discernible force in nature, i.e., gravity. It succeeds in providing a comprehensive description of electromagnetism, radioactive processes, and the structure of matter. Yet, being formulated as a quantum Yang–Mills theory, it is unclear how it can be unified with the theory of General Relativity (GR) [111–113], which is the backbone of our understanding of gravitation. Naive quantization of GR spoils renormalizability rendering the theory ambiguous and mathematically ill-defined. Thus, on the one hand, the SM obviously cannot be considered to be a Theory of Everything (ToE). On the other hand, any ToE must both describe gravity and reproduce the SM at the EW scale. The latter also applies to Grand Unified Theories (GUTs), which attempt to

¹To give two infamous examples: in 2015, both the ATLAS and CMS collaborations reported an excess in the diphoton spectrum at an invariant mass of around 750 GeV with a local significance of over 3.4σ [105, 106]. After hundreds of follow-up publications searching for viable explanations, the excess disappeared in updated analyses by the LHC collaborations in 2016 [107, 108]. Moreover, in 2013, the LHCb collaboration reported a 3.1σ disagreement with the measured value of the $\mathcal{R}_{K^{(*)}}$ observable. This anomaly in the flavor sector disappeared since the LHCb collaboration published an updated analysis almost a decade later, in December 2022 [109, 110]. We further dwell on the $\mathcal{R}_{K^{(*)}}$ anomaly in Chap. 2.

unify EW theory and QCD into a simpler mathematical structure (see the pioneering works [114–117] and Ref. [118] for a comprehensive review on the matter) in a similar fashion as electromagnetism and weak interactions have been unified in the GSW model.

Unification is commonly achieved by organizing quarks and leptons into a common representation of a simple Lie group which breaks down to the SM gauge group at lower energies via spontaneous symmetry breaking (SSB). GUTs can provide explanations of several properties that are introduced ad hoc in the SM. There are 19 a priori free parameters in the SM² that cannot be predicted in any way, which appears quite arbitrary for the fundamental theory governing the laws of nature. GUTs succeed in relating the fermion masses and explaining the hierarchies among them. In particular, they also predict the quantization of the elementary electric charge. Without further knowledge, the charge assignment of elementary particles is arbitrary and could take any continuous value since the weak hypercharge is associated with the abelian Lie group $U(1)_Y$. Therefore, it seems like an unlikely coincidence that electrons and protons have the same charge, and macroscopic matter is electrically neutral. In a GUT, however, the SM gauge group is embedded in a simple non-abelian Lie group, hence explaining charge quantization and the cancellation of electron and proton charges. The staggering quasi-coincidence of the running gauge couplings of the SM at the energy scale of $\mathcal{O}(10^{16} \text{ GeV})$ further hints at the unification of the known elementary forces in the SM (see, for instance, Ref. [119]).³

In the SM, the different generations of fermions only differ by the particle masses (or, equivalently, their Yukawa couplings to the Higgs boson). However, some hints of Lepton Flavor Universality (LFU) violation have endured until this day. While LFU appears to be exactly realized, e.g., in Z boson decays into pairs of charged leptons [13], the over 2σ anomaly in the decay $b \rightarrow c\ell\nu$ reported first by the BABAR collaboration in 2012 persists until today [120–122]. In recent years, it has been pointed out that the anomaly might be connected to certain theories of grand unification matching exactly the observed discrepancy from the SM prediction.

Another cumbersome puzzle that hints at physics beyond the SM is the question of the origin of the EW energy scale. We would like to understand why the separation of the EW scale and the Planck or the GUT scales is so large. At the Planck scale of $\mathcal{O}(10^{19} \text{ GeV})$, gravity is expected to lead to meaningful quantum corrections, which

²The only non-dimensionless free parameter is the mass of the Higgs boson, setting the scale of EW theory.

³The gauge couplings can be exactly unified at the GUT scale, e.g., when the theory is augmented by Supersymmetry.

means that a different description of fundamental physics, a theory of quantum gravity, is direly needed. Due to the separation of 14 and 17 orders of magnitude between the EW scale and the Planck and GUT scales, respectively, the hierarchy problem boils down to the question of why the Higgs boson mass m_h is so small in comparison. This problem becomes evident when we compute quantum corrections to m_h , which are very sensitive to physics at high energy scales. Hence, one would expect new particles at the GUT or Planck scale to yield an enormous contribution to the Higgs boson mass, raising the question of what could cancel those contributions to spawn the small Higgs boson mass of around 125 GeV.⁴ Historically, the most popular attempt to solve this riddle was Supersymmetry (SUSY),⁵ which introduces a symmetry between bosonic and fermionic degrees of freedom and leads to the introduction of a lot of new particles. Since no supersymmetric particles have been found at the LHC to this day, future prospects of SUSY research remain uncertain and alternative solutions to the EW hierarchy problem are gaining increasing attention.

Beyond the phenomenology at particle colliders, the cosmological history of the universe bears many mysteries that need to be unraveled by GR and particle physics in unison. For instance, the fact that we observe large amounts of matter in the cosmos compared to just a tiny fraction of antimatter still lacks an explanation. This baryon asymmetry has been famously linked to unknown sources of CP violation [133] that cannot be explained by the SM alone. Moreover, the cosmological constant of GR, which determines the expansion and the fate of the universe, introduces yet another hierarchy problem, and its origin remains elusive. Additionally, we observe a lack of gravitating matter in the universe to accurately describe certain astrophysical phenomena, such as galaxy rotation curves. While we see its gravitational impact, we have not yet seen this Dark Matter (DM) directly in experiments. There is a vast amount of ideas that might explain the DM puzzle, in many of which DM manifests itself in the form of elementary particles beyond the SM. These models of particle DM represent a promising opportunity for the discovery of BSM physics at the LHC.

So, what do these issues—inferred from experimental observation or theoretical reasoning—tell us about the SM and what lies beyond it? It depends on how we tackle

⁴The problem arises even if the BSM particles at the high energy scales do not couple directly to the Higgs boson when we take into account corrections at higher loop orders (see, e.g. Ref. [123]).

⁵There exists an enormous amount of literature on SUSY. Early works include Refs. [124–132], and Ref. [123] provides a comprehensive introduction to the topic.

these problems. Following the reasoning of the anthropic principle (see, e.g., Ref. [134]), the observed values of natural constants in the SM are just what they are; otherwise, we could not exist as observers of the universe in the first place. In that sense, the SM has to be as it is for us to exist, and hierarchy problems do not emerge as relevant questions to be asked. Another rather agnostic approach to probing for new physics is provided by effective field theories (EFTs) like the Standard Model Effective Field Theory (SMEFT). This ansatz has increased in popularity in recent years as the LHC has not found any direct evidence of new physics. EFTs are well-suited to parametrize deviations from SM predictions observed in experiments in a nearly model-independent fashion and to indicate the directions where to search for BSM physics. In the end, however, we want to find a renormalizable Quantum Field Theory to describe LHC phenomenology accurately, a self-consistent theory of particles and their interactions from the Planck scale down to LHC energies. As alluded to above, the past has taught us that the challenges with which established theory is confronted may be overcome by dynamical mechanisms predicting the existence of new particles. This is precisely the approach we adopt in this thesis to discuss possible explanations for the EW hierarchy problem, the origin of DM, and the flavor anomalies. After all, studying specific models guides us to deep knowledge about nature.

The remainder of this thesis is structured as follows. Chap. 2 is devoted to the SM and describes its structure in detail. We shed light on both the gauge and scalar sectors as well as the fermion content as it is known to this day. Furthermore, we elaborate on its successes and shortcomings, emphasizing the EW hierarchy problem, the need for additional particles to explain the DM observed in the universe, and the flavor anomalies. These three issues at the core of the SM represent the main motivation for the subsequent discussions.

It seems appealing to solve multiple of the above-mentioned problems of the SM at once. We thus discuss a class of models with weakly interacting massive particles that both solve the DM puzzle and yield an explanation for the small mass of the Higgs boson. This can be achieved in models in which both DM and the SM Higgs boson emerge as composite pseudo Nambu–Goldstone bosons of a novel strongly-coupled sector at the TeV scale. The production of this kind of DM alongside top quarks at the LHC is discussed in Chap. 3. Moreover, we discuss constraints implied by the observed relic abundance of DM in the universe and the limits obtained from DM indirect and direct detection experiments.

The complex symmetry-breaking patterns and extended gauge structures of GUTs generally predict the existence of additional gauge bosons and more Higgs-like scalar particles, which could, in principle, be directly produced at particle colliders. One generic candidate class of particles is the leptoquark, which is a boson exerting a tree-level interaction with a lepton-quark pair. Leptoquarks have attracted much attention over the past years as they readily provide possible explanations, e.g., for the flavor anomalies and the anomalous magnetic moment of the muon. The search for leptoquarks at the LHC is the topic of the publications [2,3] and is dealt with in detail in Chap. 4.

In Chap. 5, we conclude our results and provide a glimpse of the future of particle physics and the LHC research program in the years to come.

2 Review of the Standard Model of Particle Physics

The Standard Model of Particle Physics (SM) represents the leading paradigm in particle physics. Therefore, in this chapter, we want to provide an introduction to the SM and discuss in more detail some of its successes and shortcomings, that we already touched upon in the previous chapter. We put particular emphasis on the EW hierarchy problem, the lack of an explanation for Dark Matter within the SM, and the anomalies observed in the flavor sector. Of course, this review is not meant to be comprehensive. The discussions rather aim to pave the way for the following chapters.

2.1 The Standard Model of Particle Physics

From a structural point of view, the SM is formulated as a quantum Yang–Mills theory [135] with spontaneously broken gauge symmetries. Although relativistic Quantum Field Theory (QFT) may be posed on an unclear foundation¹, its unprecedented predictive power and remarkable accuracy motivate its use in particle physics phenomenology. Since it is free of gauge anomalies and renormalizable, its implied numerical results are unambiguous, and perturbation theory can be used to obtain finite results both in the infrared (IR) and ultraviolet (UV) energy regimes. Following Ref. [142], we can define the SM as the most general renormalizable field theory with gauge group

$$\mathcal{G}_{\text{SM}} = \text{SU}(3)_C \times \text{SU}(2)_L \times \text{U}(1)_Y, \quad (2.1)$$

three generations of fermions, and a scalar, where the latter fields transform as

$$\begin{aligned} (\mathbf{3}, \mathbf{2}, 1/6) + (\bar{\mathbf{3}}, \mathbf{1}, -2/3) + (\bar{\mathbf{3}}, \mathbf{1}, 1/3) + (\mathbf{1}, \mathbf{2}, -1/2) + (\mathbf{1}, \mathbf{1}, 1) \\ \text{and } (\mathbf{1}, \mathbf{2}, 1/2). \end{aligned} \quad (2.2)$$

¹A mathematically rigorous formulation of QFT remains an open problem (see, e.g., Ref. [136] for a modern review on the status quo of the field). A landmark contribution was due to the development of the Wightman axioms [137, 138]. Yet, it seems like the quantum mechanical interaction picture commonly used for all perturbative calculations is ill-defined [139–141]. However, a further discussion of these striking findings is well beyond the scope of this dissertation.

Here, the first and second lines of eq. (2.2) contain all fermion and scalar representations under \mathcal{G}_{SM} , respectively. Though mathematically precise, this formal definition obscures the phenomenological implications that we seek to study in the following. For this reason, it proves useful to further expand on this definition. If we drop all unphysical terms, such as those including ghost particles from the Faddeev–Popov quantization procedure for non-abelian gauge theories [143], as well as gauge-fixing terms, we can write the Lagrangian of the SM as

$$\begin{aligned}
 \mathcal{L}_{\text{SM}} = & -\frac{1}{4}B_{\mu\nu}B^{\mu\nu} - \frac{1}{4}W_{\mu\nu}^a W^{a,\mu\nu} - \frac{1}{4}G_{\mu\nu}^a G^{a,\mu\nu} \\
 & + \sum_{\ell \in \{e, \mu, \tau\}} \left[\bar{L}_L^\ell i\not{D} L_L^\ell + \bar{\ell}_R i\not{D} \ell_R \right] \\
 & + \sum_{j=1}^3 \left[\bar{Q}_L^j i\not{D} Q_L^j + \bar{u}_R^j i\not{D} u_R^j + \bar{d}_R^j i\not{D} d_R^j \right] \\
 & - \sum_{\ell \in \{e, \mu, \tau\}} \left[y_\ell \bar{L}_L^\ell H \ell_R + \text{h.c.} \right] \\
 & - \sum_{i, j=1}^3 \left[y_u^{ij} \bar{Q}_L^i H^C u_R^j + y_d^{ij} \bar{Q}_L^i H d_R^j + \text{h.c.} \right] \\
 & + (\mathcal{D}_\mu H)^\dagger (\mathcal{D}^\mu H) - \mu^2 H^\dagger H - \lambda (H^\dagger H)^2 .
 \end{aligned} \tag{2.3}$$

Here,

$$\mathcal{D}_\mu = \partial_\mu - ig_1 Y B_\mu - ig_2 I^a W_\mu^a - ig_s T^a A_\mu^a \tag{2.4}$$

is the gauge covariant derivative associated with the SM gauge group, where we write the corresponding gauge coupling constants as g_i . We denote the weak hypercharge operator by Y and the corresponding gauge field by B . These are associated with the $U(1)_Y$ symmetry of the Lagrangian. Moreover, the components I^a are the generators of the weak isospin $SU(2)_L$ symmetry, and W^a are the related gauge fields. Here, $\mathbf{a} \in \{1, 2, 3\}$. All EW phenomena are encapsulated in the terms involving the gauge fields B and W^a in eqs. (2.3) and (2.4). The last term in the SM-gauge covariant derivative eq. (2.4) describes the strong force, i.e., Quantum Chromodynamics (QCD). We denote the eight generators of the color group $SU(3)_C$ and the associated gluon gauge fields by T^a and G^a , respectively, where the index $a \in \{1, \dots, 8\}$. The kinetic terms of the gauge fields, including their self-interactions, are given in the first line of eq. (2.3) in terms of the corresponding field-strength tensors

$$F_{\mu\nu}^a = \partial_\mu A_\nu^a - \partial_\nu A_\mu^a + g f^{abc} A_\mu^b A_\nu^c . \tag{2.5}$$

Here, we have introduced the general field strength $F_{\mu\nu}$ in terms of $SU(N)$ gauge fields A_μ with coupling g and the $SU(N)$ structure constants f^{abc} , which are defined through

the commutation relation

$$[T^a, T^b] = if^{abc}T^c \quad (2.6)$$

for generic $SU(N)$ generators T^a . The $SU(2)_L \times U(1)_Y$ gauge fields mix according to

$$W_\mu^\pm = \frac{1}{\sqrt{2}}(W_\mu^1 \mp iW_\mu^2) \quad (2.7)$$

to yield the physical W^\pm bosons. Similarly, the remaining $SU(2)_L$ and $U(1)_Y$ gauge fields can be combined via

$$\begin{pmatrix} W_\mu^3 \\ B_\mu \end{pmatrix} = \begin{pmatrix} \cos \theta_W & \sin \theta_W \\ -\sin \theta_W & \cos \theta_W \end{pmatrix} \begin{pmatrix} Z_\mu \\ A_\mu \end{pmatrix}, \quad (2.8)$$

to constitute the electrically neutral Z boson and the photon. Here, θ_W is the weak mixing angle and in later chapters, we use the abbreviations $s_W \equiv \sin \theta_W$ and $c_W \equiv \cos \theta_W$. The photon A mediates the electromagnetic interaction, and the W^\pm and Z bosons mediate weak interactions.

The fermionic kinetic terms in the second and the third lines of eq. (2.3) specify the whole matter content of the SM and the interactions of the SM fermions with the gauge bosons. In Table 2.1, we provide the assignment of the symbols in \mathcal{L}_{SM} to the \mathcal{G}_{SM} representations in eq. (2.2). The left-handed components of the quarks and leptons are denoted by $SU(2)_L$ doublets

$$Q_L^i = \begin{pmatrix} u_L^i \\ d_L^i \end{pmatrix} \quad \text{and} \quad L_L^\ell = \begin{pmatrix} \nu_L^\ell \\ \ell_L \end{pmatrix}. \quad (2.9)$$

There are three generations of both quarks and leptons, i.e., there exist three up-type quarks (u, c, t), three down-type quarks (d, s, b), three charged leptons (e, μ, τ), and their associated neutrinos (ν_e, ν_μ, ν_τ). u_R^i, d_R^i , and ℓ_R denote the corresponding right-handed components of the fermions, which transform as singlets under $SU(2)_L$. Due to the gauge structure of the GSW model, EW theory fundamentally distinguishes left- and right-chiral fields. Considering only pure QCD, we could simply add Dirac mass terms for the fermions to the SM Lagrangian \mathcal{L}_{SM} . However, the chirality property of EW interactions forbids the presence of Dirac mass terms as they would break EW gauge invariance. Fermions aside, the mass terms also for the massive Z and W^\pm vector bosons break the $SU(2)_L \times U(1)_Y$ invariance demanded by the GSW model. The spontaneous symmetry breaking (SSB) in the form of the Higgs mechanism circumvents this issue. By introducing a complex scalar Higgs field H that transforms as a doublet

$$H = \begin{pmatrix} \phi^+ \\ \phi^0 \end{pmatrix} \quad (2.10)$$

Symbol	Spin	\mathcal{G}_{SM} representation
ℓ_R	1/2	$(\mathbf{1}, \mathbf{1}, 1)$
u_R		$(\bar{\mathbf{3}}, \mathbf{1}, 1/3)$
d_R		$(\bar{\mathbf{3}}, \mathbf{1}, -2/3)$
L_L		$(\mathbf{1}, \mathbf{2}, -1/2)$
Q_L		$(\mathbf{3}, \mathbf{2}, 1/6)$
H	0	$(\mathbf{1}, \mathbf{2}, 1/2)$

Table 2.1: Fermion and scalar representations in the SM. This table matches the particle content of the SM Lagrangian \mathcal{L}_{SM} in eq. (2.3) to the representations given in eq. (2.2).

under $\text{SU}(2)_L$ rotations with a self-interacting potential $\mathcal{V}(H) = \mu^2 H^\dagger H + \lambda (H^\dagger H)^2$, with $\mu^2 < 0$ and $\lambda > 0$, the scalar adopts a non-trivial vacuum configuration. It acquires a vacuum expectation value (VEV) that we can parametrize in unitary gauge as

$$H \longrightarrow \frac{1}{\sqrt{2}} \begin{pmatrix} 0 \\ v + h \end{pmatrix} \quad (2.11)$$

such that the gauge-kinetic term $(\mathcal{D}_\mu H)^\dagger (\mathcal{D}^\mu H)$ of the scalar generates mass terms for the massive EW gauge bosons. Furthermore, the Higgs potential gives rise to a mass term of the scalar field h . In unitary gauge, the occurring Goldstone modes [144–148] associated with the symmetry breaking are absorbed into the longitudinal degrees of freedom of the massive vector bosons. SSB provides a dynamic mechanism that describes how gauge invariance is broken below energies $\sim v$, where EW symmetry reduces according to the pattern $\text{SU}(2)_L \times \text{U}(1)_Y \rightarrow \text{U}(1)_{\text{em}}$ leaving QED as a remnant at low energies. This can be readily seen as the vacuum configuration of the Higgs field is neutral with respect to the electromagnetic charge

$$Q \equiv (T^3 + Y) , \quad (2.12)$$

meaning

$$Q \langle H \rangle = 0 . \quad (2.13)$$

This simply describes the conservation of electromagnetic charge in this vacuum configuration. At high energies, when the VEV of the Higgs field can be neglected, gauge invariance is restored, ensuring the renormalizability of EW theory. All this is realized in the SM, following from the last line of eq. (2.3). Moreover, via electroweak symmetry breaking (EWSB), the Yukawa couplings of the Higgs field with the SM fermions as

Z boson decay mode	relative partial width $\Gamma_i/\Gamma_{\text{tot}}[\%]$
e^+e^-	3.3632 ± 0.0042
$\mu^+\mu^-$	3.3662 ± 0.0066
$\tau^+\tau^-$	3.3696 ± 0.0083

Table 2.2: Measured partial decay widths of the Z boson into charged leptons as stated in Ref. [13], corresponding to $\Gamma_{\text{tot}} = 2.4952 \pm 0.0023$ GeV.

given in the fourth and fifth lines of eq. (2.3) lead to Dirac mass terms for the SM fermions at low energies. The up-type quarks require the definition of the conjugated doublet $H^C = i\sigma^2 H^\dagger$, with σ^2 being the second Pauli matrix.

Disregarding the Yukawa couplings of the quarks in the fifth line of the SM Lagrangian and acknowledging the fact that there are three generations of both leptons and quarks, we immediately see that the SM admits a $U(3)^5$ symmetry in the fermionic sector (see, e.g., Ref. [149]). This can be understood by realizing that none of the terms introduce any mixing between the three generations, which is true for all five relevant fermion representations Q_L , L_L , u_R , d_R , and e_R . This accidental symmetry is realized exactly among the leptons, a fact commonly referred to as Lepton Flavor Universality (LFU). In simple terms, the gauge interactions of the SM do not distinguish between the different generations. This prediction of the SM is observed in experiments to remarkable precision, for instance, in the decay modes of the Z boson. In Table 2.2, we provide the partial decay widths into charged leptons, normalized by the total Z decay width, as stated in Ref. [13]. Within the margin of error, the Z boson seems to decay into electrons just as often as into muons or tau leptons.

In the quark sector, universality among the three generations is violated explicitly by the Yukawa interactions with the Higgs field in the fifth line of eq. (2.3). Here, y_u^{ij} and y_d^{ij} are complex non-diagonal 3×3 matrices. The quark representations in the SM Lagrangian above are eigenstates regarding EW interactions. However, a shift to mass eigenstates can be achieved with unitary transformations that diagonalize the mass terms. This procedure leads to the notion of the CKM matrix, which is also the only source of CP violation in the SM.

As indicated in Chap. 1, there are plenty of examples of the successes of the SM. Not only the anticipation of particles many years before their observation, as was the

case, e.g., for the top quark and the Higgs boson. But also its numerical predictions seem to be in outstanding agreement with the recorded data. For example, since its first observation in 2012, the Higgs boson appears very much SM-like as the accumulating data suggests—this is, e.g., demonstrated exceptionally by the linear relationship between particle mass and coupling strength to the Higgs field (see Ref. [150] for a state-of-the-art overview). The proportionality is observed to remarkable precision and is confirmed for W and Z bosons, top and bottom quarks, as well as tau leptons and muons to this day. An important precision observable from Higgs phenomenology is the ρ parameter, that was first discussed in Ref. [151] and was established as crucial observable parametrizing departures from SM-like EWSB [152–154]. It can be defined according to

$$\rho = \frac{m_W^2}{m_Z^2 \cos^2 \theta_W} \quad (2.14)$$

and assumes a value of exactly 1 in the SM. It is protected from large radiative corrections by the so-called custodial symmetry in the SM Higgs sector: in the limit of vanishing Yukawa couplings and $g_1 \rightarrow 0$, the Higgs sector admits a $SU(2)_L \times SU(2)_R$ global symmetry, which is reduced to $SU(2)_{L+R}$ after EWSB. The measured value is in perfect agreement with the SM prediction.² Aside from Higgs physics, any new physics at the TeV scale that contributes to the EW vacuum polarization functions would numerically impact the Peskin–Takeuchi parameters [156–159] S , T , and U . These parametrize deviations from the SM and can be inferred, for instance, from measurements of the Z mass, decay width, and the W -boson mass and show little correlation among each other. Current EW precision tests underline the excellent agreement with the SM prediction of $S = T = U = 0$ [13]. In addition to the Peskin–Takeuchi parameters, the precise measurement of the invisible partial decay width of the Z boson allows us to infer the number of neutrinos (under the working hypothesis that there are no BSM particles canceling additional neutrino contributions). The measurement is in excellent agreement with the SM count of three neutrino species, which is needed for consistency with the remaining fermion content of the SM. Table 2.3 summarizes the above-discussed EW precision observables and states the up-to-date measured values.

On the other end of the SM, QCD continues to flourish in experimental tests. For example, di-top production has been calculated at the next-to-next-to-leading order (NNLO) [160–165] in QCD. Both the total cross section and the differential distributions agree precisely with the data recorded at the LHC. At the precision frontier, further NNLO results were computed for the $H + \text{jet}$ [166], $Z + \text{jet}$ [167], and di-jet pro-

²An excellent overview of Higgs phenomenology and possible extensions of the SM Higgs sector is provided by Ref. [155].

Observable	Measured value	SM prediction
S	-0.02 ± 0.10	0
T	0.03 ± 0.12	0
U	0.01 ± 0.11	0
ρ	1.00038 ± 0.00020	1
N_ν	3.0026 ± 0.0061	3

Table 2.3: Measured EW precision observables as stated in Ref. [13]. S , T , and U denote the Peskin–Takeuchi parameters parametrizing new physics contributing to the EW two-point functions. The ρ parameter serves as a useful observable sensitive to any non-SM-like EWSB patterns. Moreover, the number of neutrino species N_ν can be inferred from the invisible decay width of the Z boson. All measurements pose serious limits on any BSM physics.

duction [168]. The same also applies to, e.g., $W^\pm Z$ and W^+W^- production at hadron colliders [169–171]. All calculations are aligned with the observed data and underline the validity of the SM at LHC energy scales. One of the first NNLO calculations in QCD was crucial for the discovery of the Higgs boson, i.e., the production of an on-shell Higgs boson which is dominated at the LHC by gluon fusion [172–174]. Recently, these results have been refined to include quark mass effects, even refining the NNLO prediction [175, 176]. Endeavors in this direction will continue to push the boundaries of precision calculations. A comprehensive overview of the status quo of QCD precision calculations is given in Ref. [177]. For a summary of SM measurements by the ATLAS collaboration, we redirect the reader to Ref. [178], where the predictive accuracy of the SM is demonstrated in an astounding way.

At low energies, where partons form bound states, QCD succeeds in describing the hadron spectrum. This traces back to the first successes of the quark model in the early 1960s [179–183], which was able to fundamentally organize the vast amount of baryons and mesons that were found at the time. Crucially, it anticipated the existence of the Ω^- hyperon, which is a bound state consisting of three strange quarks and was observed immediately after its prediction at a dedicated experiment at BNL in 1964 [184]. The completion of the hadronic spectrum continues until today. Meanwhile, even exotic states like tetraquarks and pentaquarks, which are bound states of four and five quarks, were undisputedly observed for the first time in the 2010s at the LHCb experiment (see Refs. [185, 186] and Ref. [187], respectively).

In the low-energy regime of QCD, calculations rely on non-perturbative approaches like lattice QCD, which poses considerable challenges to a thorough understanding of the physics of hadrons. This is due to the fact that the strong force increases for larger distances. In technical terms, this is reflected by the renormalization group equation (RGE) of the strong coupling constant $\alpha_s = \frac{g_s^2}{4\pi}$, which has the opposite overall sign compared to the running coupling of QED. At high energies, as probed at the LHC, quarks become essentially free particles, a property referred to as *asymptotic freedom* [188, 189]. Below energies of around 1 GeV, perturbation theory cannot be applied anymore, and the RGE of α_s leads to a Landau pole at $\Lambda_{\text{QCD}} \simeq 200$ MeV. The quarks are confined to form bound states such as the proton, and to this day, we lack a proper description of the internal proton structure derived from first principles. Hence, at a proton collider like the LHC, we rely on phenomenological parton distribution functions (PDFs, see, e.g., Refs. [190–192]) in order to reckon with non-perturbative QCD effects in our calculations. In a nutshell, the production of a final state X at the LHC at an energy scale Q^2 can be described by applying the master formula

$$\sigma_X = \sum_{i,j} \int_0^1 dx_1 dx_2 f_i(x_1, \mu_F^2) f_j(x_2, \mu_F^2) \times \hat{\sigma}_{ij \rightarrow X}(x_1, x_2, Q^2, \mu_R^2, \mu_F^2) + \mathcal{O}\left(\frac{\Lambda_{\text{QCD}}^2}{Q^2}\right), \quad (2.15)$$

i.e., a convolution of the hard scattering cross section with the PDFs f_i as functions of the kinematic variable commonly known as Bjorken- x . Pictorially, a PDF $f_i(x, \mu_F^2)$ encodes the probability of finding a parton i with longitudinal momentum fraction x in a proton at a given factorization scale μ_F . The partonic scattering cross section $\hat{\sigma}$ can be derived from a Lagrangian, using the common techniques from perturbative QFT. However, $\hat{\sigma}$ may suffer from the presence of collinear infrared singularities, which can be absorbed into the PDFs. This factorization procedure resembles renormalization in order to tame UV divergences. Likewise, we need to introduce an unphysical factorization scale μ_F . The fact that observables must not depend on μ_F leads to the Dokshitzer–Gribov–Lipatov–Altarelli–Parisi (DGLAP) evolution equations [193–195], in analogy to the RGEs for the running couplings. Our understanding of QCD, which has been pushed ever since the beginning of the quark model in the 1960s, lays the foundation for the achievements of hadron colliders like the LHC.

The overall success of the SM predictions represents a hard case for any BSM physics model, and the precision measurements put stringent constraints on many popular extensions of the SM. Yet, theoretical considerations and experimental observations have crystallized the main avenues for new physics beyond the SM. One obvious issue of

the SM Lagrangian as defined in eq. (2.3) is the lack of neutrino masses. Neutrinos are known to be massive as a result of the first observations of neutrino oscillations in various experiments around the beginning of this century (see, among others, Refs. [196–200]). Admittedly, it would be unproblematic to introduce a right-handed neutrino, which as a singlet under \mathcal{G}_{SM} , does not interact with the SM gauge bosons and enables neutrino mass terms as a consequence of Yukawa couplings with the Higgs field and EWSB.³ However, the exact values of the neutrino masses as well as the hierarchy of the three generations are yet to be determined in experiments (see, for instance, Refs. [203, 204]). Moreover, it is still unclear whether mass terms should be introduced in the Dirac form, as is the case for all other SM fermions, or whether neutrinos are rather of Majorana [205] nature on a fundamental level. This would have a handful of phenomenological implications. For instance, neutrinos would be their own antiparticles, which would be a unique property among the SM fermions. Another intriguing implication of Majorana neutrinos would be the prediction of neutrinoless double- β decays. Considerable experimental efforts are dedicated to the first observation of the so-called $0\nu\beta\beta$ reactions (see, e.g., Refs. [206–208]).

Aside from neutrino physics, the strong CP problem (see, e.g., Ref. [209]) has been puzzling theorists already for decades. On a fundamental level, there is no particular reason why strong interactions should respect the discrete CP symmetry. To be more precise, the formal definition of the SM in Ref. [142] allows for a renormalizable term of the form $\theta \frac{g_s^2}{32\pi^2} G_{\mu\nu}^a \tilde{G}^{\mu\nu a}$, with the dual gluon field strength tensor $\tilde{G}^{\mu\nu} = \frac{1}{2} \varepsilon^{\mu\nu\alpha\beta} G_{\alpha\beta}$, in the SM Lagrangian. However, measurements of the electric dipole moment of the neutron constrain the physical $\bar{\theta}$ parameter tightly to be $\bar{\theta} \lesssim 10^{-10}$ [210]. Subsequently, the CP -violating interaction is either unnaturally small or absent in QCD. Both options demand a theoretically motivated explanation. A very popular dynamic solution to the strong CP problem is provided by the Peccei–Quinn (PQ) mechanism [211, 212], which leads to the notion of the axion [213, 214] as pseudo Nambu–Goldstone boson (pNGB) of the broken PQ symmetry. The quest for the axion remains a great challenge for experimental collaborations continuing to constrain the viable parameter space of the axion (see, for instance, Refs. [215–218]). Both the fundamental nature of the neutrino as well as the strong CP problem represent fascinating pathways for BSM physics. Further exploration of these topics is beyond the scope of this dissertation, and we

³Since the EW neutrino eigenstates mix, the Yukawa interaction terms would resemble those of the quarks, leading to the notion of the Pontecorvo–Maki–Nakagawa–Sakata (PMNS) matrix [201, 202] as analog to the CKM matrix.

focus on other open questions instead.

In the past decades, progresses in particle theory were stimulated by the EW hierarchy problem, which we already sketched in Chap. 1. More thoroughly, it addresses the fact that any heavy new particle that contributes to physics at the energy scale of grand unification or the Planck scale that also (effectively) couples to the SM Higgs field gives rise to enormous corrections to the Higgs mass. If we consider a cut-off momentum at an energy scale Λ_{BSM} indicating a scale at which BSM physics effects become relevant, then the renormalization of the Higgs mass leads to [219]

$$(m_h^2)_{\text{renormalized}} = (m_h^2)_{\text{bare}} + \mathcal{O}(\lambda, g^2, h^2)\Lambda_{\text{BSM}}^2. \quad (2.16)$$

Since $(m_h^2)_{\text{renormalized}}$ depends quadratically on Λ_{BSM} , the Higgs mass is particularly sensitive to new physics at high energies. If there is no BSM physics up to the Planck scale, the corrections $\mathcal{O}(\lambda, g^2, h^2)$ must be incredibly small to compensate for the large cut-off. Moreover, they must be unnaturally fine-tuned in order to yield the Higgs-boson mass at 125 GeV.⁴ Since we do not know what lies beyond the SM and what the laws of nature that govern physics at such high energies look like, this fine-tuning of the cancellation seems unnatural. Any change in the high-scale BSM contribution to the Higgs mass by just a fraction of a percent would potentially change the Higgs mass by orders of magnitude. One way to address this problem would be the introduction of new particles that exactly cancel the problematic contributions. This is precisely the approach that rendered SUSY the paramount paradigm of the past. SUSY not only maximally generalizes mixed internal and Poincaré symmetries of space-time [126] and appears to be a generic feature of string theories that allow for fermionic matter. It also provides a neat solution to the EW hierarchy problem. It is clear that SUSY must be broken in order to explain the SM particle spectrum. However, the null results from LHC searches for SUSY particles to this day raise doubts that SUSY is a fundamental property of nature. Alternative approaches to the EW hierarchy problem include those models in which the Higgs boson is described as a pNGB of a strongly-coupled sector at higher energies which naturally explains the small value of the Higgs mass. This promising line of thinking is further developed in Chap. 3.

As another issue of the SM, the fermionic sector is plagued by redundancy. All of the non-relativistic matter that we observe in the universe can, in principle, be constructed

⁴We should note that this reasoning would apply to any fundamental scalar, and a similar argument could also be constructed for fermions. However, in the latter case, chiral symmetry protects the SM fermions from large radiative corrections in the UV.

out of the first-generation fermions $\{\nu_e, e, u, d\}$. Yet two further exact copies were observed, only distinguished by the different particle masses and the origin of the observed mass hierarchy between the generations remains another open question. The structure of the fermionic sector of the SM has recently been challenged by several anomalies observed in the decays of B mesons (i.e., quark-antiquark bound states containing a bottom and a first-generation quark).⁵ During the past decade, the LHCb collaboration reported a combined 3.1σ anomaly in the \mathcal{R}_K and \mathcal{R}_{K^*} observables in a series of different publications [221–225]. This quantity is a sensitive probe testing LFU violations originating from unknown sources in the neutral-current transitions $b \rightarrow s\ell^+\ell^-$. To be precise, \mathcal{R}_K and \mathcal{R}_{K^*} are defined in an energy interval $[q_a^2, q_b^2]$ according to

$$\mathcal{R}_{(K,K^*)}^{[q_a, q_b]} = \frac{\int_{q_a^2}^{q_b^2} \frac{d\Gamma(B^{(+,0)} \rightarrow K^{(+,*0)}\mu^+\mu^-)}{dq^2} dq^2}{\int_{q_a^2}^{q_b^2} \frac{d\Gamma(B^{(+,0)} \rightarrow K^{(+,*0)}e^+e^-)}{dq^2} dq^2}. \quad (2.17)$$

Figuratively, they parametrize whether the decay of a B meson into a K meson with an associated light lepton pair happens more or less often with final state $\mu^+\mu^-$ pairs than with e^+e^- pairs. The corresponding prediction in the SM would give a ratio equal to one (up to minuscule lepton mass corrections [226]), and any deviation would be a direct violation of the LFU principle and would represent a strong hint for BSM physics. In particular, \mathcal{R}_K and \mathcal{R}_{K^*} are theoretically clean observables since any hadronic uncertainties cancel in the ratio of branching fractions. Moreover, the SM prediction of related angular distributions in B -meson decays appears discordant with the measurement with a global 3.4σ significance [227]. On the other hand, the rare process $B_s^0 \rightarrow \mu^+\mu^-$ was first observed in 2014 by a joint effort of the LHCb and CMS collaborations and is in agreement with the SM prediction. Similar to the $\mathcal{R}_{K^{(*)}}$ observables, the BABAR collaborations reported 2.0σ and 2.7σ excesses in the \mathcal{R}_D and \mathcal{R}_{D^*} observables, which are defined in analogy to eq. (2.17) but for the decays $\bar{B} \rightarrow D^{(*)}\tau^-\bar{\nu}_\tau$ relative to $\bar{B} \rightarrow D^{(*)}\ell^-\bar{\nu}_\ell$ for a light lepton ℓ [120, 121]. These anomalies were later also observed by LHCb [228]. These LFU ratios are associated with the charged-current decays $b \rightarrow c\tau^-\bar{\nu}_\tau$ and $b \rightarrow c\ell^-\bar{\nu}_\ell$, and in combination, they represented a 3.4σ excess. However, the BELLE experiment could not confirm these findings [229]. Moreover, observables linked to the τ polarization in the decay seem to be consistent with the SM [230] and the same also applies to the $\mathcal{R}_{D^{*0}}$ observable [231, 232].

In combination, the $\mathcal{R}_{K^{(*)}}$ and $\mathcal{R}_{D^{(*)}}$ anomalies amounted to a staggering 4.6σ tension with the SM, which has triggered lots of model-building ideas explaining the

⁵A comprehensive overview of the flavor anomalies from the theory side is provided in Ref. [220].

anomalies [220]. It was understood early that in an EFT framework, the $\mathcal{R}_{K^{(*)}}$ anomalies could be parametrized with purely left-chiral contact interactions with muons [233]. Connected to efforts to explain the angular anomalies [234–236], several global studies have narrowed down possible directions for concrete BSM scenarios [237–242]. It was shown that the anomalies could potentially be traced back to explicitly LFU-violating new physics of third-generation fermions [243]. The combination of the anomalies in the neutral-current $b \rightarrow s\ell^+\ell^-$ and charged-current $b \rightarrow c\ell^-\bar{\nu}_\ell$ was thoroughly studied in EFT frameworks and continued to propose effective left-handed interactions as the main source of the observations [244–247]. Linking these effective operators to more specific BSM models led to the increasing interest in so-called leptoquarks, which arise as a generic feature in GUTs (see, e.g., Refs. [220, 248, 249]). Leptoquarks are the main topic of Chap. 4, in which we discuss their impact on dilepton searches at the LHC. We note that the LHCb collaboration has recently published an updated analysis on their data, finding no significant excess in the $\mathcal{R}_{K^{(*)}}$ observable [109, 110]. However, the $\mathcal{R}_{D^{(*)}}$ anomaly has been confirmed once more in an updated analysis [122], which maintains the prospects of finding LFU-violating BSM physics in B -meson decays.

Last year’s measurement of the W -boson mass by the CDF Collaboration [250] raises doubts about a parameter that has a crucial impact also on EW precision observables like the Peskin–Takeuchi parameters. With unprecedented accuracy, they measured a value of $m_W = 80.4335 \pm 0.0094$ GeV at the Tevatron collider at Fermilab, which deviates by 7 standard deviations from the SM value 80.357 ± 0.006 GeV [250]. Prior to the CDF measurement, the global average was set to 80.379 ± 0.012 GeV [12] and thus was well in agreement with the SM prediction. Throughout the past months, several explanations for the W -mass anomaly were discussed in the community, suggesting that past measurements were biased toward the SM value, hence hiding BSM physics contributions. In particular, interesting connections to leptoquarks [251–253] and Dark Matter (see, e.g., Refs. [254, 255]) were put on the table. However, the role of hadronic uncertainties [253] may be underestimated such that doubts on the new-physics explanation of the CDF measurement persevere until today.

While the magnetic moment of the electron in QED is one of the most accurate and most well-tested predictions in physics [57, 58], the same observable of the muon deviates significantly in experiments from its theoretical prediction. The long-standing anomalous $(g - 2)_\mu$ may be considered one of the most compelling tensions hinting at new physics of particle nature. Since its first measurement showing a deviation with up to 2.7σ significance at BNL in the early 2000s [258–261], it has driven much progress in model building, connecting the experimental result with new particles around the TeV

Observable	Current reference value
a_e^{th}	$(1\,159\,652\,181.664 \pm 763) \times 10^{-12}$
a_e^{exp}	$(1\,159\,652\,180.73 \pm 0.28) \times 10^{-12}$
a_μ^{th}	$(116\,591\,810 \pm 43) \times 10^{-11}$
a_μ^{exp}	$(116\,592\,061 \pm 41) \times 10^{-11}$

Table 2.4: SM theory prediction and experimental measurements of the anomalous magnetic moments of the electron and muon. Here, we have used the definition $g_\ell = 2(1+a_\ell)$. The SM and the experimentally observed values for the electron perfectly agree, while for the muon a total 4.2σ tension exists. For a_e^{th} , we only quote the dominating error, which is due to uncertainties regarding the exact values of $\alpha_{\text{em}} = \frac{e^2}{4\pi}$. The values are taken from Refs. [57, 58, 256, 257].

scale. In particular, SUSY models like the minimal supersymmetric model (MSSM) were fit to match the anomaly, further igniting the enthusiasm for the LHC discovery potential for supersymmetric particles. Clearly, the muon $(g-2)_\mu$ anomaly is yet another hint of LFU violation since it indicates BSM contributions to muon interactions while the first-generation fermions obey the SM. This behavior can also be explained by leptoquarks that couple to muons and heavy quarks (see, for instance, Ref. [262]), which was considered to be strengthening the case for leptoquarks as explanation for the $\mathcal{R}_{K^{(*)}}$ anomaly. Other than the latter, the anomalous magnetic moment has recently been confirmed by the Muon $(g-2)$ Collaboration with measurements at Fermilab in 2021 [256]. Combined with the old data, the tension has grown in significance to 4.2 standard deviations. However, one should note that the impact of hadronic uncertainties in the theory prediction of $(g-2)_\mu$, which relies on lattice QCD calculations, is still intensely debated. For a theory review on the matter, we refer to Ref. [257], while a review of the lattice calculations is provided in Ref. [263]. In Table 2.4, we summarize the electronic anomalous magnetic moment at four-loop in QED [57] and its currently most precisely measured value [58], and the corresponding values for the muon. Finally, regarding the hadronic uncertainties, we would like to add that Ref. [253] suggests that the W -boson and $(g-2)_\mu$ anomalies pull the hadronic uncertainties in different directions. This hints that BSM contributions may be the key to at least one of the observed anomalies.

Beyond the collider phenomenology, the SM should describe the particle content observed in the universe. Together with Einstein’s GR, we aspire to give a consistent

description of the large-scale structure of the universe and its expansion, the motion of galaxies, and the remnants of its cosmological history. It seems, though, that the SM fails to provide the answers to several open questions in astrophysics and cosmology. We examine some of the core issues in the following section.

2.2 The Standard Model and the Cosmological History of the Universe

We do not attempt to comprehensively recap on GR and the status of modern cosmology. For this, we direct the reader to the classic literature (see, for instance, Refs. [8–11]). However, we provide a brief review of important aspects of the status quo of the field and discuss some hints for BSM physics, i.e., those junctions between topics from gravitational physics and particle physics.

Einstein’s theory of GR is best summarized by his famous field equations,

$$R_{\mu\nu} - \frac{1}{2}Rg_{\mu\nu} + \Lambda g_{\mu\nu} = 8\pi GT_{\mu\nu} , \quad (2.18)$$

with the Ricci tensor and curvature scalar $R_{\mu\nu}$ and R , Newton’s constant G , and the energy-momentum tensor $T_{\mu\nu}$. This relation follows from the equivalence principle and the requirement of Newtonian gravity in the limit of small masses and the validity of special relativity [52]. Astonishingly, this single-line differential equation for the metric $g_{\mu\nu}$ entails all gravitational physics—from the big bang and black holes to galaxy formation and the dynamics of the solar system, among others. For over a century, the predictions from GR have continued to be confirmed by experiments. The successes range from the correct description of Mercury’s perihelion [113] to the observation of gravitational red shift (see, e.g., Ref. [264]), and the observation of gravitational lensing [265]. In the past years, the remarkable observation of gravitational waves with the LIGO experiment [266–268] confirmed a long-sought prediction of GR, previously deemed impossible to ever be observed. Note that we have included the cosmological constant Λ in eq. (2.18), although its origin and connection to particle physics remain supposedly one of the most fundamental questions in physics. In the following, we are not going into the details of gravitational physics. We rather focus on what is encapsulated on the right-hand side of eq. (2.18), i.e., the matter content.

The Standard Model of Cosmology, often referred to as Λ CDM, is built under the assumption of the validity of GR, the existence of a cosmological constant Λ , and the

existence of cold Dark Matter (CDM). The latter was first hypothesized in the 1930s [269, 270] when the first studies of the motion of galaxy clusters pointed at some non-luminous source of gravitation that must be present in order to explain the dynamics in the Newtonian limit. The argumentation was based on the validity of the virial theorem in gravitational systems, and in the 1970s, the observation of single galaxies came to the same conclusion [271, 272]. Some hidden matter must be distributed in the galaxy to allow rotation curves to be concordant with Newtonian gravity. Later, the strongest clue for collisionless CDM was provided by the observation of colliding galaxy clusters, where the separation of baryonic matter and the dominating gravitational sources was inferred using gravitational lensing methods [273]. This observation of the Bullet cluster remains one of the greatest phenomenological challenges to proposals like modified Newtonian dynamics (see, e.g., Refs. [274–277]) alternative to CDM. The Λ CDM paradigm agrees with the properties of the cosmic microwave background (CMB), which was discovered in 1965 as the relic radiation of the universe’s era of recombination [278].⁶ The observed power spectra of the CMB exactly align with the predictions of the Standard Model of Big Bang cosmology (see, e.g., Refs. [279, 280]).

Despite the mounting astrophysical and cosmological evidence for the existence of Dark Matter (DM), its fundamental nature remains enigmatic, and many ideas exist for possible candidates for DM. We know for sure that it is stable (or its lifetime is at least of the order of the age of the universe) and that it is electrically neutral (or at most milli-charged). It cannot be any sort of baryonic matter since this would not be compatible with our understanding of big bang nucleosynthesis and the CMB power spectra. It must be essentially collisionless and dissipationless, which we can infer from our observation of the Bullet cluster. The stability of the large-scale structure of the universe suggests further that DM must be cold, i.e., moving at non-relativistic speeds. None of the known particles of the SM is equipped with all these properties. Therefore, these very properties might hint at novel particles beyond the SM.⁷ Candidates for particle DM include the axion or sterile neutrinos, which are connected to the previously discussed strong CP problem and the origin of neutrino masses, respectively. However, the existence of weakly-interacting massive particles (WIMPs) as DM is the prevailing paradigm of particle DM and represents one of the cornerstones of the quest for the true nature of DM. This is due to what is commonly referred to as the *WIMP miracle*:

⁶The CMB is the remnant electromagnetic radiation from roughly 378,000 years after the big bang.

⁷Though, it is not clear whether DM manifests as an elementary particle. Hypothetical primordial black holes [281, 282], which are thought to be formed in the early universe, represent an interesting way to account for DM without the introduction of new elementary particles [283].

given a particle χ with the mass around the EW scale and assuming a typical $\chi\chi \rightarrow f\bar{f}$ annihilation cross section into pairs of SM fermions f of the order of the EW interaction, we can explain the observed DM relic abundance. This means that such a particle departs from the thermal equilibrium in the early universe exactly to leave the correct amount of DM in the universe today to explain, for instance, our observations of the CMB. In App. A.1, we present the line of thought of the WIMP miracle more concretely.

In a nutshell, the search for WIMPs is organized into three categories. Indirect detection experiments search for DM annihilations in astrophysical objects like nearby galaxies or galaxy clusters [284]. In the present universe, the DM can be assumed to be at rest. This means that if, for example, there exists the possibility of DM particles annihilating into a pair of photons, i.e., the reaction $\chi\chi \rightarrow \gamma\gamma$ is allowed, then we should, in principle, be able to observe an excess in the γ -ray spectrum of a galaxy that is densely populated with DM. The same reasoning also applies to any other final state particles. For sufficiently large cross sections, the annihilation rate might be large enough to leave a signal in the observed particle spectra. Given that astrophysical objects have highly non-trivial many-body dynamics and the exact particle spectra are difficult to predict, indirect detection experiments are plagued with large systematic uncertainties that are hard to overcome. Hence, the report of excesses is always debatable to some extent. As a famous example, the Large Area Telescope (LAT) onboard of the Fermi Gamma Ray Space Telescope [285] reported an excess in the gamma ray spectrum of the galactic center at energies of $\simeq 1$ to 10 GeV in 2009 [286, 287]. However, the source of the galactic center excess remains elusive until today [288]. Another example is the anomalous positron fraction at high energies in cosmic rays, which was first observed by the PAMELA experiment [289, 290]. These results were later confirmed by measurement of the Fermi-LAT [291] and AMS-02 [292, 293] experiments, among others. Large contributions by astrophysical objects like pulsars remain a possible explanation [294–296] such that we still lack a definitive answer to what causes the excess in the leptonic spectra.

Direct detection experiments follow a different approach. The general idea to directly observe DM relies on the assumption that the Earth traverses the local DM halo in the Milky Way. Therefore, DM particles might scatter off the atomic nuclei of detector materials (see, e.g., Refs. [297–299]). If DM interacts with SM particles in any way other than gravitationally, then these scattering events should deposit enough recoil energy in the detectors to be, in principle, measurable. Exposing the detector target to the local DM flux for an extended period of time, we can derive tight constraints on the DM mass and couplings when no excess is reported. A pedagogical review of

the physics of direct detection experiments, including many calculational details, is provided in Ref. [300].

One example of the many direct detection experiments is the XENON1T experiment [301–303], which is focused on detecting DM particles with masses $\gtrsim 1$ GeV and uses a tank filled with 1 ton of liquid xenon as detector material. As common for basically all direct detection experiments, it works underground in order to suppress background cosmic radiation as much as possible. Therefore, these experiments especially need a thorough understanding of the background signals originating from radioactive decays of the underground materials surrounding the experiment. In 2020, the XENON collaboration reported a 3σ excess in electron recoil energies around 2.3 keV, which could potentially be explained by the existence of solar axions [304]. However, the hypothesis of tritium beta decays due to detector contamination as the origin of the excess cannot yet be rejected [304]. Hopefully, the upgraded XENONnT experiment will resolve this unclarity.

Another infamous claim for measuring an excess in a direct detection experiment stems from the DAMA and LIBRA collaborations [305–307]. They insist that they have successfully detected DM due to the observed annual modulation of events expected of DM particles since the Earth is moving around the Sun while moving through the galactic DM halo. However, the results are very much debated and still open to interpretation. In order to clarify the situation, experiments like COSINUS [308] are supposed to reproduce the DAMA/LIBRA results as its NaI detector is designed as an exact copy of the DAMA/LIBRA experiment. To this day, the DAMA/LIBRA measurement could not be reproduced by any other experiment.

In addition to the mere detection of DM, we would like to study its fundamental properties. And if DM is realized as an elementary particle with more than just gravitational couplings to SM particles, then the best way to test its characteristics would be to directly produce DM at a particle collider, where we maintain control over the production mechanism. There are various ideas on how DM could be produced at the LHC. Promising collider signatures searched for by the ATLAS and CMS collaborations are mono- X searches, where the X can, for instance, be a jet or an EW vector boson. Consider the observation of a single jet with large transverse momentum p_T relative to the beam axis but no signature to compensate for the p_T . Such a scenario would be explained by the production of DM, leaving the detectors unobserved and canceling the transverse momentum of the jet. Therefore, the search for large amounts of missing transverse momentum \vec{p}_T^{miss} is assumed to be a promising path for the search for DM (see, e.g., Refs. [309, 310] for up-to-date search results).

Another interesting avenue to search for DM at the LHC would be given if DM contributed to the invisible decay width of the SM Higgs boson. Since the precise study of the properties of the Higgs boson is a central goal of the LHC research program, the measurements of its partial decay widths continue to be refined. Most recently, an upper bound of $\mathcal{B}(h \rightarrow \text{inv}) < 10.7\%$ has been published on the decay of the Higgs boson into invisible particles [311]. These precision studies put stringent constraints on the DM parameter space whenever the process $h \rightarrow \chi\chi$ is kinematically allowed, i.e., whenever $m_\chi \leq m_h/2$. Many more searches are dedicated to the observation of DM, including, among others, the associated production with top quarks and EW gauge bosons [312–314]. So far, the LHC has not succeeded with its DM search ambitions but progress continues to be made in various directions. An illuminating review of collider searches is given in Ref. [315], and the research program as proposed by the LHC Dark Matter Working Group is provided in Refs. [316–318].

The prototype WIMP candidate, which is discussed extensively in the literature, is the neutralino in supersymmetric theories. In the MSSM, the fermionic SUSY partner of the EW gauge bosons as the lightest supersymmetric particle would satisfy all requirements for a generic WIMP. Moreover, in addition to the solution to the DM puzzle, we would also have an immediate solution to the EW hierarchy problem in such a setting. However, due to the non-observation of SUSY at the LHC, such approaches decrease in popularity. In the following Chap. 3, we discuss an alternative approach which assumes that both the SM Higgs boson and a WIMP emerge as composite pseudo Nambu–Goldstone bosons from a strongly-coupled sector at the TeV scale. As a pNGB, the Higgs boson would naturally be light, and the hierarchy problem would, therefore, be solved. Moreover, the couplings of a generic pNGB DM candidate seem to evade the challenging experimental exclusion limits from direct detection experiments. Hence, we deem it a promising endeavor to examine this approach in more detail in the following.

3 Probing Pseudo Nambu–Goldstone Boson Dark Matter Interactions with Top Quarks

In this chapter, we examine the prospects of experimentally testing a certain class of models for Dark Matter (DM)—those in which both the DM candidate and the SM Higgs boson arise as pseudo Nambu–Goldstone bosons (pNGBs) from a strongly-coupled sector that is assumed as an extension of the SM. Since these models generically predict dominant couplings between the DM candidate to top quarks, our work focuses on pinning down the sensitivity of $t\bar{t} + E_T^{\text{miss}}$, $tW + E_T^{\text{miss}}$, and $j + E_T^{\text{miss}}$ searches at the LHC. Here, we denote missing transverse energy by E_T^{miss} . We compare our results to the limits inferred from off-shell Higgs production via vector-boson fusion, which are presented in the context of Ref. [319]. Furthermore, we discuss the experimental accessibility via indirect and direct detection experiments and how pNGB DM could constitute all of the observed DM relic density in the cosmos. This chapter reports the findings of publication [1] and starts with a general introduction to the physics of pNGB DM in the subsequent section.

3.1 An Introduction to pNGB Dark Matter

As already elucidated in Sect. 2.2, weakly-interacting massive particles (WIMPs) have been the prime dark matter (DM) candidate for more than three decades because they can give rise to the correct abundance of DM today via thermal freeze-out production. However, the null results from DM direct and indirect detection experiments (see, for instance, Refs. [320, 321]) along with the still unsuccessful search for anomalous E_T^{miss} production at the LHC (see Ref. [322] for an experimental status report) have by now ruled out large portions of the parameter space of the simplest WIMP hypotheses such as the neutralino in supersymmetric theories.

Compelling examples of still viable WIMP models are provided by scenarios in which DM consists of pNGBs. Suppose, for example, we add a complex scalar field ϕ equipped with a global U(1) symmetry to the SM. Assuming ϕ to be a singlet under \mathcal{G}_{SM} , we can write down the renormalizable Lagrangian [319, 323–325]

$$\mathcal{L} = \mathcal{L}_{\text{SM}} + |\partial_\mu \phi|^2 + \frac{\mu_\phi^2}{2} |\phi|^2 - \frac{\lambda_\phi}{2} |\phi|^4 - \lambda_{H\phi} |\phi|^2 |H|^2 + \frac{\mu_\phi'^2}{4} (\phi^2 + \text{h.c.}) . \quad (3.1)$$

The U(1) symmetry is broken explicitly by the last term proportional to $\mu_\phi'^2$, and, due to the shape of the potential, it is spontaneously broken and assumes a VEV v_ϕ . We can, therefore, parametrize the field $\phi = (v_\phi + \sigma) e^{i\varphi/v_\phi}/\sqrt{2}$, distinguishing the radial and angular modes σ and φ , respectively. This leaves the real scalar field φ as pNGB DM candidate endowed with a mass μ_ϕ' . From the original continuous U(1) symmetry solely the invariance under $\phi \rightarrow \phi^*$ remains. If we assume the radial mode to be sufficiently heavy, we can separate its phenomenology from low energy dynamics. This is technically achieved by *integrating out* σ in the Wilsonian sense leaving us with an EFT for the SM and the pNGB DM candidate φ . In this setting, the leading interaction of the DM with the SM is provided by the operator $\partial_\mu |\varphi|^2 \partial^\mu |H|^2$, which we refer to as the *derivative Higgs portal*. The dominance of the derivative interaction might explain why no DM scattering events in direct detection experiments have been reported. This can readily be understood by imagining the Earth traversing the local DM halo of the Milky Way. Since the Earth’s motion is slow compared to the speed of light, DM particles scattering off atomic nuclei in experiments on Earth are highly unlikely due to the momentum suppression resulting from the derivative interaction. Thus, the constraints from direct detection experiments are naturally evaded, this being a common feature of models in which DM arises as a pNGB. On the other hand, the annihilation of DM to SM particles mediated by the derivative Higgs portal is an *s*-wave process, and thermal freeze-out can, therefore, yield the observed relic density for a DM mass of the order of 100 GeV, preserving the case of the WIMP miracle for EW-scale DM (see Sect. 2.2 and App. A.1).

In Sect. 2.1, we already established the EW hierarchy problem of the SM, which can be boiled down to the question of why the Higgs boson is so light despite possible large corrections from any new particles at the Planck or GUT energy scale. We also briefly pointed at SUSY as one of the most popular solutions to this fine-tuning problem. However, other ways exist to explain a small Higgs mass that do not require as many new degrees of freedom beyond the SM. One promising approach is given by the class of composite Higgs models (see Refs. [326, 327] for in-depth reviews). There, the Higgs

boson emerges as pNGB from a strongly-interacting sector and, as such, is naturally light. The minimal realistic model, including a pNGB Higgs boson, is constructed from a strongly-coupled sector endowed with a global $SO(5)$ symmetry which is spontaneously broken to $SO(4)$ at the TeV scale [328]. This results in four real pNGBs, which can then be identified with the components of the complex Higgs doublet within the SM. In general [327], the construction assumes a new sector endowed with a global Lie group symmetry \mathcal{G} , referred to as the composite sector. Its vacuum state, however, is only assumed to be invariant under a subgroup $\mathcal{H} \subset \mathcal{G}$, which results in the SSB $\mathcal{G} \rightarrow \mathcal{H}$ and the emergence of massless exact NGBs in the coset \mathcal{G}/\mathcal{H} . In analogy to the previously mentioned minimal example, for the SM Higgs doublet to emerge as pNGB, the subgroup \mathcal{H} must contain the EW gauge group, i.e., $SU(2)_L \times U(1)_Y \subseteq \mathcal{H}$. Taking into account also \mathcal{G} -breaking interactions of the SM gauge fields and fermions with the composite sector such that \mathcal{G} is not exactly realized, renders the NGBs massive. Hence, we speak of pNGBs which is necessary to obtain a massive Higgs boson in the model. Various such models have been studied in detail and represent fascinating opportunities to resolve the EW naturalness problem of the SM [326].¹

The simple DM model described by the Lagrangian in eq. (3.1) and composite Higgs scenarios appear to yield interesting phenomenological ramifications in their own rights. However, it seems particularly intriguing to consider both DM and the SM Higgs boson to arise as composite pNGBs from a single TeV-scale strongly-coupled sector. Models of this type can address simultaneously the EW hierarchy problem of the SM and the DM puzzle [330], and as a result, they have received notable attention in recent years [319, 323–325, 331–354]. Probes of composite pNGB DM include indirect detection searches and collider experiments. The collider reach on the derivative Higgs portal has been recently analyzed in vector-boson fusion (VBF) Higgs production [319], finding a limited sensitivity at the LHC. This motivates studies of the indirect constraints on the derivative Higgs portal that arise from off-shell single-Higgs and on-shell double-Higgs production at hadron colliders [355].

Besides the derivative Higgs portal, composite pNGB DM models necessarily contain additional interactions to provide a potential and Yukawa couplings for the Higgs boson and a mass for the DM candidate. A theoretically motivated situation is one in which DM couples most strongly to the third generation of SM fermions. At the level of dimension-six operators, such interactions can either be of Yukawa type or involve

¹See also Ref. [329] as a pedagogical introduction to the theory of Goldstone bosons and the coset construction.

the product of a DM and a SM current. Detailed studies of the DM phenomenology of composite pNGB models where the Goldstone shift symmetry of DM is broken by the top or the bottom Yukawa coupling can be found in Refs. [340, 343]. These analyses show that scenarios in which the shift symmetry is broken in the bottom sector are significantly less constrained by DM direct detection than those in which the top sector provides the leading symmetry breaking. In composite pNGB models with sizeable DM-SM Yukawa couplings and a successful DM phenomenology, the leading E_T^{miss} signature is, therefore, expected to be DM production in association with bottom quarks. Unfortunately, this process can only be constrained poorly at the LHC [356–358]. Let us suppose, on the other hand, that effective current-current interactions provide a relevant portal between the dark and the visible sector. In this case, large DM-top couplings would be compatible with both the bounds from DM (in)direct detection and the observed relic abundance if DM was sufficiently heavy [319]. As a result, such composite pNGB DM models can be tested at the LHC by searching for DM production in association with top-quark pairs ($t\bar{t} + E_T^{\text{miss}}$) or a top quark and a W boson ($tW + E_T^{\text{miss}}$). These mono- X channels, from now on referred to as $tX + E_T^{\text{miss}}$, have received a lot of attention from the DM collider community [312, 356, 357, 359–368].

The main goal of this chapter is to analyze the LHC reach of the $tX + E_T^{\text{miss}}$ channels and to constrain the parameter space of composite pNGB DM models. To keep our discussion as model-independent as possible we work in an effective field theory (EFT) focusing on the subset of operators that lead to DM production in association with top quarks. Through loops such operators also lead to a $j + E_T^{\text{miss}}$ signal, and we study the limits on the parameter space of the pNGB DM effective field theory that are imposed by the corresponding mono-jet searches. We then offer a comprehensive discussion of the phenomenological features of pNGB DM models, including an analysis of the DM direct and indirect detection constraints as well as of the physics of thermal freeze-out. The search strategies and pNGB DM benchmark models that we discuss are meant to set the stage for dedicated experimental analyses by ATLAS and CMS.

Our work is organized as follows. In Sect. 3.2, we describe the structure of the composite pNGB DM models that we consider. Our Monte Carlo (MC) generation and our detector simulation are spelled out in Sect. 3.3. Sect. 3.4 describes the analysis strategies to search for the relevant mono- X signals. In Sect. 3.5, we examine the sensitivity of the studied pNGB DM signatures at upcoming LHC runs. The present and future constraints on the pNGB DM effective field theory that arise from invisible

Higgs decays are discussed in Sect. 3.6. The relevant non-collider limits are presented in Sect. 3.7. We discuss our main results and give an outlook in Sect. 3.8. The impact of the assumed systematic background uncertainties on our $tX + E_T^{\text{miss}}$ projections is studied in the supplementary material that can be found in App. A.3.

3.2 Theoretical Framework

Throughout this chapter, we consider theories in which both the SM Higgs doublet H and the DM candidate χ arise as light pNGBs from a strongly-coupled sector. The DM candidate is a singlet under the SM gauge group \mathcal{G}_{SM} and we assume it to be a complex scalar. We can, therefore, describe the model under scrutiny by a Lagrangian of the form

$$\mathcal{L} = \mathcal{L}_{\text{SM}} + |\partial_\mu \chi|^2 - m_\chi^2 |\chi|^2 + \mathcal{L}_{\text{int}}^\chi, \quad (3.2)$$

where m_χ denotes the DM mass and all interactions of the DM particle are encoded in $\mathcal{L}_{\text{int}}^\chi$. For further discussion, it proves useful to disentangle

$$\mathcal{L}_{\text{int}}^\chi = \mathcal{L}_{\chi H} + \mathcal{L}_{\chi\psi}, \quad (3.3)$$

distinguishing interactions of DM with the SM Higgs doublet H and SM fermions, respectively. More concretely, we are interested in interactions of the form

$$\begin{aligned} \mathcal{L}_{\chi H} &= \frac{c_d}{f^2} \partial_\mu |\chi|^2 \partial^\mu |H|^2 - \lambda |\chi|^2 |H|^2, \\ \mathcal{L}_{\chi\psi} &= \frac{|\chi|^2}{f^2} \left(c_t y_t \bar{Q}_L \tilde{H} t_R + \text{h.c.} \right) + \frac{i}{f^2} \chi^* \overleftrightarrow{\partial}_\mu \chi \sum_{\psi=Q_L, t_R, b_R} d_\psi \bar{\psi} \gamma^\mu \psi. \end{aligned} \quad (3.4)$$

These operators are part of an EFT model put forth in Ref. [319], which is equivalent to the one discussed in Refs. [369, 370]. The terms in $\mathcal{L}_{\chi H}$ correspond to the derivative and marginal Higgs portal, respectively. Moreover, the terms in $\mathcal{L}_{\chi\psi}$ correspond to the Yukawa-type DM-top coupling and the current-current type interactions between DM and the third-generation SM quarks, respectively. The common decay constant of the pNGBs is denoted by f , while the coefficients c_i , λ , and d_j are $\mathcal{O}(1)$ constants that we assume to be real such that CP is conserved. Furthermore, in eq. (3.4), we have used the definition $\chi^* \overleftrightarrow{\partial}_\mu \chi = \chi^* \partial_\mu \chi - \chi \partial_\mu \chi^*$. $Q_L = (t_L, b_L)^T$ denotes the left-handed third-generation quark doublet, t_R (b_R) is the right-handed top-quark (bottom-quark) singlet, $y_t = \sqrt{2} m_t / v$ is the top Yukawa coupling with $m_t \simeq 163$ GeV the top mass and $v \simeq 246$ GeV the Higgs vacuum expectation value (VEV), and we have defined $\tilde{H}^i = \varepsilon_{ij} (H^j)^*$ with ε_{ij} totally antisymmetric and $\varepsilon_{12} = 1$. Notice that the current-current type operator in $\mathcal{L}_{\chi\psi}$ is absent if hidden-charge conjugation (i.e., $\chi \rightarrow -\chi^*$ and

$\psi \rightarrow \psi$) is preserved as in all explicit pNGB DM models studied in Ref. [343]. Moreover, this operator vanishes trivially if the DM candidate is a real scalar. Furthermore, we note that the DM interactions with SM quarks respect the Yukawa hierarchy of the SM. Hence, the model follows the principle of minimal flavor violation (MFV) [371], which guarantees that the stringent constraints from the absence of FCNCs are circumvented.

Besides the four types of interactions introduced in eq. (3.4), the full pNGB DM effective field theory can contain additional dimension-six operators such as $\chi^* \overleftrightarrow{\partial}_\mu \chi \partial_\nu B^{\mu\nu}$ and $|\chi|^2 V_{\mu\nu} V^{\mu\nu}$. Here, $V_{\mu\nu} = B_{\mu\nu}, W_{\mu\nu}^i, G_{\mu\nu}^a$ denotes the $U(1)_Y$, $SU(2)_L$, and $SU(3)_C$ field-strength tensor, respectively. Since the latter two types of operators do not lead to a relevant $tX + E_T^{\text{miss}}$ signal at tree level, such terms are not directly testable in DM production in association with top quarks. In contrast, the presence of DM couplings with gauge bosons may have an important impact on the calculation of the DM (in)direct detection bounds and on the derivation of the DM relic density. Let us highlight the complementarity of collider and non-collider bounds in a simple fashion. To this purpose, we restrict our analysis to the subclass of models in which the leading effects are well captured by the effective Lagrangians $\mathcal{L}_{\chi H}$ and $\mathcal{L}_{\chi\psi}$ at the scale at which DM and the Higgs boson emerge as composite pNGBs. However, we will discuss and include pNGB DM interactions with gauge bosons that are generated from eq. (3.4) once radiative corrections are included, whenever these yield significant contributions (see Sect. 3.7).

We further mention that, under the assumption that the cancellation of gauge anomalies only depends on the SM fermion representations and not on the structure of the pNGB DM effective field theory (in particular the coefficients d_ψ in eq. (3.4)), the current-current type DM-top operator does not lead to a $j + E_T^{\text{miss}}$ signal. In practice, this requires us to introduce local counterterms that cancel the anomalous contributions in the five-point diagrams like the one shown on the right-hand side in Fig. 3.2 (see Refs. [372–374] for related discussions of gauge anomalies in the context of the so-called SMEFT). Since we envisage that eq. (3.4) describes new-physics scenarios in which the full SM gauge symmetry is preserved, a matching calculation in the full theory will always result in the required anomaly cancellation, and consequently, a cancellation of the current-current type contributions to the mono-jet signature for any value of the parameters d_ψ .

As a final remark on the model under consideration, we have implemented the interactions given by the operators in eq. (3.4) into a `FeynRules` model file [22,23]. Thus, our analytical calculations are performed using `FeynArts` [14] and `FormCalc` [15], and the transition into the `UFO` format [21] enables the Monte Carlo (MC) generation of events

employing `MadGraph` [24]. Some analytical calculations are backed up by computations performed using `FeynCalc` [18–20].

3.3 MC Event Generation and Detector Simulation

In our work, we study the $t\bar{t} + E_T^{\text{miss}}$, the $tW + E_T^{\text{miss}}$, and the $j + E_T^{\text{miss}}$ signatures that arise from insertions of the pNGB DM operators introduced eq. (3.4). Examples of leading-order (LO) diagrams that involve DM-Higgs and DM-top operators are displayed in Fig. 3.1 and Fig. 3.2, respectively. Notice that only DM-top operators can lead to a LO mono-jet signal as illustrated by the graph shown on the right-hand side in Fig. 3.2. All our signal predictions assume proton-proton (pp) collisions at a center-of-mass (CM) energy of 14 TeV and are calculated using a `FeynRules` [23] implementation of the Lagrangian (3.4) in the `UFO` format [21]. The generation and showering of the mono- X samples is performed with `MadGraph` [24] at LO and `PYTHIA 8` [35], respectively, using `NNPDF 3.0` PDFs [191]. In order to preserve both spin correlations and finite-width effects, final-state top quarks and W bosons are decayed with `MadSpin` [25].

In the case of the $tX + E_T^{\text{miss}}$ signatures, all SM processes that contain at least two charged leptons ($\ell = e, \mu$) coming from the decay of an EW gauge boson $V = W, Z$ are included in the background simulation. We do not consider backgrounds with either fake electrons from jet misidentification or with real non-isolated leptons from the decay of heavy-flavored hadrons. A reliable estimate of these backgrounds depends on a detailed simulation of detector effects beyond the scope of this thesis. For the most recent ATLAS analyses involving leptonic final states [367, 368], the background from non-prompt leptons is a few percent of the total background.² The backgrounds from $t\bar{t}$ [375], tW [376], WW , WZ , and ZZ production [377, 378] are all generated at the next-to-leading order (NLO) in QCD with `POWHEG-BOX` [28]. The $V + \text{jets}$ backgrounds are generated at LO using `MadGraph` and include up to four additional jets. `MadGraph` is also used to simulate the $t\bar{t}V$ backgrounds with a multiplicity of up to two jets, while the tZ and tWZ backgrounds are obtained at LO with the same MC generator. All partonic events are showered with `PYTHIA 8`. The samples produced with `POWHEG-BOX` are normalized to the corresponding NLO QCD cross sections, except for $t\bar{t}$, which is normalized to the cross section obtained at the next-to-next-to-leading order (NNLO) in QCD plus next-to-next-to-leading logarithmic QCD corrections [163, 379]. The $V + \text{jets}$ sam-

²We distinguish between prompt and non-prompt leptons. The former can be directly traced back to the hard scattering event. The latter are the byproduct of secondary processes like, e.g., hadronization or are objects misidentified as leptons in the detector.

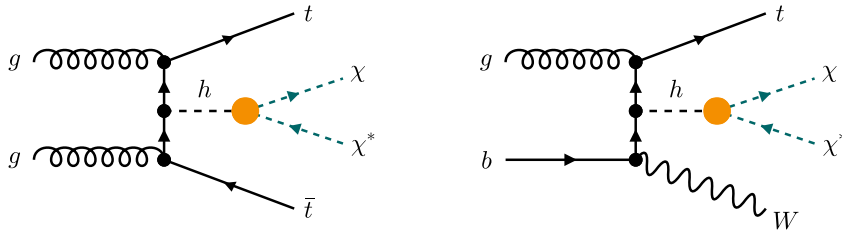


Figure 3.1: Examples of Feynman diagrams with insertions of the DM-Higgs operators (filled orange circles) in eq. (3.4) that lead to a $t\bar{t} + E_T^{\text{miss}}$ (left) and $tW + E_T^{\text{miss}}$ (right) signal. The black dots indicate SM interactions.

ples are normalized to the NNLO QCD cross sections [380, 381] and the $t\bar{t}V$ samples are normalized to the NLO QCD cross section as calculated by `MadGraph`.

For the $j + E_T^{\text{miss}}$ signature, the dominant SM backgrounds arise from $V + \text{jets}$ production. The only relevant process not included in the $tX + E_T^{\text{miss}}$ backgrounds described above is the $Z + \text{jets}$ channel followed by the decay $Z \rightarrow \nu\bar{\nu}$. As done in related works [382, 383], the corresponding background is generated at LO with `MadGraph`, and can contain up to two additional jets. The generation is performed in slices of the vector-boson transverse momentum (p_T), and the resulting events are showered with `PYTHIA 8` employing a Catani–Krauss–Kuhn–Webber jet matching procedure [384]. The inclusive signal region IM3 of the ATLAS analysis [309] requires $E_T^{\text{miss}} > 350$ GeV, and for these selections the background from $V + \text{jets}$ production amounts to around 95% of the total SM background. The $V + \text{jets}$ samples are normalized such that the different contributions match the number of events in the IM3 signal region as estimated by ATLAS scaled from a CM energy of 13 TeV to 14 TeV and to the appropriate integrated luminosity. The additional minor backgrounds from $t\bar{t}$, tW , and diboson production are the same as in the $tX + E_T^{\text{miss}}$ case.

The actual physics analyses use experimentally identified electrons, muons, photons, jets (j), and E_T^{miss} . These objects are constructed from the stable particles in the generator output. Jets are built out of the momenta of all the stable particles depositing energy in the calorimeter except for muons using the anti- k_t algorithm [385] with a radius parameter of $R = 0.4$, as implemented in `FastJet` [47]. Jets originating from the hadronization of bottom quarks (b -jets) are experimentally identified (i.e., b -tagged) with high efficiency. The \vec{p}_T^{miss} vector with magnitude E_T^{miss} is constructed from the transverse momenta of all the invisible particles in the event. Detector effects are simulated by smearing the momenta of the analysis objects and by applying efficiency factors

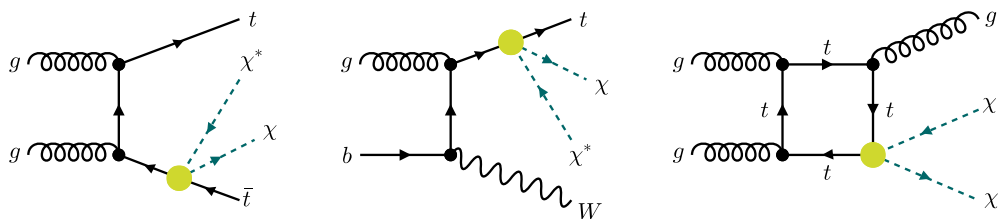


Figure 3.2: Assortment of graphs with insertions of the DM-top operators (filled green circles) entering eq. (3.4) that give rise to a $t\bar{t} + E_T^{\text{miss}}$ (left), $tW + E_T^{\text{miss}}$ (middle), and $j + E_T^{\text{miss}}$ (right) signature.

where applicable. The used smearing and efficiency functions are tuned to reproduce the performance of the ATLAS detector [386, 387]. In particular, the performance of the ATLAS b -tagging algorithm is taken from Ref. [388]. For the mono- X analyses performed in this chapter, a b -tagging working point is chosen that yields a b -tagging efficiency of 77%, a c -jet rejection of 5, and a light-flavor jet rejection of 110. This means that generated b -jets are correctly identified as such in 77% of the cases. Likewise, the probability of wrongly identifying a c -jet (light-flavor jet) as b -jet amounts to $1/5 = 20\%$ ($1/110 \simeq 0.9\%$). More details on our detector simulation can be found in the related papers [363, 389].

3.4 Mono- X Analysis Strategies

Below, we describe the analysis strategies to target the $tX + E_T^{\text{miss}}$ and $j + E_T^{\text{miss}}$ signals that are due to the interactions described by eq. (3.4). For each analysis strategy we define the signal regions, spell out all selection criteria, and quantify the systematic uncertainties that plague the search strategy in question.

3.4.1 $tX + E_T^{\text{miss}}$ Final States

The considered signal events include the decays of two W bosons. We address the final states where only one or both of the W bosons decay into charged leptons, which hereafter will be called semileptonic or fully-leptonic, respectively. The branching fraction for hadronic W decays amounts to $\mathcal{B}(W \rightarrow \text{hadrons}) \simeq 67\%$. However, leptonic decays $W \rightarrow \ell\nu_\ell$ offer a much cleaner final state without much QCD activity, which improves the sensitivity decisively. For a specific charged lepton flavor ℓ , the corresponding lep-

tonic decay branching fraction is measured to be $\mathcal{B}(W \rightarrow \ell\nu_\ell) \simeq 11\%$. Since we are interested in DM production in association with top quarks, one should further note that top quarks decay in over 99% of the cases into a W boson and a bottom-type quark. We can anticipate enhanced b -jet activity since $\Gamma(t \rightarrow Wb)/\Gamma(t \rightarrow Wq) \simeq 96\%$. All these numbers are quoted from Ref. [13].

Our $tX + E_T^{\text{miss}}$ analysis is based on the definition of three orthogonal signal regions. The first two signal regions target the associated production of a $t\bar{t}$ pair and DM with SR1 (SR2) selecting semileptonic (fully-leptonic) events. The third signal region called SR3, instead, considers the associated production of a top quark, a W boson and DM, which is searched for in fully-leptonic events. The corresponding final states, therefore, involve a single isolated charged lepton and two b -tagged jets (SR1), two isolated charged leptons and two b -tagged jets (SR2), or two isolated charged leptons and a single b -tagged jet (SR3). Notice that $tW + E_T^{\text{miss}}$ production typically has a smaller cross section than $t\bar{t} + E_T^{\text{miss}}$ production. However, in the case of the two-lepton final state, it has been shown in Ref. [366] that it is possible to devise a selection strategy that combines the $t\bar{t} + E_T^{\text{miss}}$ and the $tW + E_T^{\text{miss}}$ channels and has a significantly larger sensitivity than $t\bar{t} + E_T^{\text{miss}}$ alone.

Such a selection is based on the observation that events produced by a fully-leptonic $t\bar{t}$ decay contain two ℓb pairs for both of which the invariant mass $m_{\ell b}$ is bounded from above by $\sqrt{m_t^2 - m_W^2} \simeq 153 \text{ GeV}$. This is not the case for the tW production, which contains only one ℓb pair satisfying this bound. The two processes can thus be separated by defining the variable

$$m_{b\ell}^t = \min \left(\max \left(m_{\ell_1 j_a}, m_{\ell_2 j_b} \right) \right), \quad (3.5)$$

and putting a cut on $m_{b\ell}^t$ of around 160 GeV to separate $t\bar{t}$ from tW events. In eq. (3.5), the variables $m_{\ell_1 j_a}$ and $m_{\ell_2 j_b}$ denote the invariant mass of the leading and subleading leptons ℓ_1 and ℓ_2 , and the jets j_a and j_b . The minimization with respect to the jet pairs j_a and j_b runs over all of the b -tagged jets if the number of b -tagged jets satisfies $N_b \geq 3$ or over the b -tagged jets and the untagged jet with the highest b -tagging weight if $N_b \leq 2$. Since the three signal regions are designed to have no events in common, the final search sensitivity of the $tX + E_T^{\text{miss}}$ channel will be calculated after the statistical combination of SR1, SR2, and SR3. The selection criteria corresponding to the three signal regions are summarized in Tables 3.1 and 3.2.

In the case of SR1, the selection requirements are similar to the ones imposed in the signal region DM of Ref. [367]. However, some variables have been modified and the values of the cuts have been optimized to our MC simulations of both the signal and the

Variable	SR1 selection
N_ℓ	= 1
$p_T(\ell)$	> 25 GeV
$ \eta(\ell) $	< 2.5
N_j	≥ 4
$p_T(j)$	> (80, 60, 30, 25) GeV
$ \eta(j) $	< 2.5
N_b	≥ 2
$p_T(b)$	> (80, 25) GeV
$ \eta(b) $	< 2.5
E_T^{miss}	> 550 GeV
m_T^ℓ	> 180 GeV
Topness	> 8
$m_{\text{top}}^{\text{reclustered}}$	> 150 GeV
$H_{T,\text{sig}}^{\text{miss}}$	> 15
$ \Delta\phi_{\ell,\text{miss}} $	> 1.3
$ \Delta\phi_{\text{min}} $	> 0.9
$ \Delta\phi_{bb} $	< 2.5

Table 3.1: Definition of the signal region SR1. The number of charged leptons, light-flavored jets, and b -tagged jets are denoted by N_ℓ , N_j , and N_b , respectively.

background at the high-luminosity upgrade of the LHC (HL-LHC). The basic selection requires one and only one isolated charged lepton and at least four jets of which at least two must be tagged as b -jets. Furthermore, jets tagged as hadronic decays of a τ lepton are vetoed. The employed cuts on the p_T and pseudorapidities (η) of the leptons and jets can be found in Table 3.1. After the initial selections, the dominant background is $t\bar{t}$ production with one top quark decaying leptonically and the other one decaying hadronically. This background is strongly reduced by demanding $E_T^{\text{miss}} > 550$ GeV and requiring a lower limit of 180 GeV on the transverse mass of the charged lepton defined as

$$m_T^\ell = \sqrt{2 |\vec{p}_T(\ell)| |\vec{p}_T^{\text{miss}}| (1 - \cos \Delta\phi_{\ell,\text{miss}})}. \quad (3.6)$$

Here, $\vec{p}_T(\ell)$ denotes the components of the lepton momentum transverse to the beam, \vec{p}_T^{miss} is the vector sum of the transverse momenta of the invisible particles and $\Delta\phi_{\ell,\text{miss}} = \Delta\phi(\vec{p}_T(\ell), \vec{p}_T^{\text{miss}})$ is the azimuthal angular separation between these two vectors. To re-

Variable	SR2 selection	SR3 selection
N_ℓ		= 2
$p_T(\ell)$		> (25, 20) GeV
$ \eta(\ell) $		< 2.5
$m_{\ell\ell}$		> 20 GeV
	Z-boson veto for OSSF leptons	
N_b		≥ 1
$p_T(b)$		> 30 GeV
$ \eta(b) $		< 2.5
$m_{b\ell}^t$	< 160 GeV	> 160 GeV or $N_j = 1$
E_T^{miss}	> 550 GeV	> 350 GeV
$ \Delta\phi_{\text{min}} $	n/a	> 0.8
$ \Delta\phi_{\text{boost}} $	< 1.5	< 2.5
M_{scal}	n/a	< 500 GeV
m_{T2}	> 100 GeV, shape fit	> 170 GeV

Table 3.2: As Table 3.1 but for the signal regions SR2 and SR3.

ject events which are incompatible with top-quark decays, selections on the variables topness [390] and $m_{\text{top}}^{\text{reclustered}}$ [367] are imposed. An additional rejection of the SM background is achieved with selections on $H_{T,\text{sig}}^{\text{miss}}$, i.e., the ratio of E_T^{miss} built as the vector sum of the momenta of all the signal jets and leptons in the event, reduced by 100 GeV and divided by its experimental resolution [391, 392]. Finally, cuts on the azimuthal angular separations $\Delta\phi_{\ell,\text{miss}}$, $\Delta\phi_{\text{min}}$ between $\vec{p}_T(j)$ and \vec{p}_T^{miss} for the four leading jets and on $\Delta\phi_{bb}$ between the two b -tagged jets are imposed as detailed in Table 3.1.

The basis selection of events is common for the signal regions SR2 and SR3. It consists of the requirement of having exactly two isolated opposite-sign (OS) leptons and the invariant mass of the OS leptons has to fulfil $m_{\ell\ell} > 20$ GeV. If the charged leptons are of the same flavor, events with $71 \text{ GeV} < m_{\ell\ell} < 111 \text{ GeV}$ are discarded to suppress backgrounds where the lepton pair arises from the decay $Z \rightarrow \ell^+\ell^-$. Furthermore, each event is required to contain at least one b -tagged jet. The relevant p_T and η selections of the OS leptons and b -jets are specified in Table 3.2. The first selection that differs between the two signal regions is a cut on the $m_{b\ell}^t$ observable defined in eq. (3.5), which for SR2 (SR3) is required to be smaller (larger) than 160 GeV. The variable $m_{b\ell}^t$ is only defined for events with at least two reconstructed jets and events

with only one reconstructed jet are assigned to SR3. Further selections are used to optimize the rejection of the SM backgrounds. In the case of SR2 (SR3), we require $E_T^{\text{miss}} > 550$ GeV ($E_T^{\text{miss}} > 350$ GeV). Furthermore, the four leading jets have to satisfy $|\Delta\phi_{\text{min}}| > 0.8$ in the signal region SR3. The variable $\Delta\phi_{\text{boost}}$ defined as the azimuthal angle difference between \vec{p}_T^{miss} and the vector sum of \vec{p}_T^{miss} , $\vec{p}_T(\ell_1)$, and $\vec{p}_T(\ell_2)$, must satisfy the requirement $|\Delta\phi_{\text{boost}}| < 1.5$ ($|\Delta\phi_{\text{boost}}| < 2.5$) for SR2 (SR3). In the case of the signal region SR3, we additionally demand that the scalar sum M_{scal} of the transverse momenta of all the jets observed in the event satisfies $M_{\text{scal}} < 500$ GeV. Finally, in the signal region SR2, we require $m_{T2} > 100$ GeV and fit the shape of the m_{T2} distribution (see, for instance, Ref. [366]), whereas for the signal region SR3 we impose the cut $m_{T2} > 170$ GeV. Here, m_{T2} denotes the transverse mass introduced in Ref. [393].

Assuming an integrated luminosity of 3 ab^{-1} at a CM energy of 14 TeV, the number of background events surviving the discussed requirements amounts to 123, 34, and 48 in the case of SR1, SR2, and SR3, respectively. The signal efficiency depends on the DM mass and on the specific pNGB DM model, and in the considered cases it is between a few tens of a percent and a few percent. Given the relatively large number of surviving background events, the experimental reach depends sensitively on the systematic uncertainty of the estimated SM backgrounds. The size of these uncertainties depends on the detector performance and the techniques used for the background evaluation, which are typically based on a mixed MC and data-driven approach. Existing LHC analyses addressing signatures and a phase space similar to our $tX + E_T^{\text{miss}}$ strategy have background uncertainties of 10 % to 30 % (see Refs. [357, 367, 368]). In our numerical analysis, we assume a 15 % uncertainty on the backgrounds and a 5 % uncertainty on the pNGB DM signals. The latter uncertainty should account for the effect of scale variations and PDF uncertainties on the signal modeling.

In addition to the analysis strategy described in detail above, we have also studied the sensitivity of the fully-leptonic signal regions SRt3 of Ref. [357] and SR^{2-body} of Ref. [368]. Moreover, we also considered the semileptonic signal region DM of Ref. [367], the fully-hadronic signal regions SRt1 and SRt2 of Ref. [357], and SRA-TT of Ref. [394] to the parameter space of the pNGB DM effective field theory. Our analyses rely in these cases on CheckMATE 2 [45], which uses DELPHES 3 [48] as a fast detector simulation. We find that for what concerns leptonic final states, the best limits on the parameters of eq. (3.4) follow either from the signal region DM or SR^{2-body}, while in the case of a fully-hadronic search the strategies SRt2 and SRA-TT fare equally well. Furthermore, the event selections employed in Refs. [357, 367, 368, 394] perform at

most as good but not better than our optimized $tX + E_T^{\text{miss}}$ search strategy. We finally observe that for comparable sets of selection criteria the results from our parametrized simulation and the recast of the ATLAS analyses are in good agreement. This validates our simulation approach.

3.4.2 $j + E_T^{\text{miss}}$ Final State

In the case of the $j + E_T^{\text{miss}}$ final state, the relevant pNGB DM signal consists of a single high-transverse momentum jet and E_T^{miss} associated to the production of a pair of DM particles. Therefore, the signature resembles the canonical mono-jet signal, which has received a significant amount of experimental [395–398] and theoretical [399] attention at the LHC. This results in high-precision estimates of the dominant E_T^{miss} backgrounds that are associated to the production of an EW gauge boson accompanied by at least one high-transverse momentum jet.

In our work, we rely on the ATLAS mono-jet analysis in Ref. [309]. Specifically, we employ $E_T^{\text{miss}} > 350 \text{ GeV}$ and require a high-transverse momentum jet with $p_T(j) > 150 \text{ GeV}$ within $|\eta(j)| < 2.4$, and no more than four jets with $p_T(j) > 30 \text{ GeV}$ within $|\eta(j)| < 2.8$. The selection $|\Delta\phi_{\text{min}}| > 0.4$ is used to fully suppress the multi-jet background. All events containing a reconstructed electron or muon, or the hadronic decay of a tau lepton are rejected. Thus, our selection closely resembles the signal region IM3 of Ref. [309]. The systematic uncertainty quoted by ATLAS in IM3 is 1.4%, and we adopt this value as the systematic uncertainty on the total number of background events. Since we perform a multi-bin comparison of the shape of the E_T^{miss} variable, we also need to take into account uncertainties related to the E_T^{miss} shape. For each of the E_T^{miss} bins considered in the analysis, ATLAS gives an uncertainty which increases from around 1.4% to 4% between 350 GeV to 1.2 TeV. We apply these systematic uncertainties as bin-by-bin shape uncertainties in our $j + E_T^{\text{miss}}$ analysis. For the bins between 1.5 TeV and 2 TeV, we further assume an uncertainty of 5%, while we take an uncertainty of 8% for the total number of events in the overflow bin with $E_T^{\text{miss}} > 2 \text{ TeV}$. Notice that our uncertainty treatment corresponds to taking the uncertainties among different E_T^{miss} bins to be uncorrelated. In addition, since the statistical uncertainties of the control regions, that are used to constrain the background, will get reduced with more luminosity, also the systematic uncertainties are expected to decrease with larger data samples. We thus believe that our mono-jet study provides conservative results when applied to the full data set of the HL-LHC.

m_χ [GeV]	$f/\sqrt{ c_d }$ [GeV]	$ \lambda $	$f/\sqrt{ c_t }$ [GeV]	$f/\sqrt{ d_{tR} }$ [GeV]
70	165	2.4	153	325
100	154	6.0	150	324
200	138	(23)	137	305
300	123	(55)	122	278
400	109	(107)	107	255
500	96	(198)	96	231
1000	51	(2315)	50	129

Table 3.3: 95% CL bounds that derive from the $tX + E_T^{\text{miss}}$ search strategy described in Sect. 3.4.1 for seven different DM masses. All bounds assume 3 ab^{-1} of integrated luminosity collected at a CM energy of 14 TeV. Only the parameter shown in each line is taken into account, while all the remaining couplings in eq. (3.4) are set to zero.

m_χ [GeV]	$f/\sqrt{ c_t }$ [GeV]
70	96
100	95
200	90
300	81
400	74
500	65
1000	36

Table 3.4: As Table 3.3 but for the $j + E_T^{\text{miss}}$ search strategy described in Sect. 3.4.2.

3.5 Constraints from $tX + E_T^{\text{miss}}$ and $j + E_T^{\text{miss}}$ Searches at the LHC

On the basis of the selection criteria given in Sect. 3.4, we study the LHC sensitivity to the discussed mono- X signatures. For each signature and each studied pNGB DM benchmark, we calculate the value of the cross section which can be excluded at 95% confidence level (CL) normalized to the nominal LO cross section for the relevant model realization as calculated by `MadGraph`. The experimental sensitivity is evaluated using a test statistic based on a profiled likelihood ratio and we make use of the CLs method [400] as implemented in `Roostats` [401].

In Table 3.3, we present the 95 % CL bounds that derive from our $tX + E_T^{\text{miss}}$ analysis for seven different DM masses in the range from 70 GeV to 1 TeV. DM masses $m_\chi < m_h/2$ where $m_h \simeq 125$ GeV is the SM Higgs mass are not considered, because, in this case, invisible Higgs decays generically represent the best way to probe pNGB DM (see the discussion in Sect. 3.6). The shown limits correspond to the full data set of 3 ab^{-1} that the HL-LHC is expected to collect at a CM energy of 14 TeV. Only one free pNGB DM effective field theory parameter is allowed at a time. One observes that HL-LHC $tX + E_T^{\text{miss}}$ searches are most sensitive to the current-current type DM-fermion operators followed by the derivative Higgs portal operator and the Yukawa-type DM-top operator. The most difficult operator to probe is the marginal Higgs portal since, compared to the other pNGB DM effective field theory interactions in eq. (3.4), it leads to softer kinematic distributions, making a background suppression generically harder. Notice that in the case of the marginal Higgs portal, we have indicated the limits that correspond to a non-perturbative coupling, i.e., $|\lambda| > 4\pi$, by putting parentheses around the corresponding results. We finally add that for $m_\chi = 1$ TeV the bounds on $f/\sqrt{|c_d|}$ and $f/\sqrt{|c_t|}$ following from our $tX + E_T^{\text{miss}}$ search strategy are so low that an EFT description might not be valid. The corresponding exclusion limits are, therefore, only indicative.

The 95 % CL bounds that follow from our $j + E_T^{\text{miss}}$ search strategy are collected in Table 3.4. As discussed at the end of Sect. 3.2, mono-jet searches only allow to test the Wilson coefficient c_t of the Yukawa-type DM-top operator in eq. (3.4). From the shown results, it is evident that the mono-jet bounds on $f/\sqrt{|c_t|}$ are not competitive with those obtained from $tX + E_T^{\text{miss}}$. We add that neglecting the uncertainty on the shape of the E_T^{miss} distribution (see Sect. 3.4.2) in our $j + E_T^{\text{miss}}$ analysis would improve the given 95 % CL limits by around 35 %. However, even then the mono-jet limits on $f/\sqrt{|c_t|}$ fall short of the bounds obtained from our $tX + E_T^{\text{miss}}$ search strategy. Like in the case of the $tX + E_T^{\text{miss}}$ bounds, at high DM mass the $j + E_T^{\text{miss}}$ limits should only be taken as indicative because an EFT description may not be applicable in this regime. Benchmark scenarios with more than one non-zero pNGB DM effective field theory coefficient c_i , λ , and d_j are discussed in Sect. 3.8.

3.6 Constraints from Invisible Higgs Decays at the LHC

The interaction Lagrangian $\mathcal{L}_{\chi H}$ in the first line of eq. (3.4) leads to invisible Higgs decays at tree level if this process is kinematically allowed, i.e., for $m_\chi < m_h/2$. The LO partial Higgs decay width can be calculated straightforwardly by hand or with tools

like `FeynCalc` and reads

$$\Gamma(h \rightarrow \chi^* \chi) = \frac{v^2}{16\pi m_h} \sqrt{1 - \frac{4m_\chi^2}{m_h^2}} \left(\frac{m_h^2 c_d}{f^2} - \lambda \right)^2. \quad (3.7)$$

This formula can be used to translate experimental limits on the Higgs invisible branching ratio $\mathcal{B}(h \rightarrow \text{inv})$ into constraints on $f/\sqrt{|c_d|}$ and $|\lambda|$. In fact, in the limit $m_\chi \ll m_h/2$ one obtains the 95% CL exclusion limits

$$\frac{f}{\sqrt{|c_d|}} > 1.5 \text{ TeV}, \quad |\lambda| < 7.2 \cdot 10^{-3} \quad (\text{LHC Run II}), \quad (3.8)$$

by employing the LHC bound of $\mathcal{B}(h \rightarrow \text{inv}) < 11\%$ [402]. This bound is the partial result of a combination of Run I and Run II data.³ At the HL-LHC, it may be possible to set a limit on the Higgs invisible branching ratio of $\mathcal{B}(h \rightarrow \text{inv}) < 2.5\%$ [403]. This implies that the bounds in eq. (3.8) may be improved to

$$\frac{f}{\sqrt{|c_d|}} > 2.2 \text{ TeV}, \quad |\lambda| < 3.3 \cdot 10^{-3} \quad (\text{HL-LHC}). \quad (3.9)$$

Similar limits have also been given in Ref. [319]. Although the exclusion limits in eqs. (3.8) and (3.9) have been derived under the assumption that either c_d or λ is non-zero but not both, the obtained stringent limits indicate that invisible Higgs decays are the main avenue to probe the pNGB DM couplings c_d and λ for DM masses $m_\chi < m_h/2$. We make this evident later in Sect. 3.8 when we compare all different exclusion limits.

At the loop level, the DM interaction Lagrangian with SM fermions $\mathcal{L}_{\chi\psi}$ in the second line of eq. (3.4) can, in principle, also lead to invisible Higgs decays. The relevant Feynman diagrams are displayed in Fig. 3.3. After SSB, we can read the diagrams as if one of the Higgs doublets H was replaced by its VEV v , leading to a diagram for $h \rightarrow \chi^* \chi$ with an intermediate top-quark loop. For this one-loop amplitude induced by $\mathcal{L}_{\chi\psi}$ we find, using `FeynArts` and `FormCalc` and neglecting the top mass,

$$\mathcal{M}(h \rightarrow \chi^* \chi) = -\frac{3v c_t m_h^2 y_t^2}{16\pi^2 f^2} \mathbf{B}_0(m_h^2; 0, 0). \quad (3.10)$$

The first notable thing to observe is the fact that for on-shell Higgs decays the current-current-type interactions $\sim d_{t_R}$ do not contribute to the amplitude, which consequently is $\sim c_t$. The symbol \mathbf{B}_0 denotes a Passarino–Veltman (PV) function representing a scalar one-loop integral resulting from the PV reduction of the amplitude [404]. These functions have been systematically classified (see, e.g., Refs. [405, 406]) and can be

³Very recently, a refined analysis taking into account the full Run I and Run II data states the slightly better observed upper bound of $\mathcal{B}(h \rightarrow \text{inv}) < 10.7\%$ [311], which does not change our bounds in any meaningful way.

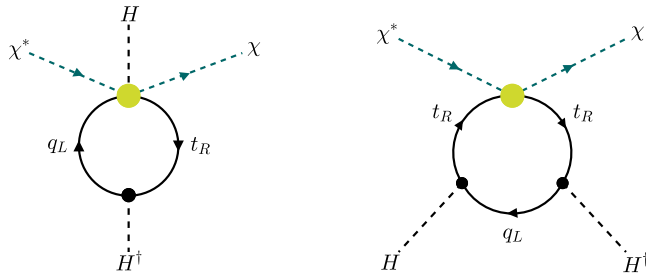


Figure 3.3: Left: An example of a diagram that describes the mixing of the Yukawa-type DM-top operator into the marginal Higgs portal operator. Right: Example graph that could lead to a mixing of the current-current type DM-top operator into the DM-Higgs operators in eq. (3.4).

translated into more conventional expressions using `Package-X` [16, 17]. Assuming that the marginal Higgs portal coupling vanishes at the scale $\mu_f = \mathcal{O}(f)$, we can match the result of our one-loop calculation in eq. (3.10) to the expression for the tree-level amplitude and obtain the leading-logarithmic (LL) result

$$\lambda = -\frac{3m_h^2 y_t^2 c_t}{8\pi^2 f^2} \ln \frac{\mu_f}{\mu_h}, \quad (3.11)$$

for the marginal Higgs portal coupling at the EW scale $\mu_h = \mathcal{O}(m_h)$. Switching from the energy scale μ_f to the EW scale is achieved by means of the renormalization group (RG) equations for λ . Our calculation agrees with analogous RG flow results for dimension-six operators presented in Ref. [407]. Notice that, despite the fact that the contributions of the Yukawa-type DM-top operator to the invisible decays of the Higgs boson are loop suppressed, the resulting constraints can still be important given the stringent bounds on $\mathcal{B}(h \rightarrow \text{inv})$ that the HL-LHC is expected to set. For instance, taking as an example $c_t = 1$, $y_t \simeq 0.94$, $\mu_f = f$ and $\mu_h = m_h$, we find numerically that the bound on $|\lambda|$ quoted in eq. (3.9) leads to the limit

$$f > 450 \text{ GeV} \quad (c_t = 1, \text{ HL-LHC}), \quad (3.12)$$

on the common decay constant f of the pNGBs introduced in eq. (3.4). In contrast to the Yukawa-type DM-top interaction, the current-current type DM-quark operators do not mix into the $\mathcal{L}_{\chi H}$ operators appearing in eq. (3.4). This is because the sum over all one-loop diagrams of the type shown on the right-hand side of Fig. 3.3 vanishes. The pNGB DM current-current type interactions, therefore, cannot be constrained by invisible Higgs boson decays even if $m_\chi < m_h/2$.

3.7 Constraints from DM (In)Direct Detection and the Relic Density

3.7.1 pNGB DM scattering off Atomic Nuclei

Given the model under consideration, one would naively assume that the DM particle solely interacts with the heavy quarks and the SM Higgs boson. But even under the assumption that the interactions in eq. (3.4) provide the leading new-physics effects at the scale μ_f at which the spin-0 fields emerge as composite pNGBs, the inclusion of radiative corrections can spoil this picture at the low energies probed in DM-nucleon scattering or DM annihilation. Interactions of the DM with the light quarks and gauge bosons that constitute non-relativistic (NR) matter arise at the one-loop order (see, e.g., Refs. [408–419] for further examples of relevant loop corrections in DM interactions).

In fact, in the case at hand, we find that loop diagrams like those displayed in Fig. 3.4 induce couplings between DM and the $U(1)_Y$ gauge boson or a pair of gluons. After EW symmetry breaking, the DM gauge-boson interactions relevant for DM-nucleon scattering can be cast into the form

$$\mathcal{L}_{\chi V} = \frac{ie c_A}{16\pi^2 f^2} \chi^* \overleftrightarrow{\partial}_\mu \chi \partial_\nu F^{\mu\nu} + \frac{g_s^2 d_G}{16\pi^2 f^2} |\chi|^2 G_{\mu\nu}^a G^{a,\mu\nu}, \quad (3.13)$$

where $e \simeq 0.3$ is the elementary electromagnetic charge, $g_s \simeq 1.2$ denotes the strong coupling constant and $F_{\mu\nu}$ represents the electromagnetic field-strength tensor. We can match the tree-level diagrams for $\chi^* \chi \rightarrow \gamma$ annihilation and $g\chi \rightarrow g\chi$ scattering induced by the interactions given in eq. (3.13) to the loop diagrams given in Fig. 3.4 with the interactions of the original Lagrangian $\mathcal{L}_{\text{int}}^\chi$ in eq. (3.4). The resulting leading contributions to the Wilson coefficients of the operators in eq. (3.13) read

$$c_A = \frac{4}{3} (d_{qL} + 2d_{tR} - d_{bR}) \ln \frac{\mu_f}{\mu_h}, \quad d_G = -\frac{c_t}{3}. \quad (3.14)$$

Notice that the Wilson coefficient c_A contains only the LL correction associated to operator mixing, while the result for d_G corresponds to a finite matching correction obtained in the limit of infinite top-quark mass.

In addition to $\mathcal{L}_{\chi V}$, the pNGB DM interactions with the Higgs boson given by $\mathcal{L}_{\chi H}$ in eq. (3.4) induce further interactions at low energies. Due to the momentum suppression of the derivative Higgs portal, only the marginal Higgs portal needs to be taken into account. Through this operator, the SM Higgs boson acts as CP -even scalar mediator between the pNGB DM and the light valence quarks that are the building blocks of nuclear matter. Hence, we can map the marginal Higgs portal onto the low-energy

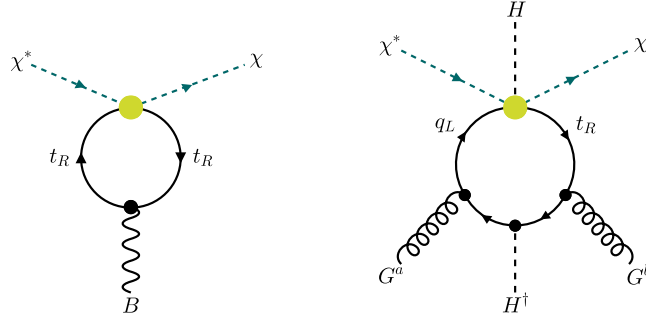


Figure 3.4: Left: Example diagram that describes the LL contribution of the current-current type DM-fermion operators to the Wilson coefficient of the DM-photon operator appearing in eq. (3.13). Right: A possible graph involving the insertion of the Yukawa-type DM-top operator that leads to a finite matching correction to the Wilson coefficient of the DM-gluon operator in eq. (3.13).

effective operator

$$\mathcal{L}_{\chi qq} = \sum_{q \in \{u, d, s\}} m_q a_q |\chi|^2 \bar{q} q \quad (3.15)$$

by matching the $q\chi \rightarrow q\chi$ contact interaction from $\mathcal{L}_{\chi qq}$ with t -channel Higgs-boson exchange at the tree level via the marginal Higgs portal. The simple calculation yields

$$a_q = \frac{\lambda}{m_h^2} \quad (3.16)$$

in agreement with the result given in Ref. [319]. We note that also the Yukawa-type interaction from $\mathcal{L}_{\chi\psi}$ in eq. (3.4) leads to effective interactions of the same form if we allow the tree-level coupling of pNGB DM to light quarks. However, the suppression by both the small Yukawa couplings as well as the high energy scale of symmetry breaking f renders these contributions obsolete.

With the three effective operators at low energies given by $\mathcal{L}_{\chi V}$ and $\mathcal{L}_{\chi qq}$, we can start to compute the DM-nucleon cross section needed to derive constraints on the pNGB DM effective field theory parameter space from direct detection experiments. An excellent review of DM direct detection phenomenology and a step-by-step manual for the relevant computations is provided by Ref. [300]. Following the reasoning put forward there and starting from the DM interactions $\mathcal{L}_{\chi V}$ and $\mathcal{L}_{\chi qq}$, the DM-nucleon scattering amplitude must be computed. This is necessary since, at the low energy scales relevant for DM direct detection experiments, the DM interacts effectively with

the atomic nuclei of the detector material. $\mathcal{L}_{\chi V}$ and $\mathcal{L}_{\chi qq}$ must then be expanded in the NR limit such that we can map the operators in $\mathcal{L}_{\chi V}$ and $\mathcal{L}_{\chi qq}$ onto a suitable basis of NR operators. This operator basis has been systematically constructed [420–423], and the matching of operators can, therefore, be looked up in the corresponding tables. For reference, the relevant steps are sketched in App. A.2.

Including the tree-level contributions that arise from the marginal Higgs portal operator as well as the loop-induced interactions from $\mathcal{L}_{\chi V}$, the spin-independent (SI) DM-nucleon cross section can be written as

$$\sigma_{\text{SI}} = \frac{1}{\pi} \left(\frac{m_\chi m_N}{m_\chi + m_N} \right)^2 \frac{1}{A^2} \left\{ \frac{Am_N}{2m_\chi} \left[\left(1 - \frac{7f_{T_G}^N}{9} \right) \frac{\lambda}{m_h^2} - \frac{2f_{T_G}^N d_G}{9f^2} \right] + \frac{Ze^2 c_A}{16\pi^2 f^2} \right\}^2. \quad (3.17)$$

Here A (Z) is the mass (atomic) number of the nucleus, $m_N \simeq 0.939$ GeV denotes the average nucleon mass and $f_{T_G}^N = 1 - \sum_{q=u,d,s} f_{T_q}^N \simeq 0.89$ is the effective gluon-nucleon coupling, and its numerical value corresponds to the values $f_{T_u}^N \simeq 0.019$, $f_{T_d}^N \simeq 0.045$ and $f_{T_s}^N \simeq 0.043$ [424, 425] for the quark-nucleon matrix elements. Furthermore, notice that the contribution in eq. (3.17) proportional to c_A arises from t -channel photon exchange and that the corresponding form factors simply count the number of valence quarks of the nucleons, i.e., $f_{V_u}^p = f_{V_d}^n = 2$ and $f_{V_d}^p = f_{V_u}^n = 1$.

For $m_\chi = 100$ GeV, the latest XENON1T 90% CL upper limit on the SI DM-nucleon cross section reads $\sigma_{\text{SI}} < 9.12 \cdot 10^{-47}$ cm² [303]. Using eq. (3.17) with $A = 131$ and $Z = 54$ for xenon, this bound can be readily translated into limits on the Wilson coefficients of the relevant pNGB DM operators in eq. (3.4). In the case of the marginal Higgs portal alone, we find in agreement with Ref. [319] the 90% CL exclusion limit

$$|\lambda| < 1.0 \cdot 10^{-2}. \quad (3.18)$$

Setting $c_t = 1$ in eqs. (3.11) and (3.14) as well as using $\mu_f = f$ and $\mu_h = m_h$, and setting $d_{qL} = d_{tR} = d_{bR} = 1$ in eq. (3.14), we obtain in addition the lower bounds

$$\begin{aligned} f &> 510 \text{ GeV} & (c_t = 1), \\ f &> 1.3 \text{ TeV} & (d_{qL} = d_{tR} = d_{bR} = 1), \end{aligned} \quad (3.19)$$

on the suppression scale of the Yukawa-type and the current-current type DM-fermion interactions entering eq. (3.4), respectively. Although we have considered in all cases only the effect of one type of pNGB DM operator at the scale μ_f at a time, the limits in eqs. (3.18) and (3.19) show that the null results of the DM direct detection experiments generically allow to set stringent bounds on the Wilson coefficients of the

marginal Higgs portal and the pNGB DM-fermion operators in eq. (3.4). In contrast, the derivative Higgs portal operator remains unconstrained by DM direct detection even after one-loop corrections are included in the calculation of the SI DM-nucleon cross section.

3.7.2 The Annihilation of pNGB DM in the Early and Present Universe

In order to understand the physics of DM indirect detection and thermal freeze-out in composite pNGB DM models, we first expand the thermally averaged cross section for annihilation of DM into a SM final state X , namely $\langle \sigma(\chi^*\chi \rightarrow X)v \rangle$, in the DM temperature T . Following Refs. [426–428], we can write⁴

$$\begin{aligned} \langle \sigma(\chi^*\chi \rightarrow X)v \rangle &= \langle a_X + b_X v^2 + \mathcal{O}(v^4) \rangle \\ &= a_X + \frac{3}{2} b_X \frac{T}{m_\chi} + \mathcal{O}\left(\frac{T^2}{m_\chi^2}\right), \end{aligned} \quad (3.20)$$

where the coefficient a_X (b_X) describes the so-called s -wave (p -wave) contribution. Notice that in today’s universe $T_0 \simeq 0$, while at freeze-out $T_f \simeq m_\chi/25$. This means that the p -wave coefficient b_X can usually be neglected in the calculation of the DM indirect detection constraints, while it can be relevant in the computation of the relic abundance $\Omega_\chi h^2$, in particular if the corresponding s -wave coefficient a_X is parametrically suppressed.

An example where such a parametric suppression is at work in the context of the model defined in eq. (3.4) is the annihilation of DM into a bottom-antibottom quark pair, i.e., $\chi^*\chi \rightarrow b\bar{b}$. In this case, we find that the relevant s -wave and p -wave coefficients are well approximated by

$$\begin{aligned} a_{b\bar{b}} &\simeq \frac{3m_b^2}{4\pi} \left| \frac{1}{4m_\chi^2 - m_h^2 + im_h\Gamma_h} \left(\frac{4m_\chi^2 c_d}{f^2} - \lambda \right) \right|^2 + \mathcal{O}\left(\frac{m_b^3}{m_\chi^5}\right), \\ b_{b\bar{b}} &\simeq \frac{m_\chi^2}{4\pi} \frac{d_{qL}^2 + d_{bR}^2}{f^4} + \mathcal{O}\left(\frac{m_b^2}{m_\chi^4}\right), \end{aligned} \quad (3.21)$$

if the pNGB DM mass m_χ is sufficiently above the bottom-quark threshold, i.e., if $m_\chi \gg m_b \simeq 4.2 \text{ GeV}$. In the above expression for $a_{b\bar{b}}$, the total decay width of the Higgs boson, including contributions from $h \rightarrow \chi^*\chi$ (see Sect. 3.6), is denoted by Γ_h . For $m_b < m_\chi \lesssim m_W$ with the W -boson mass $m_W \simeq 80.4 \text{ GeV}$, the $\chi^*\chi \rightarrow b\bar{b}$ channel generically provides the dominant mechanism to set $\Omega_\chi h^2$ in composite

⁴Some background knowledge on DM freeze-out, the related WIMP miracle, and the calculations presented here is provided in App. A.1.

pNGB DM models described by eq. (3.4). In fact, it turns out that for $m_\chi \ll m_h/2$ the velocity suppression of the p -wave contribution is less severe than the bottom-mass suppression of the s -wave contribution in eq. (3.21). The current-current type DM-fermion operators introduced in eq. (3.4) can, therefore, play an important role in thermal freeze-out for $m_\chi < m_h/2$.

For $m_\chi \gtrsim m_W$ the $\chi^*\chi \rightarrow W^+W^-, ZZ, hh, t\bar{t}$ channels dominate DM annihilation. These processes all receive unsuppressed s -wave contributions, rendering the associated p -wave contributions phenomenologically irrelevant. For DM masses sufficiently far above the EW scale, we find

$$\begin{aligned} a_X &\simeq \frac{N_X m_\chi^2}{4\pi} \left[\frac{c_d}{f^2} - \frac{\lambda}{4m_\chi^2} \right]^2 + \mathcal{O}\left(\frac{m_h^2}{m_\chi^4}\right), \\ a_{t\bar{t}} &\simeq \frac{3m_t^2}{4\pi} \left[\frac{c_d + c_t}{f^2} - \frac{\lambda}{4m_\chi^2} \right]^2 + \mathcal{O}\left(\frac{m_t^2 m_h^2}{m_\chi^6}\right), \end{aligned} \quad (3.22)$$

as approximations for the s -wave coefficients, where $X = W^+W^-, ZZ, hh$, and $N_{W^+W^-} = 2$, $N_{ZZ} = N_{hh} = 1$. These results can be shown to agree with the calculations performed in Ref. [429] after taking the limit of large DM mass. Notice that in this limit, DM annihilation to W and Z bosons reduces to three times the contribution from annihilation to the Higgs boson, as expected in the $SU(2)_L \times U(1)_Y$ symmetric limit. Given that the size of the marginal Higgs portal coupling λ is strongly constrained by DM direct detection (see eq. (3.18)), the expressions in eq. (3.22) also imply that in viable composite pNGB DM models the derivative Higgs portal operator generically provides the dominant contribution to DM annihilation for $m_\chi \gg m_t$. As a result, thermal freeze-out becomes a model-independent prediction in this limit, in the sense that the value of $\Omega_\chi h^2$ to first approximation only depends on m_χ and $f/\sqrt{|c_d|}$.

In addition to the DM annihilation channels discussed so far, DM annihilation into mono-chromatic photons can provide a relevant indirect-detection signature in composite pNGB DM models. As shown in Fig. 3.5, this signature receives two types of contributions. The first is associated to s -channel exchange of a Higgs boson with subsequent decay of the Higgs into a pair of photons, i.e., $\chi^*\chi \rightarrow h \rightarrow \gamma\gamma$, and proceeds through the insertion of a DM-Higgs operator and a loop of top quarks (left diagram) or W bosons (middle diagram). The corresponding form factors describing fermion and

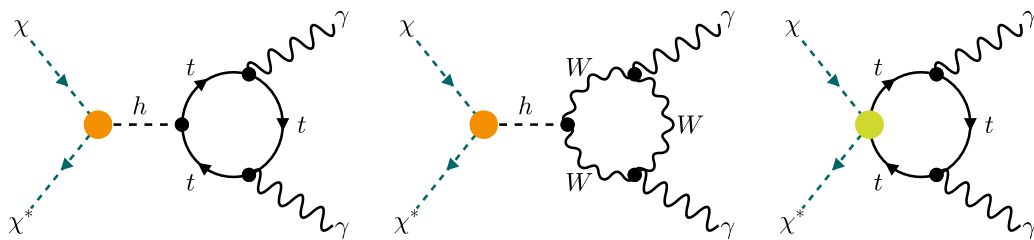


Figure 3.5: Example diagrams that lead to the process $\chi^* \chi \rightarrow \gamma\gamma$.

gauge-boson loops are given by

$$F_\psi(\tau) = \frac{3\tau}{2} \left[1 + (1 - \tau) \arctan^2 \frac{1}{\sqrt{\tau - 1}} \right], \quad (3.23)$$

$$F_V(\tau) = \frac{1}{7} \left[2 + 3\tau + 3\tau(2 - \tau) \arctan^2 \frac{1}{\sqrt{\tau - 1}} \right],$$

respectively, and are normalized such that $F_\psi(\infty) = F_V(\infty) = 1$. The calculation of the gauge-boson form factor in the Feynman–’t Hooft gauge requires the inclusion of Faddeev–Popov ghosts due to the presence of $SU(2)_L$ triple gauge couplings and the Goldstone bosons associated with EWSB in the SM. Similar calculations involving the same PV functions have been performed before, e.g., in the context of Higgs decays into a pair of photons.⁵ Our form factors agree with the results stated in Ref. [432].

The second type of contributions involves the insertion of the Yukawa-type DM-top operator introduced in eq. (3.4) and leads directly to the $\chi^* \chi \rightarrow \gamma\gamma$ transition via a top-quark loop (right diagram in Fig. 3.5). Including both types of contributions, the s -wave coefficient corresponding to $\chi^* \chi \rightarrow \gamma\gamma$ annihilation can be written as

$$a_{\gamma\gamma} = \frac{\alpha_{\text{em}}^2 m_\chi^2}{8\pi^3} \left| \frac{1}{4m_\chi^2 - m_h^2 + im_h\Gamma_h} \left(\frac{4m_\chi^2 c_d}{f^2} - \lambda \right) \left[\frac{8F_\psi(\tau_t)}{9} - \frac{7F_V(\tau_W)}{2} \right] + \frac{8c_t}{9f^2} F_\psi(\tau_t) \right|^2, \quad (3.24)$$

where $\tau_i = m_i^2/m_\chi^2 - i\varepsilon$ with ε being a positive infinitesimal real number. Notice that the s -channel Higgs exchange contribution in eq. (3.24) is resonantly enhanced at $m_\chi = m_h/2$, and as a result the DM indirect detection constraints from the observation of γ -ray lines are generically most stringent in the vicinity of the Higgs pole.

⁵The observation of the decay channel $h \rightarrow \gamma\gamma$ in 2012 was crucial to identify the resonance at an energy of around 125 GeV as the Higgs boson. A vector particle cannot decay into a pair of photons due to the Landau–Yang theorem [430, 431]. Therefore, the resonance could be attributed to a scalar particle and understanding $h \rightarrow \gamma\gamma$ decays was crucial to the success of the LHC.

Based on eqs. (3.20) to (3.22), the present abundance of DM in the universe is approximately given by

$$\frac{\Omega_\chi h^2}{0.12} \simeq \frac{3 \cdot 10^{-26} \text{ cm}^3/\text{s}}{\langle \sigma v \rangle_f}, \quad \langle \sigma v \rangle_f = \frac{1}{2} \sum_X \langle \sigma (\chi^* \chi \rightarrow X) v \rangle (T_f), \quad (3.25)$$

where the sum over X involves all annihilation channels that are kinematically accessible at a given DM mass (see, e.g., Ref. [433]). Notice that the factor of 1/2 in the definition of $\langle \sigma v \rangle_f$ takes into account that DM is not self-conjugate in our case. The same factor of 1/2 appears when one calculates the γ -ray flux from the annihilation cross section eq. (3.24). While eq. (3.25) represents a useful expression to estimate $\Omega_\chi h^2$, we use `micrOMEGAs` [49] in our numerical analysis of the constraints on the pNGB DM parameter space following from the requirement to reproduce the relic abundance of $\Omega_\chi h^2 = 0.120 \pm 0.001$ as measured by the PLANCK collaboration [279]. `micrOMEGAs` is also used to determine the DM indirect detection exclusion limits.

3.8 Discussion

In Figs. 3.6 to 3.8, we summarize the most important constraints in the m_χ - f plane for the three benchmark models with $c_d = 1$, $c_d = c_t = 1$, and $c_d = d_{qL} = d_{tR} = d_{bR} = 1$. Similar benchmark models have also been considered in Ref. [319]. The pNGB DM effective field theory parameters not shown in the headline of each figure are set to zero to obtain the displayed results. The light green and light blue regions are excluded by the projected HL-LHC limit on the Higgs invisible branching ratio of $\mathcal{B}(h \rightarrow \text{inv}) < 2.5 \cdot 10^{-2}$ [403] and by the 90% CL bounds on the SI DM-nucleon cross section set by XENON1T [303], respectively. The vertical gray bands indicate the DM mass ranges that are excluded at 95% CL by the γ -ray observations of dwarf spheroidal galaxies (dSphs) of the Fermi-LAT and DES collaborations in Ref. [434]. The used experimental bounds assume DM annihilation into $b\bar{b}$ final states and that the measured relic density is reproduced. The constraints that follow from the latest Fermi-LAT search for γ -ray lines [435] lead to weaker constraints on the DM mass of $62.5 \text{ GeV} \lesssim m_\chi \lesssim 64 \text{ GeV}$ compared to $\chi^* \chi \rightarrow b\bar{b}$ even if a favorable DM distribution (such as an adiabatically contracted Navarro-Frenk-White profile [436]) is used to calculate the limits. These bounds are hence not shown in Figs. 3.6 to 3.9. The dark green curves correspond to the PLANCK value $\Omega_\chi h^2 = 0.12$ [279] of the DM relic abundance. In the parameter space above the green curves, the corresponding pNGB DM benchmark model predicts $\Omega_\chi h^2 > 0.12$. The orange regions displayed in the figures correspond to the 95% CL exclusion limits found in Ref. [319] from a

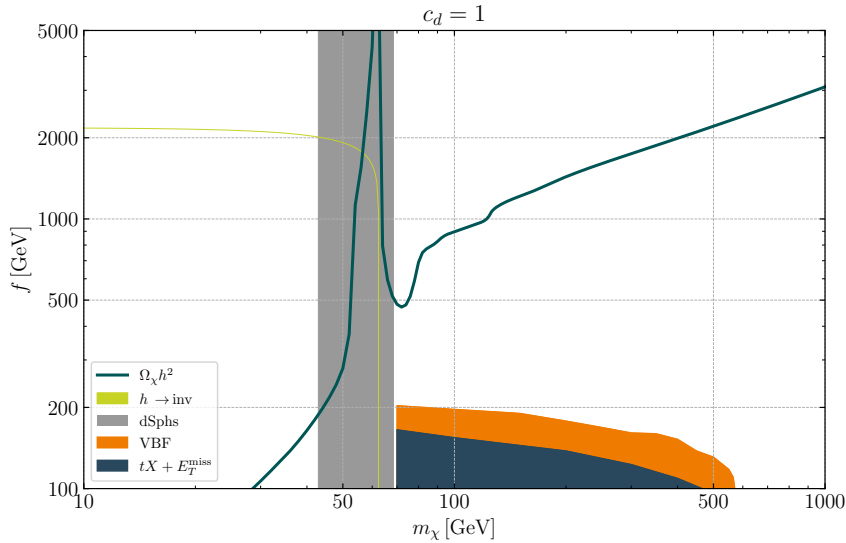


Figure 3.6: Constraints in the m_χ – f plane for the derivative Higgs portal model. The pNGB DM effective field theory parameters not shown in the headline of the plot are set to zero to obtain the displayed results. The light green region is excluded by the projected HL-LHC 95% CL limit on the Higgs invisible branching ratio of $\mathcal{B}(h \rightarrow \text{inv}) < 2.5 \cdot 10^{-2}$ [403]. The vertical gray band displays the DM mass range that is excluded at 95% CL by the dSphs analysis of Fermi–LAT and DES [434] assuming $\chi^* \chi \rightarrow b\bar{b}$ annihilation. The dark green curve corresponds to the value $\Omega_\chi h^2 = 0.12$ of the DM relic density as determined by PLANCK [279]. In the parameter space above the dark green curve the universe is overclosed. The orange region indicates the 95% CL exclusion limit derived in Ref. [319] from a study of off-shell invisible Higgs production in the VBF channel at the HL-LHC, while the dark blue region represents the corresponding exclusion limit obtained by our $tX + E_T^{\text{miss}}$ search strategy.

HL-LHC study of off-shell invisible Higgs production in the VBF channel. The dark blue colored domains finally correspond to the 95% CL constraints obtained by the $tX + E_T^{\text{miss}}$ analysis strategy discussed in Sect. 3.4.1.

In the case of the derivative Higgs portal model, one observes from Fig. 3.6 that in the Higgs on-shell region corresponding to $m_\chi < m_h/2$, HL-LHC measurements of invisible Higgs decays exclude large parts of the parameter space that leads to the correct DM relic density via standard thermal freeze-out. Only a narrow corridor around the Higgs resonance survives this constraint, which is, however, excluded by DM indirect detection measurements. Since the DM-nucleon scattering rate is momentum suppressed, the stringent limits from DM direct detection experiments do not put constraints on the pNGB DM benchmark model with only $c_d = 1$. This opens up the possibility to test such models with $m_\chi > m_h/2$ using mono- X searches at the HL-LHC, however, only

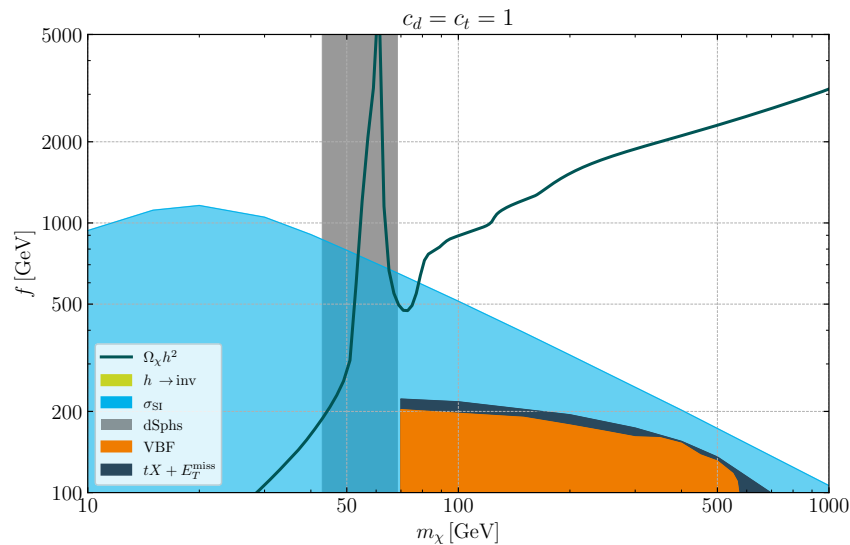


Figure 3.7: As Fig. 3.6 but for the pNGB DM benchmark model with $c_d = c_t = 1$. The light blue region is excluded by the 90% CL bound on the SI DM-nucleon cross section σ_{SI} as determined by XENON1T [303].

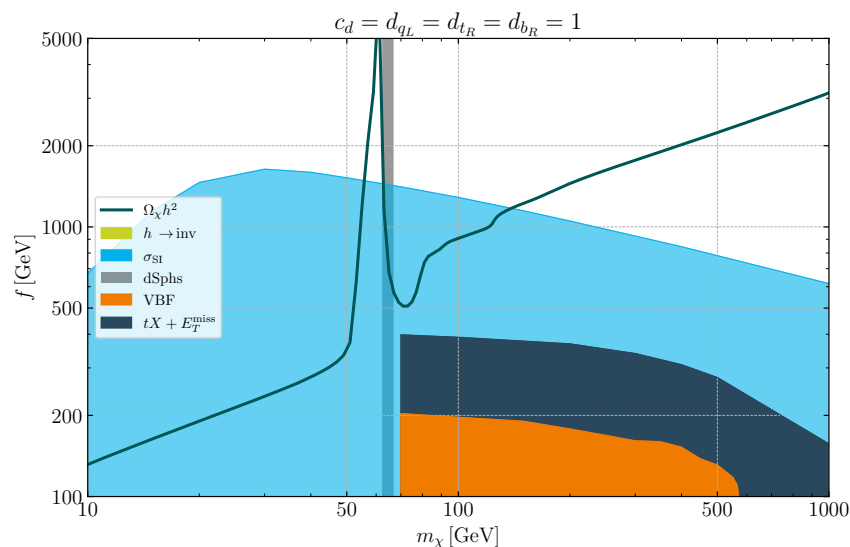


Figure 3.8: As Fig. 3.7 but for the pNGB DM benchmark model with $c_d = d_{q_L} = d_{t_R} = d_{b_R} = 1$.

if these models lead to a DM underabundance, i.e., $\Omega_\chi h^2 < 0.12$. Given that the VBF limits taken from Ref. [319] are around 30% better than the $tX + E_T^{\text{miss}}$ bounds on f , the best test of the derivative Higgs portal model in the Higgs off-shell region seems to be provided by invisible Higgs production in the VBF channel. In this context however,

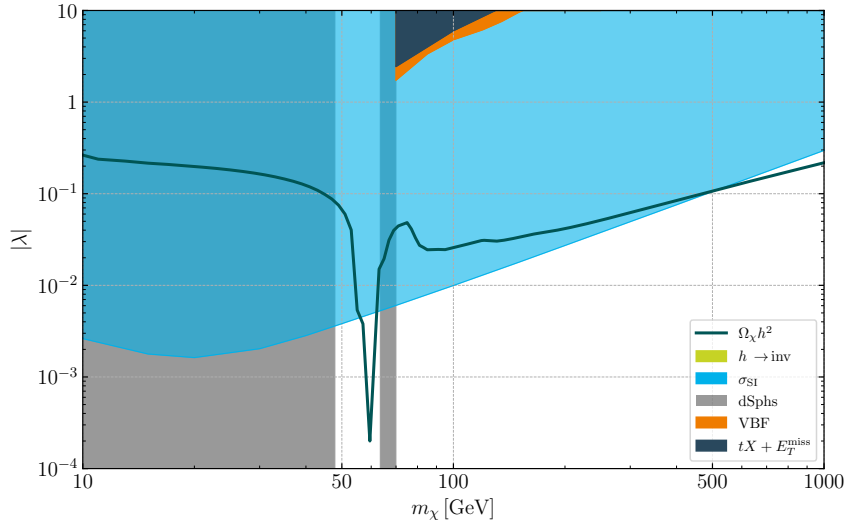


Figure 3.9: Constraints in the m_χ – $|\lambda|$ plane for the marginal Higgs portal model. The meaning and color coding of the shown constraints resemble those of Fig. 3.7.

it is important to realize that the study [319] assumes a systematic uncertainty on the relevant SM background of 1%, while the shown $tX + E_T^{\text{miss}}$ exclusion is based on a systematic uncertainty on the relevant SM background of 15% (see Sect. 3.4.1). Assuming a reduction of the systematic background uncertainties in $tX + E_T^{\text{miss}}$ down to 5% would bring the VBF and $tX + E_T^{\text{miss}}$ exclusion limits closer together (see App. A.3 for details).

As can be seen from Figs. 3.7 and 3.8, the HL-LHC potential to test viable models through mono- X searches is less favorable in the case of the pNGB DM benchmarks with $c_d = c_t = 1$ or $c_d = d_{q_L} = d_{t_R} = d_{b_R} = 1$ since in these cases the limits from DM direct detection, though loop suppressed, turn out to be still severe. In the first case, the LL corrections to λ in eq. (3.11) and the finite matching correction to d_G in eq. (3.14) are both relevant, while in the second case the LL corrections to c_A in eq. (3.14) play an essential role in determining the correct DM direct detection limits. The above LL corrections have not been discussed in the work [319], but it is known (see, for example, Refs. [411–413, 415–419]) that the inclusion of radiative corrections can have important effects in the calculation of σ_{SI} . Comparing the VBF and $tX + E_T^{\text{miss}}$ constraints, one sees that in both cases $c_d = c_t = 1$ and $c_d = d_{q_L} = d_{t_R} = d_{b_R} = 1$ the limits on f derived here are stronger than the bounds that have been obtained in Ref. [319]. This result follows straightforwardly from the fact that invisible

VBF Higgs off-shell production is only sensitive to c_d , while the $tX + E_T^{\text{miss}}$ signature receives contributions from c_d but also from c_t , d_{q_L} and d_{t_R} .

In Fig. 3.9, we finally summarize the constraints on the marginal Higgs portal model set by DM (in)direct detection experiments, the relic density, and future HL-LHC searches. One observes that the constraints on $|\lambda|$ from DM direct detection and the HL-LHC are comparable for DM masses $m_\chi < m_h/2$. However, in the case $m_\chi > m_h/2$ the bounds that follow from σ_{SI} are by more than two orders of magnitude stronger than those that one can hope to obtain at the HL-LHC from mono- X searches. Like in the case of the derivative Higgs portal model, off-shell invisible Higgs production in the VBF channel [319] again seems to be the best way to probe the marginal Higgs portal model at the LHC if $m_\chi > m_h/2$. This conclusion once more depends on the actual size of systematic background uncertainties of the VBF and $tX + E_T^{\text{miss}}$ channels in the HL-LHC environment. Combining the two mono- X channels as done in the case of the LHC searches for the invisible Higgs boson decays (see, for instance, Refs. [402, 437–439]) can be expected to improve the ultimate HL-LHC reach. Performing an actual combination of the VBF and $tX + E_T^{\text{miss}}$ channels is, however, beyond the scope of this chapter. We add that the potential of the high-energy option of the LHC, the future circular hadron-hadron collider, the compact linear collider and a muon collider in constraining the marginal Higgs portal through VBF off-shell Higgs production has been studied in the article [319] (see also Refs. [440–444] for similar analyses).

pNGB DM models in which both the SM Higgs boson as well as the DM candidate are composites of a TeV-scale strongly-coupled sector provide a simultaneous explanation of the EW hierarchy problem and the DM puzzle. Key features in this class of BSM theories are that the SM Higgs boson and the DM particle are both naturally light, and that the leading coupling between DM and the SM is the derivative Higgs portal. This interaction is strongly suppressed in the regime of small momentum transfer that is probed by DM scattering with heavy nuclei, making this type of WIMP easily compatible with the existing strong constraints from DM direct detection experiments. At the same time, the interaction strength of DM annihilation turns out to be in the right range to obtain the observed relic density through thermal freeze-out without tuning. However, as we have shown in our work, this simple and attractive picture can be significantly altered by explicit symmetry breaking effects that lead to pNGB DM interactions beyond the derivative Higgs portal. In fact, once radiative effects are taken into account, only pNGB DM realizations of the form of eq. (3.4) with $c_d \neq 0$ and all other pNGB DM effective field theory parameters sufficiently small typically sur-

vive the constraints from DM direct detection experiments. In such scenarios, collider searches for DM production are the only known direct way to explore the pNGB DM parameter space. If the DM candidate is kinematically accessible, searches for invisible Higgs boson decays play a key role in such explorations, while DM masses above the Higgs threshold can be probed by studying mono- X signatures. In our chapter, we have extended the earlier study of off-shell invisible Higgs production via VBF [319] by developing a search strategy that allows to probe pNGB DM using $tX + E_T^{\text{miss}}$ signatures. The $tX + E_T^{\text{miss}}$ channels are complementary to VBF Higgs production since they are able to test pNGB DM interactions like the Yukawa-type DM-top coupling and the current-current type interactions in eq. (3.4) that are not accessible via the latter mode. Together with Ref. [319] the work presented here provides the blueprints to search for pNGB DM at the LHC, and we encourage ATLAS and CMS to perform dedicated experimental searches and interpretations of the relevant mono- X signatures.

4 Searching for Leptoquarks in the Dilepton Channel at the LHC

This chapter examines searches for leptoquarks (LQs) in the high-energy tails of dilepton events at the LHC and reports the results of Refs. [2, 3]. We briefly introduce LQs and their phenomenology in the following Sect. 4.1. We especially examine the prospects of hadron collider searches to discover LQs. The publications [2, 3] are discussed in Sects. 4.2 and 4.3, respectively, and differ mainly in the LQ representation under consideration. Ref. [2] deals with scalar LQ representations and Ref. [3] discusses the vector case in the framework of the so-called 4321 model. We give an overall conclusion on both projects in Sect. 4.4.

4.1 An Introduction to Leptoquarks

The existence of leptoquarks (LQs) was proposed already decades ago in the context of Grand Unified Theories (GUTs) and has remained among the central questions of BSM phenomenology ever since. They were first considered in the context of the Pati–Salam model [115, 445] and are a generic feature of many GUTs (see, e.g., Ref. [446] as an extensive review on the matter), where they arise, for instance, as scalars in extended Higgs sectors or as vector particles from the generalization of the SM gauge group \mathcal{G}_{SM} . Therefore, they play a crucial role in the phenomenology of famous attempts at unification as given by the SU(5) and SO(10) gauge theories [116, 117]. Moreover, the squarks in R -parity violating formulations of SUSY are natural candidates for scalar LQs [248, 447]. Another intriguing possibility for scalar LQs embedded in a theoretically complete framework is given when they emerge as pNGBs or composite particles (see, e.g., Refs. [448–452] which discuss EWSB caused by some strongly-coupled dynamics beyond the SM, which would lead to LQs at the TeV scale). In recent years, the interest in LQs was driven by the accumulating hints of LFU violation (see, e.g., Ref. [220] for a review): the $b \rightarrow c\ell\nu$ decay anomaly [120–122, 228] may be one of the most compelling cases for BSM physics, as already discussed in Chap. 2. Moreover, the LHCb

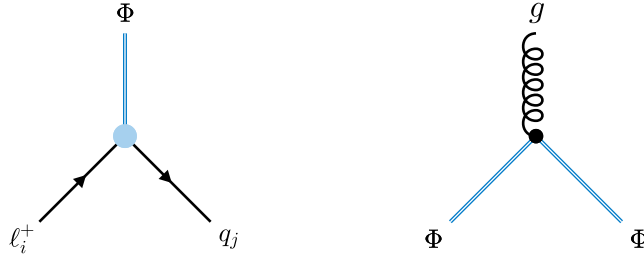


Figure 4.1: The two generic interactions of leptoquarks Φ . On the left is the defining vertex with an SM lepton and quark pair. For a generic LQ, we denote the coupling constant associated with this vertex as λ . The unbroken SM gauge symmetries require LQs to carry color charge and, therefore, couple to gluons. The latter interaction is depicted by the Feynman diagram on the right and is $\sim g_s$.

measurements of $b \rightarrow s\ell^+\ell^-$ neutral-current transitions that used to indicate LFU violation in the $\mathcal{R}_{K^{(*)}}$ observable [221, 223, 227] contributed strongly to the interest in LQs. Additionally, LQs have also been shown to possibly alleviate the tension of the anomalous magnetic moment of the muon [248, 262, 453]. Finally, also the recently observed excesses in the high-energy tails of $\tau^+\tau^-$ distributions in the CMS experiment [454, 455] indicate a further distinction between the different lepton flavors, other than the different SM Yukawa couplings. This suggests a drift away from the Drell–Yan (DY) process [456], which has already been well-understood in the SM for decades and admits a high precision due to its purely leptonic final state. The various frameworks of BSM theory as well as the predictive power and possible explanation of different long-standing experimental anomalies render LQs an astonishing new-physics case to be probed at the LHC. In the following, we denote a generic LQ without specification of its representation under \mathcal{G}_{SM} as Φ . We assign to it a mass m_{LQ} and call the generic coupling constant associated with the $\Phi - q - \ell$ vertex λ .

The defining feature of an LQ Φ may be the tree-level interaction with a SM quark and a lepton (see Fig. 4.1 on the left). As a consequence, LQs are endowed with both non-zero lepton and baryon numbers, which does not apply to any fundamental particle within the SM.¹ The coupling to a single quark-lepton pair further demands LQs to carry $\text{SU}(3)_C$ color charge which necessarily leads to the interaction with gluons

¹To be precise, a consistent ascription of B and L numbers to LQs is only possible if the LQ does not have diquark couplings. Group theoretic considerations suggest defining the fermion number $F = 3B + L$, which is well-defined for all LQ representations. All LQs fulfill $|F| = 2$ ($F = 0$) if they couple to quark-lepton (antiquark-lepton) pairs. See Ref. [453] for more details.

depicted on the right of Fig. 4.1. A comprehensive and modern overview of the phenomenology of LQs is given in Ref. [453]. Here, the authors particularly classify all viable representations of LQs in the light of a variety of precision and collider experiments. Since any phenomenologically interesting GUT must reduce to the SM at low energies, LQs are only considered in representations that respect the SM gauge symmetries \mathcal{G}_{SM} . Therefore, there are five independent scalar and five independent vector representations, where the established nomenclature was introduced in Ref. [457].² A list of the possible LQ representations is provided in Table 4.1, which introduces the conventional nomenclature, the LQ transformation properties under SM gauge transformations, and their assigned fermion quantum number F . As a common feature, the vector representations must always be embedded into some extended UV complete theory since a simple addition of a massive vector LQ to the SM particle content would spoil the renormalizability of the theory [453]. Thus, it is impossible to formulate model-independent statements about vector LQ phenomenology, and the restriction to a certain model seems inevitable. On the other hand, scalar LQs can be added to the SM without further BSM degrees of freedom, endowed with a simple scalar mass term. An alternative approach driven by LHC phenomenology classifies LQs according to possible final states at the LHC, see Refs. [248, 460].

By introducing LQs as novel degrees of freedom, we can address all the previously mentioned LFU anomalies: in particular, the (semi-) leptonic b -decay modes can receive tree-level contributions (see Fig. 4.2 on the left and in the middle) depending on the exact coupling configuration of the LQs. These processes represent a straightforward explanation for the $\mathcal{R}_{D^{(*)}}$ and the ceased $\mathcal{R}_{K^{(*)}}$ anomalies that are one of the topics of Chap. 2. Furthermore, the $(g - 2)_\mu$ might be enhanced at the one-loop level (see Fig. 4.2 on the right). Here, the new-physics contribution is proportional to the mass of the quark that virtually occurs in the loop. Hence, a sizeable deviation from the SM value of the magnetic moment of the muon could be achieved by coupling LQs to the top quark.

At the LHC, there are three main avenues to search for LQs. The pair production mode of LQs contains two on-shell LQs decaying into quark-lepton pairs and is initiated by quark-antiquark or gluon fusion (for the former, see Fig. 4.3 on the left), where the

²If we assume the existence of right-chiral neutrinos, then six scalar and six vector LQ representations can be constructed [453]. See also Refs. [458, 459] on the different viable representations. There, also `FeynRules` model files are provided, which can be used for the computations necessary to understand LQ phenomenology.

Symbol	Spin	\mathcal{G}_{SM} representation	$F = 3B + L$
S_1	0	$(\bar{\mathbf{3}}, \mathbf{1}, 1/3)$	-2
\tilde{S}_1		$(\bar{\mathbf{3}}, \mathbf{1}, 4/3)$	-2
R_2		$(\mathbf{3}, \mathbf{2}, 7/6)$	0
\tilde{R}_2		$(\mathbf{3}, \mathbf{2}, 1/6)$	0
S_3		$(\bar{\mathbf{3}}, \mathbf{3}, 1/3)$	-2
U_1	1	$(\mathbf{3}, \mathbf{1}, 2/3)$	0
\tilde{U}_1		$(\mathbf{3}, \mathbf{1}, 5/3)$	0
V_2		$(\bar{\mathbf{3}}, \mathbf{2}, 5/6)$	-2
\tilde{V}_2		$(\bar{\mathbf{3}}, \mathbf{2}, -1/6)$	-2
U_3		$(\mathbf{3}, \mathbf{3}, 2/3)$	0

Table 4.1: Viable scalar and vector LQ representations under the SM gauge group \mathcal{G}_{SM} . Since the SM quarks (antiquarks) are $\text{SU}(3)_C$ triplets (antitriplets) LQs Φ can only transform as (anti-)triplets as well due to the requirement of an existing $\Phi - q - \ell$ vertex. LQs with $F = -2$ also allow for vertices of an LQ with a quark-antiquark pair. See Ref. [453] for more details.

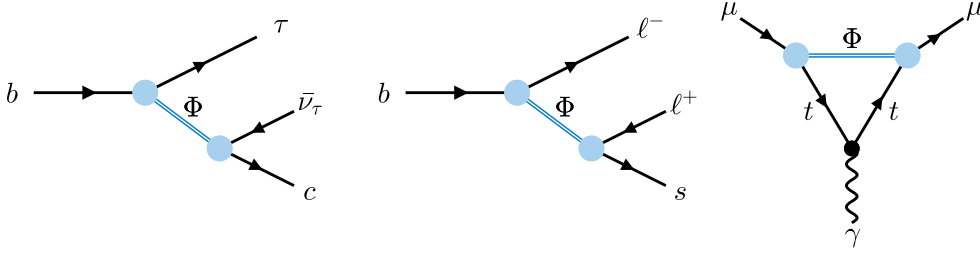


Figure 4.2: Leptoquark contributions to $b \rightarrow c\tau^-\bar{\nu}_\tau$, to $b \rightarrow s\ell^+\ell^-$, and to the magnetic moment of the muon. The first two diagrams are potential explanations for the $\mathcal{R}_{D^{(*)}}$ and the abandoned $\mathcal{R}_{K^{(*)}}$ anomalies, respectively. For an arbitrary quark q , the diagram on the right is $\sim m_q$ and therefore gives meaningful contributions to the $(g-2)_\mu$ if the LQ couples to the top quark.

dominant contribution stems from the latter. The corresponding detector signature would be an excess in events with final states with two leptons and two jets originating from the quarks. In case the LQ couples to neutrinos, events with jets and missing energy would also probe LQ pair production. LQ pair production has been thoroughly studied at hadron colliders already for decades [461–465]. A comprehensive modern review of the theory of pair production searches for different LQ couplings is given by Ref. [248]. Alongside these efforts, the experimental search for such excesses remains

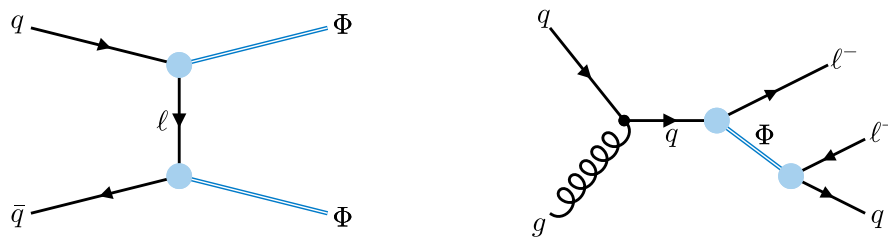


Figure 4.3: Sample diagrams for pair and single production of LQs Φ at hadron colliders. Note that the diagram on the left is dominated by pair production originating from gluon fusion. As a consequence of the negligible λ dependence of the LQ pair production cross section, these searches provide the most stringent constraint on the LQ mass m_{LQ} whenever λ is small.

at the core of the LHC research program [466–483]. The relevant amplitudes scale with g_s^2 and therefore pair production searches are less sensitive to the $\Phi - q - \ell$ coupling λ . This fact renders these kinds of searches particularly interesting in the case of small couplings to SM fermions. For large couplings, other means are necessary to explore the $m_{\text{LQ}} - \lambda$ parameter space.

Single-LQ production is the second main probe of on-shell LQ production and can be achieved with qg fusion with an s -channel quark (see Fig. 4.3 on the right) or via off-shell LQ exchange (see, e.g., Ref. [460, 484]). Both options lead to excesses in events with $\ell^+ \ell^- j$ final states. In recent years, the consideration of lepton PDFs [485] has opened the discussion to a new production channel via lepton-quark fusion in the initial state with s -channel LQ production [383, 486–488]. Lepton PDFs might be minuscule, but the resonant enhancement renders this process phenomenologically relevant. Here, the amplitudes scale as λ^2 , whereas in the qg fusion case amplitudes are $\sim g_s \lambda$. Hence, single-LQ production is crucial to provide sensitivity beyond the pure QCD interactions. Experimental studies have examined the qg annihilation case at length in the first two runs of the LHC (see, for instance, Ref. [489]).

Finally, dilepton production $q\bar{q} \rightarrow \ell^+ \ell^-$ with a t -channel exchange of an LQ completes the list of the common LHC searches for LQs. The relevant tree-level diagram is displayed in Fig. 4.4. Ref. [460] provides a comprehensive study on dilepton production in the presence of LQs. Unlike the typical peaks in the dilepton invariant mass distribution produced by s -channel mediators, the LQ t -channel exchange induces a deviation from the background distribution in the high-energy tail. Therefore, LHC searches for non-resonant anomalies are the major probe for this process. This search channel provides the most stringent bounds in the large- λ regime [460]. The production of $\tau^+ \tau^-$ pairs at high energies via the non-resonant exchange of an LQ represents a valid

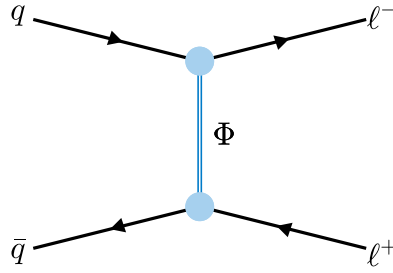


Figure 4.4: Tree-level diagram for LQ-mediated dilepton production at the LHC. This process leads to non-resonant deviations in the high-energy tail of the dilepton invariant mass distribution and is $\sim \lambda^2$. Therefore, it represents a promising path to probe the large-coupling regime of the $m_{\text{LQ}} - \lambda$ parameter space. This diagram lays the foundation of all considerations in the following sections.

explanation for the recently reported 3σ excess in the high-energy bins at CMS [454]. A further examination of the kinematics of the dilepton system, e.g., the angular distribution, paves the way for a deeper understanding of LQ-mediated $\ell^+\ell^-$ production at the LHC [490].

The three different classes of processes provide complementary sensitivity to the model parameters. However, it is naive to consider them independently one by one. Beyond the tree level of the t -channel LQ-mediated dilepton production, the single emission of real QCD radiation alters the final state to be $\ell^+\ell^-j$, which corresponds exactly to the single-LQ production case. Hence, aiming for NLO precision, proper treatment should consider both cases together. This is exactly the goal of the following two sections. There, we discuss dilepton production with LQs at NLO+PS precision at hadron colliders. For this purpose, we compute all $\mathcal{O}(\alpha_s)$ corrections to LQ-mediated $\ell^+\ell^-$ production at the LHC in the scalar and vector cases, respectively. An assortment of diagrams for generic QCD corrections to dilepton production with LQs is given in Fig. 4.5. On the left is a sample virtual QCD correction to the t -channel LQ exchange originating from the QCD correction to the $\Phi - q - \ell$ vertex. In the middle, we display a non-factorizable box diagram contributing at $\mathcal{O}(\alpha_s)$ to the same process. On the right, we show a real emission diagram of a gluon which needs to be taken into account at $\mathcal{O}(\alpha_s)$ for a safe description of the phenomenology in the IR regime.

In both the scalar and the vector case, we develop implementations of the relevant NLO corrections into the POWHEG-BOX [28]. We consider tree-level LQ-mediated dilep-

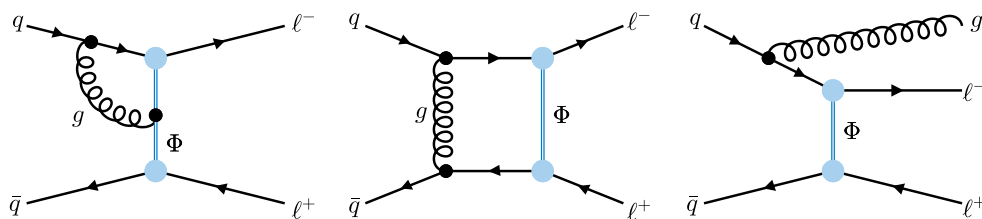


Figure 4.5: Generic $\mathcal{O}(\alpha_s)$ corrections to the $\ell^+\ell^-$ production via LQ exchange. On the left, we display the BSM vertex correction as a typical factorizable virtual QCD correction. The center diagram represents a non-factorizable box diagram. The distinct treatment of the two will be relevant in Sect. 4.3. The diagram on the right depicts initial-state QCD radiation via real emission of a gluon. Both virtual and real corrections are needed for IR finite results and NLO+PS accurate results.

ton production as well as its interference with the SM DY process at the LO. Beyond the leading order, we compute all $\mathcal{O}(\alpha_s)$ corrections to $\ell^+\ell^-$ production. In the scalar case, we also calculate the LQ correction to the DY process, which represents the dominant EW correction. The POWHEG method [26, 27] matches our fixed-order predictions consistently to the parton shower (PS) such that our implementation provides NLO+PS accuracy in QCD. The code should prove useful, especially for the experimental collaborations, when updating their existing limits on LQs inferred from searches for non-resonant deviations from the high-energy tail of dilepton production.

Motivated by the reported hints of LFU violation, we focus on LQs coupling to third-generation quarks and muons or tau leptons. In such a setting, the sensitivity of dilepton searches to BSM dynamics can be significantly improved by refining the event selection by requiring additional b -jets in the final state. This is because at the tree level, the t -channel exchange of a third-generation LQ is solely produced by bottom quark fusion, while the dominating contributions to the SM DY process stem from light $q\bar{q}$ fusion. Hence, additional b -jet requirements filter out those events which contain increased b -quark activity, which relatively discards more SM than BSM events. The effect has been demonstrated in model-independent SMEFT studies [491, 492], and the experimental LHC collaborations have already applied this searching method (see, e.g., Refs. [454, 455, 493, 494]).

In the rest of the chapter, we proceed as follows. In Sect. 4.2, we consider the scalar S_1 and \tilde{S}_1 representations and provide a detailed study of dilepton production in the presence of scalar LQs at NLO in QCD. Moreover, we discuss the LQ correction to the EW vertex, which modifies the well-understood SM DY process beyond the leading

order. The vector LQ case is dealt with in Sect. 4.3, in which we consider a U_1 vector LQ in the so-called 4321 model. We particularly examine the impact of additional colored degrees of freedom in this framework, which originate from the extended gauge group structure of the 4321 model. In Sect. 4.4, we jointly conclude our findings for both scalar and vector LQs.

4.2 Scalar Leptoquarks in the Dilepton Channel

In this section, we discuss the results obtained in the context of Ref. [2]. As discussed in the previous section, t -channel exchange of LQs could give rise to non-resonant signatures in the high- p_T region in dilepton searches at the LHC. Here, we consider the simpler and more generic scalar case by focusing on the S_1 and \tilde{S}_1 representations, which can be understood as building blocks of more complex scalar representations. In the following, we denote the rest mass and total decay width of the S_1 and \tilde{S}_1 LQs collectively as m_S and Γ_S , respectively. In order to illustrate the possible effects of scalar LQ (SLQ) contributions to the SM DY process, we focus on the following simplified LQ model

$$\mathcal{L} \supset Y_{ul} \bar{u}_R^c \ell_R S_1^\dagger + Y_{dl} \bar{d}_R^c \ell_R \tilde{S}_1^\dagger + \text{h.c.} . \quad (4.1)$$

Here, u_R , d_R , and ℓ_R represent the right-handed up-type quark, down-type quark, and charged lepton fields, respectively, and the superscript c denotes charge conjugation. The fermionic SM fields are understood to be mass eigenstates, i.e., the states that lead to diagonal SM Yukawa coupling matrices after EWSB. The couplings Y_{ul} and Y_{dl} are complex 3×3 matrices in flavor space, while the fields S_1 and \tilde{S}_1 correspond to the two $SU(2)_L$ LQ singlets allowed by gauge invariance. Explicitly, the LQ fields transform as $S_1 \sim (\mathbf{3}, \mathbf{1}, -1/3)$ and $\tilde{S}_1 \sim (\mathbf{3}, \mathbf{1}, -4/3)$ under the full SM gauge group \mathcal{G}_{SM} . Notice that the size of the modifications in $pp \rightarrow \ell^+ \ell^-$ production due to LQ exchange depends primarily on the flavor structure and the magnitude of the couplings Y_{ul} and Y_{dl} . However, once interference effects between the LQ signal and the SM background are considered, also the representation of the LQ plays a role because the interference pattern depends on the quantum numbers of the exchanged LQ [495]. In fact, in the case of S_1 (\tilde{S}_1) it turns out that the above Lagrangian gives rise to destructive (constructive) interference of the LQ signal with the SM DY background. Therefore, the interactions in eq. (4.1) can be used as a template to cover the full space of scalar LQ models which entails, besides the $SU(2)_L$ singlets S_1 and \tilde{S}_1 , the $SU(2)_L$ doublets S_2 and \tilde{S}_2 and an $SU(2)_L$ triplet S_3 . In this context, we add that the fields S_2 and S_3 lead to constructive interference, while \tilde{S}_2 interferes destructively with the SM DY background.

The subsequent discussion is organized as follows. Sect. 4.2.1 summarizes the calculations necessary for our NLO+PS POWHEG implementation of dilepton production with SLQs. All computations are done using the `FeynRules` model files given in the `Mathematica` packages `FeynArts` and `FormCalc`, as well as `Package-X`. In Sect. 4.2.2,

we provide a detailed analysis of how the model parameters impact the possible new-physics signal. Finally, Sect. 4.2.3 deals with the exclusion limits that we infer from the recent LHC studies for $\mu^+\mu^-$ final states, allowing for different additional jet multiplicities [494, 496], and $\tau^+\tau^- (+j)$ final states [454].

4.2.1 NLO Calculations of SLQ-mediated Dilepton Production

Dilepton production at the LHC in the presence of SLQs, as described by the simplified model defined in eq. (4.1), receives BSM contributions at the tree level as discussed in Sect. 4.1 (see Fig. 4.4). Therefore, we can separate the corresponding scattering amplitude $\mathcal{M}^S(q\bar{q} \rightarrow \ell^+\ell^-)$ up to NLO accuracy in α_s according to

$$\mathcal{M}^S(q\bar{q} \rightarrow \ell^+\ell^-) = \mathcal{M}_{\text{SM}} + \mathcal{M}_{\text{tree}}^S + \mathcal{M}_{\text{NLOQCD}}^S + \mathcal{M}_{\text{NLOEW}}^S. \quad (4.2)$$

Here, \mathcal{M}_{SM} denotes the SM DY contribution, which is independent of any LQ contributions, and $\mathcal{M}_{\text{tree}}^S$ is the tree-level matrix element originating from the diagram in Fig. 4.4. Beyond the LO, virtual QCD corrections are described by $\mathcal{M}_{\text{NLOQCD}}^S$, and $\mathcal{M}_{\text{NLOEW}}^S$ encodes the SLQ corrections to the SM DY process as displayed on the left of Fig. 4.6.

For now, let us restrict ourselves to one of the most interesting cases, i.e., dimuon production resulting from an \tilde{S}_1 LQ coupling to muons and bottom quarks. In this case, the LQ-mediated tree-level process and its virtual corrections stem from bottom-quark ($b\bar{b}$) fusion.³ The squared and spin- and color-averaged tree-level amplitude of the t -channel process is then given by the well-known result

$$\left| \mathcal{M}_{\text{tree}}^S \right|^2 = \frac{u^2 |Y_{b\mu}|^4}{12 \left((m_S^2 - u)^2 + m_S^2 \Gamma_S^2 \right)}. \quad (4.3)$$

Since we do not have to consider top quarks in the initial state, we can safely neglect all initial and final state fermion masses as we are interested in LQs at the TeV energy scale. Thus, we can also use the relation $s + t + u = 0$ between the Mandelstam variables defined following the usual definition for $2 \rightarrow 2$ processes. In addition to the pure BSM Born diagram, the new-physics tree-level contribution interferes with the SM DY process. We treat these contributions at the LO in perturbation theory, leading us to the result

³Throughout this chapter, we work in the five-flavor scheme, where charm and bottom quarks are considered as partons in the proton and, as such, have a corresponding parton distribution function.

$$\overline{\mathcal{M}_{\text{SM}}^* \mathcal{M}_{\text{tree}}^S} = -\frac{2\pi\alpha_{\text{em}}u^2 Y_{b\mu}^2 \left(\frac{s_W^2}{c_W^2(s-m_Z^2)} + \frac{1}{s} \right)}{9(u-m_S(m_S+i\Gamma_S))}, \quad (4.4)$$

where we have neglected the decay width of the Z boson.

Beyond the LO in perturbation theory, we find diagrams such as the two on the left of Fig. 4.5 as virtual QCD corrections to the t -channel diagram. For finite results of the $\mathcal{O}(\alpha_s)$ corrections in the IR regime, we must also consider real emissions of a single parton. The real corrections include, for instance, a gluon radiated off an initial-state quark, which is depicted in Fig. 4.5 on the right. However, in addition to that, we must also take into account resonant single-LQ production with subsequent decay of the LQ to a pair of a bottom quark and an antimuon, i.e., $gb \rightarrow \tilde{S}_1 \mu^-$ with $\tilde{S}_1 \rightarrow b\mu^+$ (see Fig. 4.3 on the right). All these processes represent $\mathcal{O}(\alpha_s)$ corrections to the inclusive DY dilepton production rate. Therefore, in order to achieve NLO accuracy in QCD, we have to include all three classes of graphs.

For the correct implementation of virtual QCD corrections, the POWHEG method requires us to compute the averaged interference of the tree-level matrix element with the NLO diagrams. In terms of PV functions, we find

$$\begin{aligned} \overline{(\mathcal{M}_{\text{tree}}^S)^* \mathcal{M}_{\text{NLOQCD}}^S} = & -\frac{\alpha_s u^2 Y_{b\mu}^4}{36\pi(u-m_S^2)} \left\{ \frac{\mathbf{A}_0(m_S) - 2(m_S^2+u)\mathbf{B}_0(u;0,m_S)}{(m_S^2-u)^2} \right. \\ & + 2 \left[\frac{m_S^2 \Re \left(2\mathbf{B}_0(m_S^2;0,m_S) + \mathbf{B}_1(m_S^2;0,m_S) \right)}{(m_S^2-u)^2} \right. \\ & + \left(m_S^2 \left(\frac{1}{t} + \frac{1}{u} \right) - 1 \right) \mathbf{C}_0(0,0,u;0,0,m_S) \\ & - \frac{\mathbf{B}_0(u;0,m_S) - 2m_S^2 \mathbf{C}_0(0,u,0;0,0,m_S)}{m_S^2-u} - \frac{\mathbf{B}_0(u;0,m_S)}{u} \\ & \left. \left. + \frac{\mathbf{B}_0(s;0,0)}{u} - \frac{m_S^2 \mathbf{C}_0(0,0,u;0,0,m_S)}{t} \right] \right. \\ & - \frac{(m_S^2+u)s \left(\mathbf{C}_0(0,s,0;0,0,0) - \mathbf{C}_0(s,0,0;0,0,m_S) \right)}{u^2} \\ & \left. + \frac{(m_S^4+u^2)s \mathbf{D}_0(0,s,0,u;0,0;0,0,0,m_S)}{u^2} \right\}, \quad (4.5) \end{aligned}$$

which gives the finite part

$$\begin{aligned}
 \mathcal{V}_{\text{fin}}^S = & \frac{\alpha_s Y_{b\mu}^4}{108\pi (m_S^2 - u)^2} \left\{ 6u^2 \text{Li}_2 \left(\frac{m_S^2 + s}{s} \right) \right. \\
 & + u \left[-3 \log \left(-\frac{\mu^2}{s} \right) \left(-2m_S^2 + u \log \left(-\frac{\mu^2}{s} \right) + 2u \right) \right. \\
 & \quad \left. \left. + 3u \log^2 \left(-\frac{m_S^2}{s} \right) + 6(u - m_S^2) \log \left(\frac{\mu^2}{m_S^2} \right) + \pi^2 u \right] \right. \\
 & + 6(m_S^4 + u^2) \left[\text{Li}_2 \left(-\frac{u}{m_S^2 - u} \right) + 2 \log^2 \left(\frac{m_S^2}{m_S^2 - u} \right) \right. \\
 & \quad \left. \left. + \log \left(\frac{m_S^2}{m_S^2 - u} \right) \left(\log \left(\frac{\mu^2}{m_S^2} \right) - \log \left(-\frac{\mu^2}{s} \right) + 1 \right) \right] \right\}. \tag{4.6}
 \end{aligned}$$

Note that we compute all matrix elements using conventional dimensional regularization for both ultraviolet (UV) and infrared (IR) singularities, and our calculations of NLO effects are performed in the on-shell scheme. In order to deal with the soft and collinear singularities of the real corrections to the t -channel LQ exchange contribution (see the right diagram in Fig. 4.5) and to cancel the IR poles of the one-loop virtual corrections (see the left diagram in the same figure), we exploit the general implementation of the Frixione–Kunszt–Signer subtraction [497, 498] within the POWHEG-BOX framework. For this purpose, the full POWHEG-BOX machinery is used that automatically builds the soft and collinear counterterms and remnants, and also checks the behavior in the soft and collinear limits of the real squared matrix elements against their soft and collinear approximations. Notice that the real NLO QCD contributions that describe resonant single-LQ production with subsequent decay of the LQ are IR finite and, therefore, do not require a subtraction (see the right diagram in Fig. 4.3). Hence, our Monte Carlo (MC) code allows to achieve NLO+PS accuracy for DY dilepton production in any scalar LQ model described by eq. (4.1). In particular, our POWHEG implementation is able to generate events with one additional parton from the matrix element calculation without the need to introduce a merging or matching scale. Two-jet events are instead exclusively generated by the PS in our MC setup.

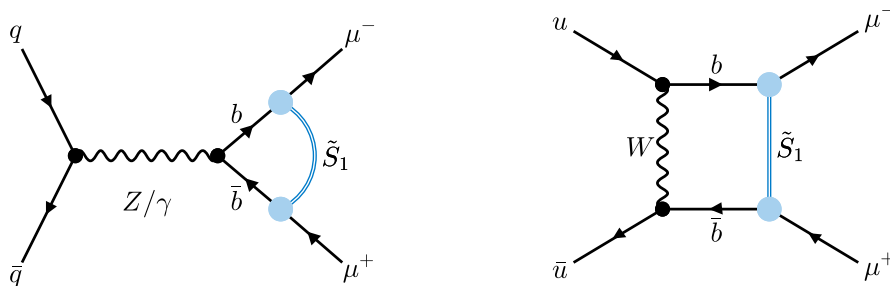


Figure 4.6: Sample diagrams for mixed EW and LQ contributions to $\mu^+\mu^-$ production at the LHC in the presence of an \tilde{S}_1 . The diagram on the left is due to the LQ correction to the EW vertex which is crucial for LO DY scattering. The same vertex correction also applies to the EW vertex of the initial state partons. On the right, we display a box contribution that we do not take into account in our calculations.

Besides QCD corrections to $pp \rightarrow \ell^+\ell^-$, we also consider mixed EW effects by taking into account also the LQ corrections to the EW interaction vertices. Two prototype graphs of mixed EW effects are shown in Fig. 4.6. The first type of diagrams encodes the virtual corrections to the $Z\ell^+\ell^-$ and $\gamma\ell^+\ell^-$ vertices involving the exchange of an LQ. These vertex corrections appear both in the initial and the final state. The second type of EW corrections is associated to one-loop Feynman graphs with W -boson exchange. Notice that due to the structure of eq. (4.1), which only involves right-handed fermionic fields, EW contributions of the latter kind are strongly chirally suppressed by small SM Yukawa couplings. Furthermore, in the case of DY production by heavy-quark fusion these corrections involve small CKM matrix elements. Therefore, we do not include EW corrections related to W -boson exchange in our analysis. Likewise, we do not consider EW contributions due to SM Higgs-boson exchange, because these corrections are insignificant as they are proportional to small SM Yukawa couplings. We treat the new-physics corrections to the EW vertex as s -dependent \mathcal{K} factors, i.e., we define

$$\overline{(\mathcal{M}_{\text{tree}}^S)^*} \mathcal{M}_{\text{NLOEW}}^S = \mathcal{B}_{\text{SM}} \times [\mathcal{K}_{\mu\mu}^S + \mathcal{K}_{bb}^S], \quad (4.7)$$

where $\mathcal{B}_{\text{SM}} = \overline{|\mathcal{M}_{\text{tree}}^S|^2}$ is the squared spin- and color-averaged Born BSM contribution stated explicitly in eq. (4.3). In terms of PV functions, we find

$$\begin{aligned}
 \mathcal{K}_{\mu\mu}^S = \frac{Y_{b\mu}^2}{32\pi^2 s} & \left[5s + (2m_S^2 - s) \left(\mathbf{B}_0(s; 0, 0) - 4\mathbf{B}_0(s; m_S, m_S) \right) + 6s\mathbf{B}_1(0; 0, m_S) \right. \\
 & \left. + 6m_S^2\mathbf{B}_0(0; 0, m_S) + 2m_S^4 \left(4\mathbf{C}_0(0, s, 0; 0, m_S, m_S) + \mathbf{C}_0(s, 0, 0; 0, 0, m_S) \right) \right]
 \end{aligned} \tag{4.8}$$

and

$$\begin{aligned}
 \mathcal{K}_{bb}^S = \frac{Y_{b\mu}^2}{32\pi^2 s} & \left[7s + (2m_S^2 - s) \left(3\mathbf{B}_0(s; 0, 0) - 4\mathbf{B}_0(s; m_S, m_S) \right) + 2m_S^2\mathbf{B}_0(0; 0, m_S) \right. \\
 & \left. + 2s\mathbf{B}_1(0; 0, m_S) + 2m_S^4 \left(4\mathbf{C}_0(0, s, 0; 0, m_S, m_S) + 3\mathbf{C}_0(s, 0, 0; 0, 0, m_S) \right) \right].
 \end{aligned} \tag{4.9}$$

Introducing the notation $\Upsilon_{sm} \equiv \sqrt{s(s - 4m_S^2)}$, we can translate the PV functions into more conventional expressions with the help of `Package-X` to find

$$\begin{aligned}
 \mathcal{K}_{\mu\mu}^S = \frac{Y_{b\mu}^2}{64\pi^2 s^2} & \left\{ 19s^2 - 2\pi^2 m_S^4 - 12m_S^2 s + 2s(s - 2m_S^2) \left(\log\left(\frac{\mu^2}{m_S^2}\right) - \log\left(-\frac{\mu^2}{s}\right) \right) \right. \\
 & + 2m_S^4 \log^2\left(-\frac{m_S^2}{s}\right) + 8\Upsilon_{sm}(s - 2m_S^2) \log\left(\frac{\Upsilon_{sm} + 2m_S^2 - s}{2m_S^2}\right) \\
 & + 4m_S^4 \left[\text{Li}_2\left(\frac{m_S^2 + s}{s}\right) + 4\text{Li}_2\left(1 - \frac{s}{m_S^2}\right) + 4\text{Li}_2\left(\frac{2m_S^2}{2m_S^2 - s + \Upsilon_{sm}}\right) \right. \\
 & \quad \left. - 4\text{Li}_2\left(\frac{2m_S^2}{s + \Upsilon_{sm}}\right) + 4\text{Li}_2\left(\frac{2s - 2m_S^2}{s + \Upsilon_{sm}}\right) - 4\text{Li}_2\left(-\frac{2(m_S^2 - s)}{-2m_S^2 + s + \Upsilon_{sm}}\right) \right] \\
 & \left. + 8m_S^4 \log^2\left(\frac{\Upsilon_{sm} + 2m_S^2 - s}{\Upsilon_{sm} + s}\right) - 8m_S^4 \log^2\left(\frac{\Upsilon_{sm} + s}{2s}\right) \right\}
 \end{aligned} \tag{4.10}$$

and

$$\begin{aligned}
 \mathcal{K}_{bb}^S = \frac{Y_{b\mu}^2}{192\pi^2 s^2} & \left\{ -2\pi^2 m_S^4 - 12m_S^2 (s - 4 \log(2)\Upsilon_{sm}) + 3s (17s - 8 \log(2)\Upsilon_{sm}) \right. \\
 & + 48m_S^4 \left[\frac{3}{4} \text{Li}_2 \left(\frac{m_S^2 + s}{s} \right) + \text{Li}_2 \left(1 - \frac{s}{m_S^2} \right) + \text{Li}_2 \left(\frac{2m_S^2}{2m_S^2 - s + \Upsilon_{sm}} \right) \right. \\
 & \quad \left. \left. - \text{Li}_2 \left(\frac{2m_S^2}{s + \Upsilon_{sm}} \right) + \text{Li}_2 \left(\frac{2s - 2m_S^2}{s + \Upsilon_{sm}} \right) - \text{Li}_2 \left(-\frac{2(m_S^2 - s)}{-2m_S^2 + s + \Upsilon_{sm}} \right) \right] \right. \\
 & + 6 \left[3s(s - 2m_S^2) \left(\log \left(\frac{\mu^2}{m_S^2} \right) - \log \left(-\frac{\mu^2}{s} \right) \right) + 3m_S^4 \log^2 \left(-\frac{m_S^2}{s} \right) \right. \\
 & \quad + 4m_S^4 \log^2 \left(\frac{\Upsilon_{sm} + 2m_S^2 - s}{\Upsilon_{sm} + s} \right) - 4m_S^4 \log^2 \left(\frac{\Upsilon_{sm} + s}{2s} \right) \\
 & \quad \left. \left. + 4\Upsilon_{sm} (s - 2m_S^2) \log \left(\frac{\Upsilon_{sm} + 2m_S^2 - s}{m_S^2} \right) \right] \right\} \quad (4.11)
 \end{aligned}$$

for the EW vertex corrections. The latter expression, expanded around $s \simeq m_S$ and analytically continued, agrees with the leading term in the heavy-mass expansion of the corresponding form factors for virtual corrections of the $Z^{\ell^+\ell^-}$ and $\gamma^{\ell^+\ell^-}$ vertices involving the exchange of an LQ, as stated in Ref. [262].

4.2.2 Phenomenological Analyses

In this section, we discuss the numerical impact of the different types of LQ corrections on the kinematic distributions that are most relevant for the existing LHC searches for non-resonant BSM physics in dilepton final states. The case of light and heavy dilepton pairs is discussed separately and in both cases signatures with no or one b -jet are considered. All results shown in the following are obtained assuming pp collisions at $\sqrt{s} = 13$ TeV and employ NNPDF40_nlo_as_01180 PDFs [192], and PYTHIA 8 [35] is used to shower the events. Effects from hadronization, underlying event modeling or QED effects in the PS are not included in our MC simulations.

4.2.2.1 Inclusive Light Dilepton Final States

The simplest LHC searches for non-resonant DY phenomena (see, for instance, Refs. [496, 499]) use inclusive measurements of the high-mass dielectron (m_{ee}) or dimuon ($m_{\mu\mu}$) tail to set constraints on non-SM physics. In Fig. 4.7, we present our results for the LQ

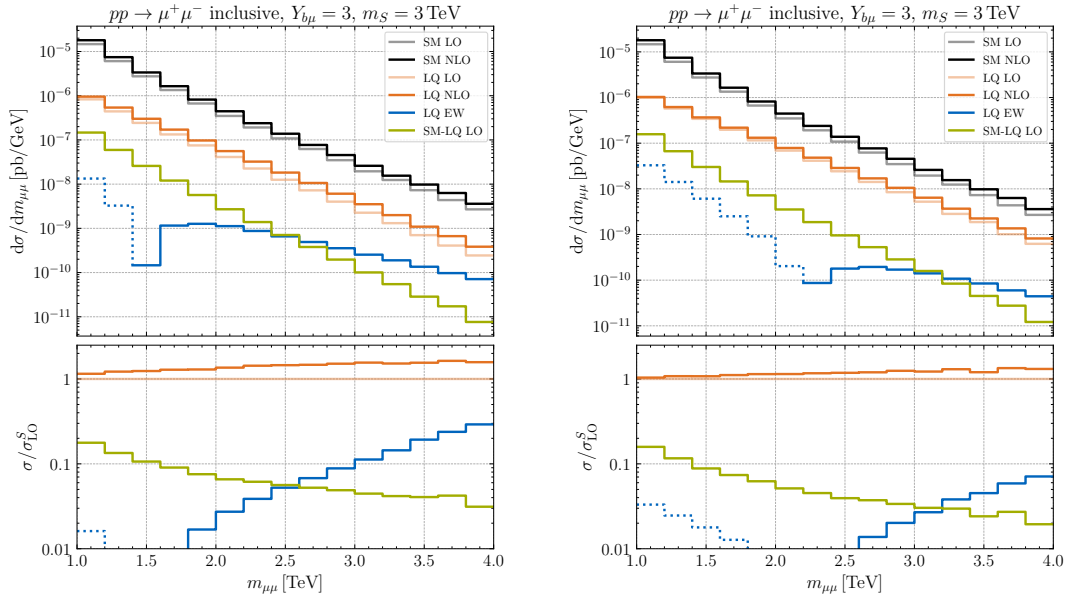


Figure 4.7: Inclusive $pp \rightarrow \mu^+\mu^-$ production cross sections as a function of $m_{\mu\mu}$. The left (right) plot shows the results for $Y_{b\mu} = 2$, $m_S = 2$ TeV ($Y_{b\mu} = 3$, $m_S = 3$ TeV). The LQ couplings not specified in the headline of the plots are set to zero. The light and dark orange curves correspond to the LQ distributions at the LO (LQ LO) and the NLO (LQ NLO) in QCD, respectively, while the blue and green histograms illustrate the impact of EW effects (LQ EW) and the size of the interference effects between the LQ signal and the SM background (SM-LQ LO). The parts of the blue curves that are dotted correspond to negative EW contributions to the differential cross sections. The gray and black lines indicate the SM spectrum at the LO and NLO in QCD, respectively. The lower panels depict the ratios between the different LQ contributions and the relevant LQ LO distribution.

corrections to the $m_{\mu\mu}$ spectrum in inclusive $pp \rightarrow \mu^+\mu^-$ production adopting two benchmark choices for $Y_{b\mu}$ and m_S . All other LQ couplings are set to zero to obtain the results shown in the figure. The light and dark orange curves in both plots correspond to the LQ distributions at the LO (LQ LO) and the NLO (LQ NLO) in QCD, respectively, while the blue and green histograms illustrate the impact of EW corrections (LQ EW) and the size of the interference effects between the LQ signal and the SM background (SM-LQ LO). The gray and black lines indicate the SM spectrum at the LO and NLO in QCD, respectively. From the lower panel of the left plot, it is evident that for the choice $Y_{b\mu} = 2$, $m_S = 2$ TeV, the NLO QCD effects play an important role in obtaining precise predictions as they amount to around 50 % (80 %) at $m_{\mu\mu} = 3$ TeV ($m_{\mu\mu} = 4$ TeV), compared to the tree-level LQ predictions. The corresponding numbers in the case of $Y_{b\mu} = 3$, $m_S = 3$ TeV are 25 % and 40 %. Higher-order EW corrections are

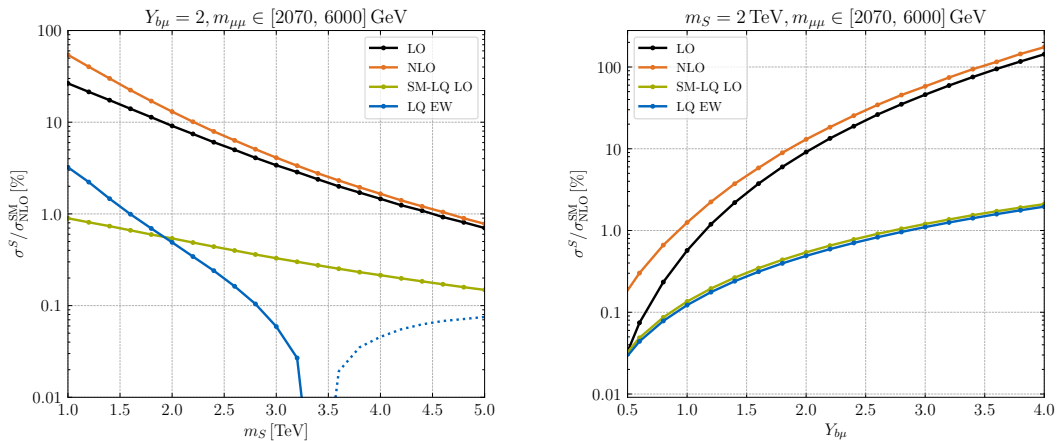


Figure 4.8: Ratios between the individual LQ corrections and the inclusive DY SM background calculated at the NLO in QCD. The shown results correspond to the fiducial region defined by $p_{T,\mu} > 30$ GeV, $|\eta_\mu| < 2.5$, and $m_{\mu\mu} \in [2070, 6000]$ GeV. The left (right) plot depicts the results as a function of m_S ($Y_{b\mu}$) for fixed $Y_{b\mu} = 2$ ($m_S = 2$ TeV). The LO is displayed in black whereas the remaining color coding and meaning of the different curves resemble those in Fig. 4.7.

far less important than the NLO QCD contributions at low invariant masses⁴ but become relevant at high energies where they can lead to enhancements of the production rates of more than 30% for $Y_{b\mu} = 2, m_S = 2$ TeV. This feature is well-known (see, for example, Ref. [500]) and due to the appearance of Sudakov logarithms of the form $\ln^2(m_{\mu\mu}^2/m_S^2)$, which are associated to virtualities $q^2 \simeq m_{\mu\mu}^2$ that are much larger than the mass of the LQ entering the loop diagrams. The double-logarithmic behavior also explains why for $Y_{b\mu} = 3, m_S = 3$ TeV the EW corrections are less pronounced than in the case of $Y_{b\mu} = 2, m_S = 2$ TeV. Interference effects between the LQ signal and the SM background amount in both cases to approximately 5% in the high-mass tail of the $m_{\mu\mu}$ spectrum and are, therefore, only of minor importance.

The results shown in Fig. 4.7 already suggest that in existing LHC searches for non-resonant phenomena in DY distributions the phenomenological impact of EW and interference effects involving LQs is limited. To further illustrate this point, we display in Fig. 4.8 the ratios between the individual LQ contributions and the inclusive DY SM background in the fiducial region. The normalization is calculated at the NLO in QCD. We select events that contain two opposite-sign (OS) muons that are both required to have a transverse momentum of $p_{T,\mu} > 30$ GeV and a pseudorapidity of $|\eta_\mu| < 2.5$. Moreover, their invariant mass must fall into the range $m_{\mu\mu} \in [2070, 6000]$ GeV. Detector efficiency corrections are not taken into account. Notice that this invariant

⁴Below the LQ threshold, the EW effects lead to a reduction of the differential DY cross section. This is indicated in Fig. 4.7 by the dotted blue parts of the histograms.

mass window corresponds to the signal region (SR) used by ATLAS in their recent non-resonant dimuon analysis [496], assuming constructive signal-background interference. The left panel displays our results as a function of m_S for fixed $Y_{b\mu} = 2$. From this plot, one sees that the relative size of the NLO QCD corrections decreases for increasing LQ mass. Numerically, we find relative effects of around 100 %, 20 %, and 10 % at $m_S = 1$ TeV, $m_S = 3$ TeV, and $m_S = 5$ TeV. This feature is readily understood by noting that the NLO QCD corrections related to s -channel single-LQ production followed by the decay of the LQ (see the right Feynman diagram in Fig. 4.3) decouple faster than the virtual and real QCD corrections to the t -channel Born-level LQ contribution (see the left and right graph in Fig. 4.5). Another property that is visible in the left panel is the strong suppression of the EW corrections for increasing m_S . This is related to the fact that, for heavy LQs, the enhancement of EW effects due to Sudakov double-logarithms is not at work in the considered SR. One furthermore observes that both the EW and the interference effects represent only subleading corrections in the mass window $m_{\mu\mu} \in [2070, 6000]$ GeV, amounting to at most 3 % and below 1 %, respectively, in the shown LQ mass range.

The right panel in Fig. 4.8 depicts our ratio predictions as a function of $Y_{b\mu}$ setting the mass of the LQ to $m_S = 2$ TeV. We see that the relative size of the NLO QCD corrections decreases for increasing coupling strength. Compared to the tree-level LQ result, the higher-order QCD effects amount to around 440 %, 40 %, and 20 % for $Y_{b\mu} = 0.5$, $Y_{b\mu} = 2$, and $Y_{b\mu} = 4$. This behavior can be understood by realizing that the squared amplitude of the t -channel Born-level contribution scales as $|Y_{b\mu}|^4$, while the resonant single-LQ production rate is proportional to $|Y_{b\mu}|^2$. Furthermore, one notices that the relative LQ EW and SM-LQ LO modifications both depend quadratically on $|Y_{b\mu}|$. One again sees that both the EW and the interference contributions are numerically subleading even for large couplings $Y_{b\mu}$, where they just reach the level of 1 %.

4.2.2.2 Light Dilepton Final States with one b -Jet

Inspired by the recently overcome $b \rightarrow s\ell^+\ell^-$ anomalies, also LHC searches for final states with two OSSF leptons and exactly one b -jet have been proposed [491] and performed by ATLAS [494]. In order to illustrate the improvement in sensitivity that is gained by targeting dilepton final states with additional b -jets, we show in Fig. 4.9 inclusive $pp \rightarrow \mu^+\mu^-$ cross sections as functions of $m_{\mu\mu}$ employing two different b -jet categories. We adopt the LQ parameter choices $Y_{b\mu} = 2, m_S = 2$ TeV and consider 139 fb^{-1} of integrated luminosity under LHC Run II conditions. Following the

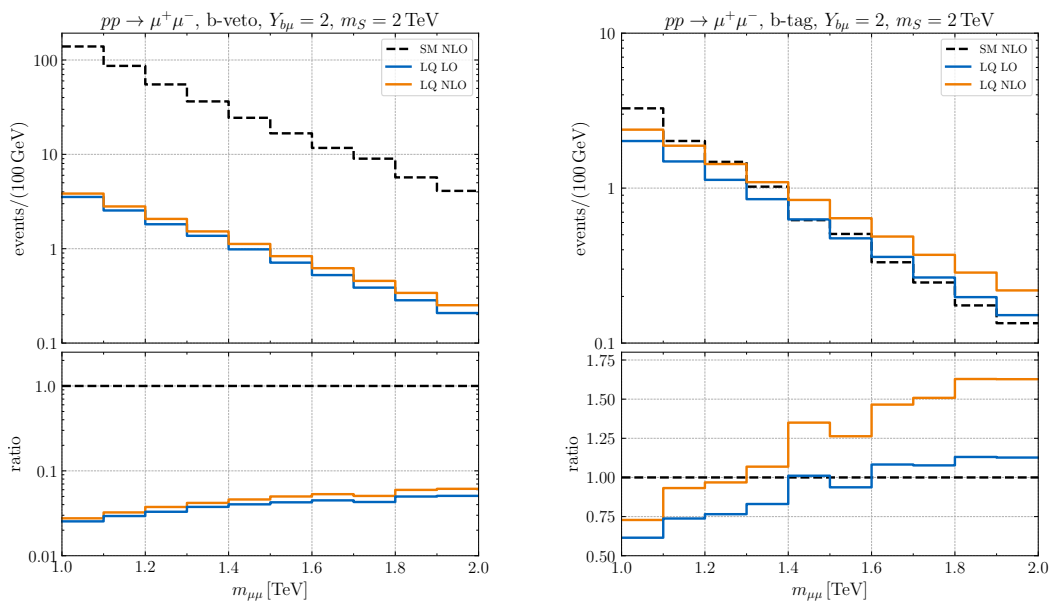


Figure 4.9: Inclusive $pp \rightarrow \mu^+ \mu^-$ production cross sections as functions of $m_{\mu\mu}$ for two different b -jet categories. The left (right) plot shows the results for $Y_{b\mu} = 2, m_S = 2$ TeV imposing a b -veto (b -tag). The dashed black, blue, and orange curves correspond to the SM results obtained at NLO in QCD (SM NLO), the LQ LO, and the LQ NLO predictions, respectively. All results assume an integrated luminosity of 139 fb^{-1} . The lower panels display the ratios between the different LQ contributions and the corresponding SM NLO spectrum.

study [494], events are selected with two OS muons that are both required to satisfy $p_{T,\mu} > 30 \text{ GeV}$ and $|\eta_\mu| < 2.5$. Jets are reconstructed using the anti- k_t algorithm [385] with radius parameter $R = 0.4$, as implemented in `FastJet` [47], and need to fulfill $p_{T,j} > 30 \text{ GeV}$ and $|\eta_j| < 2.5$. Jets originating from the hadronization of a bottom or anti-bottom quark are identified (i.e., b -tagged) adopting the performance of the ATLAS b -tagging algorithm described in Ref. [388]. For the analyses performed in this subsection, a b -tagging working point is chosen that yields a b -tagging efficiency of 77% and a light-flavor jet rejection of 110. Detector effects are simulated by applying reconstruction and identification efficiency factors tuned to mimic the performance of the ATLAS detector. In particular, muon candidates must fulfill the ATLAS quality selection criteria optimized for high- p_T performance [501, 502]. The corresponding reconstruction and identification efficiency amount to around 75% in the phase-space region of interest. Our analysis is implemented into `MadAnalysis 5` [37] and employs `DELPHES 3` [48] as a fast detector simulator. By applying our MC chain to the SM NLO prediction obtained with the `POWHEG-BOX`, we can reproduce the SM DY background

postfit $m_{\mu\mu}$ distribution in the SR provided by ATLAS in Ref. [494] at the level of 10%. This comparison represents a non-trivial cross-check of our analysis.

In the left panel of Fig. 4.9, our results for the inclusive DY dimuon cross section with no b -tagged jet (b -veto) are presented. The dashed black, blue, and orange histograms display the SM results obtained at NLO in QCD (SM NLO), the LQ LO, and the LQ NLO predictions, respectively. The size of EW and interference effects is not shown in the figure because these corrections are both very small. One observes that in the b -veto category, the LQ contributions to the differential rate amount to corrections of a few percent only, and that NLO QCD corrections modify the LO LQ spectrum by around 10% to 20% in the shown $m_{\mu\mu}$ range. Requiring one b -jet (b -tag) in addition to the two OS muons changes the picture radically. This is illustrated on the right-hand side in Fig. 4.9. In fact, the requirement of an additional b -jet reduces the SM background by roughly a factor of 35 largely independent of $m_{\mu\mu}$, while the b -jet requirement has an effect of around -60% (-15%) on the signal strength in the considered LQ realization at $m_{\mu\mu} = 1\text{ TeV}$ ($m_{\mu\mu} = 2\text{ TeV}$). It is also visible that the size of the NLO QCD corrections to the LQ signal is larger in the case of the b -tag than the b -veto category, exceeding 25% above approximately $m_{\mu\mu} = 1.5\text{ TeV}$. This feature is explained by noting that NLO QCD contributions of the form $gb \rightarrow \tilde{S}_1 \mu^-$ with $\tilde{S}_1 \rightarrow b\mu^+$ (see the right diagram in Fig. 4.3) will mostly contribute to the b -tag category. Similar statements apply to channels like $gb \rightarrow \mu^+ \mu^- b$ where the antibottom quark that partakes in the t -channel LQ process $b\bar{b} \rightarrow \mu^+ \mu^-$ arises from splitting of an initial-state gluon. However, notice that while the latter type of corrections can be partly captured by a PS when applied to the LO matrix elements, this is not the case for the former contribution associated to resonant single-LQ production. In order to achieve an accurate exclusive description of DY dilepton processes in LQ models involving heavy-flavored jets, NLO+PS predictions as provided in our work are, therefore, called for.

4.2.2.3 Heavy Dilepton Final States with and without a b -Jet

Searches for signatures involving tau pairs in the final state such as those performed at LHC Run II [454, 493] are known [220, 458, 460, 503–506] to provide strong constraints on LQ models that address the $b \rightarrow c\ell\nu$ anomalies. In the following, we consider the recent CMS search [454] for $\tau^+\tau^-$ final states with both taus decaying to hadrons (τ_h^\pm) as an example to illustrate the role that additional b -jets play in analyses of this kind. To distinguish hadronic τ candidates from jets originating from the hadronization of

quarks and gluons, and from electrons or muons, the τ -tagger described in Ref. [507] is employed. The used working points have an efficiency of approximately 50 %, 70 %, and 70 % for identification in the case of jets, electrons, and muons, respectively. The corresponding rejection factors are around 230, 20, and 770. Both hadronic τ candidates are required to have $p_{T,\tau} > 40$ GeV and $|\eta_\tau| < 2.1$, and the angular distance between them must be greater than $\Delta R_{\tau\tau} = 0.3$ in the pseudorapidity-azimuth space. Jets are clustered using the anti- k_t algorithm with radius $R = 0.4$. Jets with $p_{T,j} > 30$ GeV and $|\eta_j| < 4.7$ and b -jets with $p_{T,b} > 20$ GeV and $|\eta_b| < 2.5$ are selected. To identify b -jets, we employ the CMS b -tagging efficiencies stated in Refs. [508,509]. The used b -tagging working point yields a b -tagging efficiency of around 80 % and a light-flavor jet rejection in the ballpark of 100. We again use `MadAnalysis 5` in combination with `DELPHES 3` to analyze the events and to simulate the detector effects. We have verified that applying our analysis to the SM NLO DY prediction reproduces the SM DY background as given in Ref. [454] to within around 30 %.

To discriminate between signal and background, we consider the distributions of the total transverse mass defined as [510]

$$m_T^{\text{tot}} = \sqrt{m_T^2(\vec{p}_T^{\tau_1}, \vec{p}_T^{\tau_2}) + m_T^2(\vec{p}_T^{\tau_1}, \vec{p}_T^{\text{miss}}) + m_T^2(\vec{p}_T^{\tau_2}, \vec{p}_T^{\text{miss}})}, \quad (4.12)$$

where τ_1 (τ_2) refers to the first (second) hadronic τ candidate and $\vec{p}_T^{\tau_1}$, $\vec{p}_T^{\tau_2}$, and \vec{p}_T^{miss} are the vectors with magnitude $p_T^{\tau_1}$, $p_T^{\tau_2}$, and E_T^{miss} . Here, E_T^{miss} denotes the missing transverse energy constructed from the transverse momenta of all the neutrinos in the event. The transverse mass of two transverse momenta p_T^i and p_T^j entering eq. (4.12) is given by

$$m_T(\vec{p}_T^i, \vec{p}_T^j) = \sqrt{2p_T^i p_T^j (1 - \cos \Delta\phi)}, \quad (4.13)$$

where $\Delta\phi$ is the azimuthal angular difference between the vectors \vec{p}_T^i and \vec{p}_T^j .

In the two panels of Fig. 4.10, we compare the m_T^{tot} distributions within the SM and in the benchmark LQ model for the parameter choices $Y_{b\tau} = 2$, $m_S = 2$ TeV for two different b -jet categories. The left (right) plot shows the results for the no b -tag (b -tag) category in the $\tau_h^+ \tau_h^-$ final state. The dashed black curves represent the SM expectations of the DY background taken from Ref. [454], while the blue and orange histograms are the LQ LO and LQ NLO predictions obtained using our `POWHEG-BOX` implementation. All results assume 138 fb^{-1} of pp data collected at $\sqrt{s} = 13$ TeV. It is evident from the lower left panel that in the no b -tag category the NLO LQ contribution amounts to a relative correction of only about 10 % compared to the SM DY background for $m_T^{\text{tot}} > 1300$ GeV. In the case of the b -tag category, one instead observes from the lower right panel that in the highest m_T^{tot} bin with $m_T^{\text{tot}} > 900$ GeV the NLO LQ signal

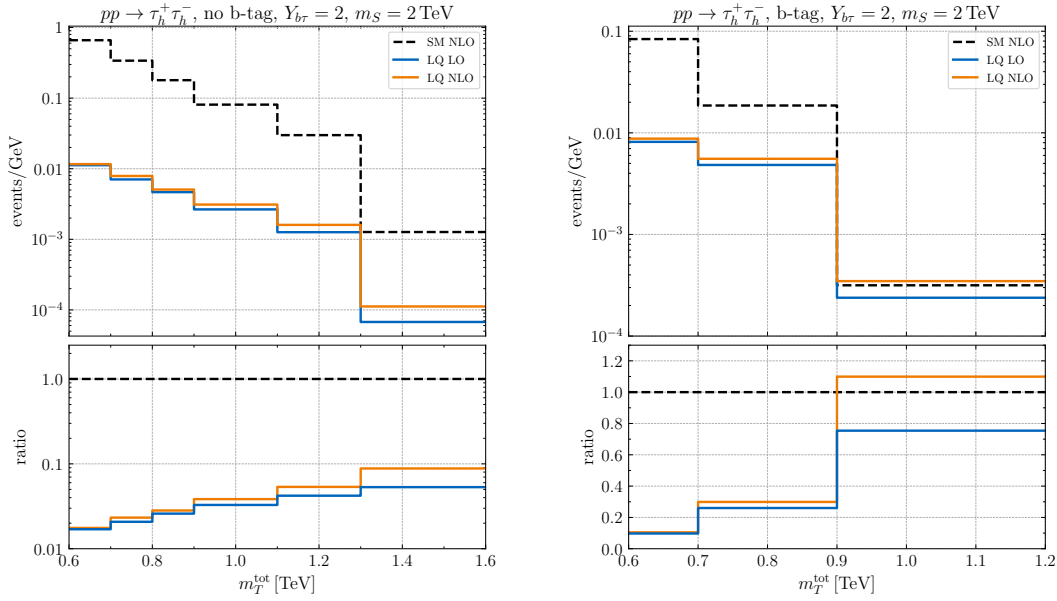


Figure 4.10: Distributions of m_T^{tot} in the no b -tag (left panel) and the b -tag (right panel) categories in the $\tau_h^+ \tau_h^-$ final state. The dashed black curves correspond to the SM expectations of the DY background provided by CMS in the search [454], which is based on 138 fb^{-1} of LHC Run II data. The blue and orange curves instead represent the corresponding LQ LO and LQ NLO results assuming $Y_{b\tau} = 2, m_S = 2 \text{ TeV}$. The definition of the SRs and other experimental details are given in the main text.

constitutes almost 110% of the SM DY background. This again demonstrates that for third-generation scalar LQs, the sensitivity of DY searches notably improves by demanding additional b -jet activity. Notice that the NLO QCD effects enhance the LO LQ predictions in the no b -tag (b -tag) category by approximately 40% (30%) in the highest m_T^{tot} bin, making higher-order QCD effects phenomenologically relevant if one wants to obtain precise predictions. On the other hand, EW and interference effects are both insignificant in the tail of the m_T^{tot} distribution and are, therefore, not shown in the figure.

4.2.3 Exclusion Limits

On the basis of the search strategies detailed in Sect. 4.2.2, we now derive 95% confidence level (CL) constraints on the $m_S - Y_{b\mu}$ and $m_S - Y_{b\tau}$ planes using the latest LHC dilepton analyses performed at LHC Run II. In the left panel of Fig. 4.11, we show the 95% CL limits on the $m_S - Y_{b\mu}$ parameter space. The black and the green bounds arise from the inclusive DY search [496] for the LQ signal at LO and NLO, respectively, and the blue and orange limits stem from the DY analysis [494] in the b -veto and b -tag cat-

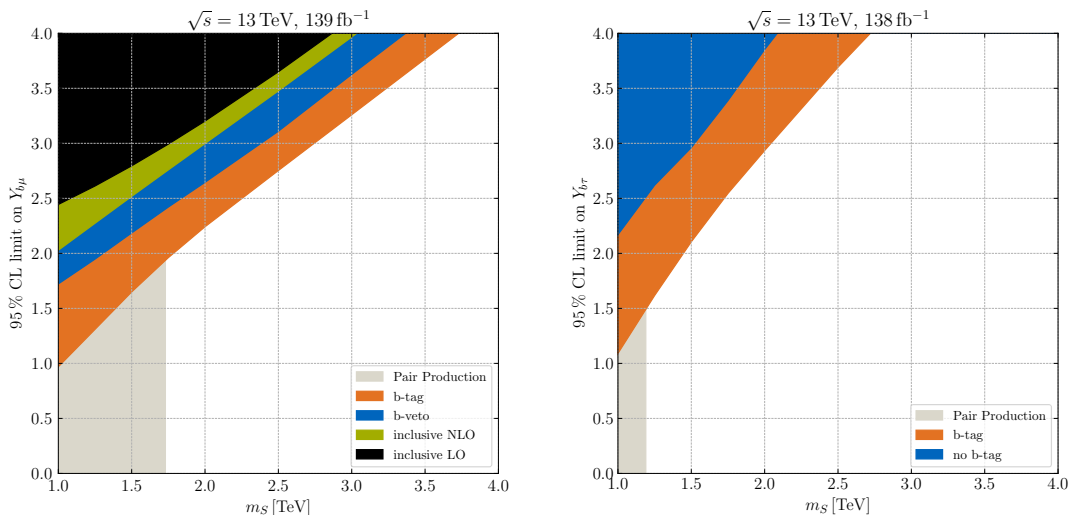


Figure 4.11: Left: Comparison of the 95% CL constraints on the $m_S - Y_{b\mu}$ plane following from different search strategies at LHC Run II. The black and green limits correspond to the inclusive DY search [496] for the LQ signal at LO and NLO, respectively. The blue and the orange bounds originate from the DY analysis [494] in the b -veto and b -tag category, respectively. The gray domain is instead excluded by the search [511] for strong LQ pair production. Right: Comparison of the 95% CL constraints on the $m_S - Y_{b\tau}$ plane that arise from the LHC Run II double hadronic ditau analysis [454]. The blue (orange) exclusion limit corresponds to the no b -tag (b -tag) category of the latter search, while the gray domain is excluded by strong pair production of third-generation LQs [512].

egory, respectively. All exclusions are based on NLO+PS predictions obtained with the POWHEG-BOX. The shaded gray region of parameter space with $m_S < 1720$ GeV is finally excluded by the search [511] for QCD pair production of scalar LQs. The displayed exclusions are derived directly from the observed model-independent upper 95% CL limits on the visible cross section times branching ratio provided in Refs. [494, 496]. From the shown results, it is evident that the search strategy that requires besides two OS muons a b -tag leads to the best exclusion. As explained in Sect. 4.2.2.2, this is to be expected because the requirement of an additional b -tagged jet leads to a strong increment of the signal-to-background ratio. Notice also that for $m_S \lesssim 1.7$ TeV, the exclusion contour starts to deviate from its linear behavior. This is a consequence of the contribution associated to single-LQ production with subsequent decay of the LQ (see the right diagram in Fig. 4.3) scaling as $|Y_{b\mu}|^2$ compared to the $|Y_{b\mu}|^4$ dependence of the squared amplitude of the t -channel Born-level LQ contribution. Another interesting feature of the results shown on the left-hand side in Fig. 4.11 is that the b -veto search performs better than the inclusive search strategy. This feature is related to the

fact that the SR with $m_{\mu\mu} \in [2070, 6000]$ GeV employed in Ref. [496] is not optimized for the LQ signals studied here. Using the model-independent limits as a function of the minimum dimuon invariant mass $m_{\mu\mu}^{\min}$, i.e., $m_{\mu\mu} > m_{\mu\mu}^{\min}$, presented in Ref. [494] that covers lower values of $m_{\mu\mu}^{\min}$ instead allows for such an optimization and, therefore, leads to a stronger bound. Moreover, comparing the black and green domains in particular, it is clear that accurate modeling of the BSM signal at NLO is crucial to derive precise exclusion limits even when employing an inclusive search strategy.

In the right panel of Fig. 4.11, we finally display the 95% CL exclusion bounds in the m_S - $Y_{b\tau}$ plane that follow from the two b -jet categories considered in the $\tau_h^+ \tau_h^-$ search [454]. The blue and orange exclusion limits correspond to the no b -tag and the b -tag category of this analysis, respectively, while the parameter space excluded by strong pair production of third-generation LQs [512] is indicated by the gray vertical band. This search excludes $m_S < 1190$ GeV at 95% CL. The significance of the individual b -jet categories of the search [454] is calculated as a Poisson ratio of likelihoods modified to incorporate systematic uncertainties on the background as Gaussian constraints [513]. Our statistical analysis includes the six (three) highest m_T^{tot} bins in the case of the no b -tag (b -tag) category. As for the exclusion limits on the coupling $Y_{b\mu}$, one observes that the bound on $Y_{b\tau}$ that follows from the search with a b -tag is more stringent than the one that derives from a strategy that vetos b -jets. Notice lastly that as an effect of single-LQ production, the slope of the exclusion limit arising from the b -tag category changes at around $m_S = 1.2$ TeV, although this effect is less visible in the case of the coupling $Y_{b\tau}$ than for $Y_{b\mu}$.

Employing the same search strategies, we further present the 95% CL exclusion limits on the m_S - $Y_{s\mu}$ and m_S - $Y_{c\tau}$ planes using the latest LHC dilepton analyses performed at LHC Run II. Such limits are of interest because, besides the Yukawa entries $Y_{b\mu}$ and $Y_{b\tau}$ discussed before, also $Y_{s\mu}$ and $Y_{c\tau}$ enter the predictions for $b \rightarrow s\mu^+\mu^-$ and $b \rightarrow c\tau\nu$ in scalar LQ models. All results are based on NLO+PS predictions obtained with our dedicated POWHEG-BOX implementation of the interaction Lagrangian in eq. (4.1).

The black and green bounds shown on the left-hand side of Fig. 4.12 correspond to the inclusive search [496] for the LQ signal at LO and NLO, respectively, and the blue exclusion limit is inferred from the analysis [494] imposing a b -veto. For comparison, we also display the parameter space with $m_S < 1730$ GeV that is excluded by the search [511] for strong LQ pair production as a gray vertical band. Like in the case of the coupling $Y_{b\mu}$ (see the left panel in Fig. 4.11), one sees that the exclusion limit following from the b -veto search surpasses the limit that derives from the inclusive analysis. The reason is again that by choosing $m_{\mu\mu}^{\min}$ appropriately, the sensitivity of

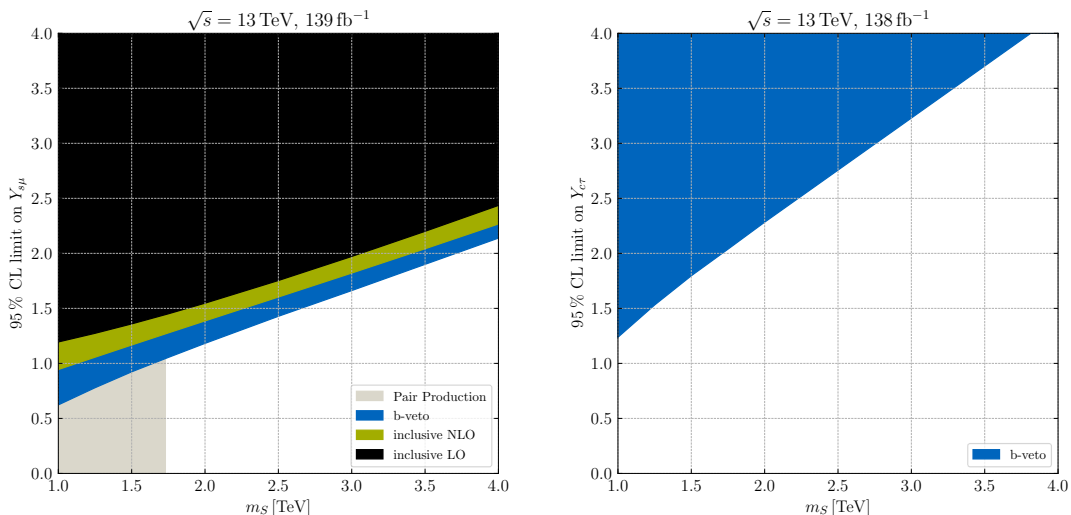


Figure 4.12: As Fig. 4.11 but for the couplings $Y_{s\mu}$ (left panel) and $Y_{c\tau}$ (right panel).

the b -veto search can be improved over that of the inclusive analysis which uses a fixed and rather high value of $m_{\mu\mu}^{\min}$. On the right in Fig. 4.12, we finally present the 95% CL exclusion limit on the m_S – $Y_{c\tau}$ plane that originates from a recast of the search with a b -veto that has been performed in the publication [494]. Notice that neither the ATLAS nor the CMS collaboration has searched for pairs of scalar LQs decaying into light-flavor quarks and tau leptons. This explains why no bound from QCD LQ pair production is included in the right panel of Fig. 4.12. Finally, we add that a DY ditau search that requires a c -tag is likely to allow to strengthen the exclusion bounds on the m_S – $Y_{c\tau}$ plane compared to the limits presented here. Given the latest advances in tagging charm quarks at the LHC [388, 514] and the successful applications of these techniques in the recent searches for the SM Higgs boson decaying to charm-quark pairs [515, 516], we believe that OSSF dilepton searches with the requirement of an additional c -jet would be an interesting addition to the exotics search canon of both the ATLAS and CMS collaborations.

4.3 Vector Leptoquarks in the Dilepton Channel

As already discussed in Sect. 4.1, the anomalies measured in the decay channels of B mesons hint at LFU violation parametrized by left-handed contact interactions [220]. It has been argued that these interactions arise naturally in models with singlet VLQs

in the $U_1 \sim (\mathbf{3}, \mathbf{1}, 2/3)$ representation.⁵ In a bottom-up approach, we can model the interactions of such a particle by employing the effective interaction Lagrangian

$$\mathcal{L}_U \supset \frac{g_U}{\sqrt{2}} \sum_{i,j=1}^3 \left[\beta_L^{ij} \bar{Q}_L^{i,a} \gamma_\mu L_L^j + \beta_R^{ij} \bar{d}_R^{i,a} \gamma_\mu e_R^j \right] U^{\mu,a} + \text{h.c.}, \quad (4.14)$$

where Q_L and L_L are the left-chiral SM quark and lepton $SU(2)_L$ doublets, and d_R and e_R denote the corresponding right-handed fields. The indices $i, j \in \{1, 2, 3\}$ refer to the SM fermion generation and $a \in \{1, \dots, 8\}$ is a QCD color index. The coupling g_U represents a general coupling strength of U to the SM fermions, whereas β_L^{ij} and β_R^{ij} are (a priori) arbitrary complex 3×3 matrices in flavor space, which distinguish the interactions to left- and right-handed fields. Inspired by phenomenology, we can assume the hierarchical pattern $|\beta_L^{33}| \simeq |\beta_R^{33}| \gtrsim |\beta_L^{23}| \gg |\beta_L^{32}| \simeq |\beta_L^{22}| > 0$. It has been demonstrated that such a configuration can fit the previously discussed bottom-quark decay anomaly in charged-current $b \rightarrow c$ transitions and the formerly observed anomaly in neutral-current $b \rightarrow s$ transitions [220]. All other couplings can vanish, in principle. Therefore, in the following, we set them to zero for the sake of simplicity. Furthermore, this implies that we restrict ourselves to $\tau^+ \tau^-$ production, where the largest impact of the VLQs is expected.

As stated in the introduction to LQs in Sect. 4.1, VLQs generally require an embedding into a UV complete theory such that higher-order perturbative calculations do not lead to ambiguities. For this reason, further colored degrees of freedom must be introduced, augmenting the phenomenology of QCD. Hence, the simplified interactions introduced in eq. (4.14) must be understood in a broader context. The famous Pati–Salam GUT represents the first UV-complete framework in which the VLQ U naturally arises. However, the tight experimental limits on FCNCs essentially exclude the relevant parameter space that can be probed at the LHC. In contrast, it has been substantiated that this tension is alleviated in so-called partial unification models like the 4321 model [517]. This particular modification of the original Pati–Salam model has received considerable attention in recent years and is introduced in the following Sect. 4.3.1. Thereafter, in Sect. 4.3.2, we discuss the renormalization at NLO in QCD in the 4321 model, which validates and partially generalizes the results stated in Ref. [518]. We restrict ourselves to those computations necessary for NLO dilepton production at the LHC, which we have already discussed in the context of scalar LQs in Sect. 4.2. In the subsequent Sect. 4.3.3, we apply our acquired knowledge about on-shell renormalization to the partial decay width $\Gamma(U \rightarrow b\tau)$ of the VLQ U and to its role as a

⁵From here on, we will drop the index 1 from the conventional nomenclature of Ref. [457] and simply refer to the VLQ in the $(\mathbf{3}, \mathbf{1}, 2/3)$ representation under \mathcal{G}_{SM} as U .

t -channel mediator for dilepton production at the LHC. Some phenomenological studies of the impact of the relevant model parameters are then presented in Sect. 4.3.4. Finally, we derive exclusion limits from current LHC analyses in Sect. 4.3.5.

4.3.1 The 4321 Model

A well-motivated and thoroughly studied class of UV-complete theories incorporating a singlet VLQ are gauge models. There, the massive U field arises from a gauge symmetry group $\mathcal{G} \supset \mathcal{G}_{\text{SM}}$, which is broken spontaneously to yield the SM Lagrangian at low energies, together with the singlet VLQ as well as additional degrees of freedom. It has been established that the minimal gauge group that yields the interaction Lagrangian of the form of eq. (4.14) and that can fit the semi-leptonic B -meson decay anomalies is [517, 519–526]

$$\mathcal{G}_{4321} = \text{SU}(4) \times \text{SU}(3)' \times \text{SU}(2)_L \times \text{U}(1)_X. \quad (4.15)$$

Due to its neat structure, this gauge group is often simply referred to as 4321. The $\text{SU}(3)_C$, which describes the strong force within the SM, is embedded as the vectorial subgroup of $\text{SU}(4) \times \text{SU}(3)'$ and $\text{SU}(2)_L$ is exactly the same as in the SM. The SM hypercharge Y is defined according to $Y = X + \sqrt{2/3}T^{15}$, where X is the generator of $\text{U}(1)_X$ and $T^{15} = 1/(2\sqrt{6})\text{diag}(1, 1, 1, -3)$ is a diagonal generator of $\text{SU}(4)$. Since we are interested in QCD corrections to the VLQ mediated $\ell^+\ell^-$ production, we restrict ourselves to the $\text{SU}(4) \times \text{SU}(3)'$ subgroup of \mathcal{G}_{4321} , denoting the corresponding gauge couplings by g_4 and g_3 . We refer to the associated gauge fields as H_μ^A and C_μ^a , where $A \in \{1, \dots, 15\}$ and $a \in \{1, \dots, 8\}$. In order to translate calculations in the 4321 model into SM terms, we can define the regular QCD gluon fields G_μ^a according to

$$G_\mu^a = s_3 H_\mu^a + c_3 C_\mu^a \quad (4.16)$$

and the associated strong coupling constant as

$$g_s = s_3 g_4 = c_3 g_3. \quad (4.17)$$

Here, we have introduced the notation $c_3 \equiv \cos \theta_3 = g_4/\sqrt{g_4^2 + g_3^2}$ and $s_3 \equiv \sin \theta_3$ for the mixing angle θ_3 for the mixing of $\text{SU}(4) \times \text{SU}(3)'$ to $\text{SU}(3)_C$. In particular, this leads to the relation

$$c_3 = \sqrt{1 - \frac{g_s^2}{g_4^2}}. \quad (4.18)$$

By means of linear combination, eq. (4.16) also points to the definition of another color octet, namely

$$G_\mu'^a = c_3 H_\mu^a - s_3 C_\mu^a, \quad (4.19)$$

which is commonly referred to as coloron. The remaining $SU(4) \times SU(3)'$ gauge fields can be used as a basis to construct

$$U_\mu^{1,2,3} = \frac{1}{\sqrt{2}} \left(H_\mu^{9,11,13} - i H_\mu^{10,12,14} \right) \quad (4.20)$$

and

$$Z'_\mu = H_\mu^{15} . \quad (4.21)$$

Under the SM gauge group \mathcal{G}_{SM} , these additional gauge fields transform as $G' \sim (\mathbf{8}, \mathbf{1}, 0)$, $U \sim (\mathbf{3}, \mathbf{1}, 2/3)$, and $Z' \sim (\mathbf{1}, \mathbf{1}, 0)$, respectively. All three fields acquire a mass after the spontaneous symmetry breaking of $SU(4) \times SU(3)' \rightarrow SU(3)_C$. Our focus on $\mathcal{O}(\alpha_s)$ corrections to non-resonant LQ-associated dilepton production allows us to neglect the impact of the Z' boson in most of the following discussions. The s -channel exchange of a Z' in a DY-like process $q\bar{q} \rightarrow Z' \rightarrow \ell^+\ell^-$ at the tree level leads to a narrow resonance peak structure around the Z' -boson mass in the invariant mass distribution of the dilepton system (see, for instance, Ref. [4]). However, as discussed before, we concentrate on non-resonant exotic contributions in the high- p_T regime, just like the one induced by the t -channel LQ exchange. Henceforth, we assume the omission of Z' contributions to be well-justified, especially since experimental searches for resonant and non-resonant BSM phenomena are conducted fully independently. For further details on the impact of Z' bosons on dilepton spectra, we refer to App. A.4.⁶

In order to explain the B -decay anomalies, the singlet VLQ is required to predominantly couple to the third quark generation. This can be achieved by an exclusive unification of the third-generation fermions into $SU(4)$ quadruplets. To be precise, the SM fermion fields can be cast into the form $\Psi_L = (Q_L^3, L_L^3)^T$ and $\Psi_R^- = (d_R^3, e_R^3)^T$, which we will from now on generically denote by $\Psi = (\psi_q, \psi_\ell)^T$. This representation transforms as $\Psi \sim (\mathbf{4}, \mathbf{1})$ under the $SU(4) \times SU(3)'$ subgroup of \mathcal{G}_{4321} . After spontaneous symmetry breaking, the interactions between the colored gauge bosons and the third-generation fermions in the 4321 model then read

$$\mathcal{L}_{4321} \supset \frac{g_4}{\sqrt{2}} \bar{\psi}_q^a \gamma_\mu \psi_\ell U^{\mu,a} + \text{h.c.} + g_s \bar{\psi}_q \gamma_\mu T^a \psi_q G^{\mu,a} + c_3 g_4 \bar{\psi}_q \gamma_\mu T^a \psi_q G'^{\mu,a} , \quad (4.22)$$

where the symbol T^a denotes the usual $SU(3)_C$ generators of QCD. The first two terms in eq. (4.22) are equivalent to the effective singlet VLQ interactions given in eq. (4.14) if one sets $g_U = g_4$ and $\beta_L^{33} = \beta_R^{33} = 1$. This shows that \mathcal{L}_U is correctly recovered if the U field is embedded into the 4321 model. As a consequence of the enlarged gauge

⁶The phenomenology of Z' bosons has been thoroughly studied in the context of simplified models for DM, in which it serves as a mediator between the SM and a dark sector. Ref. [526] considers the combination of the U VLQ and the Z' boson in the 4321 model with an additional fermionic DM agent.

group, however, the 4321 model contains a massive coloron G' besides the massless QCD gluon G . The interaction terms for both fields are equivalent in terms of their Lorentz structure, but the coloron exclusively couples to third-generation quarks (due to the quark-lepton unification being restricted to the third-generation fermions) with an effective coupling strength $(c_3 g_4)$. As a result, and with eq. (4.18) in mind, any amplitude with a single internal coloron is $\sim (c_3 g_4)^2 = g_4^2 - g_s^2$. Thus, any UV divergences occurring due to virtual gluon loops exactly cancel: singular gluon contributions $\sim (g_s)^n$ are removed by corresponding coloron contributions $\sim (g_s)^n$ in the UV, where the coloron mass $M_{G'}$ is negligible. Due to this cancellation, the combination of all one-loop amplitudes needed for $\mathcal{O}(\alpha_s)$ corrections in the full 4321 theory turns out to be UV finite. We study this behavior explicitly when we discuss the $\mathcal{O}(\alpha_s)$ renormalization of the 4321 model in Sect. 4.3.2.

As indicated before, the acquisition of mass of the heavy BSM gauge bosons is achieved in a common way by means of spontaneous symmetry breaking (SSB) in the 4321 model. The gauge group \mathcal{G}_{4321} is broken by the four scalars $\Omega_3 \sim (\bar{\mathbf{4}}, \mathbf{3}, \mathbf{1}, 1/6)$, $\Omega_1 \sim (\bar{\mathbf{4}}, \mathbf{1}, \mathbf{1}, -1/2)$, $\Omega_{15} \sim (\mathbf{15}, \mathbf{1}, \mathbf{1}, 0)$, and $H \sim (\mathbf{1}, \mathbf{1}, \mathbf{2}, 1/2)$, where phenomenology suggests the hierarchy $\langle \Omega_3 \rangle > \langle \Omega_1 \rangle \gg \langle \Omega_{15} \rangle \gg \langle H \rangle$ among the VEVs [523]. Here, H denotes the usual Higgs doublet of the SM. It has been shown that a choice of VEVs of the form

$$\langle \Omega_3 \rangle = \frac{1}{\sqrt{2}} \begin{pmatrix} v_3 & 0 & 0 \\ 0 & v_3 & 0 \\ 0 & 0 & v_3 \\ 0 & 0 & 0 \end{pmatrix} \quad \text{and} \quad \langle \Omega_1 \rangle = \frac{1}{\sqrt{2}} \begin{pmatrix} 0 \\ 0 \\ 0 \\ v_1 \end{pmatrix} \quad (4.23)$$

leads to the desired phenomenology. Just as in the SM, the scalar vacua induced by SSB lead to the required gauge boson masses through the kinetic terms

$$\mathcal{L}_{4321} \supset \sum_{i \in \{1,3,15\}} (\mathcal{D}_\mu \Omega_i)^\dagger (\mathcal{D}^\mu \Omega_i) , \quad (4.24)$$

that are part of the 4321 Lagrangian \mathcal{L}_{4321} . With the chosen scalar representations and VEVs, the coloron and the VLQ obtain conventional mass terms for vector particles. Moreover, the terms in eq. (4.24) entail the gauge boson interactions with Goldstone bosons, which will be relevant when we discuss the $\mathcal{O}(\alpha_s)$ renormalization of the 4321 model.

Due to the non-abelian nature of the 4321 model, consistent treatment of the theory at the quantum level further requires the introduction of Faddeev–Popov ghost particles for the extended gauge group. With all Goldstone boson and ghost degrees of

freedom, we end up with the expression

$$\begin{aligned}
 \mathcal{L}_{4321} \supset & ig_s \left[\left(U_{\mu\nu}^\dagger G^{\mu,a} T^a U^\nu + \text{h.c.} \right) - U_\mu^\dagger T^a U_\nu G^{\mu\nu,a} \right] \\
 & + ic_3 g_4 \left[\left(U_{\mu\nu}^\dagger G'^{\mu,a} T^a U^\nu + \text{h.c.} \right) - U_\mu^\dagger T^a U_\nu G'^{\mu\nu,a} \right] \\
 & + g_s M_U U_\mu^\dagger T^a \pi_U G^{\mu,a} + c_3 g_4 \frac{M_U^2 - M_{G'}^2}{M_U} U_\mu^\dagger T^a \pi_U G'^{\mu,a} + \text{h.c.} \\
 & + ig_s \left[\left(\partial_\mu \bar{c}_U \right) T^a U^\mu c_{G^a} - U_\mu^\dagger T^a \left(\partial^\mu \bar{c}_{U^\dagger} \right) c_{G^a} \right. \\
 & \quad \left. - \left(\partial_\mu \bar{c}_{G^a} \right) c_{U^\dagger} T^a U^\mu + \left(\partial_\mu \bar{c}_{G^a} \right) U^{\dagger\mu} T^a c_U \right] \\
 & + ic_3 g_4 \left[\left(\partial_\mu \bar{c}_U \right) T^a U^\mu c_{G'^a} - U_\mu^\dagger T^a \left(\partial^\mu \bar{c}_{U^\dagger} \right) c_{G'^a} \right. \\
 & \quad \left. - \left(\partial_\mu \bar{c}_{G'^a} \right) c_{U^\dagger} T^a U^\mu + \left(\partial_\mu \bar{c}_{G'^a} \right) U^{\dagger\mu} T^a c_U \right]
 \end{aligned} \tag{4.25}$$

describing their interactions. Here, $X_{\mu\nu} = \partial_\mu X_\nu - \partial_\nu X_\mu$ for $X = U, U^\dagger, G^a, G'^a$ are the relevant field-strength tensors, π_U is the Goldstone boson associated with the radial polarization of the singlet VLQ, and c_X are the ghost fields originating from the Faddeev–Popov gauge fixing procedure applied to the gauge boson field X .

With this brief introduction to both the structure and the particle content of the 4321 model, we can proceed with the $\mathcal{O}(\alpha_s)$ renormalization of the theory. We elaborate on this in detail in the following subsection.

4.3.2 Renormalization at $\mathcal{O}(\alpha_s)$

In this section, we discuss the one-loop $\mathcal{O}(\alpha_s)$ renormalization of the 4321 model. We state the relevant results for wave function renormalization of quarks and LQs as well as the QCD corrections to the LQ interaction vertex with the third-generation SM fermions. These are the necessary ingredients to describe the $\mathcal{O}(\alpha_s)$ corrections to the VLQ-mediated dilepton production. Since there does not exist a validated `FeynRules` model file containing the relevant degrees of freedom of the 4321 model, we perform all the following calculations using `FeynCalc` and `Package-X`. Since we are only interested in $\mathcal{O}(\alpha_s)$ corrections to dilepton production, we only keep the part $\sim g_s^2$ in any results of coloron contributions $\sim (c_3 g_4)^2 = g_4^2 - g_s^2$. Furthermore, we will explicitly observe the previously indicated cancellation of UV divergencies of the gluon and coloron contributions.

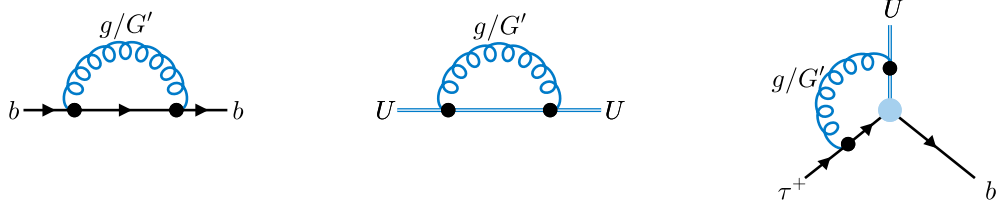


Figure 4.13: Feynman diagrams for the $\mathcal{O}(\alpha_s)$ renormalization of the 4321 model. On the left and in the middle, we display the correction to the quark and U propagators, respectively. We show the correction to the $U - b - \tau$ vertex on the right. All diagrams are due to virtual gluon and coloron contributions and are needed to compute the VLQ-mediated ditau production at the LHC and the partial $\Gamma(U \rightarrow b\tau)$ decay width at NLO accuracy in QCD. Note that the computation of the VLQ self-energy further requires to take into account Faddeev–Popov ghost and Goldstone boson degrees of freedom.

For the following calculations, we will use conventional dimensional regularization in order to parametrize poles both in the UV and the IR, working in $D = 4 - 2\varepsilon$ dimensions. The calculations are guided by Ref. [518], in which the authors have derived analogous results assuming $M_{G'} = M_U$. Hence, the calculations presented here can be considered as both a generalization and an independent validation of the results given in Ref. [518].

To give the results in a concise form, we introduce the abbreviated commutator-like notation

$$\begin{aligned} \mathbf{X}_{i_1 \dots i_j}(a_1, \dots, a_n; b_1, \dots, b_{k-1}, \langle\langle x, y \rangle\rangle, b_{k+1}, \dots, b_m) \\ := \mathbf{X}_{i_1 \dots i_j}(a_1, \dots, a_n; b_1, \dots, b_{k-1}, x, b_{k+1}, \dots, b_m) \quad (4.26) \\ - \mathbf{X}_{i_1 \dots i_j}(a_1, \dots, a_n; b_1, \dots, b_{k-1}, y, b_{k+1}, \dots, b_m) \end{aligned}$$

for the difference of PV functions with arguments differing only at one position. This structure occurs regularly due to the same form of gluon and coloron interactions.

The relevant diagram for the $\mathcal{O}(\alpha_s)$ corrections to the quark propagator is given on the left of Fig. 4.13. We need to consider both virtual gluon and coloron contributions. Translated into Feynman rules obtained with `FeynRules`, the two corresponding expressions only differ in the coupling g_s^2 and $(c_3 g_s)^2$ and the fact that the coloron propagator is endowed with the mass $M_{G'}$. Given in terms of PV functions and keeping only the terms $\sim \alpha_s$, the result for the amplitude reads

$$i\mathcal{M}(q \rightarrow q) = 4\pi\alpha_s C_F (D-2) \not{p} \left(\mathbf{B}_0(0; \langle\langle 0, M_{G'} \rangle\rangle, 0) + \mathbf{B}_1(0; \langle\langle 0, M_{G'} \rangle\rangle, 0) \right). \quad (4.27)$$

Now, in conventional dimensional regularization, a scaleless loop integral vanishes per definition since the regulators in the UV and IR are the same, i.e., $\varepsilon_{\text{UV}} = \varepsilon_{\text{IR}}$. However, we want to keep track of the different UV and IR divergences to demonstrate the finiteness in the UV due to the cancellation of gluon and coloron amplitudes. Hence, we write, for instance,

$$\int \frac{d^D k}{(2\pi)^D} \frac{1}{k^4} = \frac{i}{16\pi^2} \left(\frac{1}{\varepsilon_{\text{UV}}} - \frac{1}{\varepsilon_{\text{IR}}} \right), \quad (4.28)$$

corresponding to the scaleless loop integral $\mathbf{B}_0(0;0,0)$ occurring in eq. (4.27), and continue accordingly (see, e.g., Ref. [527]). With the PV functions translated into more conventional terms, we find

$$\begin{aligned} i\mathcal{M}^G(q \longrightarrow q) &= -i\not{p} \frac{\alpha_s}{4\pi} C_F \left(\frac{1}{\varepsilon_{\text{IR}}} - \frac{1}{\varepsilon_{\text{UV}}} \right) \\ \text{and } i\mathcal{M}^{G'}(q \longrightarrow q) &= -i\not{p} \frac{\alpha_s}{4\pi} C_F \left(L_\mu^{\text{IR}} + \frac{1}{\varepsilon_{\text{UV}}} - \frac{1}{2} \right) \end{aligned} \quad (4.29)$$

for the gluon and coloron contribution, respectively. In sum, we see that the poles in the UV exactly cancel, which we also observe in the following calculations. In the above equation, we have introduced the symbol $L_\mu^{\text{IR}} = \log(\mu_{\text{IR}}^2/M_U^2)$ for convenience. In order to renormalize the wave function of the quark, we need to differentiate the self-energy $\Sigma_q = \mathcal{M}^G(q \longrightarrow q) + \mathcal{M}^{G'}(q \longrightarrow q)$ with respect to the slashed propagator momentum, here denoted as \not{p} , i.e.,

$$\delta Z_q(p) = -\frac{d}{d\not{p}} \Sigma_q(\not{p}). \quad (4.30)$$

This established procedure in renormalized perturbation theory is explained in any standard textbook on QFT (see, e.g., Ref. [7]). Now, we need the self-energy to be evaluated at zero momentum transfer and obtain

$$\delta Z_q(0) = \frac{\alpha_s}{4\pi} C_F \left(\frac{1}{\varepsilon_{\text{IR}}} + \log \left(\frac{\mu^2}{M_{G'}^2} \right) - \frac{1}{2} \right) \quad (4.31)$$

as a final result. The result is UV finite but contains an $\mathcal{O}(\varepsilon_{\text{IR}}^{-1})$ pole. We employ this result when computing the NLO corrections to the partial $U \rightarrow b\tau$ decay width and the t -channel VLQ-mediated dilepton production. In both cases, we only need $\delta Z_q(p=0)$ since all external quarks are assumed to be massless.

For the wave function renormalization of the LQ, we separate the propagator according to

$$i\Sigma_U^{\mu\nu}(q^2) = ig^{\mu\nu} \frac{\alpha_s}{4\pi} \Sigma_U(q^2) + \mathcal{O}(q^\mu q^\nu), \quad (4.32)$$

following the definitions given in Ref. [518]. The wave function renormalization is then defined as

$$\delta Z_U(s) = \frac{\Sigma_U(s) - \Sigma_U(M_U^2)}{s - M_U^2}, \quad (4.33)$$

which approaches a common derivative in the limit $s \rightarrow M_U^2$. In Fig. 4.13, we display a sample Feynman diagram for different contributions due to virtual gluon and coloron exchange. Note that, for an accurate description, we need to take into account contributions from the Faddeev–Popov ghost fields from the non-abelian nature of the 4321 model and the Goldstone bosons associated with the SSB $SU(4) \times SU(3)' \rightarrow SU(3)_C$ [518]. As a general expression in terms of PV functions, we find

$$\begin{aligned} \Sigma_U(Q^2) = C_F \left[\frac{M_{G'}^2 - 3M_U^2}{M_U^2} M_{G'}^2 \mathbf{B}_0(Q^2; M_{G'}, M_U) + 4Q^2 \mathbf{B}_0(Q^2; \langle\langle 0, M_{G'} \rangle\rangle, M_U) \right. \\ \left. + 4(D-2) \mathbf{B}_{00}(Q^2; \langle\langle 0, M_{G'} \rangle\rangle, M_U) + \mathbf{A}_0(\langle\langle 0, M_{G'} \rangle\rangle) \right]. \end{aligned} \quad (4.34)$$

Using `Package-X`, the two last equations yield

$$\begin{aligned} \delta Z_U(Q^2) = \frac{2}{9Q^4 (M_U^2 - Q^2)} \left\{ 2M_U^2 Q^4 (x-4)^{3/2} \sqrt{x} (5x+3) \log\left(\frac{1}{2}(\sqrt{x-4} + \sqrt{x})\right) \right. \\ \left. + (M_U^2 - Q^2) \left[-4M_U^2 Q^2 (x-2)x + \log(x) \left(2M_U^4 (x-1)^3 \right. \right. \right. \\ \left. \left. \left. + M_U^2 Q^2 (x-4)(x-1)(5x+1) + 10Q^4 \right) \right. \right. \\ \left. \left. - 4 \left(M_U^4 - 2M_U^2 Q^2 - 5Q^4 \right) \log\left(\frac{M_U^2}{M_U^2 - Q^2}\right) \right] \right. \\ \left. + 2\sqrt{M_U^4 (x-1)^2 - 2M_U^2 Q^2 (x+1) + Q^4} \right. \\ \left. \times \left(-2M_U^4 (x-1)^2 + M_U^2 Q^2 ((13-3x)x+4) + 10Q^4 \right) \right. \\ \left. \times \log\left(\frac{M_U^2 (x+1) + \sqrt{M_U^4 (x-1)^2 - 2M_U^2 Q^2 (x+1) + Q^4} - Q^2}{2M_U^2 \sqrt{x}}\right) \right\} \Big|_{x=x_{G'/U}} \quad (4.35) \end{aligned}$$

as a result for the LQ wave function renormalization at a general energy scale Q^2 , where we introduced $x_{G'/U} = M_{G'}^2/M_U^2$. We have verified that, in the limit $Q^2 \rightarrow M_U^2$, our results for the individual gluon and coloron contributions agree with the ones stated in

Ref. [518]. Explicitly, this means that we find

$$\delta Z_U(M_U^2) = -\frac{8}{9} \left[\frac{3}{\varepsilon_{\text{IR}}} + 3L_\mu^{\text{IR}} + \sqrt{3}\pi - 7 \right] + \Theta(x_{G'/U}), \quad (4.36)$$

where

$$\begin{aligned} \Theta(x) = \frac{1}{9} \left[-28(x-2)(x-1) - 4\sqrt{(x-4)x}(x(7x-16)+3) \right. \\ \left. \times \log\left(\frac{1}{2}(\sqrt{x-4} + \sqrt{x})\right) + 2\left(x(x(7x-30)+21)+12\right) \log(x) + 8\sqrt{3}\pi \right], \end{aligned} \quad (4.37)$$

with $\Theta(x) \rightarrow 0$ for $x \rightarrow 1$. This validates our treatment of ghost particles and Goldstone bosons. Later, we particularly need the general form in eq. (4.35) for $Q^2 \rightarrow t$, when we compute the one-loop corrections in the 4321 model to dilepton production.

Finally, we want to calculate the correction to the LQ vertex with the SM fermions. The relevant diagram due to virtual gluon and coloron loops is given on the right of Fig. 4.13. Stripping off a factor of $i(g_4\alpha_s/(4\pi\sqrt{2}))\gamma^\mu$ from the total vertex factor, we find the vertex correction due to gluon and coloron loops to be

$$\begin{aligned} \delta V_U(Q^2) = 2C_F \left\{ 2(D-1)\mathbf{C}_{00}(Q^2, 0, 0; \langle\langle 0, M_{G'} \rangle\rangle, M_U, 0) \right. \\ \left. + Q^2 \left[\mathbf{C}_{12}(Q^2, 0, 0; \langle\langle 0, M_{G'} \rangle\rangle, M_U, 0) \right. \right. \\ \left. + \mathbf{C}_{11}(Q^2, 0, 0; \langle\langle 0, M_{G'} \rangle\rangle, M_U, 0) + \mathbf{C}_0(Q^2, 0, 0; \langle\langle 0, M_{G'} \rangle\rangle, M_U, 0) \right. \\ \left. \left. + \mathbf{C}_2(Q^2, 0, 0; \langle\langle 0, M_{G'} \rangle\rangle, M_U, 0) + \mathbf{C}_1(Q^2, 0, 0; \langle\langle 0, M_{G'} \rangle\rangle, M_U, 0) \right] \right\} \end{aligned} \quad (4.38)$$

at arbitrary energy scales Q^2 . Just like the general wave function renormalization of the VLQ propagator, we need this general expression for $Q^2 \rightarrow t$ for dilepton production. For the computation of the partial $U \rightarrow b\tau$ decay width renormalized in the on-shell scheme, we further need the vertex correction at scale $Q^2 = M_U^2$, which analytically evaluates to

$$\begin{aligned} \delta V_U(M_U^2) = C_F \left[-\frac{1}{\varepsilon_{\text{IR}}^2} - \frac{L_\mu^{\text{IR}} + 2}{\varepsilon_{\text{IR}}} + \frac{1}{12} \left(-6(L_\mu^{\text{IR}})^2 - 24L_\mu^{\text{IR}} + 7\pi^2 - 12\sqrt{3}\pi - 12 \right) \right] \\ + \Phi(x_{G'/U}). \end{aligned} \quad (4.39)$$

Here, we have defined

$$\begin{aligned}
 \Phi(x) = C_F \left\{ & -\frac{2\pi^2}{3} + \sqrt{3}\pi - 1 - \frac{1}{2}(x^2 - 4) \log(x) + x \right. \\
 & + \sqrt{(x-4)x(x+2)} \log\left(\frac{1}{2}(\sqrt{x-4} + \sqrt{x})\right) \\
 & + \frac{1}{3}(2x+1) \left[-6\text{Li}_2\left(\frac{x-1}{x}\right) - 6\text{Li}_2\left(\frac{2(x-1)}{x + \sqrt{(x-4)x-2}}\right) \right. \\
 & \quad + 6\text{Li}_2\left(\frac{2(x-1)}{x + \sqrt{(x-4)x}}\right) + 3\log^2\left(\frac{1}{2}\left(-x + \sqrt{(x-4)x+2}\right)\right) \\
 & \quad \left. \left. - 3\log^2\left(\frac{\sqrt{(x-4)x} - x}{x + \sqrt{(x-4)x-2}}\right) + \pi^2 \right] \right\}.
 \end{aligned} \tag{4.40}$$

Since $\Phi(x) \rightarrow 0$ for $x \rightarrow 1$, i.e., in the limit of equal LQ and coloron masses, we recover the result given in Ref. [518]. We also validated the partial results for the individual gluon and coloron contributions given therein.

With these formulae at hand, we compute the partial $U \rightarrow b\tau$ decay width, which is needed for NLO accurate calculations in the 4321 model involving VLQs. We further employ the obtained general expressions in the computation of dilepton production via t -channel U exchange. We present both results in the subsequent section.

4.3.3 Numerical Applications

4.3.3.1 The Partial Decay Width $U \rightarrow b\tau$

As a first application of our previously obtained results, we calculate the $\mathcal{O}(\alpha_s)$ corrections to the partial $U \rightarrow b\tau$ decay width of the singlet VLQ U . A detailed description of the calculation is already given in Ref. [518], where the result is stated in the limit $M_{G'} \rightarrow M_U$. For the three-point amplitude $U \rightarrow b\tau$, the authors define the NLO matrix element

$$\mathcal{M}_{\text{NLO}}^{\Gamma_U} = \mathcal{M}_{\text{tree}}^{\Gamma_U} \times \left[1 + \frac{\alpha_s}{4\pi} \left(\delta V_U(M_U^2) + \frac{1}{2} \delta Z_U(M_U^2) + \frac{1}{2} \delta Z_q(0) \right) \right] \tag{4.41}$$

at the one-loop level in QCD. Specifically, the virtual corrections to the decay width in D -dimensional space-time are then given by

$$\Gamma_U^V = \frac{g_4^2}{2M_U} \frac{1}{(D-1)} \left(\frac{e^{\gamma_E} \mu^2}{M_U^2} \right)^{\frac{4-D}{2}} \frac{2^{-D} (D-2)}{\sqrt{\pi} \Gamma\left(\frac{D-1}{2}\right)} \times \left[1 + \frac{\alpha_s}{4\pi} \left(2\delta V_U(M_U^2) + \delta Z_U(M_U^2) + \delta Z_q(0) \right) \right], \quad (4.42)$$

where $\gamma_E \simeq 0.577$ is the Euler–Mascheroni constant and $\Gamma(x)$ is the well-known Γ function. With the results in eqs. (4.31), (4.35), and (4.38), the computation for the virtual corrections alone suffer from the occurrence of IR singularities. Clearly, a physically viable result must be finite in four dimensions. Hence, at $\mathcal{O}(\alpha_s)$, we must factor in also diagrams with up to one real emission of a parton, i.e., the process $U \rightarrow q\ell j$. Since the real corrections are not affected by the presence of the coloron, we can assume the result given in Ref. [518], i.e.,

$$\Gamma_U^R = \frac{g_4^2}{4\pi} \frac{M_U}{(D-1)} \frac{\alpha_s}{4\pi} C_F \times \left[\frac{1}{\varepsilon_{\text{IR}}^2} + \frac{7}{2\varepsilon_{\text{IR}}} + \frac{2}{\varepsilon_{\text{IR}}} L_\mu^{\text{IR}} + 7L_\mu^{\text{IR}} + 2(L_\mu^{\text{IR}})^2 - \frac{5\pi^2}{6} + \frac{155}{12} \right], \quad (4.43)$$

in order to address IR divergent soft and collinear gluon contributions. In total, the NLO partial width then consists of the sum of the two processes

$$\Gamma_U^{\text{NLO}} = \Gamma_U^V + \Gamma_U^R. \quad (4.44)$$

Putting all pieces together, we find the partial decay width including $\mathcal{O}(\alpha_s)$ corrections, i.e., $\Gamma(U \rightarrow b\tau) = \Gamma_U^{\text{LO}} + \Gamma_U^{\text{NLO}}$, to be

$$\Gamma(U \rightarrow b\tau) = \frac{g_4^2 M_U}{24\pi} (1 + \Delta), \quad \Delta = \frac{\alpha_s}{4\pi} f(x_{G'/U}). \quad (4.45)$$

Here, we define

$$f(x) = -\frac{4}{9} (7x^2 - 27x - 37) - \frac{16\pi^2}{9} + \frac{2}{9} (7x^3 - 36x^2 + 21x + 30) \ln x - \frac{4}{9} (7x^2 - 22x - 9) B(x) - \frac{16}{3} (2x + 1) C(x), \quad (4.46)$$

where, furthermore,

$$B(x) = \sqrt{(x-4)x} \ln \left[\frac{x + \sqrt{(x-4)x}}{2\sqrt{x}} \right] \quad (4.47)$$

and

$$C(x) = -\frac{\pi^2}{6} - \frac{1}{2} \ln^2 \left[\frac{\sqrt{(x-4)x} - x}{2-x + \sqrt{(x-4)x}} \right] + \text{Li}_2 \left[\frac{2}{x + \sqrt{(x-4)x}} \right] - \text{Li}_2 \left[\frac{2}{2-x + \sqrt{(x-4)x}} \right]. \quad (4.48)$$

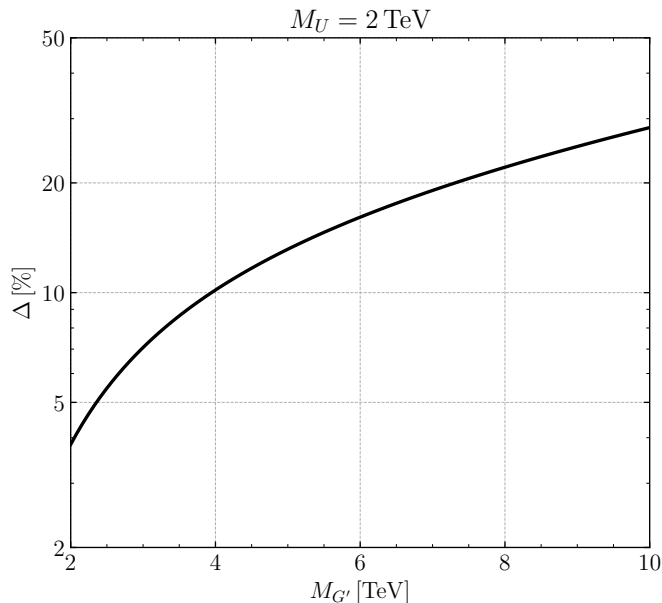


Figure 4.14: Numerical size of the $\mathcal{O}(\alpha_s)$ correction to the partial decay width $U \rightarrow b\tau$ as a function of the coloron mass $M_{G'}$, fixing the singlet vector LQ mass to $M_U = 2$ TeV.

In the result above, $\text{Li}_2(z)$ denotes the usual dilogarithm function. In the limit of degenerate singlet VLQ and coloron masses, it follows from eq. (4.46) that $f(1) = 76/3 - 32\pi/(3\sqrt{3})$, which coincides with the analytic expression reported in Ref. [518]. This agreement serves as an independent cross-check of the $\mathcal{O}(\alpha_s)$ calculations performed in the latter article. Notice that in the more generic case of the LQ-quark-lepton interactions (4.14), the total decay width of the LQ includes the processes $U \rightarrow b\tau$ and $U \rightarrow t\nu_\tau$, and can be obtained from eq. (4.45) by the simple replacement $g_4^2 \rightarrow g_U^2 \left[\left(2 - 3x_{t/U}/2 + x_{t/U}^3/2 \right) \left| \beta_L^{33} \right|^2 + \left| \beta_R^{33} \right|^2 \right] / 2$. Here, $x_{t/U} = m_t^2/M_U^2$ and we have included the corrections due to the non-negligible top-quark mass $m_t \simeq 163$ GeV that arise from the tree-level phase space and the squared matrix element at LO. Top-quark mass terms that arise at $\mathcal{O}(\alpha_s)$ and that would lead to a flavor-dependent correction Δ are instead neglected. We believe this simplification to be an excellent approximation for LQ and coloron masses in the TeV range.

In Fig. 4.14, we display the numerical size of the NLO QCD correction Δ as defined in eq. (4.45). In the plot, the mass of the singlet vector LQ is set to $M_U = 2$ TeV. One observes that the $\mathcal{O}(\alpha_s)$ corrections to the partial decay width $U \rightarrow b\tau$ grow with increasing coloron mass $M_{G'}$. For $M_{G'} = 2$ TeV, $M_{G'} = 5$ TeV, and $M_{G'} = 10$ TeV, we find that the NLO QCD corrections amount to around 4%, 14%, and 30%, respectively. Notice that the observed enhancement originates from logarithmic non-decoupling contributions of the form $\ln(M_{G'}^2/M_U^2)$ (see Refs. [518, 528] for detailed

discussions of this issue). To gauge the ambiguities in our numerical analysis that are related to the choice of the masses of the heavy colored vector states of the 4321 model, we employ two benchmarks, namely $M_{G'} = M_U$ and $M_{G'} = 2.5M_U$. While the former choice is motivated by simplicity, the second option reflects the fact that the existing LHC bounds on the mass of the coloron are more stringent than those on the singlet vector LQ by at least a factor of two [220, 511].

Note that in the following subsection, which deals with the $q\bar{q} \rightarrow \ell^+\ell^-$ process with VLQs, we adopt a more efficient notation and refer to $\Gamma(U \rightarrow b\tau)$ simply as Γ_U .

4.3.3.2 NLO Dilepton Production

Now, let us finally turn to dilepton production with the t -channel exchange of a singlet VLQ U . When computing the total amplitude $\mathcal{M}^U(q\bar{q} \rightarrow \ell^+\ell^-)$ up to NLO accuracy in α_s , we can distinguish the different contributions according to

$$\mathcal{M}^U(q\bar{q} \rightarrow \ell^+\ell^-) = \mathcal{M}_{\text{SM}} + \mathcal{M}_{\text{tree}}^U + \mathcal{M}_{\text{NLO}}^U, \quad (4.49)$$

where \mathcal{M}_{SM} is the SM amplitude, $\mathcal{M}_{\text{tree}}^U$ is the tree-level VLQ amplitude, and $\mathcal{M}_{\text{NLO}}^U$ contains all virtual NLO QCD corrections to the new-physics process. Here, the squared and spin- and color-averaged tree-level amplitude is given by the well-known result

$$\overline{|\mathcal{M}_{\text{tree}}^U|^2} = \frac{g_4^4 \left(2s^2\beta_L^2\beta_R^2 + u^2(\beta_L^4 + \beta_R^4) \right)}{12 \left(\Gamma_U^2 M_U^2 + (t - M_U^2)^2 \right)}. \quad (4.50)$$

When we compute squared amplitudes, the tree-level SM and the LO VLQ contributions interfere, giving rise to a contribution $\sim \alpha_{\text{em}}g_4^2$, which evaluates to

$$\begin{aligned} \overline{\mathcal{M}_{\text{SM}}^* \mathcal{M}_{\text{tree}}^U} &= \frac{\pi\alpha_{\text{em}}g_4^2}{9s_W^2(s_W^2 - 1)} \\ &\times \frac{u^2(t - M_U^2) \left(\beta_L^2 \left(-4s_W^2(m_Z^2 + s) + 4m_Z^2s_W^4 + 3s \right) + 4s_W^2\beta_R^2 \left(m_Z^2(s_W^2 - 1) + s \right) \right)}{s(m_Z^2 - s) \left(\Gamma_U^2 M_U^2 + (t - M_U^2)^2 \right)}. \end{aligned} \quad (4.51)$$

Note that we have neglected the decay width of the Z boson in the above expression.

At the loop level, we can eventually use the results from the previous subsection. In order to compute $\mathcal{M}_{\text{NLO}}^U$, we must further separate it into factorizable contributions, which are due to the wave-function and vertex corrections of the previous section, and

non-factorizable contributions. The latter arise from box diagrams displayed in the center of Fig. 4.5, where again, coloron contributions need to be taken into account as well. Therefore, we write

$$\mathcal{M}_{\text{NLO}}^U = \mathcal{M}_{\text{tree}}^U \times \left[1 + \frac{\alpha_s}{4\pi} \left(\delta Z_U(t) + 2\delta V_U(M_U^2) + \delta Z_q(0) \right) \right] + \mathcal{M}_{\text{box}}^U. \quad (4.52)$$

The finite box contribution must be computed independently from the factorizable pieces that stem from the renormalization of the 4321 model. For our purposes, it suffices to compute the result in terms of PV functions, which leaves us with the expression

$$\begin{aligned} \overline{\mathcal{M}_{\text{tree}}^U} * \overline{\mathcal{M}_{\text{box}}^U} = & -\frac{\alpha_s g_4^4}{36\pi (t - M_U^2)} \left\{ \left(\beta_L^4 + \beta_R^4 \right) \left[2(s+t) \mathbf{B}_0(t; \langle\langle M_{G'}, 0 \rangle\rangle, M_U) \right. \right. \\ & + \left(-2t (M_{G'}^2 + M_U^2) + 4s^2 + 4st + 2t^2 \right) \mathbf{C}_0(0, t, 0; 0, M_{G'}, M_U) \\ & - \left(M_{G'}^2 + M_U^2 + 2s + t \right) s \mathbf{C}_0(s, 0, 0; 0, 0, M_{G'}) \\ & + \left(M_U^2 + 2s + t \right) s \mathbf{C}_0(0, s, 0; 0, 0, 0) - M_{G'}^2 s \mathbf{C}_0(s, 0, 0; 0, 0, M_U) \\ & + 2 \left(M_U^2 t - 2s^2 - 2st - t^2 \right) \mathbf{C}_0(0, 0, t; 0, 0, M_U) \\ & - \left(s \left(M_{G'}^4 + 2M_{G'}^2 s + M_U^4 + 2s (M_U^2 + s) \right) \right. \\ & \quad \left. + 2t(s - M_{G'} M_U)(M_{G'} M_U + s) + st^2 \right) \mathbf{D}_0(s, 0, t, 0; 0, 0, 0, 0, M_{G'}, M_U) \\ & \left. + \left(M_U^4 + 2M_U^2 s + 2s^2 + 2st + t^2 \right) s \mathbf{D}_0(0, s, 0, t; 0, 0, 0, 0, 0, M_U) \right] \\ & + 4\beta_L^2 \beta_R^2 s^2 \left[2\mathbf{C}_0(0, t, 0; 0, M_{G'}, M_U) - 2\mathbf{C}_0(0, 0, t; 0, 0, M_U) \right. \\ & \left. + s \left(\mathbf{D}_0(0, s, 0, t; 0, 0, 0, 0, 0, M_U) - \mathbf{D}_0(s, 0, t, 0; 0, 0, 0, 0, M_{G'}, M_U) \right) \right] \left. \right\}. \quad (4.53) \end{aligned}$$

With all these analytical results implemented into the `POWHEG-BOX`, we can study how the different contributions under consideration influence the new-physics signal. Moreover, by varying the $\text{SU}(4)$ coupling constant and the heavy gauge-boson masses $M_{G'}$ and M_U , we can pin down the impact of the relevant model parameters on the VLQ-mediated dilepton production. The simplest observable that one can study in DY ditau production is the invariant mass $m_{\tau\tau}$ of the final state ditau system. In Fig. 4.15, we present our results for the LQ corrections to the corresponding spectrum in inclusive $pp \rightarrow \tau^+ \tau^-$ production, employing `NNPDF40_nlo_as_01180` PDFs [192]. The orange line

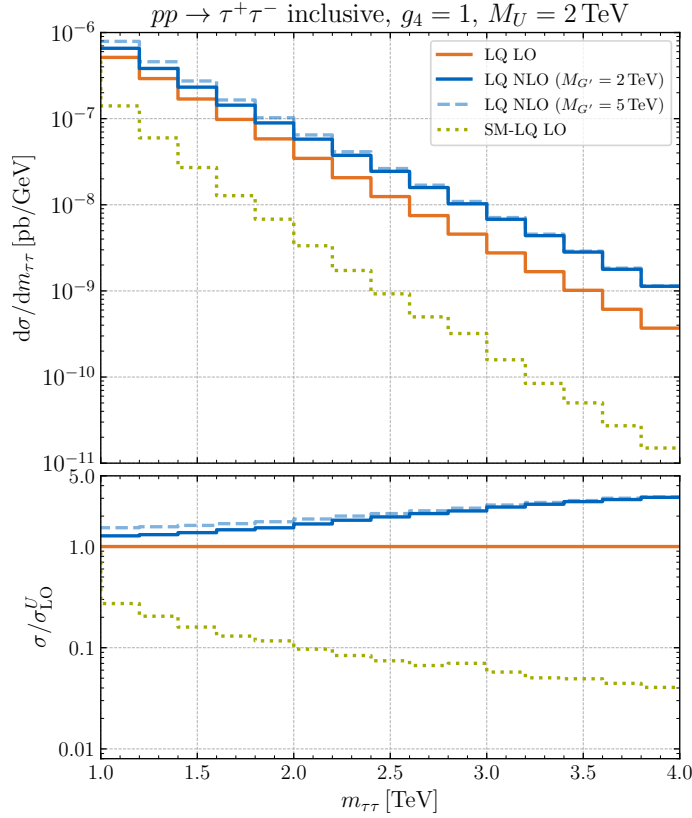


Figure 4.15: Inclusive $pp \rightarrow \tau^+\tau^-$ production cross sections as functions of $m_{\tau\tau}$ for the parameter choices $g_4 = 1$ and $M_U = 2$ TeV. The orange curve corresponds to the LQ distribution at the LO (LQ LO), and the solid (dashed light) blue line displays the result at NLO accuracy (LQ NLO) where the coloron mass is set to $M_{G'} = 2$ TeV ($M_{G'} = 5$ TeV). The dotted green histogram illustrates the magnitude of the interference effects between the SM background and the LQ signal (SM-LQ LO). The lower panel depicts the ratios between the different LQ contributions and the relevant LQ LO distribution.

describes the LQ distribution at the LO (LQ LO) in QCD, while the solid (dashed light) blue line displays the result at NLO accuracy (LQ NLO), where the coloron mass is set to $M_{G'} = 2$ TeV ($M_{G'} = 5$ TeV). The dotted green curve illustrates the size of the interference effects between the SM background and the LQ signature (SM-LQ LO). From the lower panel of the plot, it is evident that the NLO QCD effects play an important role in obtaining precise predictions as they amount to around 40% (150%) at $m_{\tau\tau} = 1.5$ TeV ($m_{\tau\tau} = 3$ TeV) compared to the tree-level LQ prediction. Notice that at NLO in QCD, the DY ditau production spectra resulting from LQ exchange depend on the mass $M_{G'}$ of the coloron. For the two choices of $M_{G'}$ shown in the figure, we find relative differences of the order of 10% between the two distributions. Therefore, the

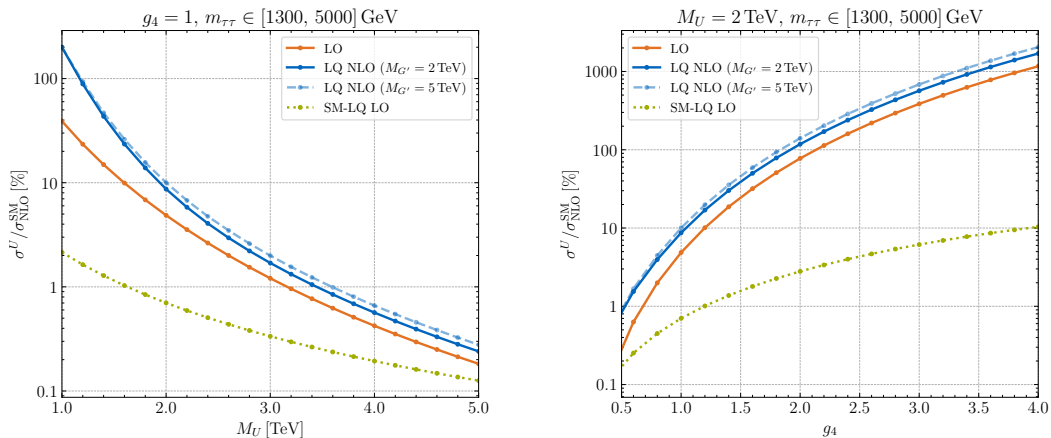


Figure 4.16: Ratios between the individual LQ corrections and the SM background for inclusive $pp \rightarrow \tau^+\tau^-$ production calculated at the NLO in QCD. The shown results correspond to the fiducial region defined by $p_{T,\tau} > 30$ GeV, $|\eta_\tau| < 2.5$, and $m_{\tau\tau} \in [1300, 5000]$ GeV. The left (right) plot depicts the results as a function of M_U (g_4) for fixed $g_4 = 1$ ($M_U = 2$ TeV). The color coding and meaning of the different curves resemble those in Fig. 4.15.

observed effects are similar in size to the $M_{G'}$ dependence of the $\mathcal{O}(\alpha_s)$ corrections to the partial decay width of the $U \rightarrow b\tau$ channel (see Fig. 4.14). The interference effects between the SM DY background and the LQ signal turn out to be destructive in the shown $m_{\tau\tau}$ range,⁷ amounting to approximately 15 % (5 %) for $m_{\tau\tau} = 1.5$ TeV ($m_{\tau\tau} = 3$ TeV).

In Fig. 4.16, we further display the ratios between the individual LQ contributions and the DY ditau SM background. The normalization is calculated at the NLO in QCD and we select events with two opposite-sign tau leptons that are both required to have a transverse momentum of $p_{T,\tau} > 30$ GeV and a pseudorapidity of $|\eta_\tau| < 2.5$. The invariant masses of the ditau pairs must fall into the range $m_{\tau\tau} \in [1300, 5000]$ GeV. Detector efficiency corrections are not taken into account. The left panel displays our results as a function of M_U , fixing the overall coupling strength that appears in eq. (4.22) to $g_4 = 1$. From this figure, it is clearly visible that the relative size of the NLO QCD corrections decreases for increasing singlet vector LQ mass. Numerically, we find relative effects of around 330 %, 50 %, and 15 % for $M_U = 1$ TeV, $M_U = 2$ TeV, and $M_U = 3$ TeV, respectively. This feature can be traced back to the fact that the NLO QCD corrections related to s -channel single-LQ production followed by the decay of the LQ (see the right Feynman diagram in Fig. 4.3) decouple faster than the real and virtual corrections to the t -channel Born-level LQ contribution (see the left and

⁷The SM-LQ LO results shown in Figs. 4.15, 4.16, and 4.17 represent the absolute magnitudes of the corresponding predictions for the interference effects between the SM background and the LQ signal.

right graph in Fig. 4.5). One also observes that the interference effects represent only subleading corrections in the mass window $m_{\tau\tau} \in [1300, 5000]$ GeV, amounting to an effect of at most -2% relative to the SM background for the considered M_U values.

On the right-hand side of Fig. 4.16, we finally depict our ratio predictions as functions of g_4 , setting the mass of the singlet VLQ to $M_U = 2$ TeV. It is evident from the plot that the relative size of the NLO QCD corrections decreases for increasing overall coupling strength. In the case of $M_{G'} = 2$ TeV, the higher-order QCD effects amount compared to the tree-level LQ result to around 140 %, 50 %, and 30 % for $g_4 = 0.5$, $g_4 = 1$, and $g_4 = 2$. For $M_{G'} = 5$ TeV, the corresponding numbers read 150 %, 70 %, and 50 %. This behavior can be understood by realizing that the squared amplitude of the t -channel Born-level LQ contribution scales as $|g_4|^4$, while the resonant single-LQ production rate is proportional to $|g_4|^2$. One again sees that the interference contributions are numerically subleading even for large couplings g_4 , where they just reach the level of -10% .

4.3.4 Phenomenological Analyses

LHC searches for signatures involving tau pairs in the final state like those performed in the publications [454, 455, 493] are known to provide strong constraints on LQ models that address the observed deviations in the charged-current $b \rightarrow c$ transitions [220, 460, 503, 505, 529, 530]. To illustrate the role that additional b -jets play in analyses of this kind, we consider as an example the recent CMS search [454] for $\tau^+\tau^-$ final states with both taus decaying to hadrons (τ_h). We used the same ditau analysis already in Sect. 4.2.2.3 for third-generation scalar LQs. However, for the convenience of the reader, we repeat the analysis set up at this point. The τ_h candidates are distinguished from jets originating from the hadronization of light-flavored quarks or gluons, and from electrons or muons by employing the τ -tagger described in the article [507]. The used working points have an efficiency of approximately 50 %, 70 %, and 70 % for identification in the case of jets, electrons, and muons, respectively. The corresponding rejection factors are about 230, 20, and 770. Both τ_h candidates are required to have $p_{T,\tau} > 40$ GeV and $|\eta_\tau| < 2.1$, and their pseudorapidity-azimuth separation must be greater than $\Delta R_{\tau\tau} = 0.3$. Jets are clustered using the anti- k_t algorithm with radius $R = 0.4$, as implemented in `FastJet` [47]. Light-flavored quark or gluon jets need to fulfill $p_{T,j} > 30$ GeV and $|\eta_j| < 4.7$, while b -jets with $p_{T,b} > 20$ GeV and $|\eta_b| < 2.5$ are selected. In order to identify b -jets, we employ the CMS b -tagging efficiencies stated in Refs. [508, 509]. The used b -tagging working point yields a b -tagging efficiency of

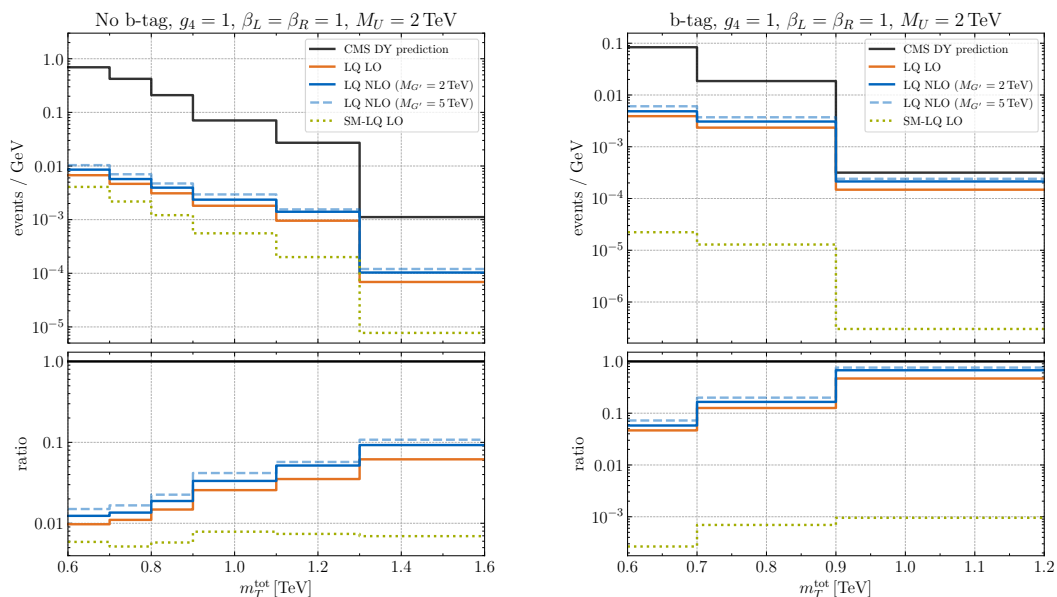


Figure 4.17: Distributions of m_T^{tot} in the no b -tag (left panel) and the b -tag (right panel) category in the final state containing two hadronic tau leptons. The black curves correspond to the SM expectations of the DY background provided by CMS in Ref. [454]. This search is based on 138 fb^{-1} of integrated luminosity collected in pp collisions at $\sqrt{s} = 13 \text{ TeV}$. The orange and blue curves instead represent the LQ LO and LQ NLO predictions assuming $g_4 = 1$ and $M_U = 2 \text{ TeV}$. In the case of the solid (dashed light) blue lines the coloron mass is set to $M_{G'} = 2 \text{ TeV}$ ($M_{G'} = 5 \text{ TeV}$). The dotted green histograms illustrate the size of the interference effects between the LQ signal and the SM background (SM-LQ LO). The definition of the signal regions (SRs) and other experimental details can be found in the main text.

around 80% and a rejection around 100 for jets arising from light-flavored quarks or gluons. Our analysis is implemented into `MadAnalysis 5` [37] and employs `DELPHES 3` [48] as a fast detector simulator. We use `PYTHIA 8` [35] to shower the events. Effects from hadronization, underlying event modeling or QED effects in the PS are not included in our MC simulations.

As in Sect. 4.2.2.3, where we discussed exclusive and inclusive ditau production in presence of scalar LQs, we use the total transverse mass as a discriminating variable [510] (see eq. (4.12) for its definition). In Fig. 4.17, we compare the m_T^{tot} distributions within the SM and the 4321 model defined in eq. (4.22) for the parameter choices $g_4 = 1$ and $M_U = 2 \text{ TeV}$. The left (right) panel displays the results for the no b -tag (b -tag) category. The black curves represent the SM expectations of the DY background taken from Ref. [454], while the orange and blue histograms are the LQ LO and LQ NLO predictions obtained using our `POWHEG-BOX` code. The solid (dashed light) blue LQ NLO

results assume $M_{G'} = 2 \text{ TeV}$ ($M_{G'} = 5 \text{ TeV}$). All predictions correspond to 138 fb^{-1} of pp data collected at $\sqrt{s} = 13 \text{ TeV}$. From the lower left panel, one sees that, in the no b -tag category, the NLO LQ contribution amounts to a relative correction of less than 10% compared to the SM DY background for $m_T^{\text{tot}} > 1300 \text{ GeV}$. For what concerns the b -tag category, one instead observes from the lower right panel that in the highest m_T^{tot} bin with $m_T^{\text{tot}} > 900 \text{ GeV}$ the NLO LQ signal constitutes around 85% of the SM DY background. This feature clearly shows that for third-generation VLQs, the sensitivity of DY searches notably improves by demanding an additional b -jet in the final state. This finding is aligned with what we found for SLQs before. Furthermore, it is important to realize that the NLO QCD effects enhance the LO LQ predictions in the no b -tag (b -tag) category by approximately 35% (30%) in the highest m_T^{tot} bin, making higher-order QCD effects phenomenologically relevant. On the other hand, the dependence of the NLO LQ distributions on $M_{G'}$ is rather weak. This renders the constraints derived below model-independent in the sense that one can set a limit on g_4 as a function of M_U , essentially without making a reference to the choice of the coloron mass as long as $M_{G'} = \mathcal{O}(M_U)$. One finally sees that the considered SM-LQ LO interference effects, displayed as dotted green curves, amount to a few permille in the case of the no b -tag category, while they can exceed the level of 5% if one requires the presence of a b -tag in the events. In contrast to what has been suggested in the recent work [454], interference effects, therefore, play only a minor role in the SRs that are relevant for non-resonant DY searches for third-generation singlet VLQs at the LHC.

4.3.5 Exclusion Limits

Based on the ditau search strategies detailed above, we now derive NLO+PS accurate 95% confidence level (CL) limits on the $M_U - g_4$ plane. The procedure is the same as in Sect. 4.2.3 for scalar LQs coupling to bottom quarks and tau leptons in the context of the CMS analysis [454]. Since we have seen in the previous Sect. 4.3.4 that the choice of coloron mass has only a minor impact on the m_T^{tot} spectrum, we employ $M_{G'} = M_U$ for simplicity when determining the exclusion bounds. Fig. 4.18 shows our 95% CL limits on the $M_U - g_4$ parameter space that follow from the two b -jet categories considered in the CMS search [454] for two hadronic tau leptons. The blue and orange exclusion corresponds to the no b -tag and the b -tag category of this analysis, respectively, while the parameter space excluded by strong pair production of third-generation LQs [531] is indicated by the gray vertical band. This search excludes $M_U < 1650 \text{ GeV}$ at 95% CL. Again, we calculate the significance of the individual b -jet categories of the search [454]

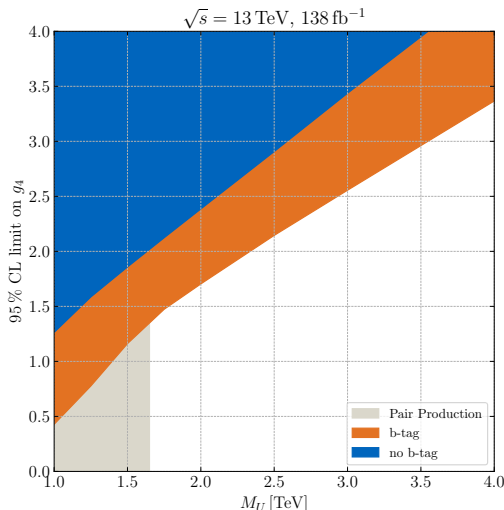


Figure 4.18: Comparison of the 95 % CL constraints on the $M_U - g_4$ plane that arise from the latest LHC Run II hadronic ditau analysis [454]. The blue (orange) exclusion corresponds to the no b -tag (b -tag) category of the latter search, while the gray shaded parameter space is excluded by strong pair production of third-generation LQs [512].

as a ratio of Poisson likelihoods taking into account systematic uncertainties on the background as Gaussian constraints [513]. Our statistical analysis includes the six (three) highest m_T^{tot} bins in the case of the no b -tag (b -tag) category.

One first observes that the bound on g_4 that follows from the search with a b -tag is more stringent than the one that derives from a strategy that requires no b -jet. We add that the difference between the no b -tag and b -tag constraints is rather pronounced in the case of the CMS analysis [454], because this search observes a resonant-like excess with a significance of around 3σ at $m_T^{\text{tot}} \simeq 1.2 \text{ TeV}$ in the no b -tag sample. Consequently, the resulting no b -tag limits on the LQ parameter space are weaker than expected. Finally, notice that for $M_U \lesssim 1.7 \text{ TeV}$ the exclusions contour starts to deviate from its linear behavior. This is again a consequence of the contribution associated to single-LQ production with subsequent decay of the LQ (see the right diagram in Fig. 4.3) scaling as $|g_4|^2$ compared to the $|g_4|^4$ dependence of the squared amplitude of the t -channel Born-level LQ contribution. Our findings mirror the conclusions of our previous work on third-generation SLQs.

Furthermore, we present the 95 % CL limits on the $M_U - g_4$ plane that follow from recasts of the LHC Run II analyses [455, 493] of ditau production. The event generation is, again, performed at the NLO+PS level using our POWHEG-BOX implementation. We use NNPDF40_nlo_as_01180 PDFs, PYTHIA 8 for PS modeling, and MadAnalysis 5 together

with DELPHES 3 as an analysis tool. As before, underlying event modeling or QED effects in the PS are not included in our MC simulations. Applying our MC chain to the SM prediction for $pp \rightarrow \tau^+ \tau^-$ obtained with the POWHEG-BOX at NLO+PS, we are able to reproduce the relevant SM DY background distributions as given in Refs. [455, 493] to about 30%. This approximate agreement serves as an important cross-check of our analysis framework.

The search strategy for hadronic tau leptons used by ATLAS in Ref. [493] is quite similar to that of CMS as described in Ref. [454]. The hadronic τ candidates are composed of a neutrino and a set of visible decay products ($\tau_{\text{had-vis}}$), usually consisting of one or three charged pions and up to two neutral pions. These $\tau_{\text{had-vis}}$ candidates are reconstructed from seeding jets [532] and are required to have $p_{T,\tau} > 65$ GeV and $|\eta_\tau| < 2.5$. The $\tau_{\text{had-vis}}$ candidates must satisfy loose or medium τ identification criteria with efficiencies of about 85% (75%) and 75% (60%) for one-track (three-track) candidates, respectively. The corresponding rejection factors in multijet events are roughly 20 (200) and 30 (500) for one-track (three-track) candidates [532]. The two hadronic τ candidates are required to have opposite electric charge and the azimuthal angular difference between the vectors $\vec{p}_T^{\tau_1}$ and $\vec{p}_T^{\tau_2}$ needs to fulfil $|\Delta\phi| > 2.7$. Jets are clustered using the anti- k_t algorithm with radius $R = 0.4$ and must satisfy $p_{T,j} > 20$ GeV and $|\eta_j| < 2.5$. Our b -jet identification is based on the information provided in the ATLAS note [388]. The used b -tagging working point yields a b -tagging efficiency of around 70% and rejections of approximately 9, 36, and 300 for c -jets, τ decays involving hadrons, and jets arising from light-flavored quarks or gluons, respectively. Like in the case of the CMS analysis [454], the total transverse mass from eq. (4.12) is used in Ref. [493] and our recast to discriminate between the LQ signal and the SM background. Two distinct SRs, one where b -jets are vetoed and another one that require at least one b -jet in the event, are then studied.

The latest ditau search by CMS [455] instead imposes the following selection requirements. Events with two hadronic τ candidates with opposite-sign electric charge are selected. The τ_h candidates are reconstructed with the so-called hadron-plus-strips algorithm [507, 533]. The medium working point of this algorithm is used in our recast, which has an efficiency of about 70% for a genuine τ_h and a misidentification rate of around 0.1% for light-flavored quark or gluon jets. Furthermore, we require that $p_{T,\tau} > 50$ GeV, $|\eta_\tau| < 2.3$, and $\Delta R_{\tau\tau} > 0.5$. Jets are clustered with the anti- k_t algorithm and $R = 0.4$. Our analysis selects all jets that satisfy $p_{T,j} > 50$ GeV and $|\eta_j| < 4.7$. The identification of b -jets employs a parametrization of the loose working point of Refs. [508, 534]. The efficiency of this b -tagger can reach up to 90%

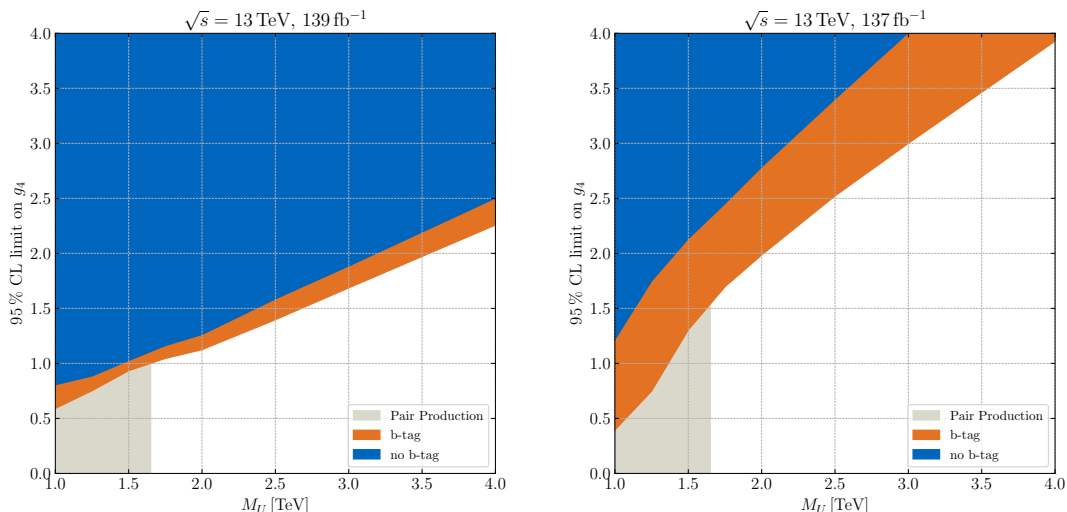


Figure 4.19: As Fig. 4.18 but using a recast of the results of the ATLAS [493] and CMS [455] ditau search in the left and right panel, respectively.

but degrades down to approximately 60% for $p_{T,b} > 500$ GeV. To remove DY background, an additional cut on the invariant mass m_{vis} of the visible tau decay products of $m_{\text{vis}} > 100$ GeV is applied. The scalar sum

$$S_T^{\text{MET}} = p_{T,\tau_1} + p_{T,\tau_2} + p_{T,j} + E_T^{\text{miss}}, \quad (4.54)$$

built from the transverse momenta p_{T,τ_1} and p_{T,τ_2} of the two τ candidates, the transverse momentum $p_{T,j}$ of the leading jet, and the missing transverse energy E_T^{miss} is used in the analysis [455] as a discriminating variable. Furthermore, two orthogonal event categories are constructed: one requires no b -jet with $p_{T,b} > 50$ GeV and another one requires at least one such jet.

The 95% CL exclusion bounds on the $M_U - g_4$ plane that follow from the recast of the ATLAS [493] and CMS [455] search are shown in the left and right panel of Fig. 4.19, respectively. For simplicity, we again employ $M_{G'} = M_U$ when determining the exclusion limits. Compared to the constraints depicted in Fig. 4.18, one observes that the difference between the no b -tag and b -tag bounds deriving from the considered ATLAS analysis is much smaller. This feature is readily understood by noticing that the ATLAS search, unlike the CMS analysis [454], does not see an excess in the high-mass m_T^{tot} distribution in the no b -tag category. In fact, ATLAS observes small deficits compared to the expected SM background in the tails of the m_T^{tot} spectra, which explains why for large values of M_U the 95% CL limits on g_4 , as shown in the left panel of Fig. 4.19, are notably better than those displayed in Fig. 4.18. To understand the shape of the exclusion limits following from the CMS search [455] presented on the

right-hand side in Fig. 4.19, one has to realize that the latter search observes a non-resonant excess with a significance of a bit more than 3σ above the SM expectation in the data. As a result, the obtained 95% CL limits in the M_U-g_4 plane turn out to be weaker than expected, particularly in the large mass regime.

4.4 Conclusion on Leptoquarks

In the previous two sections, Sect. 4.2 and Sect. 4.3, we have discussed dilepton production at the LHC mediated by scalar and vector LQs, respectively. We have refined the theoretical predictions by computing the virtual and real $\mathcal{O}(\alpha_s)$ corrections to the $pp \rightarrow \ell^+\ell^-$ process that can be described at the Born level by a simple t -channel exchange of an LQ (see Fig. 4.4). For both SLQs and VLQs we have not only considered real emission diagrams that occur due to the simple emission of a gluon from the tree-level diagram. We have also included resonant single-LQ contributions (see Fig. 4.3 on the right) that enhance the new-physics signal for smaller LQ couplings. Moreover, we computed the LO interference of the LQ exchange with the SM DY process. We have implemented all our analytical results into the POWHEG-BOX, developing an MC event generator that can be used by anyone interested in NLO+PS accurate predictions of $\ell^+\ell^-$ production at the LHC in models that include LQs. In both cases, we have demonstrated how the additional requirement of a b -tagged jet in the final state substantially improves the sensitivity to LQs coupling to third-generation quarks.

To be more precise, we have considered the S_1 and \tilde{S}_1 representations in Sect. 4.2. In this setting, we have additionally included the LQ correction to the EW vertex that alters the SM DY predictions, particularly at very high dilepton invariant masses. While our code allows us to generate events for all different couplings of the form of eq. (4.1), we have focused on the cases relevant for $b \rightarrow \mu$ and $b \rightarrow \tau$ flavor transitions in our analysis. This is motivated by the fact that in SLQ models capable of explaining the observed anomalies in semileptonic B -meson decays, the Yukawa couplings $Y_{b\mu}$ and $Y_{b\tau}$ are necessarily the largest. Moreover, in these scenarios, initial-state QCD radiation from the tree-level $b\bar{b}$ fusion will always lead to a larger amount of b -tagged events in which we are particularly interested.

We have recast the LHC Run II searches [454, 494, 496] in MadAnalysis 5, which allowed us to derive limits on SLQ masses and Yukawa couplings from roughly 140 fb^{-1} of pp collision data at $\sqrt{s} = 13 \text{ TeV}$. We have found that searches that require the events to have exactly one b -jet in addition to the $\ell^+\ell^-$ pair perform strikingly better than

fully exclusive or fully inclusive dilepton searches. The improvement in sensitivity is particularly important in the case of the $pp \rightarrow \mu^+\mu^-$ searches because the top and multijet background contributions to the b -tagged sample are less relevant compared to $pp \rightarrow \tau^+\tau^-$. Although we have presented only results for $pp \rightarrow \mu^+\mu^-$ in our work, the latter statement applies to $pp \rightarrow e^+e^-$ production as well. Additionally, we have provided analogous results for SLQs coupling to the lighter charm and strange quarks motivated by $\mathcal{R}_{K^{(*)}}$ and $\mathcal{R}_{D^{(*)}}$ anomalies. However, the improvement of the NLO calculation in these cases is limited compared to b couplings since b -jets can be identified more reliably, and we have a more precise understanding of the backgrounds for higher jet multiplicities.

As a final note, our POWHEG-BOX implementation also allows computing the DY forward-backward asymmetry A_{FB} , which can also be used to derive exclusion limits on LQ parameters [490, 535]. In this case, we have to disentangle all events with $\cos\theta > 0$ from the ones with $\cos\theta < 0$, where θ denotes the angle between the incoming quark and the outgoing negatively charged lepton in the Collins-Soper frame [536]. However, at a proton-proton collider like the LHC, a non-zero A_{FB} can only arise from the valence quarks but not the sea quarks. Since we have discussed only LQ processes initiated by heavy-quark fusion in this work, we have not studied the constraints that arise from A_{FB} . However, we emphasize that our MC implementation is able to calculate the first-generation scalar LQ contributions to A_{FB} including NLO QCD, EW, and interference effects. This summarizes the results obtained in the context of Ref. [2].

In Sect. 4.3, we studied the VLQ U_1 in the 4321 model with a very similar analysis. However, the calculation was performed using a different approach. Instead of using automated calculations enabled by FeynArts and FormCalc, we computed the 2- and 3-point amplitudes necessary for the renormalization at one-loop order in the strong coupling using Package-X directly. As a complication to the scalar case, proper calculations in the 4321 model required us to take into account the existence of additional $\text{SU}(3)_C$ colored degrees of freedom: the Goldstone bosons associated with the SSB of $\mathcal{G}_{4321} \rightarrow \mathcal{G}_{\text{SM}}$, the Faddeev-Popov ghosts from the extended non-abelian gauge group structure in Feynman gauge, and finally the massive gauge boson we refer to as coloron, whose interactions with the SM fermions have the exact same structure as those of SM gluons. All these more involved dynamics are needed to obtain consistent and unambiguous $\mathcal{O}(\alpha_s)$ corrections in the predictions for gauge VLQ models. Since the coupling structure in the 4321 model favors the U_1 to couple to τ leptons, we have focused on the case of VLQ mediated $\tau^+\tau^-$ production. The coupling hierarchy is mo-

tivated by the observation [220, 454, 460, 503, 505, 529, 530] that models explaining the charged-current $b \rightarrow c$ anomalies in general also predict enhanced $pp \rightarrow \tau^+\tau^-$ rates. We provided the first NLO QCD accurate results for ditau production in this setting. Moreover, our computation of the decay width of the LQ serves as an independent cross-check of the previously presented results from Ref. [518].

Phenomenologically, we studied not only the dependence of the predictions on the LQ mass and its couplings to SM fermions, but we also investigated the relevance of the coloron mass. The latter seems to yield minor corrections in the case of $M_{G'} \gtrsim M_U$. Besides QCD corrections, we have also studied the size of interference effects between the DY SM background and the LQ signature, finding that these effects are, in general, small in the SRs of the existing LHC DY ditau searches. Again, we implemented all our analytical results into the POWHEG-BOX, matching our fixed-order predictions consistently to the parton shower. Since the $\tau^+\tau^-$ production in this setting results from bottom-quark fusion, initial-state radiation always leads to an enhanced b -jet activity in the events, as was analogously discussed for third-generation scalar LQs. Devising search strategies with different b -jet categories is again expected to help improve the LHC sensitivity [2, 454, 455, 491–494, 506, 537–541]. To illustrate this point, we used our recast of Ref. [454] from our previous analysis that employs 138 fb^{-1} of pp data collected at $\sqrt{s} = 13 \text{ TeV}$. This analysis studies two disjoint SRs, and we found that the search strategy that requires the presence of an additional b -tagged jet consistently outperforms the search strategy that vetos b -jets. Using Ref. [454] together with our POWHEG-BOX implementation, we have finally derived NLO+PS accurate constraints on the masses and couplings of the 4321 model defined in eq. (4.22). Furthermore, we provided the constraints on the parameter space of third-generation singlet vector LQs that arise from the LHC Run II analyses [455, 493] of ditau production, confirming our phenomenological findings. This concludes the results obtained in the context of Ref. [3].

Both our SLQ and VLQ implementations into the POWHEG-BOX are publicly available on the project website of the POWHEG-BOX [30]. The presented MC event generators provide improved signal modeling compared to commonly used MadGraph generators, where the matching to the PS is performed using MLM merging [542]. By employing our code, a realistic exclusive description of DY dilepton processes in the SLQ and gauge singlet VLQ models at the level of hadronic events can be obtained without the introduction of an unphysical merging or matching scale. As a result, this should benefit future updates of exclusion limits such as given in Ref. [454] and everyone

interested in comparing accurate theory predictions of LQ models to LHC data. The same also applies to the signal generations used in the analyses [455, 493] in the $\tau^+\tau^-$ case. Therefore, our MC event generators represent essential tools for the ATLAS and CMS collaborations for their searches for scalar and gauge singlet vector LQs in ditau final states as well as general non-resonant light $\ell^+\ell^-$ searches for scalar LQs at future LHC runs.

5 Concluding Remarks

In this dissertation, we have examined the existing hints for BSM physics and how possible extensions of the SM may be tested at the LHC. The overarching focus of this study laid on models of pNGB DM that also solve the EW hierarchy problem. Moreover, in order to address the prevailing clues to LFU violation, we analyzed the phenomenology of LQs that generically emerge in the scalar and gauge sectors of GUTs.

We began with an introduction in Chap. 1, in which we gave historical examples of the progress in particle physics and the establishment of the SM. We emphasized the interplay of experiment and theory, driving predictions of novel particles toward their final discovery. Thus, we motivated the investigation of concrete BSM physics scenarios as an attempt to answer our open questions about the SM. Namely, we particularly scrutinized the lack of DM in the SM, the existing hints for LFU violation, and the hierarchy problem of EW theory, i.e., the naturalness of the Higgs mass. In the subsequent Chap. 2, we thoroughly formulated the SM as it has been known since the 1960s and further dwelled on its successes and shortcomings. The latter serve as a starting point for discussions about BSM models and how they can be tested at the LHC. Moreover, we gave a short review of GR and its connection to particle physics since our key motivation for the existence of DM is rooted in astrophysical and cosmological observations.

Chap. 3 summarized the findings of Ref. [1], which deals with pNGB DM. We argued that models, which also solve the EW hierarchy problem, can be constructed if both the SM Higgs boson and a possible DM candidate arise as composite pNGBs from a strongly-coupled sector at the TeV scale. This way, the smallness of the Higgs-boson mass is readily explained. In such a setting, the dominant interaction between the dark sector and the SM is given by a derivative Higgs coupling. Therefore, the model evades the strong constraints that are imposed on simpler DM models by direct detection experiments. In addition to the derivative Higgs portal, pNGB DM is expected to couple to the SM fermions proportional to the individual SM Yukawa couplings respecting the MFV paradigm. This is necessary for any generic scalar particle in addition to the SM

particle content to not conflict with the stringent limits on FCNCs. Hence, we studied the LHC prospects to produce pNGB DM in association with top quarks, concentrating on $t\bar{t} + E_T^{\text{miss}}$ and $tW + E_T^{\text{miss}}$ production, which we collectively denoted as $tX + E_T^{\text{miss}}$, as well as $j + E_T^{\text{miss}}$ production. We found that, in a general EFT for pNGB DM, the constraints derived from these mono- X searches are complementary to the limits from off-shell Higgs production in the VBF mode. This particularly applies if we allow for non-zero Yukawa-type and current-current type interactions of pNGB DM with top quarks. At the LHC, pNGB DM can further be tested by invisible Higgs decays. We both reproduced the previously known limits from the marginal and derivative Higgs portals and derived the loop-induced constraints on the Yukawa-type DM-top operator. For a comprehensive analysis, we also considered direct detection constraints posed by recent XENON1T data. While the derivative Higgs portal cannot be probed in any meaningful way, loop-induced interactions of pNGB DM with the SM gauge bosons represent a straightforward gateway to observe pNGB DM scatterings with atomic nuclei. Furthermore, we discussed DM annihilations into SM particles, guiding us toward examining s - and p -wave contributions to the observed DM relic abundance. The annihilation of pNGB DM into pairs of monochromatic photons allowed us to derive bounds from Fermi–LAT data on the DM-Higgs couplings in the vicinity of the Higgs pole, i.e., when $m_\chi \simeq m_h/2$. In conclusion, we consider pNGB DM a promising way to combine the correct description of the observed DM relic abundance with a solution of the naturalness problem of the Higgs mass without imposing Supersymmetry. The mono- X searches at the LHC by the ATLAS and CMS collaborations are essential for understanding such models.

In Chap. 4, we computed NLO corrections to $\ell^+\ell^-$ production via the non-resonant t -channel exchange of an LQ. We took into account both scalar and vector LQs by considering the S_1/\tilde{S}_1 and U_1 representations, respectively. In the scalar case, we calculated NLO QCD corrections, for instance, due to virtual gluons and real gluon radiation. Moreover, we computed the one-loop LQ corrections to the SM Drell–Yan process. In the vector case, we considered the U_1 LQ as realized in the 4321 model in order to consistently compute the $\mathcal{O}(\alpha_s)$ corrections to the gauge VLQ exchange. In this regard, we also needed to account for coloron contributions that arise at $\mathcal{O}(\alpha_s)$ in any viable model of gauge VLQs. In both cases, we also calculated the interference effects of the t -channel new-physics process with the SM s -channel dilepton production at the tree level. Motivated by the persisting anomaly in semi-leptonic $b \rightarrow c\tau^-\bar{\nu}_\tau$ decays, we focused on LQs coupling to heavy quark flavors. We observed that the discovery sensitivity at the LHC can be significantly increased by also requiring the presence of

a b -jet in the final state in addition to the dilepton pair. This is compatible with the findings already known in the context of EFT studies of the B -decay anomalies. For consistent modeling of the $\ell^+\ell^- + j$ final state, NLO accurate computations in QCD taking into account both resonant and non-resonant contributions are crucial. These dominate for small and large LQ masses, respectively. For both SLQs and VLQs, we implemented our analytical results into the POWHEG-BOX, making our codes publicly available. Therefore, we provided the community with a useful MC event generator for LQ associated $\ell^+\ell^-$ production with NLO+PS accuracy. The $\mathcal{R}_{K^{(*)}}$ anomaly may have ceased to exist with the updated LHCb analysis, but the $\mathcal{R}_{D^{(*)}}$ anomaly, the $(g-2)_\mu$ discrepancy, and the di-tau excess observed at CMS remain interesting cases for the presence of LQs. Independent of these experimental results, LQs generically belong to the particle content of any GUT unifying quarks and leptons. Thus, we are convinced that the interest in LQ phenomenology will prevail in the decades to come. This concludes the findings of Refs. [2, 3].

The projects described above represent fascinating paths to finding BSM particles at the LHC. Though, they only cover a small fraction of discovery opportunities, and the LHC research program entails many different models for particle DM, SUSY, and exotic particles in general. To this day, though, we lack any direct sign that there exist particles beyond the ones theorized within the SM. However, we have made clear that a variety of issues of the SM demands explanations that may be accompanied by novel particles. The LHC collaborations proceed with their mission to test the SM at unprecedented accuracy. At the time of writing, protons have been colliding at the LHC during its Run III since April 2022, and they will continue to do so until the end of 2023. During Run III, 300 fb^{-1} of proton collisions are expected to be collected. This means that, in this phase, more collision data is gathered than in Run I and Run II combined. In particular, the LHC is operated at the original target center-of-mass energy of 14 TeV for the first time. Afterwards, the Long Shutdown III will be used to further update the detector technology and prepare it for the high-luminosity (HL) upgrade of the LHC. In that era, planned from 2029 until the late 2030s, the LHC collaborations aspire to increase the integrated luminosity nine-fold to 3000 fb^{-1} . This will enable us to map the properties of SM particles with precision on a new level. We have discussed one concrete example in Sect. 3.6: the current upper bound on the branching fraction for invisible Higgs decays amounts to $\mathcal{B}(h \rightarrow \text{inv}) < 10.7\%$ [311], which will be improved at the HL-LHC to $\mathcal{B}(h \rightarrow \text{inv}) < 2.5\%$ [403]. Analogously to our pNGB DM treatment, this will significantly improve constraints on any light

enough BSM particle coupling to the SM Higgs boson. Precise measurements of the Higgs-boson mass, width, and Yukawa couplings are crucial tests for the SM, and any deviation might guide us to novel insights about what lies beyond it. Likewise, the measurement of the Higgs self-couplings, which are essential to our understanding of EWSB and the EW sector, have the potential to challenge our established picture of fundamental physics. The exact form of the Higgs potential is related to the stability of the EW vacuum and, to the best of our current knowledge, the SM lies at the edge of metastability (see, e.g., Ref. [543]). These considerations may direct us toward new physics coupling to the heavy SM particles like the Higgs boson or the top quark. Likewise, increasing precision in measurements with lighter particles is equally important. We have seen that the first signs of TeV-scale LQs may be non-resonant deviations in the high- p_T tails of dilepton systems. Investigating such signals requires large amounts of experimental data at high energies. Similarly, the increased amount of data from the HL-LHC will elucidate the $\mathcal{R}_{D^{(*)}}$ anomaly pointing toward new physics in the flavor sector. Concluding, we can look forward to the high-precision era at the HL-LHC, testing our most fundamental conception of nature.

The future of experimental particle physics after the HL-LHC is yet uncertain. The most popular ideas revolve around pushing at the energy frontier, meaning that the LHC might be upgraded to the High Energy LHC (HE-LHC) operating at center-of-mass energies $\mathcal{O}(30\text{ TeV})$. In a more distant future, a Future Circular Collider (FCC) might use the LHC as pre-accelerator and conduct proton-proton collisions at $\sqrt{s} \simeq 100\text{ TeV}$. At the energy frontier, we would be able to test the validity of the SM on uncharted territory. Whether we find BSM particles or not: we will consolidate our knowledge, gather valuable insights about the multi-TeV scale, and advance in technology. The SM may be "almost certainly the approximately correct description of the elementary particles and their interactions" [219]—but it shall not be the final answer on our quest for the deepest truths about the universe.

A Appendix

This appendix provides a few calculational details in order to clarify some of the points made in the main text of this thesis and to gather some of the formulae that were deployed.

A.1 The Dark Matter Relic Abundance and the WIMP Miracle

In this section, we want to provide the background of thermal relics in the early universe and what is commonly referred to as the WIMP miracle (see, e.g., Refs. [433,544] for more comprehensive introductions to the matter). Foundational to the cosmological Standard Model Λ CDM, which we touched upon in Sect. 2.2, is the validity of the cosmological principle, i.e., the homogeneity and isotropy of the universe on large distance scales. Figuratively, this means that the universe looks the same in every direction and from every point of view in the universe if we consider its energy, matter, and radiation distributions on a large scale. Respecting this cosmological principle, we can derive from Einstein's field equations (see eq. (2.18)) the Friedman–Lemaître–Robertson–Walker (FLRW) metric [545–549]

$$ds^2 = dt^2 - a(t)^2 \left(\frac{dr^2}{1 - kr^2} + r^2 d\Omega \right), \quad (\text{A.1})$$

employing spherical coordinates (r, Ω) , if we allow for spatial expansions and contractions of the universe. Here, we have introduced a curvature parameter $k \in \{-1, 0, 1\}$, where the different values describe negatively, flat, or positively curved spaces, respectively. Moreover, we introduced the possibly time-dependent scale factor $a(t)$, which parametrizes the spatial expansion and contraction of the universe. It proves useful to define the related Hubble parameter [550]

$$H(t) = \frac{\dot{a}(t)}{a(t)} \quad (\text{A.2})$$

for the description of the cosmological history and the accelerated expansion of the universe. Having these basic definitions at hand, we want to sketch the argument

that led to the notion of the WIMP miracle, which was the leading paradigm for DM phenomenology for many decades.

The theoretical appeal of WIMPs is usually justified by a numerical coincidence arising in the following cosmological considerations. Assume a DM agent χ is in thermal equilibrium with the SM bath in the early universe. The equilibrium is maintained by the DM annihilation and production processes

$$\chi\bar{\chi} \longleftrightarrow f\bar{f} . \quad (\text{A.3})$$

In general, following the arguments of Ref. [544], the time evolution of the phase space density $f(\mathbf{p}, \mathbf{x})$ of a particle species in equilibrium is described by the Boltzmann equation

$$\hat{L}[f] = \hat{C}[f] , \quad (\text{A.4})$$

where \hat{L} is the Liouville operator, and \hat{C} is the collision operator. Without going into details, the Boltzmann equation can be formulated explicitly for the particle number density n in an expanding universe as

$$\dot{n} + 3Hn = -\langle\sigma v\rangle \left(n^2 - (n^{\text{eq}})^2 \right) , \quad (\text{A.5})$$

with the thermal average of the total annihilation cross section σ multiplied by the velocity v . The equilibrium number density is denoted by n^{eq} . As the universe expands, the temperature decreases and particles do not interact efficiently enough to maintain thermal equilibrium. DM becomes a non-relativistic species and it cannot be produced efficiently anymore by SM particle interactions. The DM equilibrium density is Boltzmann suppressed for small temperatures, i.e.,

$$n^{\text{eq}} \propto \left(\frac{mT}{2\pi} \right)^{3/2} e^{-m/T} . \quad (\text{A.6})$$

Here, m denotes the mass of the particle, and T the temperature of the thermal bath. At the time of thermal decoupling, when $\Gamma_{\chi\chi\rightarrow f\bar{f}}(T_{\text{dec}}) = H(T_{\text{dec}})$, the increasing Hubble expansion rate exceeds the DM annihilation rate such that DM particles essentially do not participate in interactions anymore. DM has *frozen out*, and the exponential suppression of the number density has stopped. The Boltzmann equation can be used to infer the estimated dimensionless DM relic density [433]

$$\Omega_\chi h^2 \approx 0.12 \frac{x_{\text{dec}}}{28} \frac{\sqrt{g_{\text{eff}}}}{10} \frac{4 \cdot 10^{-9} \text{ GeV}^{-2}}{\langle\sigma_{\chi\chi} v\rangle} \approx 0.12 \frac{x_{\text{dec}}}{28} \frac{\sqrt{g_{\text{eff}}}}{10} \frac{2 \cdot 10^{-26} \text{ cm}^3/\text{s}}{\langle\sigma_{\chi\chi} v\rangle} . \quad (\text{A.7})$$

Here, g_{eff} is the effective number of active degrees of freedom. The entire SM particle content in thermal equilibrium corresponds to $g_{\text{eff}}(T > 175 \text{ GeV}) = 106.75$. Furthermore, $x_{\text{dec}} \equiv m_\chi/T_{\text{dec}}$ is the DM mass normalized by the temperature at the time of

decoupling, which is roughly of the order 20-30 for typical WIMP parameters. Finally, $\langle\sigma_{\chi\chi}v\rangle$ is the thermally averaged annihilation cross section of the WIMP into a pair of SM fermions. For instance, for a heavy DM agent with mass $m_\chi > m_Z$, one can estimate

$$\langle\sigma_{\chi\chi}v\rangle \approx \frac{g^4}{16\pi m_\chi^2} \quad (\text{A.8})$$

with a coupling constant g . Now, the PLANCK collaboration states the most recent result of a combined analysis for the DM relic density to be

$$\Omega_\chi h^2 = 0.120 \pm 0.001 \quad (\text{A.9})$$

in standard Λ CDM cosmology [279]. This implies that if we had

$$\langle\sigma_{\chi\chi}v\rangle \approx 4 \cdot 10^{-9} \text{ GeV}^{-2}, \quad (\text{A.10})$$

corresponding to

$$g^2 \approx \frac{m_\chi}{2.2 \text{ TeV}}, \quad (\text{A.11})$$

eq. (A.7) would yield the correct DM relic abundance. If we assume $g = \sqrt{4\pi\alpha} \approx 0.3$, which would be similar to electroweak interactions, then the DM mass would come out as roughly 200 GeV, which is also at the EW scale. This is what is usually meant by the WIMP miracle: a massive particle with mass at the EW scale interacting with SM fermions with EW-scale interactions produces the observed DM relic abundance.

From the considerations above and particularly from eq. (A.7), the crucial role of the thermally averaged annihilation cross section $\langle\sigma_{\chi\chi}v\rangle$ becomes evident. Exact formulas exist for how to compute this quantity, involving rather complicated kinematic integrals of cross sections and Bessel functions. A detailed discussion thereof, including relativistic corrections, can be found in Ref. [427], improving the previous work [551]. For our purposes, it suffices to apply the thermal expansion as stated in eq. (3.20). This boils down to computing the annihilation cross section using the commonly known S -matrix formalism from relativistic QFT and replacing the occurring Mandelstam variables for $\chi\chi \rightarrow f\bar{f}$ processes before phase-space integration according to

$$\begin{aligned} s &\simeq 4m_\chi^2 + m_\chi^2 v^2, \\ t &\simeq m_\chi^2 - \frac{1}{2}s \left(1 - \cos\theta \sqrt{1 - \frac{4m_\chi^2}{s}} \right), \\ u &\simeq m_\chi^2 - \frac{1}{2}s \left(1 + \cos\theta \sqrt{1 - \frac{4m_\chi^2}{s}} \right), \end{aligned} \quad (\text{A.12})$$

where we neglected the final state fermion mass (see also Ref. [426]). The result can then be expanded in the relative velocity v , and according to eq. (3.20), we can then read off the expansion coefficients a and b to find the relevant s - and p -wave contributions to the thermal average $\langle\sigma_{\chi\chi}v\rangle$. This summarizes the procedure to obtain the results stated in eqs. (3.21), (3.22), and (3.24).

A.2 The Direct Detection of Dark Matter

This section reconstructs the calculation of the spin-independent DM-nucleon cross section given in eq. (3.17). Ref. [300] serves as a central reference, which explains all the necessary steps to derive DM-nucleon cross sections as well as scattering cross sections with atomic nuclei as needed to derive exclusion limits on DM models from direct detection experiment data.

The non-relativistic (NR) expansion of the relevant interaction operators $\mathcal{L}_{\chi V}$ and $\mathcal{L}_{\chi qq}$ can be cast into the form

$$\mathcal{O}_{\text{NR}}^N = \sum_i f_i^N(q^2) \mathcal{O}_i^N, \quad (\text{A.13})$$

where f_i^N denotes, in principle, arbitrary functions of the squared momentum transfer q^2 as the expansion coefficient for every operator \mathcal{O}_i^N for a given nucleon N . Furthermore, \mathcal{O}_i^N denotes the NR building blocks onto which any relativistic operator can be mapped.¹ There are 16 independent operators \mathcal{O}_i^N , but in our case, only the simplest one is relevant, namely the identity element

$$\mathcal{O}_1^N = \mathbf{1}. \quad (\text{A.14})$$

Table A.1 summarizes how to translate the relativistic operators in $\mathcal{L}_{\chi V}$ and $\mathcal{L}_{\chi qq}$ in eqs. (3.13) and (3.15) into NR operators. With the replacement rules given there, we only need to consider the effective couplings $f_{T_q}^{(N)}$ and $f_{T_G}^{(N)}$ of a nucleon N , which parametrize each parton's contribution to the mass of the nucleon. The latter can be computed by means of lattice QCD and the relevant numerical values are given in the main text of this dissertation.

The NR operator in eq. (A.13) can be used to construct an effective DM-nucleon Lagrangian, which can be expressed for spin-0 DM particles as

$$\mathcal{L}_N = \frac{1}{2N} \mathcal{O}_{\text{NR}}^N \chi^* \chi \bar{N} \gamma^0 N \quad (\text{A.15})$$

¹Note that we only consider spin-independent interactions and neglect any transverse-velocity dependent operators.

EFT operator	NR operator
$\chi^* \chi q \bar{q}$	$2 \frac{m_N^2}{m_q} f_{Tq}^{(N)} \mathcal{O}_1^N$
$\frac{\alpha_s}{12\pi} \chi^* \chi G_{\mu\nu}^a G^{a\mu\nu}$	$-\frac{4}{27} m_N^2 f_{TG}^{(N)} \mathcal{O}_1^N$
$-\frac{i}{6} e \left(\chi^* \overleftrightarrow{\partial}_\mu \chi \right) \partial^\nu F_{\mu\nu}$	$\frac{4}{6} m_\chi m_N e^2 Q_N \mathcal{O}_1^N$

Table A.1: Assignment of non-relativistic operators to the pNGB DM effective field theory operators relevant for direct detection experiments. All operators are even under parity transformations and time reversal and the only necessary basis element of NR operators is the identity element $\mathcal{O}_1 = \mathbf{1}$.

with the nucleon number density operator N . This, in turn, can be used to define the effective DM interaction Lagrangian with the target nucleus T according to

$$\mathcal{L}_T = \sum_{N \in \{p,n\}} \sum_i \mathcal{L}_{N_i}, \quad (\text{A.16})$$

where the sum over i sums over all nucleons of species N_i , and n and p denote neutrons and protons, respectively. With this Lagrangian, we can derive formulae for cross sections using conventional S -matrix scattering formalism. The experimental collaborations usually provide their exclusion limits on the spin-independent cross section under the isosinglet condition $f_p = f_n$, i.e., not distinguishing between protons and neutrons. It can be shown that we can write it differentially as

$$\frac{d\sigma_T}{dE_R} \stackrel{\text{NR}}{=} \frac{m_T}{2\mu_N^2 v^2} \sigma_p A^2 F_{\text{SI}}^2(E_R). \quad (\text{A.17})$$

Here, $\mu_N = \frac{m_\chi m_N}{m_\chi + m_N}$ is the reduced DM-nucleon mass, $m_N = \frac{m_p + m_n}{2} \approx 939$ MeV is the average nucleon mass, A is the atomic number, and m_T is the mass of the target nucleus. Furthermore, F_{SI} denotes the nuclear form factor, parametrizing the structure of the target nucleus as a function of the recoil energy $E_R = q^2/(2m_T)$. Assuming the form factor to be equal to one would correspond to assuming a point-like nucleus. In our consideration, the isosinglet condition does not appear to be a valid assumption since we take into account the electromagnetic interaction $\sim F_{\mu\nu}$ in $\mathcal{L}_{\chi V}$, which clearly affects protons more strongly than neutrons. In general, the DM-nucleus cross section is defined as

$$\frac{d\sigma_T}{dE_R} \stackrel{\text{NR}}{=} \frac{m_T}{2\pi v^2} (Z f_p + (A - Z) f_n)^2 F_{\text{SI}}^2(E_R). \quad (\text{A.18})$$

Setting the two above equations equal, we find the DM-nucleon cross section, which we want to constrain, as

$$\sigma_p = \frac{\mu_N^2}{\pi} \frac{1}{A^2} (Z f_p + (A - Z) f_n)^2, \quad (\text{A.19})$$

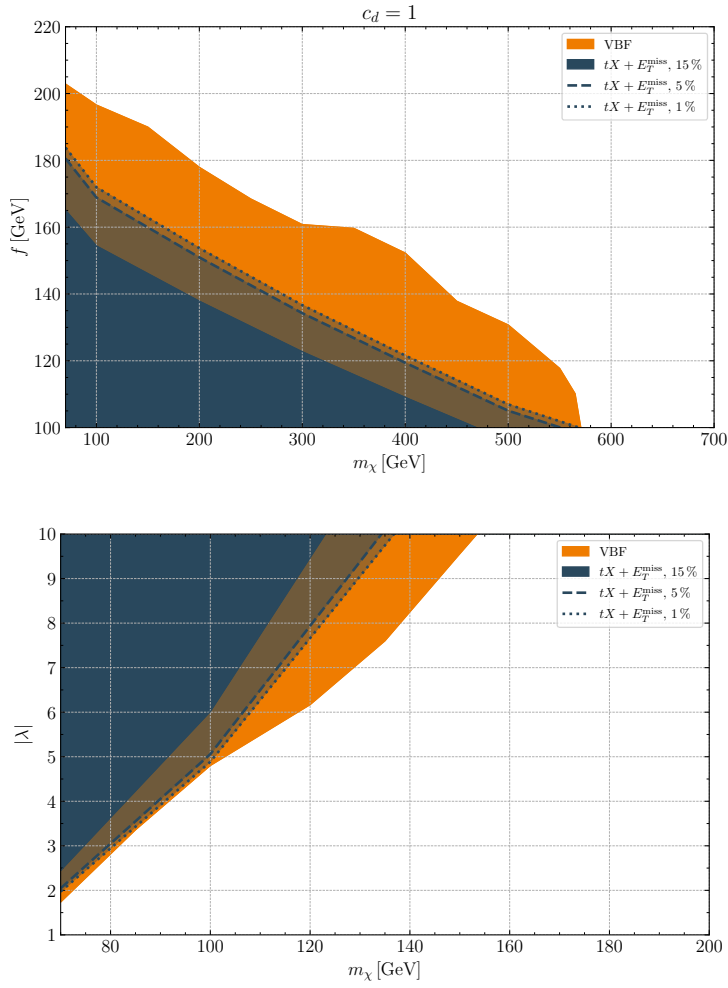


Figure A.1: 95 % CL constraints in the m_χ - f plane for the derivative Higgs portal model (upper panel) and in the m_χ - $|\lambda|$ plane for the marginal Higgs portal model (lower panel). The orange regions correspond to the 95 % CL exclusion limits determined in [319] from an HL-LHC study of off-shell invisible Higgs production in the VBF channel, while the dark blue contours represent the results of our $tX + E_T^{\text{miss}}$ search assuming a systematic background uncertainty of 15 % (solid curves), 5 % (dashed curves), and 1 % (dotted curves).

which can be interpreted as weighted average of nucleons over the contents of the target nucleus. With this formula, by inserting the relevant functions f_N for our NR operators, we immediately arrive at the result stated in the main text in eq. (3.17).

A.3 Systematic Errors for the Higgs Portal Operators of pNGB DM

In this appendix, we present HL-LHC projections based on alternative more aggressive assumptions about the systematic uncertainties of our $tX + E_T^{\text{miss}}$ search strategy. Anticipating improvements in detector performance and modeling of SM background processes, we assume that the systematic uncertainties on the number of expected events in the signal regions SR1, SR2, and SR3 are reduced from 15% to 5% and 1%. In Fig. A.1, we show the 95% CL constraints in the m_χ - f plane for the derivative Higgs portal model (upper panel) and in the m_χ - $|\lambda|$ plane for the marginal Higgs portal model (lower panel). The orange regions indicate the exclusion limits derived in the study of off-shell invisible Higgs production in the VBF channel [319]. The displayed results assume a 1% systematic uncertainty on the relevant SM backgrounds. For comparison, we show in dark blue the 95% CL limits that derive from the $tX + E_T^{\text{miss}}$ search strategy discussed in Sect. 3.4.1. Here the solid, dashed, and dotted contours correspond to assumed systematic background uncertainties of 15%, 5%, and 1%, respectively. It is evident from both panels that reducing the systematic uncertainties from 15% to 5% has a visible impact on the obtained $tX + E_T^{\text{miss}}$ exclusion limits, while a further uncertainty reduction to 1% has only a minor effect on the bounds in the shown parameter planes. Notice that a reduction of the systematic uncertainties to 5% may be possible given the steady progress of both experiment and theory. In the case of the marginal Higgs portal, such an improvement would lead to a reach in the $tX + E_T^{\text{miss}}$ channel that is very similar to the one of VBF invisible Higgs production in the off-shell region.

A.4 Ditau Production from Z' Exchange

In this appendix, we study the possible impact of Z' exchange in DY ditau production. Following Ref. [505], we parametrize the interactions between the color singlet state $Z' \sim (\mathbf{1}, \mathbf{1}, 0)$ that appears in the spectrum of the 4321 model after spontaneous symmetry breaking and the SM fermions by

$$\mathcal{L}_{Z'} \supset \frac{g_{Z'}}{2\sqrt{6}} \left[\sum_{q=Q,u,d} \zeta_q^{ij} \bar{q}^i \gamma_\mu q^j - 3 \sum_{\ell=L,e} \zeta_\ell^{ij} \bar{\ell}^i \gamma_\mu \ell^j \right] Z'^\mu, \quad (\text{A.20})$$

where $g_{Z'}$ represents the overall coupling strength of the new neutral gauge boson to SM matter fields, while ζ_ψ^{ij} with $\psi = Q, u, d, L, e$ are 3×3 matrices in flavor space. The

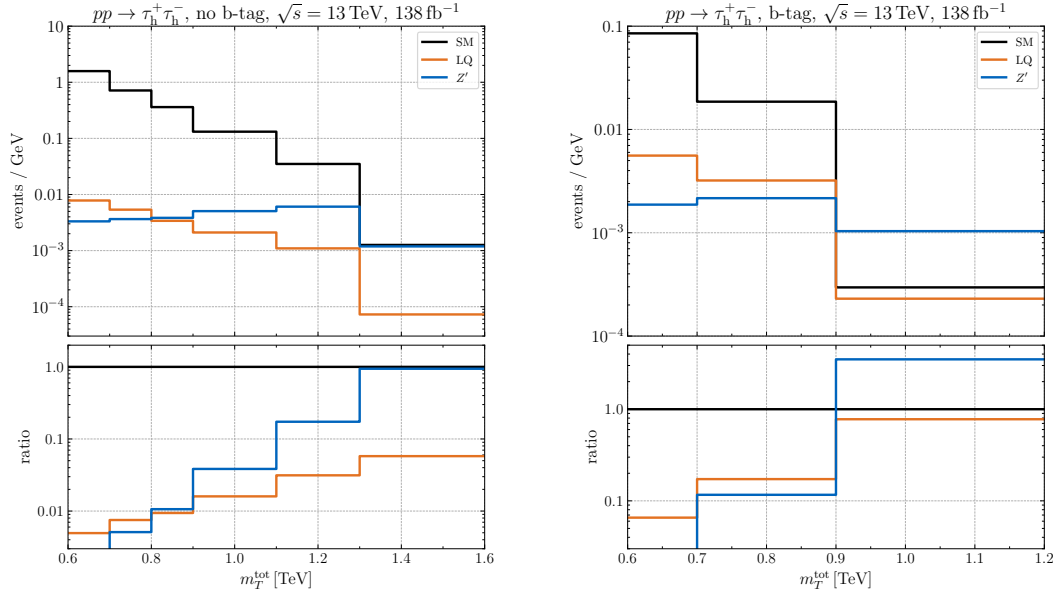


Figure A.2: As Fig. 4.17 but comparing a LQ and a Z' signal hypothesis. The black curves correspond to the SM expectations of the DY background provided by CMS in the publication [454]. The orange curves represent the LQ NLO predictions assuming $g_4 = 1$, $M_U = 2$ TeV and $M_{G'} = 2$ TeV, while the blue histograms illustrate the LO Z' predictions for $g'_{Z'} = 1$ and $M_{Z'} = 2$ TeV. Further details such as the choice of the flavor-dependent Z' -boson couplings ζ_{ψ}^{ij} can be found in the main text.

observed semi-leptonic B -decay anomalies can naturally be fulfilled for $g_{Z'} = \mathcal{O}(1)$ and $|\zeta_{\psi}^{33}| = \mathcal{O}(1)$, while the remaining flavor-dependent couplings can be small or vanish.

In Fig. A.2, we display m_T^{tot} distributions assuming an LQ and a Z' signal hypothesis. For comparison, the SM expectations of the DY background taken from Ref. [454] are also shown as black histograms. Details on the CMS search and our analysis chain can be found at the beginning of Sect. 4.3.5. The orange curves are the LQ NLO predictions obtained using our POWHEG-BOX code and they employ the parameter choices $g_4 = 1$, $M_U = 2$ TeV, and $M_{G'} = 2$ TeV. The Z' predictions have instead been obtained at LO using MadGraph together with the implementation of eq. (A.20) provided in the article [505]. Our Z' -boson event samples correspond to $g'_{Z'} = 1$, $\zeta_{\psi}^{33} = 1$, and $M_{Z'} = 2$ TeV, while setting all remaining flavor-dependent couplings ζ_{ψ}^{ij} to zero. From both panels, one observes that the m_T^{tot} spectra of the Z' signal are on average harder than the distributions resulting from LQ exchange. This is expected because the Z' signal arises from s -channel exchange, while the LQ contributions are dominantly associated to t -channel scattering. It is also evident that a simple cut-and-count analysis based on the observable m_T^{tot} will only have limited power to distinguish between an LQ and a

Z' hypothesis. Multivariate discriminants that incorporate the event kinematics of the selected ditau events in both the no b -tag and the b -tag category are likely to enhance the sensitivity to different realizations of the 4321 model. A dedicated analysis of this issue is, however, clearly beyond the scope of this appendix.

Bibliography

- [1] U. Haisch, G. Polesello and S. Schulte, *Searching for pseudo Nambu-Goldstone boson dark matter production in association with top quarks*, *JHEP* **09** (2021) 206 [[2107.12389](#)].
- [2] U. Haisch, L. Schnell and S. Schulte, *On Drell-Yan production of scalar leptoquarks coupling to heavy-quark flavours*, *JHEP* **11** (2022) 106 [[2207.00356](#)].
- [3] U. Haisch, L. Schnell and S. Schulte, *Drell-Yan production in third-generation gauge vector leptoquark models at NLO+PS in QCD*, *JHEP* **02** (2023) 70 [[2209.12780](#)].
- [4] F. Kahlhoefer, A. Mück, S. Schulte and P. Tunney, *Interference effects in dilepton resonance searches for Z' bosons and dark matter mediators*, *JHEP* **03** (2020) 104 [[1912.06374](#)].
- [5] M.E. Peskin and D.V. Schroeder, *An Introduction to quantum field theory*, Addison-Wesley, Reading, USA (1995).
- [6] R.K. Ellis, W.J. Stirling and B.R. Webber, *QCD and Collider Physics*, vol. 8, Cambridge University Press (2011).
- [7] M.D. Schwartz, *Quantum Field Theory and the Standard Model*, Cambridge University Press (2014).
- [8] S. Weinberg, *Gravitation and Cosmology: Principles and Applications of the General Theory of Relativity*, John Wiley and Sons, New York (1972).
- [9] C.W. Misner, K.S. Thorne and J.A. Wheeler, *Gravitation*, W. H. Freeman, San Francisco (1973).
- [10] S.M. Carroll, *Lecture Notes on General Relativity*, [[gr-qc/9712019](#)].
- [11] S. Weinberg, *Cosmology*, Oxford University Press (2008).
- [12] P.A. Zyla et al. (Particle Data Group), *Review of Particle Physics*, *Prog.Theor.Exp.Phys.* **2020** (2020) 083C01.
- [13] R.L. Workman et al. (Particle Data Group), *Review of Particle Physics*, *Prog.Theor.Exp.Phys.* **2022** (2022) 083C01.

- [14] T. Hahn, *Generating Feynman diagrams and amplitudes with FeynArts 3*, *Comput. Phys. Commun.* **140** (2001) 418 [[hep-ph/0012260](#)].
- [15] T. Hahn and M. Pérez-Victoria, *Automated one-loop calculations in four and D dimensions*, *Comput. Phys. Commun.* **118** (1999) 153 [[hep-ph/9807565](#)].
- [16] H.H. Patel, *Package-X: A Mathematica package for the analytic calculation of one-loop integrals*, *Comput. Phys. Commun.* **197** (2015) 276 [[1503.01469](#)].
- [17] H.H. Patel, *Package-X 2.0: A Mathematica package for the analytic calculation of one-loop integrals*, *Comput. Phys. Commun.* **218** (2017) 66 [[1612.00009](#)].
- [18] R. Mertig, M. Böhm and A. Denner, *Feyn Calc – Computer-algebraic calculation of Feynman amplitudes*, *Comput. Phys. Commun.* **64** (1991) 345.
- [19] V. Shtabovenko, R. Mertig and F. Orellana, *New developments in FeynCalc 9.0*, *Comput. Phys. Commun.* **207** (2016) 432 [[1601.01167](#)].
- [20] V. Shtabovenko, R. Mertig and F. Orellana, *FeynCalc 9.3: New features and improvements*, *Comput. Phys. Commun.* **256** (2020) 107478 [[2001.04407](#)].
- [21] C. Degrande et al., *UFO - The Universal FEYNRULES Output*, *Comput. Phys. Commun.* **183** (2012) 1201 [[1108.2040](#)].
- [22] N.D. Christensen and C. Duhr, *FeynRules - Feynman rules made easy*, *Comput. Phys. Commun.* **180** (2009) 1614 [[0806.4194](#)].
- [23] A. Alloul et al., *FEYNRULES 2.0 — A complete toolbox for tree-level phenomenology*, *Comput. Phys. Commun.* **185** (2014) 2250 [[1310.1921](#)].
- [24] J. Alwall et al., *The automated computation of tree-level and next-to-leading order differential cross sections, and their matching to parton shower simulations*, *JHEP* **07** (2014) 79 [[1405.0301](#)].
- [25] P. Artoisenet, R. Frederix, O. Mattelaer and R. Rietkerk, *Automatic spin-entangled decays of heavy resonances in Monte Carlo simulations*, *JHEP* **03** (2013) 15 [[1212.3460](#)].
- [26] P. Nason, *A new method for combining NLO QCD with shower Monte Carlo algorithms*, *JHEP* **11** (2004) 040 [[hep-ph/0409146](#)].
- [27] S. Frixione, P. Nason and C. Oleari, *Matching NLO QCD computations with parton shower simulations: the POWHEG method*, *JHEP* **11** (2007) 70 [[0709.2092](#)].
- [28] S. Alioli, P. Nason, C. Oleari and E. Re, *A general framework for implementing NLO calculations in shower Monte Carlo programs: the POWHEG BOX*, *JHEP* **06** (2010) 43 [[1002.2581](#)].

-
- [29] S. Alioli, P. Nason, C. Oleari and E. Re, *The POWHEG BOX user manual: common features*, 2011.
- [30] S. Alioli et al., “[The POWHEG BOX.](#)”
- [31] A. Buckley et al., *LHAPDF6: parton density access in the LHC precision era*, *Eur. Phys. J. C* **75** (2015) 132 [[1412.7420](#)].
- [32] J. Alwall et al., *A Standard format for Les Houches Event Files*, *Comput. Phys. Commun.* **176** (2007) 300 [[hep-ph/0609017](#)].
- [33] T. Sjöstrand, S. Mrenna and P.Z. Skands, *PYTHIA 6.4 physics and manual*, *JHEP* **05** (2006) 26 [[hep-ph/0603175](#)].
- [34] T. Sjostrand, S. Mrenna and P.Z. Skands, *A brief introduction to PYTHIA 8.1*, *Comput. Phys. Commun.* **178** (2008) 852 [[0710.3820](#)].
- [35] T. Sjöstrand et al., *An introduction to PYTHIA 8.2*, *Comput. Phys. Commun.* **191** (2015) 159 [[1410.3012](#)].
- [36] M. Dobbs and J.B. Hansen, *The HepMC C++ Monte Carlo event record for High Energy Physics*, *Comput. Phys. Commun.* **134** (2001) 41.
- [37] E. Conte, B. Fuks and G. Serret, *MADANALYSIS5, a user-friendly framework for collider phenomenology*, *Comput. Phys. Commun.* **184** (2013) 222 [[1206.1599](#)].
- [38] E. Conte, B. Dumont, B. Fuks and C. Wymant, *Designing and recasting LHC analyses with MADANALYSIS 5*, *Eur. Phys. J. C* **74** (2014) 3103 [[1405.3982](#)].
- [39] B. Dumont et al., *Toward a public analysis database for LHC new physics searches using MADANALYSIS 5*, *Eur. Phys. J. C* **75** (2015) 56 [[1407.3278](#)].
- [40] E. Conte and B. Fuks, *Confronting new physics theories to LHC data with MADANALYSIS 5*, *Int. J. Mod. Phys. A* **33** (2018) 1830027 [[1808.00480](#)].
- [41] J.Y. Araz, M. Frank and B. Fuks, *Reinterpreting the results of the LHC with MADANALYSIS 5: uncertainties and higher-luminosity estimates*, *Eur. Phys. J. C* **80** (2020) 531 [[1910.11418](#)].
- [42] J.Y. Araz, B. Fuks and G. Polykratis, *Simplified fast detector simulation in MADANALYSIS 5*, *Eur. Phys. J. C* **81** (2021) 329 [[2006.09387](#)].
- [43] M. Drees et al., *CheckMATE: Confronting your favourite new physics model with LHC data*, *Comput. Phys. Commun.* **187** (2015) 227 [[1312.2591](#)].
- [44] J.S. Kim, D. Schmeier, J. Tattersall and K. Rolbiecki, *A framework to create customised LHC analyses within CheckMATE*, *Comput. Phys. Commun.* **196** (2015) 535 [[1503.01123](#)].

- [45] D. Dercks et al., *CheckMATE 2: From the model to the limit*, *Comput. Phys. Commun.* **221** (2017) 383 [[1611.09856](#)].
- [46] M. Cacciari and G.P. Salam, *Dispelling the N^3 myth for the k_t jet-finder*, *Phys. Lett. B* **641** (2006) 57 [[hep-ph/0512210](#)].
- [47] M. Cacciari, G.P. Salam and G. Soyez, *FastJet user manual*, *Eur. Phys. J. C* **72** (2012) 1896 [[1111.6097](#)].
- [48] J. de Favereau et al. (The DELPHES 3 Collaboration), *DELPHES 3: a modular framework for fast simulation of a generic collider experiment*, *JHEP* **02** (2014) 57 [[1307.6346](#)].
- [49] G. Bélanger et al., *micrOMEGAs5.0 : Freeze-in*, *Comput. Phys. Commun.* **231** (2018) 173 [[1801.03509](#)].
- [50] A. Belyaev, N.D. Christensen and A. Pukhov, *CalcHEP 3.4 for collider physics within and beyond the Standard Model*, *Comput. Phys. Commun.* **184** (2013) 1729 [[1207.6082](#)].
- [51] R.V. Harlander, S.Y. Klein and M. Lipp, *FeynGame*, *Comput. Phys. Commun.* **256** (2020) 107465 [[2003.00896](#)].
- [52] A. Einstein, *Zur Elektrodynamik bewegter Körper*, *Ann. Phys.* **322** (1905) 891.
- [53] P.A.M. Dirac, *The quantum theory of the electron*, *Proc. Roy. Soc. Lond. A* **117** (1928) 610.
- [54] P.A.M. Dirac, *A Theory of Electrons and Protons*, *Proc. Roy. Soc. Lond. A* **126** (1930) 360.
- [55] P.A.M. Dirac, *Quantised singularities in the electromagnetic field*, *Proc. Roy. Soc. Lond. A* **133** (1931) 60.
- [56] C.D. Anderson, *The Positive Electron*, *Phys. Rev.* **43** (1933) 491.
- [57] S. Laporta, *High-precision calculation of the 4-loop contribution to the electron $g-2$ in QED*, *Phys. Lett. B* **772** (2017) 232 [[1704.06996](#)].
- [58] D. Hanneke, S. Fogwell and G. Gabrielse, *New Measurement of the Electron Magnetic Moment and the Fine Structure Constant*, *Phys. Rev. Lett.* **100** (2008) 120801.
- [59] W. Pauli, *Dear radioactive ladies and gentlemen*, *Phys. Today* **31N9** (1978) 27.
- [60] F. Reines and C.L. Cowan, *Detection of the Free Neutrino*, *Phys. Rev.* **92** (1953) 830.
- [61] C.L. Cowan et al., *Detection of the Free Neutrino: a Confirmation*, *Science* **124** (1956) 103.
- [62] F. Reines and C.L. Cowan, *The Neutrino*, *Nature* **178** (1956) 446.

-
- [63] S.L. Glashow, J. Iliopoulos and L. Maiani, *Weak Interactions with Lepton-Hadron Symmetry*, *Phys. Rev. D* **2** (1970) 1285.
- [64] J.E. Augustin et al., *Discovery of a Narrow Resonance in e^+e^- Annihilation*, *Phys. Rev. Lett.* **33** (1974) 1406.
- [65] J.J. Aubert et al., *Experimental Observation of a Heavy Particle J* , *Phys. Rev. Lett.* **33** (1974) 1404.
- [66] J.H. Christenson, J.W. Cronin, V.L. Fitch and R. Turlay, *Evidence for the 2π Decay of the K_2^0 Meson*, *Phys. Rev. Lett.* **13** (1964) 138.
- [67] N. Cabibbo, *Unitary Symmetry and Leptonic Decays*, *Phys. Rev. Lett.* **10** (1963) 531.
- [68] M. Kobayashi and T. Maskawa, *CP-Violation in the Renormalizable Theory of Weak Interaction*, *Prog. Theor. Phys.* **49** (1973) 652.
- [69] S.W. Herb et al., *Observation of a Dimuon Resonance at 9.5 GeV in 400-GeV Proton-Nucleus Collisions*, *Phys. Rev. Lett.* **39** (1977) 252.
- [70] F. Abe et al. (The CDF Collaboration), *Observation of Top Quark Production in $\bar{p}p$ Collisions with the Collider Detector at Fermilab*, *Phys. Rev. Lett.* **74** (1995) 2626 [[hep-ex/9503002](#)].
- [71] S. Abachi et al. (The DØ Collaboration), *Observation of the Top Quark*, *Phys. Rev. Lett.* **74** (1995) 2632 [[hep-ex/9503003](#)].
- [72] S.L. Adler, *Axial-Vector vertex in Spinor Electrodynamics*, *Phys. Rev.* **177** (1969) 2426.
- [73] J.S. Bell and R. Jackiw, *A PCAC puzzle: $\pi^0 \rightarrow \gamma\gamma$ in the σ -model*, *Nuovo Cim. A* **60** (1969) 47.
- [74] M.L. Perl et al., *Evidence for Anomalous Lepton Production in $e^+ - e^-$ Annihilation*, *Phys. Rev. Lett.* **35** (1975) 1489.
- [75] P.W. Higgs, *Broken symmetries, massless particles and gauge fields*, *Phys. Lett.* **12** (1964) 132.
- [76] P.W. Higgs, *Broken Symmetries and the Masses of Gauge Bosons*, *Phys. Rev. Lett.* **13** (1964) 508.
- [77] P.W. Higgs, *Spontaneous Symmetry Breakdown without Massless Bosons*, *Phys. Rev.* **145** (1966) 1156.
- [78] F. Englert and R. Brout, *Broken Symmetry and the Mass of Gauge Vector Mesons*, *Phys. Rev. Lett.* **13** (1964) 321.
- [79] G.S. Guralnik, C.R. Hagen and T.W.B. Kibble, *Global Conservation Laws and Massless Particles*, *Phys. Rev. Lett.* **13** (1964) 585.

- [80] S.L. Glashow, *Partial-symmetries of weak interactions*, *Nucl. Phys.* **22** (1961) 579.
- [81] A. Salam, *Weak and electromagnetic interactions*, *Conf. Proc. C* **680519** (1968) 367.
- [82] S. Weinberg, *A Model of Leptons*, *Phys. Rev. Lett.* **19** (1967) 1264.
- [83] F.J. Hasert et al. (The Gargamelle Collaboration), *Observation of neutrino-like interactions without muon or electron in the gargamelle neutrino experiment*, *Phys. Lett. B* **46** (1973) 138.
- [84] F.J. Hasert et al., *Search for elastic muon-neutrino electron scattering*, *Phys. Lett. B* **46** (1973) 121.
- [85] F.J. Hasert et al. (The Gargamelle Collaboration), *Observation of neutrino-like interactions without muon or electron in the Gargamelle neutrino experiment*, *Nucl. Phys. B* **73** (1974) 1.
- [86] G. Arnison et al. (The UA1 Collaboration), *Experimental observation of isolated large transverse energy electrons with associated missing energy at $\sqrt{s} = 540$ GeV*, *Phys. Lett. B* **122** (1983) 103.
- [87] G. Arnison et al., *Experimental observation of lepton pairs of invariant mass around 95 GeV/c² at the CERN SPS collider*, *Phys. Lett. B* **126** (1983) 398.
- [88] G. Arnison et al. (The UA1 Collaboration), *Further evidence for charged intermediate vector bosons at the SPS collider*, *Phys. Lett. B* **129** (1983) 273.
- [89] M. Banner et al. (The UA2 Collaboration), *Observation of single isolated electrons of high transverse momentum in events with missing transverse energy at the CERN $\bar{p}p$ collider*, *Phys. Lett. B* **122** (1983) 476.
- [90] P. Bagnaia et al. (The UA2 Collaboration), *Evidence for $Z^0 \rightarrow e^+e^-$ at the CERN $\bar{p}p$ Collider*, *Phys. Lett. B* **129** (1983) 130.
- [91] G. 't Hooft, *Renormalization of massless Yang-Mills fields*, *Nucl. Phys. B* **33** (1971) 173.
- [92] G. 't Hooft, *Renormalizable Lagrangians for massive Yang-Mills fields*, *Nucl. Phys.* **B35** (1971) 167.
- [93] G. 't Hooft and M.J.G. Veltman, *Regularization and renormalization of gauge fields*, *Nucl. Phys.* **B44** (1972) 189.
- [94] S.D. Bass, A. De Roeck and M. Kado, *The Higgs boson implications and prospects for future discoveries*, *Nat. Rev. Phys.* **3** (2021) 608 [2104.06821].
- [95] B.W. Lee, C. Quigg and H.B. Thacker, *Strength of Weak Interactions at Very High Energies and the Higgs Boson Mass*, *Phys. Rev. Lett.* **38** (1977) 883.

-
- [96] B.W. Lee, C. Quigg and H.B. Thacker, *Weak interactions at very high energies: The role of the Higgs-Boson mass*, *Phys. Rev. D* **16** (1977) 1519.
- [97] The LEP Collaborations ALEPH, DELPHI, L3, OPAL, and the LEP Electroweak Working Group, *A Combination of preliminary electroweak measurements and constraints on the standard model*, [[hep-ex/0612034](#)].
- [98] G. Aad et al. (The ATLAS Collaboration), *Observation of a new particle in the search for the Standard Model Higgs boson with the ATLAS detector at the LHC*, *Phys. Lett. B* **716** (2012) 1 [[1207.7214](#)].
- [99] S. Chatrchyan et al. (The CMS Collaboration), *Observation of a new boson at a mass of 125 GeV with the CMS experiment at the LHC*, *Phys. Lett. B* **716** (2012) 30 [[1207.7235](#)].
- [100] S. Chatrchyan et al. (The CMS Collaboration), *Study of the Mass and Spin-Parity of the Higgs Boson Candidate via Its Decays to Z Boson Pairs*, *Phys. Rev. Lett.* **110** (2013) 81803 [[1212.6639](#)].
- [101] V. Khachatryan et al. (The CMS Collaboration), *Constraints on the spin-parity and anomalous HVV couplings of the Higgs boson in proton collisions at 7 and 8 TeV*, *Phys. Rev. D* **92** (2015) 12004 [[1411.3441](#)].
- [102] G. Aad et al. (The ATLAS Collaboration), *Evidence for the spin-0 nature of the Higgs boson using ATLAS data*, *Phys. Lett. B* **726** (2013) 120 [[1307.1432](#)].
- [103] A.M. Sirunyan et al. (The CMS Collaboration), *Evidence for Higgs boson decay to a pair of muons*, *JHEP* **01** (2021) 148 [[2009.04363](#)].
- [104] J. Ellis, *SMEFT Constraints on New Physics Beyond the Standard Model*, [[2105.14942](#)].
- [105] M. Aaboud et al. (The ATLAS Collaboration), *Search for resonances in diphoton events at $\sqrt{s}=13$ TeV with the ATLAS detector*, *JHEP* **09** (2016) 1 [[1606.03833](#)].
- [106] V. Khachatryan et al. (The CMS Collaboration), *Search for Resonant Production of High-Mass Photon Pairs in Proton-Proton Collisions at $\sqrt{s} = 8$ and 13 TeV*, *Phys. Rev. Lett.* **117** (2016) 51802 [[1606.04093](#)].
- [107] V. Khachatryan et al. (The CMS Collaboration), *Search for high-mass diphoton resonances in proton-proton collisions at 13 TeV and combination with 8 TeV search*, *Phys. Lett. B* **767** (2017) 147 [[1609.02507](#)].
- [108] M. Aaboud et al. (The ATLAS Collaboration), *Search for new phenomena in high-mass diphoton final states using 37 fb^{-1} of proton-proton collisions collected at $\sqrt{s} = 13$ TeV with the ATLAS detector*, *Phys. Lett. B* **775** (2017) 105 [[1707.04147](#)].
- [109] The LHCb collaboration, *Test of lepton universality in $b \rightarrow s \ell^+ \ell^-$ decays*, [[2212.09152](#)].

- [110] The LHCb collaboration, *Measurement of lepton universality parameters in $B^+ \rightarrow K^+\ell^+\ell^-$ and $B^0 \rightarrow K^{*0}\ell^+\ell^-$ decays*, [[2212.09153](#)].
- [111] A. Einstein, *Zur Allgemeinen Relativitätstheorie*, *Sitzungsber. Preuss. Akad. Wiss. Berlin (Math. Phys.)* **1915** (1915) 778.
- [112] A. Einstein, *Die Feldgleichungen der Gravitation*, *Sitzungsber. Preuss. Akad. Wiss. Berlin (Math. Phys.)* **1915** (1915) 844.
- [113] A. Einstein, *Die Grundlage der allgemeinen Relativitätstheorie*, *Ann. Phys.* **49** (1916) 769.
- [114] J.C. Pati and A. Salam, *Lepton number as the fourth "color"*, *Phys. Rev. D* **10** (1974) 275.
- [115] J.C. Pati and A. Salam, *Erratum: Lepton number as the fourth "color"*, *Phys. Rev. D* **11** (1975) 703.
- [116] H. Georgi and S.L. Glashow, *Unity of All Elementary-Particle Forces*, *Phys. Rev. Lett.* **32** (1974) 438.
- [117] H. Fritzsch and P. Minkowski, *Unified interactions of leptons and hadrons*, *Ann. Phys. (N. Y.)* **93** (1975) 193.
- [118] G.G. Ross, *Grand Unified Theories*, Benjamin/Cummings Series in the Life Sciences, Benjamin/Cummings Publishing Company (1984).
- [119] W. de Boer, *Grand unified theories and supersymmetry in particle physics and cosmology*, *Prog. Part. Nucl. Phys.* **33** (1994) 201 [[hep-ph/9402266](#)].
- [120] J.P. Lees et al. (The BABAR Collaboration), *Evidence for an Excess of $\bar{B} \rightarrow D^{(*)}\tau^-\bar{\nu}_\tau$ Decays*, *Phys. Rev. Lett.* **109** (2012) 101802 [[1205.5442](#)].
- [121] J.P. Lees et al. (The BABAR Collaboration), *Measurement of an excess of $\bar{B} \rightarrow D^{(*)}\tau^-\bar{\nu}_\tau$ decays and implications for charged Higgs bosons*, *Phys. Rev. D* **88** (2013) 072012 [[1303.0571](#)].
- [122] The LHCb Collaboration, *Measurement of the ratios of branching fractions $\mathcal{R}(D^*)$ and $\mathcal{R}(D^0)$* , [[2302.02886](#)].
- [123] S.P. Martin, *A Supersymmetry primer*, *Adv. Ser. Direct. High Energy Phys.* **18** (1998) 1 [[hep-ph/9709356](#)].
- [124] J.-L. Gervais and B. Sakita, *Field theory interpretation of supergauges in dual models*, *Nucl. Phys. B* **34** (1971) 632.
- [125] D.V. Volkov and V.P. Akulov, *Is the neutrino a goldstone particle?*, *Phys. Lett. B* **46** (1973) 109.

-
- [126] R. Haag, J.T. Lopuszański and M. Sohnius, *All possible generators of supersymmetries of the S-Matrix*, *Nucl. Phys. B* **88** (1975) 257.
- [127] J. Wess and B. Zumino, *Supergauge transformations in four dimensions*, *Nucl. Phys. B* **70** (1974) 39.
- [128] A. Salam and J.A. Strathdee, *Super-gauge transformations*, *Nucl. Phys. B* **76** (1974) 477.
- [129] A. Salam and J.A. Strathdee, *Super-symmetry and non-Abelian gauges*, *Phys. Lett. B* **51** (1974) 353.
- [130] P. Fayet, *Supergauge invariant extension of the Higgs mechanism and a model for the electron and its neutrino*, *Nucl. Phys. B* **90** (1975) 104.
- [131] P. Fayet and J. Iliopoulos, *Spontaneously broken supergauge symmetries and goldstone spinors*, *Phys. Lett. B* **51** (1974) 461.
- [132] P. Fayet and S. Ferrara, *Supersymmetry*, *Phys. Rept.* **32** (1977) 249.
- [133] A.D. Sakharov, *Violation of CP Invariance, C asymmetry, and baryon asymmetry of the universe*, *Sov. Phys. Usp.* **34** (1991) 392.
- [134] S. Weinberg, *Living in the multiverse*, in *Universe or multiverse?*, B. Carr, ed., pp. 29–42, Cambridge University Press, 2005 [[hep-th/0511037](#)].
- [135] C.-N. Yang and R.L. Mills, *Conservation of Isotopic Spin and Isotopic Gauge Invariance*, *Phys. Rev.* **96** (1954) 191.
- [136] M. Dedushenko, *Snowmass White Paper: The Quest to Define QFT*, [[2203.08053](#)].
- [137] A.S. Wightman, *Quantum Field Theory in Terms of Vacuum Expectation Values*, *Phys. Rev.* **101** (1956) 860.
- [138] A.S. Wightman, *On the Localizability of Quantum Mechanical Systems*, *Rev. Mod. Phys.* **34** (1962) 845.
- [139] R. Haag, *On quantum field theories*, *Dan. Mat. Fys. Medd.* **29N12** (1955) 1.
- [140] D. Hall and A.S. Wightman, *A Theorem on Invariant Analytic Functions with Applications to Relativistic Quantum Field Theory*, Foundations of the Theory of Dynamical Systems of Infinitely Many Degrees of Freedom, I kommission hos Munksgaard (1957).
- [141] M. Reed and B. Simon, *Methods of Modern Mathematical Physics. 2. Fourier Analysis, Self-adjointness*, Academic Press (1975).
- [142] A. Hebecker, *Naturalness, String Landscape and Multiverse. A Modern Introduction with Exercises*, Springer Nature, 1 ed. (2021), [[2008.10625](#)].

- [143] L.D. Faddeev and V.N. Popov, *Feynman diagrams for the Yang-Mills field*, *Phys. Lett. B* **25** (1967) 29.
- [144] Y. Nambu, *Quasi-Particles and Gauge Invariance in the Theory of Superconductivity*, *Phys. Rev.* **117** (1960) 648.
- [145] Y. Nambu and G. Jona-Lasinio, *Dynamical Model of Elementary Particles Based on an Analogy with Superconductivity. I.*, *Phys. Rev.* **122** (1961) 345.
- [146] Y. Nambu and G. Jona-Lasinio, *Dynamical Model of Elementary Particles Based on an Analogy with Superconductivity. II.*, *Phys.Rev.* **124** (1961) 246.
- [147] J. Goldstone, *Field theories with « Superconductor » solutions*, *Nuovo Cim.* **19** (1961) 154.
- [148] J. Goldstone, A. Salam and S. Weinberg, *Broken Symmetries*, *Phys. Rev.* **127** (1962) 965.
- [149] F.F. Deppisch, *Lepton flavour violation and flavour symmetries*, *Fortsch. Phys.* **61** (2013) 622 [1206.5212].
- [150] The ATLAS Collaboration, *A detailed map of Higgs boson interactions by the ATLAS experiment ten years after the discovery*, *Nature* **607** (2022) 52 [2207.00092].
- [151] D.A. Ross and M.J.G. Veltman, *Neutral currents and the Higgs mechanism*, *Nucl. Phys. B* **95** (1975) 135.
- [152] M.J.G. Veltman, *Limit on mass differences in the Weinberg model*, *Nucl. Phys.B* **123** (1977) 89.
- [153] P. Sikivie, L. Susskind, M.B. Voloshin and V.I. Zakharov, *Isospin breaking in technicolor models*, *Nucl. Phys. B* **173** (1980) 189.
- [154] J. van der Bij and M.J.G. Veltman, *Two-loop large Higgs mass correction to the ρ -parameter*, *Nucl. Phys. B* **231** (1984) 205.
- [155] J.F. Gunion, H.E. Haber, G.L. Kane and S. Dawson, *The Higgs Hunter's Guide*, vol. Front.Phys, Taylor & Francis (1990).
- [156] M.E. Peskin and T. Takeuchi, *A new constraint on a strongly interacting Higgs sector*, *Phys. Rev. Lett.* **65** (1990) 964.
- [157] M.E. Peskin and T. Takeuchi, *Estimation of oblique electroweak corrections*, *Phys. Rev. D* **46** (1992) 381.
- [158] W.J. Marciano and J.L. Rosner, *Atomic parity violation as a probe of new physics*, *Phys. Rev. Lett.* **65** (1990) 2963.
- [159] D.C. Kennedy and P. Langacker, *Precision electroweak experiments and heavy physics: A global analysis*, *Phys. Rev. Lett.* **65** (1990) 2967.

-
- [160] P. Bärnreuther, M. Czakon and A. Mitov, *Percent-Level-Precision Physics at the Tevatron: Next-to-Next-to-Leading Order QCD Corrections to $q\bar{q} \rightarrow t\bar{t} + X$* , *Phys. Rev. Lett.* **109** (2012) 132001 [[1204.5201](#)].
- [161] M. Czakon and A. Mitov, *NNLO corrections to top-pair production at hadron colliders: the all-fermionic scattering channels*, *JHEP* **12** (2012) 54 [[1207.0236](#)].
- [162] M. Czakon and A. Mitov, *NNLO corrections to top pair production at hadron colliders: the quark-gluon reaction*, *JHEP* **01** (2013) 80 [[1210.6832](#)].
- [163] M. Czakon, P. Fiedler and A. Mitov, *Total Top-Quark Pair-Production Cross Section at Hadron Colliders Through $\mathcal{O}(\alpha_S^4)$* , *Phys. Rev. Lett.* **110** (2013) 252004 [[1303.6254](#)].
- [164] M. Czakon, D. Heymes and A. Mitov, *High-Precision Differential Predictions for Top-Quark Pairs at the LHC*, *Phys. Rev. Lett.* **116** (2016) 82003 [[1511.00549](#)].
- [165] S. Catani et al., *Top-quark pair hadroproduction at next-to-next-to-leading order in QCD*, *Phys. Rev. D* **99** (2019) 51501 [[1901.04005](#)].
- [166] X. Chen et al., *NNLO QCD corrections to Higgs boson production at large transverse momentum*, *JHEP* **10** (2016) 66 [[1607.08817](#)].
- [167] A. Gehrmann-De Ridder et al., *NNLO QCD corrections for Drell-Yan p_T^Z and ϕ^* observables at the LHC*, *JHEP* **11** (2016) 94 [[1610.01843](#)].
- [168] J. Currie et al., *Precise Predictions for Dijet Production at the LHC*, *Phys. Rev. Lett.* **119** (2017) 152001 [[1705.10271](#)].
- [169] M. Grazzini, S. Kallweit, D. Rathlev and M. Wiesemann, *$W^\pm Z$ production at hadron colliders in NNLO QCD*, *Phys. Lett. B* **761** (2016) 179 [[1604.08576](#)].
- [170] M. Grazzini, S. Kallweit, D. Rathlev and M. Wiesemann, *$W^\pm Z$ production at the LHC: fiducial cross sections and distributions in NNLO QCD*, *JHEP* **05** (2017) 139 [[1703.09065](#)].
- [171] M. Grazzini et al., *W^+W^- production at the LHC: fiducial cross sections and distributions in NNLO QCD*, *JHEP* **08** (2016) 140 [[1605.02716](#)].
- [172] R.V. Harlander, *Virtual corrections to $g\bar{g} \rightarrow H$ to two loops in the heavy top limit*, *Phys. Lett. B* **492** (2000) 74 [[hep-ph/0007289](#)].
- [173] R.V. Harlander and W.B. Kilgore, *Soft and virtual corrections to $pp \rightarrow H + X$ at next-to-next-to-leading order*, *Phys. Rev. D* **64** (2001) 13015 [[hep-ph/0102241](#)].
- [174] R.V. Harlander and W.B. Kilgore, *Next-to-Next-to-Leading Order Higgs Production at Hadron Colliders*, *Phys. Rev. Lett.* **88** (2002) 201801 [[hep-ph/0201206](#)].
- [175] M. Czakon and M. Niggetiedt, *Exact quark-mass dependence of the Higgs-gluon form factor at three loops in QCD*, *JHEP* **05** (2020) 149 [[2001.03008](#)].

- [176] M. Czakon, R.V. Harlander, J. Klappert and M. Niggetiedt, *Exact Top-Quark Mass Dependence in Hadronic Higgs Production*, *Phys. Rev. Lett.* **127** (2021) 162002 [2105.04436].
- [177] G. Heinrich, *Collider physics at the precision frontier*, *Phys. Rept.* **922** (2021) 1 [2009.00516].
- [178] The ATLAS Collaboration, *Standard Model Summary Plots February 2022*, *ATL-PHYS-PUB-2022-009* (2022) .
- [179] Y. Ne'eman, *Derivation of strong interactions from a gauge invariance*, *Nucl. Phys.* **26** (1961) 222.
- [180] M. Gell-Mann, *Symmetries of Baryons and Mesons*, *Phys. Rev.* **125** (1962) 1067.
- [181] M. Gell-Mann, *A schematic model of baryons and mesons*, *Phys. Lett.* **8** (1964) 214.
- [182] G. Zweig, *An SU(3) model for strong interaction symmetry and its breaking*, 1964.
- [183] H. Fritzsch, M. Gell-Mann and H. Leutwyler, *Advantages of the color octet gluon picture*, *Phys. Lett. B* **47** (1973) 365.
- [184] V.E. Barnes et al., *Observation of a Hyperon with Strangeness Minus Three*, *Phys. Rev. Lett.* **12** (1964) 204.
- [185] R. Aaij et al. (The LHCb Collaboration), *Observation of $J/\psi\phi$ Structures Consistent with Exotic States from Amplitude Analysis of $B^+ \rightarrow J/\psi\phi K^+$ Decays*, *Phys. Rev. Lett.* **118** (2017) 22003 [1606.07895].
- [186] R. Aaij et al. (The LHCb Collaboration), *Amplitude analysis of $B^+ \rightarrow J/\psi\phi K^+$ decays*, *Phys. Rev. D* **95** (2017) 12002 [1606.07898].
- [187] R. Aaij et al. (The LHCb Collaboration), *Observation of $J/\psi p$ Resonances Consistent with Pentaquark States in $\Lambda_b^0 \rightarrow J/\psi K^- p$ Decays*, *Phys. Rev. Lett.* **115** (2015) 72001 [1507.03414].
- [188] D.J. Gross and F. Wilczek, *Ultraviolet Behavior of Non-Abelian Gauge Theories*, *Phys.Rev.Lett.* **30** (1973) 1343.
- [189] H. Politzer, *Reliable Perturbative Results for Strong Interactions?*, *Phys.Rev.Lett.* **30** (1973) 1346.
- [190] A.D. Martin, W.J. Stirling, R.S. Thorne and G. Watt, *Parton distributions for the LHC*, *Eur.Phys.J.* **C63** (2009) 189 [0901.0002].
- [191] R.D. Ball et al. (The NNPDF Collaboration) and Others, *Parton distributions for the LHC run II*, *JHEP* **04** (2015) 40 [1410.8849].
- [192] R.D. Ball et al. (The NNPDF Collaboration), *The path to proton structure at 1% accuracy*, *Eur. Phys. J. C* **82** (2022) 428 [2109.02653].

-
- [193] V.N. Gribov and L.N. Lipatov, *Deep inelastic $e p$ scattering in perturbation theory*, *Sov. J. Nucl. Phys.* **15** (1972) 438.
- [194] Y.L. Dokshitzer, *Calculation of the Structure Functions for Deep Inelastic Scattering and $e^+ e^-$ Annihilation by Perturbation Theory in Quantum Chromodynamics.*, *Sov. Phys. JETP* **46** (1977) 641.
- [195] G. Altarelli and G. Parisi, *Asymptotic freedom in parton language*, *Nucl. Phys. B* **126** (1977) 298.
- [196] B.T. Cleveland et al., *Measurement of the Solar Electron Neutrino Flux with the Homestake Chlorine Detector*, *Astrophys. J.* **496** (1998) 505.
- [197] Y. Fukuda et al. (The Super-Kamiokande Collaboration), *Evidence for Oscillation of Atmospheric Neutrinos*, *Phys. Rev. Lett.* **81** (1998) 1562 [[hep-ex/9807003](#)].
- [198] K. Eguchi et al. (The KamLAND Collaboration), *First Results from KamLAND: Evidence for Reactor Antineutrino Disappearance*, *Phys. Rev. Lett.* **90** (2003) 21802 [[hep-ex/0212021](#)].
- [199] M.H. Ahn et al. (The K2K Collaboration), *Indications of Neutrino Oscillation in a 250 km Long-Baseline Experiment*, *Phys. Rev. Lett.* **90** (2003) 41801 [[hep-ex/0212007](#)].
- [200] M.H. Ahn et al. (The K2K Collaboration), *Measurement of neutrino oscillation by the K2K experiment*, *Phys. Rev. D* **74** (2006) 72003 [[hep-ex/0606032](#)].
- [201] B. Pontecorvo, *Inverse beta processes and nonconservation of lepton charge*, *Zh. Eksp. Teor. Fiz.* **34** (1957) 247.
- [202] Z. Maki, M. Nakagawa and S. Sakata, *Remarks on the Unified Model of Elementary Particles*, *Prog. Theor. Phys.* **28** (1962) 870.
- [203] F. An et al. (The JUNO Collaboration), *Neutrino physics with JUNO*, *J. Phys. G* **43** (2016) 30401 [[1507.05613](#)].
- [204] M. Aker et al. (The KATRIN Collaboration), *Improved Upper Limit on the Neutrino Mass from a Direct Kinematic Method by KATRIN*, *Phys. Rev. Lett.* **123** (2019) 221802 [[1909.06048](#)].
- [205] E. Majorana, *Teoria simmetrica dell'elettrone e del positrone*, *Nuovo Cim.* **14** (1937) 171.
- [206] N. Abgrall et al. (The Majorana Collaboration), *The MAJORANA DEMONSTRATOR Neutrinoless Double-Beta Decay Experiment*, *Adv. High Energy Phys.* **2014** (2014) 365432 [[1308.1633](#)].
- [207] M. Agostini et al. (The GERDA Collaboration), *Improved Limit on Neutrinoless Double- β Decay of ^{76}Ge from GERDA Phase II*, *Phys. Rev. Lett.* **120** (2018) 132503 [[1803.11100](#)].

- [208] N. Abgrall et al. (The LEGEND Collaboration), *The large enriched germanium experiment for neutrinoless double beta decay (LEGEND)*, *AIP Conf. Proc.* **1894** (2017) 20027 [[1709.01980](#)].
- [209] A. Hook, *TASI Lectures on the Strong CP Problem and Axions*, *PoS TASI2018* (2019) 4 [[1812.02669](#)].
- [210] C.A. Baker et al., *An Improved Experimental Limit on the Electric Dipole Moment of the Neutron*, *Phys. Rev. Lett.* **97** (2006) 131801 [[hep-ex/0602020](#)].
- [211] R.D. Peccei and H.R. Quinn, *CP Conservation in the Presence of Pseudoparticles*, *Phys. Rev. Lett.* **38** (1977) 1440.
- [212] R.D. Peccei and H.R. Quinn, *Constraints imposed by CP conservation in the presence of pseudoparticles*, *Phys. Rev. D* **16** (1977) 1791.
- [213] F. Wilczek, *Problem of Strong P and T Invariance in the Presence of Instantons*, *Phys. Rev. Lett.* **40** (1978) 279.
- [214] S. Weinberg, *A New Light Boson?*, *Phys. Rev. Lett.* **40** (1978) 223.
- [215] P. Sikivie, *Experimental Tests of the "Invisible" Axion*, *Phys. Rev. Lett.* **51** (1983) 1415.
- [216] E. Armengaud et al. (The IAXO Collaboration), *Conceptual Design of the International Axion Observatory (IAOX)*, *JINST* **9** (2014) T05002 [[1401.3233](#)].
- [217] P. Brun et al. (The MADMAX Collaboration), *A new experimental approach to probe QCD axion dark matter in the mass range above 40 μeV* , *Eur. Phys. J. C* **79** (2019) 186 [[1901.07401](#)].
- [218] O. Kwon et al. (The CAPP Collaboration), *First Results from an Axion Haloscope at CAPP around 10.7 μeV* , *Phys. Rev. Lett.* **126** (2021) 191802 [[2012.10764](#)].
- [219] P. Langacker, *The standard model and beyond*, Taylor & Francis (2017).
- [220] C. Cornella et al., *Reading the footprints of the B-meson flavor anomalies*, *JHEP* **08** (2021) 50 [[2103.16558](#)].
- [221] R. Aaij et al. (The LHCb Collaboration), *Measurement of Form-Factor-Independent Observables in the Decay $B^0 \rightarrow K^{*0} \mu^+ \mu^-$* , *Phys. Rev. Lett.* **111** (2013) 191801 [[1308.1707](#)].
- [222] R. Aaij et al. (The LHCb Collaboration), *Test of Lepton Universality Using $B^+ \rightarrow K^+ \ell^+ \ell^-$ Decays*, *Phys. Rev. Lett.* **113** (2014) 151601 [[1406.6482](#)].
- [223] R. Aaij et al. (The LHCb Collaboration), *Test of lepton universality with $B^0 \rightarrow K^{*0} \ell^+ \ell^-$ decays*, *JHEP* **8** (2017) 55 [[1705.05802](#)].
- [224] R. Aaij et al. (The LHCb Collaboration), *Search for Lepton-Universality Violation in $B^+ \rightarrow K^+ \ell^+ \ell^-$ decays*, *Phys. Rev. Lett.* **122** (2019) 191801 [[1903.09252](#)].

-
- [225] R. Aaij et al. (The LHCb Collaboration), *Test of lepton universality in beauty-quark decays*, *Nat. Phys.* **18** (2022) 277 [2103.11769].
- [226] C. Bobeth, G. Hiller and G. Piranishvili, *Angular distributions of $\bar{B} \rightarrow \bar{K} \ell^+ \ell^-$ decays*, *JHEP* **2007** (2007) 40 [0709.4174].
- [227] R. Aaij et al. (The LHCb Collaboration), *Angular analysis of the $B^0 \rightarrow K^{*0} \mu^+ \mu^-$ decay using 3 fb^{-1} of integrated luminosity*, *JHEP* **2016** (2016) 104 [1512.04442].
- [228] R. Aaij et al. (The LHCb Collaboration), *Measurement of the Ratio of Branching Fractions $\mathcal{B}(\bar{B}^0 \rightarrow D^{*+} \tau^- \bar{\nu}_\tau) / \mathcal{B}(\bar{B}^0 \rightarrow D^{*+} \mu^- \bar{\nu}_\mu)$* , *Phys. Rev. Lett.* **115** (2015) 111803 [1506.08614].
- [229] M. Huschle et al. (The Belle Collaboration), *Measurement of the branching ratio of $\bar{B} \rightarrow D^{(*)} \tau^- \bar{\nu}_\tau$ relative to $\bar{B} \rightarrow D^{(*)} \ell^- \bar{\nu}_\ell$ decays with hadronic tagging at Belle*, *Phys. Rev. D* **92** (2015) 072014 [1507.03233].
- [230] S. Hirose et al. (The Belle Collaboration), *Measurement of the τ Lepton Polarization and $R(D^*)$ in the Decay $\bar{B} \rightarrow D^* \tau^- \bar{\nu}_\tau$* , *Phys. Rev. Lett.* **118** (2017) 211801 [1612.00529].
- [231] R. Aaij et al. (The LHCb Collaboration), *Test of Lepton Flavor Universality by the measurement of the $B^0 \rightarrow D^{*-} \tau^+ \nu_\tau$ branching fraction using three-prong τ decays*, *Phys. Rev. D* **97** (2017) 072013 [1711.02505].
- [232] R. Aaij et al. (The LHCb Collaboration), *Measurement of the Ratio of the $B^0 \rightarrow D^{*-} \tau^+ \nu_\tau$ and $B^0 \rightarrow D^{*-} \mu^+ \nu_\mu$ Branching Fractions Using Three-Prong τ -Lepton Decays*, *Phys. Rev. Lett.* **120** (2018) 171802 [1708.08856].
- [233] G. Hiller and M. Schmaltz, *R_K and future $b \rightarrow s \ell \ell$ physics beyond the standard model opportunities*, *Phys. Rev. D* **90** (2014) 054014 [1408.1627].
- [234] S. Descotes-Genon, J. Matias and J. Virto, *Understanding the $B \rightarrow K^* \mu^+ \mu^-$ anomaly*, *Phys. Rev. D* **88** (2013) 074002 [1307.5683].
- [235] W. Altmannshofer and D.M. Straub, *New Physics in $B \rightarrow K^* \mu \mu$?*, *Eur. Phys. J. C* **73** (2013) 2646 [1308.1501].
- [236] T. Hurth and F. Mahmoudi, *On the LHCb anomaly in $B \rightarrow K^* \ell^+ \ell^-$* , *JHEP* **04** (2014) 97 [1312.5267].
- [237] T. Hurth, F. Mahmoudi and S. Neshatpour, *Global fits to $b \rightarrow s \ell \ell$ data and signs for lepton non-universality*, *JHEP* **12** (2014) 53 [1410.4545].
- [238] W. Altmannshofer and D.M. Straub, *New physics in $b \rightarrow s$ transitions after LHC run 1*, *Eur. Phys. J. C* **75** (2015) 382 [1411.3161].
- [239] S. Descotes-Genon, L. Hofer, J. Matias and J. Virto, *Global analysis of $b \rightarrow s \ell \ell$ anomalies*, *JHEP* **06** (2016) 92 [1510.04239].

- [240] M. Ciuchini, *On flavourful Easter eggs for New Physics hunger and lepton flavour universality violation*, *Eur. Phys. J. C* **77** (2017) 688 [1704.05447].
- [241] M. Algueró et al., *Emerging patterns of New Physics with and without Lepton Flavour Universal contributions*, *Eur. Phys. J. C* **79** (2019) 714 [1903.09578].
- [242] M. Ciuchini et al., *Lessons from the $B^{0,+} \rightarrow K^{*0,+} \mu^+ \mu^-$ angular analyses*, *Phys. Rev. D* **103** (2021) 015030 [2011.01212].
- [243] S.L. Glashow, D. Guadagnoli and K. Lane, *Lepton Flavor Violation in B Decays?*, *Phys. Rev. Lett.* **114** (2015) 091801 [1411.0565].
- [244] B. Bhattacharya, A. Datta, D. London and S. Shivashankara, *Simultaneous explanation of the R_K and $R(D^{(*)})$ puzzles*, *Phys. Lett. B* **742** (2015) 370 [1412.7164].
- [245] R. Alonso, B. Grinstein and J. Martin Camalich, *Lepton universality violation and lepton flavor conservation in B-meson decays*, *JHEP* **10** (2015) 184 [1505.05164].
- [246] A. Greljo, G. Isidori and D. Marzocca, *On the breaking of lepton flavor universality in B decays*, *JHEP* **07** (2015) 142 [1506.01705].
- [247] L. Calibbi, A. Crivellin and T. Ota, *Effective Field Theory Approach to $b \rightarrow s \ell \ell'$, $B \rightarrow K^{(*)} \nu \bar{\nu}$ and $B \rightarrow D^{(*)} \tau \nu$ with Third Generation Couplings*, *Phys. Rev. Lett.* **115** (2015) 181801 [1506.02661].
- [248] B. Diaz, M. Schmaltz and Y.M. Zhong, *The leptoquark hunter's guide: pair production*, *JHEP* **10** (2017) 97 [1706.05033].
- [249] A.C. Reimers (on behalf of the ATLAS and CMS Collaborations), *Searches for leptoquarks in scenarios of lepton flavor universality anomalies*, *Proc. Sci.* **PANIC2021** (2022) 140 [2111.11756].
- [250] T. Aaltonen et al. (The CDF Collaboration), *High-precision measurement of the W boson mass with the CDF II detector*, *Science* **376** (2022) 170.
- [251] A. Bhaskar, A.A. Madathil, T. Mandal and S. Mitra, *Combined explanation of W-mass, muon $g - 2$, $R_{K^{(*)}}$ and $R_{D^{(*)}}$ anomalies in a singlet-triplet scalar leptoquark model*, *Phys. Rev. D* **106** (2022) 115009 [2204.09031].
- [252] T.A. Chowdhury and S. Saad, *Leptoquark-vectorlike quark model for the CDF m_W , $(g - 2)_\mu$, $R_{K^{(*)}}$ anomalies, and neutrino masses*, *Phys. Rev. D* **106** (2022) 55017 [2205.03917].
- [253] P. Athron et al., *Hadronic uncertainties versus new physics for the W boson mass and Muon $g - 2$ anomalies*, *Nat. Commun.* **14** (2023) 659 [2204.03996].
- [254] G. Arcadi and A. Djouadi, *2HD plus light pseudoscalar model for a combined explanation of the possible excesses in the CDF M_W measurement and $(g - 2)_\mu$ with dark matter*, *Phys. Rev. D* **106** (2022) 95008 [2204.08406].

-
- [255] G. Arcadi and A. Djouadi, *A model for fermionic dark matter addressing both the CDF M_W and the $(g - 2)_\mu$ anomalies*, *Front. Phys.* **11** (2023) 1143932 [2301.06476].
- [256] B. Abi et al. (Muon $(g - 2)$ Collaboration), *Measurement of the Positive Muon Anomalous Magnetic Moment to 0.46 ppm*, *Phys. Rev. Lett.* **126** (2021) 141801 [2104.03281].
- [257] T. Aoyama et al., *The anomalous magnetic moment of the muon in the Standard Model*, *Phys. Rep.* **887** (2020) 1 [2006.04822].
- [258] H.N. Brown et al. (The Muon $(g - 2)$), *Precise Measurement of the Positive Muon Anomalous Magnetic Moment*, *Phys. Rev. Lett.* **86** (2001) 2227 [hep-ex/0102017].
- [259] G.W. Bennett et al. (The Muon $(g - 2)$ Collaboration), *Measurement of the Positive Muon Anomalous Magnetic Moment to 0.7 ppm*, *Phys. Rev. Lett.* **89** (2002) 101804 [hep-ex/0208001].
- [260] G.W. Bennett et al. (The Muon $(g - 2)$ Collaboration), *Measurement of the Negative Muon Anomalous Magnetic Moment to 0.7 ppm*, *Phys. Rev. Lett.* **92** (2004) 161802 [hep-ex/0401008].
- [261] G.W. Bennett et al. (The Muon $(g - 2)$ Collaboration), *Final report of the E821 muon anomalous magnetic moment measurement at BNL*, *Phys. Rev. D* **73** (2006) 072003 [hep-ex/0602035].
- [262] A. Crivellin, C. Greub, D. Müller and F. Saturnino, *Scalar leptoquarks in leptonic processes*, *JHEP* **02** (2021) 182 [2010.06593].
- [263] A. Gérardin, *The anomalous magnetic moment of the muon: status of lattice QCD calculations*, *Eur. Phys. J. A* **57** (2021) 1 [2012.03931].
- [264] J.I. González Hernández et al., *The solar gravitational redshift from HARPS-LFC Moon spectra: A test of the general theory of relativity*, *Astron. Astrophys.* **643** (2020) A146 [2009.10558].
- [265] D. Walsh, R.F. Carswell and R.J. Weymann, *0957+ 561 A, B: twin quasistellar objects or gravitational lens?*, *Nature* **279** (1979) 381.
- [266] B.P. Abbott et al. (The LIGO Scientific and Virgo Collaborations), *Observation of Gravitational Waves from a Binary Black Hole Merger*, *Phys. Rev. Lett.* **116** (2016) 61102 [1602.03837].
- [267] B.P. Abbott et al. (The LIGO Scientific and Virgo Collaborations), *GW151226: Observation of Gravitational Waves from a 22-Solar-Mass Binary Black Hole Coalescence*, *Phys. Rev. Lett.* **116** (2016) 241103 [1606.04855].

- [268] B.P. Abbott et al. (The LIGO Scientific and Virgo Collaborations), *GW170817: Observation of Gravitational Waves from a Binary Neutron Star Inspiral*, *Phys. Rev. Lett.* **119** (2017) 161101 [[1710.05832](#)].
- [269] F. Zwicky, *Die Rotverschiebung von extragalaktischen Nebeln*, *Helv. Phys. Acta* **6** (1933) 110.
- [270] F. Zwicky, *On the Masses of Nebulae and of Clusters of Nebulae*, *Astrophys. J.* **86** (1937) 217.
- [271] V.C. Rubin and W.K. Ford Jr., *Rotation of the Andromeda Nebula from a Spectroscopic Survey of Emission Regions*, *Astrophys. J.* **159** (1970) 379.
- [272] V.C. Rubin, N. Thonnard and W.K. Ford Jr., *Rotational properties of 21 SC galaxies with a large range of luminosities and radii, from NGC 4605 ($R = 4\text{kpc}$) to UGC 2885 ($R = 122\text{kpc}$)*, *Astrophys. J.* **238** (1980) 471.
- [273] D. Clowe et al., *A Direct Empirical Proof of the Existence of Dark Matter*, *Astrophys. J.* **648** (2006) L109 [[astro-ph/0608407](#)].
- [274] M. Milgrom, *A modification of the Newtonian dynamics as a possible alternative to the hidden mass hypothesis*, *Astrophys. J.* **270** (1983) 365.
- [275] M. Milgrom, *A Modification of the Newtonian dynamics: Implications for galaxies*, *Astrophys. J.* **270** (1983) 371.
- [276] M. Milgrom, *A modification of the newtonian dynamics: implications for galaxy systems*, *Astrophys. J.* **270** (1983) 384.
- [277] J. Bekenstein and M. Milgrom, *Does the missing mass problem signal the breakdown of Newtonian gravity?*, *Astrophys. J.* **286** (1984) 7.
- [278] A.A. Penzias and R.W. Wilson, *A Measurement of Excess Antenna Temperature at 4080-Mc/s*, *Astrophys. J.* **142** (1965) 419.
- [279] N. Aghanim et al. (The Planck Collaboration), *Planck 2018 results. VI. Cosmological parameters*, *Astron. Astrophys.* **641** (2020) A6 [[1807.06209](#)].
- [280] N. Aghanim et al. (The Planck Collaboration), *Planck 2018 results. V. CMB power spectra and likelihoods*, *Astron. Astrophys.* **641** (2020) A5 [[1907.12875](#)].
- [281] Y. Zel'dovich and I. Novikov, *The Hypothesis of Cores Retarded during Expansion and the Hot Cosmological Model*, *Sov. Astron.* **10** (1967) 602.
- [282] S. Hawking, *Gravitationally Collapsed Objects of Very Low Mass*, *Mon. Not. Roy. Astron. Soc.* **152** (1971) 75.
- [283] B. Carr, F. Kuhnel and M. Sandstad, *Primordial black holes as dark matter*, *Phys. Rev.* **D94** (2016) 83504 [[1607.06077](#)].

-
- [284] J.M. Gaskins, *A review of indirect searches for particle dark matter*, *Contemp. Phys.* **57** (2016) 496 [[1604.00014](#)].
- [285] W.B. Atwood et al., *The Large Area Telescope on the Fermi Gamma-ray Space Telescope Mission*, *Astrophys. J.* **697** (2009) 1071 [[0902.1089](#)].
- [286] L. Goodenough and D. Hooper, *Possible Evidence For Dark Matter Annihilation In The Inner Milky Way From The Fermi Gamma Ray Space Telescope*, [[0910.2998](#)].
- [287] D. Hooper and L. Goodenough, *Dark matter annihilation in the Galactic Center As Seen by the Fermi Gamma Ray Space Telescope*, *Phys. Lett.* **B697** (2011) 412 [[1010.2752](#)].
- [288] M. Ackermann et al. (The Fermi–LAT Collaboration), *The Fermi Galactic Center GeV Excess and Implications for Dark Matter*, *Astrophys. J.* **840** (2017) 43 [[1704.03910](#)].
- [289] O. Adriani et al., *An anomalous positron abundance in cosmic rays with energies 1.5-100 GeV*, *Nature* **458** (2009) 607 [[0810.4995](#)].
- [290] O. Adriani et al., *Cosmic-Ray Positron Energy Spectrum Measured by PAMELA*, *Phys. Rev. Lett.* **111** (2013) 81102 [[1308.0133](#)].
- [291] M. Ackermann et al. (The Fermi–LAT Collaboration), *Measurement of separate cosmic-ray electron and positron spectra with the Fermi Large Area Telescope*, *Phys. Rev. Lett.* **108** (2012) 11103 [[1109.0521](#)].
- [292] M. Aguilar et al. (The AMS Collaboration), *First Result from the Alpha Magnetic Spectrometer on the International Space Station: Precision Measurement of the Positron Fraction in Primary Cosmic Rays of 0.5–350 GeV*, *Phys. Rev. Lett.* **110** (2013) 141102.
- [293] L. Accardo et al. (The AMS Collaboration), *High Statistics Measurement of the Positron Fraction in Primary Cosmic Rays of 0.5-500 GeV with the Alpha Magnetic Spectrometer on the International Space Station*, *Phys. Rev. Lett.* **113** (2014) 121101.
- [294] D. Hooper, P. Blasi and P.D. Serpico, *Pulsars as the sources of high energy cosmic ray positrons*, *JCAP* **0901** (2009) 25 [[0810.1527](#)].
- [295] S. Profumo, *Dissecting cosmic-ray electron-positron data with Occam’s Razor: the role of known pulsars*, *Cent. Eur. J. Phys.* **10** (2011) 1 [[0812.4457](#)].
- [296] J. Feng and H.-H. Zhang, *Pulsar interpretation of lepton spectra measured by AMS-02*, *Eur. Phys. J.* **C76** (2016) 229 [[1504.03312](#)].
- [297] D.G. Cerdeno and A.M. Green, *Direct detection of WIMPs*, [[1002.1912](#)].
- [298] A.H.G. Peter et al., *WIMP physics with ensembles of direct-detection experiments*, *Phys. Dark Univ.* **5-6** (2014) 45 [[1310.7039](#)].

- [299] T. Marrodán Undagoitia and L. Rauch, *Dark matter direct-detection experiments*, *J. Phys.* **G43** (2016) 13001 [[1509.08767](#)].
- [300] E. Del Nobile, *The Theory of Direct Dark Matter Detection. A Guide to Computations*, Lecture Notes in Physics, Springer Nature, Cham, 1 ed. (2022), [[2104.12785](#)].
- [301] E. Aprile et al. (The XENON Collaboration), *The XENON1T Dark Matter Search Experiment*, *Springer Proc. Phys.* **148** (2013) 93 [[1206.6288](#)].
- [302] E. Aprile et al. (The XENON Collaboration), *Physics reach of the XENON1T dark matter experiment*, *JCAP* **1604** (2016) 27 [[1512.07501](#)].
- [303] E. Aprile et al. (The XENON Collaboration), *Dark Matter Search Results from a One Ton-Year Exposure of XENON1T*, *Phys. Rev. Lett.* **121** (2018) 111302 [[1805.12562](#)].
- [304] E. Aprile et al. (The XENON Collaboration), *Excess electronic recoil events in XENON1T*, *Phys. Rev. D* **102** (2020) 72004 [[2006.09721](#)].
- [305] R. Bernabei et al. (The DAMA and LIBRA Collaborations), *First results from DAMA/LIBRA and the combined results with DAMA/NaI*, *Eur. Phys. J. C* **56** (2008) 333 [[0804.2741](#)].
- [306] R. Bernabei et al. (The DAMA and LIBRA Collaborations), *New results from DAMA/LIBRA*, *Eur. Phys. J. C* **67** (2010) 39 [[1002.1028](#)].
- [307] R. Bernabei et al., *Final model independent result of DAMA/LIBRA-phase1*, *Eur.Phys.J.* **C73** (2013) 2648 [[1308.5109](#)].
- [308] G. Angloher et al. (The COSINUS Collaboration), *Results from the first cryogenic NaI detector for the COSINUS project*, *JINST* **12** (2017) P11007 [[1705.11028](#)].
- [309] G. Aad et al. (The ATLAS Collaboration), *Search for new phenomena in events with an energetic jet and missing transverse momentum in pp collisions at $\sqrt{s} = 13$ TeV with the ATLAS detector*, *Phys. Rev. D* **103** (2021) 112006 [[2102.10874](#)].
- [310] A. Tumasyan et al. (The CMS Collaboration), *Search for new particles in events with energetic jets and large missing transverse momentum in proton-proton collisions at $\sqrt{s} = 13$ TeV*, *JHEP* **11** (2021) 153 [[2107.13021](#)].
- [311] The ATLAS Collaboration, *Combination of searches for invisible decays of the Higgs boson using 139 fb^{-1} of proton-proton collision data at $\sqrt{s} = 13$ TeV collected with the ATLAS experiment*, [[2301.10731](#)].
- [312] A.M. Sirunyan et al. (The CMS Collaboration), *Search for dark matter produced in association with a single top quark or a top quark pair in proton-proton collisions at $\sqrt{s} = 13$ TeV*, *JHEP* **03** (2019) 141 [[1901.01553](#)].

-
- [313] G. Aad et al. (The ATLAS Collaboration), *Search for dark matter produced in association with a single top quark in $\sqrt{s} = 13\text{TeV}$ pp collisions with the ATLAS detector*, *Eur. Phys. J. C* **81** (2021) 860 [[2011.09308](#)].
- [314] The ATLAS Collaboration, *Search for dark matter produced in association with a single top quark and an energetic W boson in $\sqrt{s} = 13\text{ TeV}$ pp collisions with the ATLAS detector*, [[2211.13138](#)].
- [315] F. Kahlhoefer, *Review of LHC dark matter searches*, *Int. J. Mod. Phys. A* **32** (2017) 1730006 [[1702.02430](#)].
- [316] A. Boveia et al. (The LHC Dark Matter Working Group), *Recommendations on presenting LHC searches for missing transverse energy signals using simplified s -channel models of dark matter*, *Phys. Dark Univ.* **27** (2020) 100365 [[1603.04156](#)].
- [317] A. Albert et al. (The LHC Dark Matter Working Group), *Recommendations of the LHC Dark Matter Working Group: Comparing LHC searches for dark matter mediators in visible and invisible decay channels and calculations of the thermal relic density*, *Phys. Dark Univ.* **26** (2019) 100377 [[1703.05703](#)].
- [318] T. Abe et al. (The LHC Dark Matter Working Group), *LHC Dark Matter Working Group: Next-generation spin-0 dark matter models*, *Phys. Dark Univ.* **27** (2020) 100351 [[1810.09420](#)].
- [319] M. Ruhdorfer, E. Salvioni and A. Weiler, *A global view of the off-shell Higgs portal*, *SciPost Phys.* **8** (2020) 027 [[1910.04170](#)].
- [320] M. Klasen, M. Pohl and G. Sigl, *Indirect and direct search for dark matter*, *Prog. Part. Nucl. Phys.* **85** (2015) 1 [[1507.03800](#)].
- [321] M. Schumann, *Direct detection of WIMP dark matter: concepts and status*, *J. Phys. G Nucl. Part. Phys.* **46** (2019) 103003 [[1903.03026](#)].
- [322] M. Aaboud et al. (The ATLAS Collaboration), *Constraints on mediator-based dark matter and scalar dark energy models using $\sqrt{s} = 13\text{ TeV}$ pp collision data collected by the ATLAS detector*, *JHEP* **05** (2019) 142 [[1903.01400](#)].
- [323] V. Barger et al., *Complex singlet extension of the standard model*, *Phys. Rev. D* **79** (2009) 015018 [[0811.0393](#)].
- [324] V. Barger, M. McCaskey and G. Shaughnessy, *Complex scalar dark matter vis-à-vis CoGeNT, DAMA/LIBRA, and XENON100*, *Phys. Rev. D* **82** (2010) 035019 [[1005.3328](#)].
- [325] C. Gross, O. Lebedev and T. Toma, *Cancellation Mechanism for Dark-Matter–Nucleon Interaction*, *Phys. Rev. Lett.* **119** (2017) 191801 [[1708.02253](#)].

- [326] B. Bellazzini, C. Csáki and J. Serra, *Composite Higgses*, *Eur. Phys. J. C* **74** (2014) 2766 [[1401.2457](#)].
- [327] G. Panico and A. Wulzer, *The Composite Nambu-Goldstone Higgs*, vol. 913, Springer (2016), [[1506.01961](#)].
- [328] K. Agashe, R. Contino and A. Pomarol, *The minimal composite Higgs model*, *Nucl. Phys. B* **719** (2005) 165 [[hep-ph/0412089](#)].
- [329] D. Naegels, *An introduction to Goldstone boson physics and to the coset construction*, [[2110.14504](#)].
- [330] M. Frigerio, A. Pomarol, F. Riva and A. Urbano, *Composite scalar dark matter*, *JHEP* **07** (2012) 15 [[1204.2808](#)].
- [331] M. Chala, *$h \rightarrow \gamma\gamma$ excess and dark matter from composite Higgs models*, *JHEP* **01** (2013) 122 [[1210.6208](#)].
- [332] D. Marzocca and A. Urbano, *Composite dark matter and LHC interplay*, *JHEP* **07** (2014) 107 [[1404.7419](#)].
- [333] J. Barnard, T. Gherghetta, T.S. Ray and A. Spray, *The unnatural composite Higgs*, *JHEP* **01** (2015) 67 [[1409.7391](#)].
- [334] N. Fonseca, R. Zukanovich Funchal, A. Lessa and L. Lopez-Honorez, *Dark Matter constraints on composite Higgs models*, *JHEP* **06** (2015) 154 [[1501.05957](#)].
- [335] I. Brivio et al., *Non-linear Higgs portal to Dark Matter*, *JHEP* **04** (2016) 141 [[1511.01099](#)].
- [336] M. Kim, S.J. Lee and A. Parolini, *WIMP Dark Matter in Composite Higgs Models and the Dilaton Portal*, [[1602.05590](#)].
- [337] M. Chala, G. Nardini and I. Sobolev, *Unified explanation for dark matter and electroweak baryogenesis with direct detection and gravitational wave signatures*, *Phys. Rev. D* **94** (2016) 55006 [[1605.08663](#)].
- [338] D. Barducci et al., *Monojet searches for momentum-dependent dark matter interactions*, *JHEP* **01** (2017) 78 [[1609.07490](#)].
- [339] Y. Wu, T. Ma, B. Zhang and G. Cacciapaglia, *Composite dark matter and Higgs*, *JHEP* **11** (2017) 58 [[1703.06903](#)].
- [340] R. Balkin, M. Ruhdorfer, E. Salvioni and A. Weiler, *Charged composite scalar dark matter*, *JHEP* **11** (2017) 94 [[1707.07685](#)].
- [341] R. Balkin, G. Perez and A. Weiler, *Little composite dark matter*, *Eur. Phys. J. C* **78** (2018) 104 [[1707.09980](#)].

-
- [342] T. Alanne, D. Buarque Franzosi, M.T. Frandsen and M. Rosenlyst, *Dark matter in (partially) composite Higgs models*, *JHEP* **12** (2018) 88 [[1808.07515](#)].
- [343] R. Balkin, M. Ruhdorfer, E. Salvioni and A. Weiler, *Dark matter shifts away from direct detection*, *JCAP* **11** (2018) 050 [[1809.09106](#)].
- [344] K. Ishiwata and T. Toma, *Probing pseudo Nambu-Goldstone boson dark matter at loop level*, *JHEP* **12** (2018) 89 [[1810.08139](#)].
- [345] K. Huitu et al., *Probing pseudo-Goldstone dark matter at the LHC*, *Phys. Rev. D* **100** (2019) 15009 [[1812.05952](#)].
- [346] D. Karamitros, *Pseudo-Nambu-Goldstone dark matter: Examples of vanishing direct detection cross section*, *Phys. Rev. D* **99** (2019) 95036 [[1901.09751](#)].
- [347] A. Davoli, A. De Simone, D. Marzocca and A. Morandini, *Composite 2HDM with singlets: a viable dark matter scenario*, *JHEP* **10** (2019) 196 [[1905.13244](#)].
- [348] M. Ramos, *Composite dark matter phenomenology in the presence of lighter degrees of freedom*, *JHEP* **07** (2020) 128 [[1912.11061](#)].
- [349] C. Arina et al., *Global fit of pseudo-Nambu-Goldstone Dark Matter*, *JHEP* **04** (2020) 15 [[1912.04008](#)].
- [350] Y. Abe, T. Toma and K. Tsumura, *Pseudo-Nambu-Goldstone dark matter from gauged $U(1)_{B-L}$ symmetry*, *JHEP* **05** (2020) 57 [[2001.03954](#)].
- [351] N. Okada, D. Raut and Q. Shafi, *Pseudo-Goldstone dark matter in a gauged $B - L$ extended standard model*, *Phys. Rev. D* **103** (2021) 55024 [[2001.05910](#)].
- [352] C.-Y. Xing, L.-X. Xu and S.-h. Zhu, *Softly shifting away from dark matter direct detection*, *Phys. Rev. D* **103** (2021) 113006 [[2011.06264](#)].
- [353] N. Okada, D. Raut, Q. Shafi and A. Thapa, *Pseudo-Goldstone dark matter in $SO(10)$* , *Phys. Rev. D* **104** (2021) 095002 [[2105.03419](#)].
- [354] L. Coito, C. Faubel, J. Herrero-García and A. Santamaria, *Dark matter from a complex scalar singlet: the role of dark CP and other discrete symmetries*, *JHEP* **11** (2021) 202 [[2106.05289](#)].
- [355] U. Haisch et al., *Singlet night in Feynman-ville: one-loop matching of a real scalar*, *JHEP* **04** (2020) 164 [[2003.05936](#)].
- [356] A.M. Sirunyan et al. (The CMS Collaboration), *Search for dark matter produced in association with heavy-flavor quark pairs in proton-proton collisions at $\sqrt{s} = 13$ TeV*, *Eur. Phys. J. C* **77** (2017) 845 [[1706.02581](#)].

- [357] M. Aaboud et al. (The ATLAS Collaboration), *Search for dark matter produced in association with bottom or top quarks in $\sqrt{s} = 13$ TeV pp collisions with the ATLAS detector*, *Eur. Phys. J. C* **78** (2018) 18 [[1710.11412](#)].
- [358] G. Aad et al. (The ATLAS Collaboration), *Search for new phenomena in final states with b-jets and missing transverse momentum in $\sqrt{s} = 13$ TeV pp collisions with the ATLAS detector*, [[2101.12527](#)].
- [359] T. Lin, E.W. Kolb and L.-T. Wang, *Probing dark matter couplings to top and bottom quarks at the LHC*, *Phys. Rev. D* **88** (2013) 63510 [[1303.6638](#)].
- [360] M.R. Buckley, D. Feld and D. Goncalves, *Scalar simplified models for Dark Matter*, *Phys. Rev. D* **91** (2015) 15017 [[1410.6497](#)].
- [361] U. Haisch and E. Re, *Simplified dark matter top-quark interactions at the LHC*, *JHEP* **06** (2015) 78 [[1503.00691](#)].
- [362] C. Arina et al., *A comprehensive approach to dark matter studies: exploration of simplified top-philic models*, *JHEP* **11** (2016) 111 [[1605.09242](#)].
- [363] U. Haisch, P. Pani and G. Polesello, *Determining the CP nature of spin-0 mediators in associated production of dark matter and $t\bar{t}$ pairs*, *JHEP* **02** (2017) 131 [[1611.09841](#)].
- [364] A.M. Sirunyan et al. (The CMS Collaboration), *Search for top squarks and dark matter particles in opposite-charge dilepton final states at $\sqrt{s} = 13$ TeV*, *Phys. Rev. D* **97** (2018) 32009 [[1711.00752](#)].
- [365] A.M. Sirunyan et al. (The CMS Collaboration), *Search for Dark Matter Particles Produced in Association with a Top Quark Pair at $\sqrt{s} = 13$ TeV*, *Phys. Rev. Lett.* **122** (2019) 11803 [[1807.06522](#)].
- [366] U. Haisch and G. Polesello, *Searching for production of dark matter in association with top quarks at the LHC*, *JHEP* **02** (2019) 29 [[1812.00694](#)].
- [367] G. Aad et al. (The ATLAS Collaboration), *Search for new phenomena with top quark pairs in final states with one lepton, jets, and missing transverse momentum in pp collisions at $\sqrt{s} = 13$ TeV with the ATLAS detector*, *JHEP* **04** (2021) 174 [[2012.03799](#)].
- [368] G. Aad et al. (The ATLAS Collaboration), *Search for new phenomena in events with two opposite-charge leptons, jets and missing transverse momentum in pp collisions at $\sqrt{s} = 13$ TeV with the ATLAS detector*, *JHEP* **04** (2021) 165 [[2102.01444](#)].
- [369] S. Bruggisser, F. Riva and A. Urbano, *The last gasp of dark matter effective theory*, *JHEP* **11** (2016) 69 [[1607.02475](#)].
- [370] S. Bruggisser, F. Riva and A. Urbano, *Strongly Interacting Light Dark Matter*, *SciPost Phys.* **3** (2017) 017 [[1607.02474](#)].

-
- [371] G. D'Ambrosio, G.F. Giudice, G. Isidori and A. Strumia, *Minimal flavour violation: an effective field theory approach*, *Nucl. Phys. B* **645** (2002) 155 [[hep-ph/0207036](#)].
- [372] G. Durieux, J. Gu, E. Vryonidou and C. Zhang, *Probing top-quark couplings indirectly at Higgs factories*, *Chin. Phys. C* **42** (2018) 123107 [[1809.03520](#)].
- [373] Q. Bonnefoy et al., *Comments on gauge anomalies at dimension-six in the Standard Model Effective Field Theory*, *JHEP* **05** (2021) 153 [[2012.07740](#)].
- [374] F. Feruglio, *A note on gauge anomaly cancellation in effective field theories*, *JHEP* **03** (2021) 128 [[2012.13989](#)].
- [375] J.M. Campbell, R.K. Ellis, P. Nason and E. Re, *Top-pair production and decay at NLO matched with parton showers*, *JHEP* **04** (2015) 114 [[1412.1828](#)].
- [376] E. Re, *Single-top Wt -channel production matched with parton showers using the POWHEG method*, *Eur. Phys. J. C* **71** (2011) 1547 [[1009.2450](#)].
- [377] T. Melia, P. Nason, R. Röntsch and G. Zanderighi, *W^+W^- , WZ and ZZ production in the POWHEG BOX*, *JHEP* **11** (2011) 78 [[1107.5051](#)].
- [378] P. Nason and G. Zanderighi, *W^+W^- , WZ and ZZ production in the POWHEG-BOX-V2*, *Eur. Phys. J. C* **74** (2014) 2702 [[1311.1365](#)].
- [379] M. Czakon and A. Mitov, *Top++: A program for the calculation of the top-pair cross-section at hadron colliders*, *Comput. Phys. Commun.* **185** (2014) 2930 [[1112.5675](#)].
- [380] C. Anastasiou, L.J. Dixon, K. Melnikov and F. Petriello, *High precision QCD at hadron colliders: Electroweak gauge boson rapidity distributions at next-to-next-to leading order*, *Phys. Rev. D* **69** (2004) 94008 [[hep-ph/0312266](#)].
- [381] R. Gavin, Y. Li, F. Petriello and S. Quackenbush, *W physics at the LHC with FEWZ 2.1*, *Comput. Phys. Commun.* **184** (2013) 208 [[1201.5896](#)].
- [382] U. Haisch and G. Polesello, *Searching for dark matter in final states with two jets and missing transverse energy*, *JHEP* **02** (2019) 128 [[1812.08129](#)].
- [383] U. Haisch and G. Polesello, *Resonant third-generation leptoquark signatures at the Large Hadron Collider*, *JHEP* **05** (2021) 57 [[2012.11474](#)].
- [384] S. Catani, F. Krauss, B.R. Webber and R. Kuhn, *QCD Matrix Elements + Parton Showers*, *JHEP* **11** (2002) 63 [[hep-ph/0109231](#)].
- [385] M. Cacciari, G.P. Salam and G. Soyez, *The anti- k_t jet clustering algorithm*, *JHEP* **04** (2008) 63 [[0802.1189](#)].
- [386] G. Aad et al. (The ATLAS Collaboration), *The ATLAS Experiment at the CERN Large Hadron Collider*, *JINST* **3** (2008) S08003.

- [387] G. Aad et al. (The ATLAS Collaboration), *Expected Performance of the ATLAS Experiment - Detector, Trigger and Physics*, [[0901.0512](#)].
- [388] G. Aad et al. (The ATLAS Collaboration), *ATLAS b-jet identification performance and efficiency measurement with $t\bar{t}$ events in pp collisions at $\sqrt{s} = 13$ TeV*, *Eur. Phys. J. C* **79** (2019) 970 [[1907.05120](#)].
- [389] U. Haisch and G. Polesello, *Searching for heavy Higgs bosons in the $t\bar{t}Z$ and tbW final states*, *JHEP* **09** (2018) 151 [[1807.07734](#)].
- [390] M.L. Graesser and J. Shelton, *Hunting Mixed Top Squark Decays*, *Phys. Rev. Lett.* **111** (2013) 121802 [[1212.4495](#)].
- [391] G. Aad et al. (The ATLAS Collaboration), *Search for top squark pair production in final states with one isolated lepton, jets, and missing transverse momentum in $\sqrt{s} = 8$ TeV pp collisions with the ATLAS detector*, *JHEP* **11** (2014) 118 [[1407.0583](#)].
- [392] The ATLAS Collaboration, *Object-based missing transverse momentum significance in the ATLAS detector*, Tech. Rep. [ATLAS-CONF-2018-038](#), CERN, Geneva (2018).
- [393] C.G. Lester and D.J. Summers, *Measuring masses of semiinvisibly decaying particles pair produced at hadron colliders*, *Phys. Lett. B* **463** (1999) 99 [[hep-ph/9906349](#)].
- [394] G. Aad et al. (The ATLAS Collaboration), *Search for a scalar partner of the top quark in the all-hadronic $t\bar{t}$ plus missing transverse momentum final state at $\sqrt{s} = 13$ TeV with the ATLAS detector*, *Eur. Phys. J. C* **80** (2020) 737 [[2004.14060](#)].
- [395] M. Aaboud et al. (The ATLAS Collaboration), *Search for new phenomena in final states with an energetic jet and large missing transverse momentum in pp collisions at $\sqrt{s} = 13$ TeV using the ATLAS detector*, *Phys. Rev. D* **94** (2016) 32005 [[1604.07773](#)].
- [396] M. Aaboud et al. (The ATLAS Collaboration), *Search for dark matter and other new phenomena in events with an energetic jet and large missing transverse momentum using the ATLAS detector*, *JHEP* **01** (2018) 126 [[1711.03301](#)].
- [397] A.M. Sirunyan et al. (The CMS Collaboration), *Search for dark matter produced with an energetic jet or a hadronically decaying W or Z boson at $\sqrt{s} = 13$ TeV*, *JHEP* **07** (2017) 14 [[1703.01651](#)].
- [398] The ATLAS Collaboration, *Search for new phenomena in events with jets and missing transverse momentum in pp collisions at $\sqrt{s} = 13$ TeV with the ATLAS detector*, Tech. Rep. [ATLAS-CONF-2020-048](#), CERN, Geneva (jul, 2020).
- [399] J.M. Lindert et al., *Precise predictions for V+ jets dark matter backgrounds*, *Eur. Phys. J. C* **77** (2017) 829 [[1705.04664](#)].
- [400] A.L. Read, *Presentation of search results: the CL_s technique*, *J. Phys.* **G28** (2002) 2693.
- [401] L. Moneta et al., *The RooStats Project*, *PoS ACAT2010* (2010) 57 [[1009.1003](#)].

-
- [402] The ATLAS Collaboration, *Combination of searches for invisible Higgs boson decays with the ATLAS experiment*, Tech. Rep. [ATLAS-CONF-2020-052](#), CERN, Geneva (oct, 2020).
- [403] M. Cepeda et al., *Report from Working Group 2: Higgs Physics at the HL-LHC and HE-LHC*, *Cern Yellow Rep. Monogr.* **7** (2019) 221 [[1902.00134](#)].
- [404] G. Passarino and M.J.G. Veltman, *One-loop corrections for e^+e^- annihilation into $\mu^+\mu^-$ in the Weinberg model*, *Nucl. Phys. B* **160** (1979) 151.
- [405] R.K. Ellis and G. Zanderighi, *Scalar one-loop integrals for QCD*, *JHEP* **02** (2008) 2 [[0712.1851](#)].
- [406] R.K. Ellis, Z. Kunszt, K. Melnikov and G. Zanderighi, *One-loop calculations in quantum field theory: From Feynman diagrams to unitarity cuts*, *Phys. Rep.* **518** (2012) 141 [[1105.4319](#)].
- [407] E.E. Jenkins, A.V. Manohar and M. Trott, *Renormalization group evolution of the standard model dimension six operators. I: formalism and λ dependence*, *JHEP* **10** (2013) 87 [[1308.2627](#)].
- [408] J. Hisano, K. Ishiwata and N. Nagata, *Gluon contribution to the dark matter direct detection*, *Phys. Rev. D* **82** (2010) 115007 [[1007.2601](#)].
- [409] M. Freytsis and Z. Ligeti, *On dark matter models with uniquely spin-dependent detection possibilities*, *Phys. Rev. D* **83** (2011) 115009 [[1012.5317](#)].
- [410] J. Hisano, K. Ishiwata, N. Nagata and T. Takesako, *Direct detection of electroweak-interacting dark matter*, *JHEP* **07** (2011) 5 [[1104.0228](#)].
- [411] R.J. Hill and M.P. Solon, *Universal behavior in the scattering of heavy, weakly interacting dark matter on nuclear targets*, *Phys. Lett. B* **707** (2012) 539 [[1111.0016](#)].
- [412] M.T. Frandsen et al., *Loop-induced dark matter direct detection signals from γ -ray lines*, *JCAP* **10** (2012) 33 [[1207.3971](#)].
- [413] U. Haisch and F. Kahlhoefer, *On the importance of loop-induced spin-independent interactions for dark matter direct detection*, *JCAP* **04** (2013) 50 [[1302.4454](#)].
- [414] R.J. Hill and M.P. Solon, *WIMP-nucleon scattering with heavy WIMP effective theory*, *Phys. Rev. Lett.* **112** (2014) 211602 [[1309.4092](#)].
- [415] A. Crivellin, F. D'Eramo and M. Procura, *New Constraints on Dark Matter Effective Theories from Standard Model Loops*, *Phys. Rev. Lett.* **112** (2014) 191304 [[1402.1173](#)].
- [416] A. Crivellin and U. Haisch, *Dark matter direct detection constraints from gauge bosons loops*, *Phys. Rev. D* **90** (2014) 115011 [[1408.5046](#)].

- [417] F. D’Eramo and M. Procura, *Connecting dark matter UV complete models to direct detection rates via effective field theory*, *JHEP* **04** (2015) 54 [[1411.3342](#)].
- [418] F. D’Eramo, B.J. Kavanagh and P. Panci, *You can hide but you have to run: direct detection with vector mediators*, *JHEP* **08** (2016) 111 [[1605.04917](#)].
- [419] F. Bishara, J. Brod, B. Grinstein and J. Zupan, *Renormalization group effects in dark matter interactions*, *JHEP* **03** (2020) 89 [[1809.03506](#)].
- [420] B.A. Dobrescu and I. Mocioiu, *Spin-dependent macroscopic forces from new particle exchange*, *JHEP* **11** (2006) 5 [[hep-ph/0605342](#)].
- [421] A.L. Fitzpatrick et al., *The effective field theory of dark matter direct detection*, *JCAP* **02** (2013) 4 [[1203.3542](#)].
- [422] N. Anand, A.L. Fitzpatrick and W.C. Haxton, *Weakly interacting massive particle-nucleus elastic scattering response*, *Phys. Rev. C* **89** (2014) 65501 [[1308.6288](#)].
- [423] E. Del Nobile, *Complete Lorentz-to-Galileo dictionary for direct dark matter detection*, *Phys. Rev. D* **98** (2018) 123003 [[1806.01291](#)].
- [424] P. Junnarkar and A. Walker-Loud, *Scalar strange content of the nucleon from lattice QCD*, *Phys. Rev. D* **87** (2013) 114510 [[1301.1114](#)].
- [425] M. Hoferichter, J. de Elvira, B. Kubis and U.-G. Meissner, *High-Precision Determination of the Pion-Nucleon σ Term from Roy-Steiner Equations*, *Phys. Rev. Lett.* **115** (2015) 92301 [[1506.04142](#)].
- [426] E.W. Kolb and M. Turner, *The Early Universe*, Westview Press (1990).
- [427] P. Gondolo and G. Gelmini, *Cosmic abundances of stable particles: Improved analysis*, *Nucl.Phys.* **B360** (1991) 145.
- [428] S. Profumo, *An Introduction to Particle Dark Matter*, World Scientific (2017).
- [429] J. McDonald, *Gauge singlet scalars as cold dark matter*, *Phys. Rev. D* **50** (1994) 3637 [[hep-ph/0702143](#)].
- [430] L.D. Landau, *On the angular momentum of a system of two photons*, *Dokl. Akad. Nauk SSSR* **60** (1948) 207.
- [431] C.-N. Yang, *Selection Rules for the Dematerialization of a Particle Into Two Photons*, *Phys. Rev.* **77** (1950) 242.
- [432] A. Djouadi, *The anatomy of electroweak symmetry breaking: Tome I: The Higgs boson in the Standard Model*, *Phys. Rept.* **457** (2008) 1 [[hep-ph/0503172](#)].
- [433] M. Bauer and T. Plehn, *Yet Another Introduction to Dark Matter*, *Lect. Notes Phys.* **959** (2019) [[1705.01987](#)].

-
- [434] A. Albert et al. (The Fermi-LAT and DES Collaborations), *Searching for Dark Matter Annihilation in Recently Discovered Milky Way Satellites with Fermi-LAT*, *Astrophys. J.* **834** (2017) 110 [[1611.03184](#)].
- [435] M. Ackermann et al. (The Fermi-LAT Collaboration), *Updated search for spectral lines from Galactic dark matter interactions with pass 8 data from the Fermi Large Area Telescope*, *Phys. Rev. D* **91** (2015) 122002 [[1506.00013](#)].
- [436] J.F. Navarro, C.S. Frenk and S.D.M. White, *The Structure of Cold Dark Matter Halos*, *Astrophys. J.* **462** (1996) 563 [[astro-ph/9508025](#)].
- [437] M. Aaboud et al. (The ATLAS Collaboration), *Combination of Searches for Invisible Higgs Boson Decays with the ATLAS Experiment*, *Phys. Rev. Lett.* **122** (2019) 231801 [[1904.05105](#)].
- [438] A.M. Sirunyan et al. (The CMS Collaboration), *Search for invisible decays of a Higgs boson produced through vector boson fusion in proton-proton collisions at $\sqrt{s} = 13$ TeV*, *Phys. Lett. B* **793** (2019) 520 [[1809.05937](#)].
- [439] The CMS Collaboration, *First constraints on invisible Higgs boson decays using $t\bar{t}H$ production at $\sqrt{s} = 13$ TeV*, Tech. Rep. [CMS-PAS-HIG-18-008](#), CERN, Geneva (2019).
- [440] S. Matsumoto et al., *Observing the Coupling between Dark Matter and Higgs Boson at the ILC*, in *Int. Linear Collid. Work.*, 2010 [[1006.5268](#)].
- [441] S. Kanemura, S. Matsumoto, T. Nabeshima and H. Taniguchi, *Testing Higgs portal dark matter via Z fusion at a linear collider*, *Phys. Lett. B* **701** (2011) 591 [[1102.5147](#)].
- [442] Z. Chacko, Y. Cui and S. Hong, *Exploring a dark sector through the Higgs portal at a lepton collider*, *Phys. Lett. B* **732** (2014) 75 [[1311.3306](#)].
- [443] N. Craig, H.K. Lou, M. McCullough and A. Thalappilil, *The Higgs portal above threshold*, *JHEP* **02** (2016) 127 [[1412.0258](#)].
- [444] P. Ko and H. Yokoya, *Search for Higgs portal DM at the ILC*, *JHEP* **08** (2016) 109 [[1603.04737](#)].
- [445] J.C. Pati and A. Salam, *Unified Lepton-Hadron Symmetry and a Gauge Theory of the Basic Interactions*, *Phys. Rev. D* **8** (1973) 1240.
- [446] D. Croon et al., *GUT Physics in the Era of the LHC*, *Front. Phys.* **7** (2019) 76 [[1903.04977](#)].
- [447] W. Altmannshofer, P.S.B. Dev, A. Soni and Y. Sui, *Addressing $R_{D^{(*)}}$, $R_{K^{(*)}}$, muon $g - 2$ and ANITA anomalies in a minimal R -parity violating supersymmetric framework*, *Phys. Rev. D* **102** (2020) 015031 [[2002.12910](#)].
- [448] B. Gripaios, *Composite leptoquarks at the LHC*, *JHEP* **02** (2010) 45 [[0910.1789](#)].

- [449] B. Gripaios, A. Papaefstathiou, K. Sakurai and B. Webber, *Searching for third-generation composite leptoquarks at the LHC*, *JHEP* **01** (2011) 156 [[1010.3962](#)].
- [450] B. Gripaios, M. Nardecchia and S.A. Renner, *Composite leptoquarks and anomalies in B-meson decays*, *JHEP* **05** (2015) 6 [[1412.1791](#)].
- [451] R. Barbieri and A. Tesi, *B-decay anomalies in Pati-Salam SU(4)*, *Eur. Phys. J. C* **78** (2018) 193 [[1712.06844](#)].
- [452] D. Marzocca, *Addressing the B-physics anomalies in a fundamental Composite Higgs model*, *JHEP* **07** (2018) 121 [[1803.10972](#)].
- [453] I. Doršner et al., *Physics of leptoquarks in precision experiments and at particle colliders*, *Phys. Rep.* **641** (2016) 1 [[1603.04993](#)].
- [454] The CMS Collaboration, *Searches for additional Higgs bosons and for vector Leptoquarks in $\tau\tau$ final states in proton-proton collisions at $\sqrt{s} = 13$ TeV*, *CMS-HIG-21-001* (2022) [[2208.02717](#)].
- [455] The CMS Collaboration, *Search for a third-generation leptoquark coupling to a τ lepton and a b quark through single, pair and nonresonant production at $\sqrt{s} = 13$ TeV*, *CMS-PAS-EXO-19-016* (2022) .
- [456] S.D. Drell and T.-M. Yan, *Massive Lepton-Pair Production in Hadron-Hadron Collisions at High Energies*, *Phys. Rev. Lett.* **25** (1970) 316.
- [457] W. Buchmüller, R. Rückl and D. Wyler, *Leptoquarks in lepton-quark collisions*, *Phys. Lett. B* **191** (1987) 442.
- [458] I. Doršner and A. Greljo, *Leptoquark toolbox for precision collider studies*, *JHEP* **05** (2018) 126 [[1801.07641](#)].
- [459] A. Crivellin and L. Schnell, *Complete Lagrangian and set of Feynman rules for scalar leptoquarks*, *Comput. Phys. Commun.* **271** (2022) 108188 [[2105.04844](#)].
- [460] M. Schmaltz and Y.-M. Zhong, *The leptoquark Hunter's Guide: large coupling*, *JHEP* **01** (2019) 132 [[1810.10017](#)].
- [461] M. Krämer, T. Plehn, M. Spira and P.M. Zerwas, *Pair Production of Scalar Leptoquarks at the Fermilab Tevatron*, *Phys. Rev. Lett.* **79** (1997) 341 [[hep-ph/9704322](#)].
- [462] M. Krämer, T. Plehn, M. Spira and P.M. Zerwas, *Pair production of scalar leptoquarks at the CERN LHC*, *Phys. Rev. D* **71** (2005) 57503 [[hep-ph/0411038](#)].
- [463] J. Blümlein, E. Boos and A. Kryukov, *Leptoquark pair production in hadronic interactions*, *Zeitschrift für Phys. C Part. Fields* **76** (1997) 137 [[hep-ph/9610408](#)].
- [464] J. Blümlein, E. Boos and A. Kryukov, *Leptoquark Pair Production Cross Sections at Hadron Colliders*, [[hep-ph/9811271](#)].

-
- [465] T. Mandal, S. Mitra and S. Seth, *Pair production of scalar leptoquarks at the LHC to NLO parton shower accuracy*, *Phys. Rev. D* **93** (2016) 035018 [[1506.07369](#)].
- [466] V. Khachatryan et al. (The CMS Collaboration), *Search for Pair Production of First-Generation Scalar Leptoquarks in pp Collisions at $\sqrt{s} = 7$ TeV*, *Phys. Rev. Lett.* **106** (2011) 201802 [[1012.4031](#)].
- [467] V. Khachatryan et al. (The CMS Collaboration), *Search for Pair Production of Second-Generation Scalar Leptoquarks in pp Collisions at $\sqrt{s} = 7$ TeV*, *Phys. Rev. Lett.* **106** (2011) 201803 [[1012.4033](#)].
- [468] G. Aad et al. (The ATLAS Collaboration), *Search for first generation scalar leptoquarks in pp collisions at $\sqrt{s} = 7$ TeV with the ATLAS detector*, *Phys. Lett. B* **709** (2012) 158 [[1112.4828](#)].
- [469] G. Aad et al. (The ATLAS Collaboration), *Search for pair production of first or second generation leptoquarks in proton-proton collisions at $\sqrt{s} = 7$ TeV using the ATLAS detector at the LHC*, *Phys. Rev. D* **83** (2011) 112006 [[1104.4481](#)].
- [470] S. Chatrchyan et al. (The CMS Collaboration), *Search for first generation scalar leptoquarks in the $evjj$ channel in pp collisions at $\sqrt{s} = 7$ TeV*, *Phys. Lett. B* **703** (2011) 246 [[1105.5237](#)].
- [471] G. Aad et al. (The ATLAS Collaboration), *Search for second generation scalar leptoquarks in pp collisions at $\sqrt{s} = 7$ TeV with the ATLAS detector*, *Eur. Phys. J. C* **72** (2012) 2151 [[1203.3172](#)].
- [472] S. Chatrchyan et al. (The CMS Collaboration), *Search for pair production of first- and second-generation scalar leptoquarks in pp collisions at $\sqrt{s} = 7$ TeV*, *Phys. Rev. D* **86** (2012) 052013 [[1207.5406](#)].
- [473] S. Chatrchyan et al. (The CMS Collaboration), *Search for Pair Production of Third-Generation Leptoquarks and Top Squarks in pp Collisions at $\sqrt{s} = 7$ TeV*, *Phys. Rev. Lett.* **110** (2013) 081801 [[1210.5629](#)].
- [474] S. Chatrchyan et al. (The CMS Collaboration), *Search for Third-Generation Leptoquarks and Scalar Bottom Quarks in pp Collisions at $\sqrt{s} = 7$ TeV*, *JHEP* **12** (2012) 55 [[1210.5627](#)].
- [475] G. Aad et al. (The ATLAS Collaboration), *Search for third generation scalar leptoquarks in pp collisions at $\sqrt{s} = 7$ TeV with the ATLAS detector*, *JHEP* **06** (2013) 33 [[1303.0526](#)].
- [476] V. Khachatryan et al. (The CMS Collaboration), *Search for pair production of third-generation scalar leptoquarks and top squarks in proton-proton collisions at $\sqrt{s} = 8$ TeV*, *Phys. Lett. B* **739** (2014) 229 [[1408.0806](#)].

- [477] G. Aad et al. (The ATLAS Collaboration), *Searches for scalar leptoquarks in pp collisions at $\sqrt{s} = 8$ TeV with the ATLAS detector*, *Eur. Phys. J. C* **76** (2016) 5 [[1508.04735](#)].
- [478] V. Khachatryan et al. (The CMS Collaboration), *Search for pair production of first and second generation leptoquarks in proton-proton collisions at $\sqrt{s} = 8$ TeV*, *Phys. Rev. D* **93** (2016) 032004 [[1509.03744](#)].
- [479] V. Khachatryan et al. (The CMS Collaboration), *Search for third-generation scalar leptoquarks in the $t\bar{t}$ channel in proton-proton collisions at $\sqrt{s} = 8$ TeV*, *JHEP* **11** (2016) 56 [[1503.09049](#)].
- [480] M. Aaboud et al. (The ATLAS Collaboration), *Search for scalar leptoquarks in pp collisions at $\sqrt{s} = 13$ TeV with the ATLAS experiment*, *New J. Phys.* **18** (2016) 93016 [[1605.06035](#)].
- [481] The CMS Collaboration, *Search for pair-production of second-generation scalar leptoquarks in pp collisions at $\sqrt{s} = 13$ TeV with the CMS detector*, *CMS-PAS-EXO-16-007* (2016) .
- [482] V. Khachatryan et al. (The CMS Collaboration), *Search for heavy neutrinos or third-generation leptoquarks in final states with two hadronically decaying τ leptons and two jets in proton-proton collisions at $\sqrt{s} = 13$ TeV*, *JHEP* **03** (2017) 77 [[1612.01190](#)].
- [483] A.M. Sirunyan et al. (The CMS Collaboration), *Search for third-generation scalar leptoquarks and heavy right-handed neutrinos in final states with two tau leptons and two jets in proton-proton collisions at $\sqrt{s} = 13$ TeV*, *JHEP* **07** (2017) 121 [[1703.03995](#)].
- [484] B. Schrempp and F. Schrempp, *Light leptoquarks*, *Phys. Lett. B* **153** (1985) 101.
- [485] L. Buonocore, P. Nason, F. Tramontano and G. Zanderighi, *Leptons in the proton*, *JHEP* **08** (2020) 19 [[2005.06477](#)].
- [486] L. Buonocore et al., *Lepton-Quark Collisions at the Large Hadron Collider*, *Phys. Rev. Lett.* **125** (2020) 231804 [[2005.06475](#)].
- [487] A. Greljo and N. Selimović, *Lepton-quark fusion at Hadron Colliders, precisely*, *JHEP* **03** (2021) 279 [[2012.02092](#)].
- [488] L. Buonocore et al., *Resonant leptoquark at NLO with POWHEG*, *JHEP* **11** (2022) 129 [[2209.02599](#)].
- [489] V. Khachatryan et al. (The CMS Collaboration), *Search for single production of scalar leptoquarks in proton-proton collisions at $\sqrt{s} = 8$ TeV*, *Phys. Rev. D* **93** (2016) 032005 [[1509.03750](#)].
- [490] N. Raj, *Anticipating nonresonant new physics in dilepton angular spectra at the LHC*, *Phys. Rev. D* **95** (2017) 015011 [[1610.03795](#)].

-
- [491] Y. Afik et al., *Establishing a search for $b \rightarrow s\ell^+\ell^-$ anomalies at the LHC*, *JHEP* **08** (2018) 56 [[1805.11402](#)].
- [492] Y. Afik, S. Bar-Shalom, J. Cohen and Y. Rozen, *Searching for New Physics with $b\bar{b}\ell^+\ell^-$ contact interactions*, *Phys. Lett. B* **807** (2020) 135541 [[1912.00425](#)].
- [493] G. Aad et al. (The ATLAS Collaboration), *Search for Heavy Higgs Bosons Decaying into Two Tau Leptons with the ATLAS Detector Using pp Collisions at $\sqrt{s} = 13$ TeV*, *Phys. Rev. Lett.* **125** (2020) 051801 [[2002.12223](#)].
- [494] G. Aad et al. (The ATLAS Collaboration), *Search for New Phenomena in Final States with Two Leptons and One or No b -Tagged Jets at $\sqrt{s} = 13$ TeV Using the ATLAS Detector*, *Phys. Rev. Lett.* **127** (2021) 141801 [[2105.13847](#)].
- [495] A. Crivellin, C.A. Manzari and M. Montull, *Correlating nonresonant di-electron searches at the LHC to the Cabibbo-angle anomaly and lepton flavor universality violation*, *Phys. Rev. D* **104** (2021) 115016 [[2103.12003](#)].
- [496] G. Aad et al. (The ATLAS Collaboration), *Search for new non-resonant phenomena in high-mass dilepton final states with the ATLAS detector*, *JHEP* **11** (2020) 5 [[2006.12946](#)].
- [497] S. Frixione, Z. Kunszt and A. Signer, *Three-jet cross sections to next-to-leading order*, *Nucl. Phys. B* **467** (1996) 399 [[hep-ph/9512328](#)].
- [498] S. Frixione, *A general approach to jet cross sections in QCD*, *Nucl. Phys. B* **507** (1997) 295 [[hep-ph/9706545](#)].
- [499] A.M. Sirunyan et al. (The CMS Collaboration), *Search for resonant and nonresonant new phenomena in high-mass dilepton final states at $\sqrt{s} = 13$ TeV*, *JHEP* **07** (2021) 208 [[2103.02708](#)].
- [500] P. Ciafaloni and D. Comelli, *Sudakov effects in electroweak corrections*, *Phys. Lett. B* **446** (1999) 278 [[hep-ph/9809321](#)].
- [501] G. Aad et al. (The ATLAS Collaboration), *Muon reconstruction performance of the ATLAS detector in proton–proton collision data at $\sqrt{s} = 13$ TeV*, *Eur. Phys. J. C* **76** (2016) 292 [[1603.05598](#)].
- [502] G. Aad et al. (The ATLAS Collaboration), *Performance of the ATLAS muon triggers in Run 2*, *JINST* **15** (2020) P09015 [[2004.13447](#)].
- [503] D.A. Faroughy, A. Greljo and J.F. Kamenik, *Confronting lepton flavor universality violation in B decays with high- p_T tau lepton searches at LHC*, *Phys. Lett. B* **764** (2017) 126 [[1609.07138](#)].

- [504] T. Mandal, S. Mitra and S. Raz, $R_{D^{(*)}}$ motivated \mathcal{S}_1 leptoquark scenarios: Impact of interference on the exclusion limits from LHC data, *Phys. Rev. D* **99** (2019) 055028 [[1811.03561](#)].
- [505] M.J. Baker, J. Fuentes-Martín, G. Isidori and M. König, High- p_T signatures in vector-leptoquark models, *Eur. Phys. J. C* **79** (2019) 334 [[1901.10480](#)].
- [506] D. Choudhury, N. Kumar and A. Kundu, Search for an opposite sign muon-tau pair and a b-jet at the LHC in the context of flavor anomalies, *Phys. Rev. D* **100** (2019) 075001 [[1905.07982](#)].
- [507] A. Tumasyan et al. (The CMS Collaboration), Identification of hadronic tau lepton decays using a deep neural network, *J. Instrum.* **17** (2022) P07023 [[2201.08458](#)].
- [508] A.M. Sirunyan et al. (The CMS Collaboration), Identification of heavy-flavour jets with the CMS detector in pp collisions at 13 TeV, *JINST* **13** (2018) P05011 [[1712.07158](#)].
- [509] E. Bols et al., Jet flavour classification using DeepJet, *JINST* **15** (2020) P12012 [[2008.10519](#)].
- [510] G. Aad et al. (The ATLAS Collaboration), Search for neutral Higgs bosons of the minimal supersymmetric standard model in pp collisions at $\sqrt{s} = 8$ TeV with the ATLAS detector, *JHEP* **11** (2014) 56 [[1409.6064](#)].
- [511] G. Aad et al. (The ATLAS Collaboration), Search for pairs of scalar leptoquarks decaying into quarks and electrons or muons in $\sqrt{s} = 13$ TeV pp collisions with the ATLAS detector, *JHEP* **10** (2020) 112 [[2006.05872](#)].
- [512] G. Aad et al. (The ATLAS Collaboration), Search for new phenomena in pp collisions in final states with tau leptons, b-jets, and missing transverse momentum with the ATLAS detector, *Phys. Rev. D* **104** (2021) 112005 [[2108.07665](#)].
- [513] G. Cowan, K. Cranmer, E. Gross and O. Vitells, Asymptotic formulae for likelihood-based tests of new physics, *Eur. Phys. J. C* **71** (2011) 1554 [[1007.1727](#)].
- [514] H. Qu and L. Gouskos, Jet tagging via particle clouds, *Phys. Rev. D* **101** (2020) 056019 [[1902.08570](#)].
- [515] G. Aad et al. (The ATLAS Collaboration), Direct constraint on the Higgs-charm coupling from a search for Higgs boson decays into charm quarks with the ATLAS detector, *Eur. Phys. J. C* **82** (2022) 717 [[2201.11428](#)].
- [516] The CMS Collaboration, Search for Higgs boson decay to a charm quark-antiquark pair in proton-proton collisions at $\sqrt{s} = 13$ TeV, *CMS-HIG-21-008* (2022) [[2205.05550](#)].
- [517] A. Greljo and B.A. Stefanek, Third family quark-lepton unification at the TeV scale, *Phys. Lett. B* **782** (2018) 131 [[1802.04274](#)].

-
- [518] J. Fuentes-Martín, G. Isidori, M. König and N. Selimović, *Vector leptoquarks beyond tree level. II. $\mathcal{O}(\alpha_s)$ corrections and radial modes*, *Phys. Rev. D* **102** (2020) 1 [2006.16250].
- [519] H. Georgi and Y. Nakai, *Diphoton Resonance from a New Strong Force*, *Phys. Rev. D* **94** (2016) 075005 [1606.05865].
- [520] L. Di Luzio, A. Greljo and M. Nardecchia, *Gauge leptoquark as the origin of B-physics anomalies*, *Phys. Rev. D* **96** (2017) 115011 [1708.08450].
- [521] M. Bordone, C. Cornella, J. Fuentes-Martín and G. Isidori, *A three-site gauge model for flavor hierarchies and flavor anomalies*, *Phys. Lett. B* **779** (2018) 317 [1712.01368].
- [522] M. Bordone, C. Cornella, J. Fuentes-Martín and G. Isidori, *Low-energy signatures of the PS^3 model: from B-physics anomalies to LFV*, *JHEP* **10** (2018) 148 [1805.09328].
- [523] L. Di Luzio et al., *Maximal flavour violation: a Cabibbo mechanism for leptoquarks*, *JHEP* **11** (2018) 81 [1808.00942].
- [524] C. Cornella, J. Fuentes-Martín and G. Isidori, *Revisiting the vector leptoquark explanation of the B-physics anomalies*, *JHEP* **07** (2019) 168 [1903.11517].
- [525] J. Fuentes-Martín and P. Stangl, *Third-family quark-lepton unification with a fundamental composite Higgs*, *Phys. Lett. B* **811** (2020) 135953 [2004.11376].
- [526] D. Guadagnoli, M. Reboud and P. Stangl, *The dark side of 4321*, *JHEP* **10** (2020) 84 [2005.10117].
- [527] V. Shtabovenko, *FeynHelpers: Connecting FeynCalc to FIRE and Package-X*, *Comput. Phys. Commun.* **218** (2017) 48 [1611.06793].
- [528] J. Fuentes-Martín, G. Isidori, M. König and N. Selimović, *Vector leptoquarks beyond tree level*, *Phys. Rev. D* **101** (2020) 1 [1910.13474].
- [529] A. Angelescu et al., *Single leptoquark solutions to the B-physics anomalies*, *Phys. Rev. D* **104** (2021) 055017 [2103.12504].
- [530] A. Bhaskar et al., *Precise limits on the charge-2/3 U_1 vector leptoquark*, *Phys. Rev. D* **104** (2021) 035016 [2101.12069].
- [531] A.M. Sirunyan et al. (The CMS Collaboration), *Search for singly and pair-produced leptoquarks coupling to third-generation fermions in proton-proton collisions at $\sqrt{s} = 13$ TeV*, *Phys. Lett. B* **819** (2021) 136446 [2012.04178].
- [532] The ATLAS Collaboration, *Measurement of the tau lepton reconstruction and identification performance in the ATLAS experiment using pp collisions at $\sqrt{s} = 13$ TeV*, *ATLAS-CONF-2017-029* (2017) .

- [533] A.M. Sirunyan et al. (The CMS Collaboration), *Performance of reconstruction and identification of τ leptons decaying to hadrons and ν_τ in pp collisions at $\sqrt{s} = 13$ TeV*, *JINST* **13** (2018) P10005 [[1809.02816](#)].
- [534] D. Guest et al., *Jet flavor classification in high-energy physics with deep neural networks*, *Phys. Rev. D* **94** (2016) 112002 [[1607.08633](#)].
- [535] A. Tumasyan et al. (The CMS Collaboration), *Measurement of the Drell-Yan forward-backward asymmetry at high dilepton masses in proton-proton collisions at $\sqrt{s} = 13$ TeV*, *JHEP* **08** (2022) 063 [[2202.12327](#)].
- [536] J.C. Collins and D.E. Soper, *Angular distribution of dileptons in high-energy hadron collisions*, *Phys. Rev. D* **16** (1977) 2219.
- [537] W. Altmannshofer, P.S. Bhupal Dev and A. Soni, *$R_{D^{(*)}}$ anomaly: A possible hint for natural supersymmetry with R -parity violation*, *Phys. Rev. D* **96** (2017) 095010 [[1704.06659](#)].
- [538] S. Iguro and K. Tobe, *$R(D^{(*)})$ in a general two Higgs doublet model*, *Nucl. Phys. B* **925** (2017) 560 [[1708.06176](#)].
- [539] M. Abdullah et al., *Probing a simplified W' model of $R(D^{(*)})$ anomalies using b tags, τ leptons, and missing energy*, *Phys. Rev. D* **98** (2018) 055016 [[1805.01869](#)].
- [540] D. Marzocca, U. Min and M. Son, *Bottom-flavored mono-tau tails at the LHC*, *JHEP* **12** (2020) 35 [[2008.07541](#)].
- [541] M. Endo et al., *Non-resonant new physics search at the LHC for the $b \rightarrow c\tau\nu$ anomalies*, *JHEP* **02** (2022) 106 [[2111.04748](#)].
- [542] J. Alwall et al., *Comparative study of various algorithms for the merging of parton showers and matrix elements in hadronic collisions*, *Eur. Phys. J. C* **53** (2008) 473 [[0706.2569](#)].
- [543] S. Alekhin, A. Djouadi and S. Moch, *The top quark and Higgs boson masses and the stability of the electroweak vacuum*, *Phys. Lett. B* **716** (2012) 214 [[1207.0980](#)].
- [544] G. Bertone, D. Hooper and J. Silk, *Particle dark matter: Evidence, candidates and constraints*, *Phys. Rept.* **405** (2005) 279 [[hep-ph/0404175](#)].
- [545] A. Friedmann, *Über die Möglichkeit einer Welt mit konstanter negativer Krümmung des Raumes*, *Z. Phys.* **21** (1924) 326.
- [546] G. Lemaître, *Republication of: A homogeneous universe of constant mass and growing radius accounting for the radial velocity of extra-galactic nebulae*, *Gen. Relativ. Gravit.* **45** (2013) 1635.
- [547] G. Lemaître, *The Expanding Universe*, *Gen. Relativ. Gravit.* **29** (1997) 641.

- [548] H.P. Robertson, *Kinematics and World-Structure*, *Astrophys. J.* **82** (1935) 284.
- [549] A. Walker, *On Milne's Theory of World-Structure*, *Proc. London Math. Soc.* **42** (1937) 90.
- [550] E. Hubble, *A relation between distance and radial velocity among extra-galactic nebulae*, *Proc. Nat. Acad. Sci.* **15** (1929) 168.
- [551] M. Srednicki, R. Watkins and K.A. Olive, *Calculations of relic densities in the early universe*, *Nucl.Phys.* **B310** (1988) 693.